NUMERICAL MODELLING OF TUNED LIQUID DAMPERS USING IMPLICIT SPH

NUMERICAL MODELLING OF

TUNED LIQUID DAMPERS USING

IMPLICIT SMOOTHED PARTICLE HYDRODYNAMICS

By

BISHOY NADI AWAD, B.Sc., M.Sc.

A Thesis Submitted to the School of Graduate Studies

In Partial Fulfillment of the Requirements

For the Degree

Doctor of Philosophy

DOCTOR OF PHYLOSIPHY (2023) McMaster University

(Civil Engineering) Hamilton, Ontario

TITLE: Numerical Modelling of Tuned Liquid Dampers Using Implicit Smoothed Particle Hydrodynamics

AUTHOR: Bishoy Nadi Awad, B.Sc., M.Sc. (McMaster University, Hamilton, Ontario)

SUPERVISOR: Professor Michael J. Tait

NUMBER OF PAGER: vii, xxv

LAY ABSTRACT

Modern skyscrapers are both tall and made of lightweight materials, and as such wind-induced motions can lead to occupant discomfort and service operation (e.g., elevators) issues. A tuned liquid damper (TLD) is a partially filled water tank often installed near the top of the structure to reduce resonant building motion through water sloshing. TLDs are often outfitted with screens to improve their damping performance. The fluid motion within a TLD equipped with screens is complex; however, accurately modelling its response is necessary to achieve a suitable performance level. This study presents an efficient computer model to accurately simulate the response of a TLD using practical computational power. The model results are validated against physical test data. Findings reveal that the proposed computer model can be a robust tool in simulating complex real-world TLD applications.

ABSTRACT

Tuned liquid dampers (TLDs) are one of the most common systems used to control the resonant response of buildings due to their simplicity and affordability. A TLD comprises a partially water-filled tank, which can be of different shapes, installed near the top of the building and tuned to the natural frequency of the building. Typically, the inherent damping of the TLD is improved by adding additional damping devices, such as screens. Studying the nonlinear flow of TLDs is imperative for designers in order to understand their response, and numerical modelling is essential for their effective design. Existing numerical models are typically restricted to a range of liquid depths, excitation amplitudes, tank-bottom geometries, and screen implementation configurations or require significant computational time and resources.

Motivated by designer needs and existing limitations described above, this research aims to develop a computationally efficient numerical model to simulate TLDs equipped with screens without the current restrictions. The model is based on solving the free-surface flow of the TLD using the mesh-free Smoothed Particle Hydrodynamics (SPH) method. The model is complemented by a novel macroscopic screen model, which allows for larger computational resolution and a significant reduction in computational time compared to explicitly modelling the screens. Model results are validated using a wide range of experimental data, with a good agreement observed.

The model is expanded to include tanks with irregular bottom geometries using an efficient particle-generating algorithm, and their response is studied under large harmonic excitation amplitudes. Finally, the model is used to investigate a realistic situation of a dual-function tank coupled to a structure to study its response under random excitation. It is found that the model

efficiently captured the response of the structure under a range of excitation amplitudes using reasonable computational time and resources.

To my one and only, *Sara.*

ACKNOWLEDGEMENTS

"The Lord was with Joseph so that he prospered" Genesis 39:2

First and foremost, I would like to praise and thank God, the Almighty, for His graces, unconditional love, and guidance throughout all the challenging moments of my life.

I want to convey my utmost gratitude and appreciation to my supervisor Dr. Michael Tait for his continued support and valuable guidance. His unique supervision, encouragement, and mentoring have always been appreciated. I also want to thank Dr. Tait for his flexibility and understanding during the numerous occasions and the pandemic. I would also like to extend my gratitude to Dr. Wael El-Dakhakhni for his invaluable encouragement and thoughtfulness and to Dr. Yiping Guo and Dr. Robin Zhao for their valuable time, efforts, and suggestions during my committee meetings. I want to thank Dr. Waguih Ishak for his continued support and advice.

I would like to thank my colleague Dr. Kevin McNamara for his willingness to help, answering my nonending questions and working on the SPH code with me. I would also like to express my appreciation to Dr. Shayne Love for his valuable comments, helpful suggestions, and industrial input. The support received from Dr. David Nakhla and Dr. Sameh Saad is much appreciated.

There are no words to express my gratitude to my wife, Sara, who has stood by me through all my travails, my absences, my fits of pique and impatience. Without her encouragement and support, this thesis would not have been completed. Along with her, I would like to thank my parents for raising me to be who I am today. Without their endless love, encouragement, and support throughout those years, this work would not have been possible.

This thesis is dedicated to my beloved son, Selim.

TABLE OF CONTENTS

LIST OF FIGURES

LIST OF TABLES

NOMENCLATURE

List of Symbols

A_p	Particle Surface Area
a_c	Hourly Peak Structural Acceleration
a_{xj}	Artificial Wall Acceleration
b_{tank}	TLD Tank Width
C_l	Screen Loss Coefficient
C_s	The Smagorinsky Constant
Cs	Generalized Structural Damping
C_t	Turbulence Characteristics Constant
D/Dt	Material Time Derivative
D_c	Average Particle Diameter
d_E	Characteristic Length
D_{ij}	Shear Strain Rate Tensor
dp	Particle Spacing
dp_{sc}	Screen Particle Spacing
$dt, \Delta t$	Simulation Time Step
E_w	Energy Dissipated Per Cycle
f	Frequency
$f(y)$	Tank Wall Parabola Function
f_e	Excitation Frequency
F_{floor}	Drag Force from The False Floor
f_{iw}	Artificial Repulsive Force
$F_{sc,i}$	Screen Drag Force Applied to Fluid
F_{sw}	TLD Sloshing Force

F_{TLD}	TLD Force Transported to Structure
F_w	Screen Drag Force
F_w	Base Shear Force
$\boldsymbol{g}$	Gravitational Force Vector
h_{fluid}	Initial Fluid Depth
h_{gap}	Slat Gap Height
h_r	Kernel Radius
h_{sc}	Screen Particle Kernel Radius
h_{slat}	Solid Slats Height
J	Bessel Function
K_P	Permeability
Ks	Generalized Structural Stiffness
k_t	Turbulence Kinetic Energy
L	Length of the Macroscopic Pressure Gradient in The Flow Direction
L_{baffle}	Horizontal Baffle Length
L_{tank}	TLD Tank Length
m^*	TLD Generalized Mass
m_{eq}	TLD Equivalent Mass
m_j	Particle Mass
m_w	Fluid Mass
n_w	Porosity
P	Fluid Pressure
P_H	Fluid Dynamic Pressure
$\boldsymbol{r}$	Position Vector
R	Convergence Ratio
$\boldsymbol{r}^*$	Intermediate Particle Position Vector

R_{eb}	Reynolds Number in Packed Soil Ped
t	Time Variable
t_{sc}	Screen Length in The Flow Direction
$\boldsymbol{u}$	Particle Velocity Vector
$\boldsymbol{u}^*$	Intermediate Particle Velocity Vector
$\boldsymbol{u}_S$	Average Superficial Velocity
U_w	Annual Maximum Wind Speed
$\boldsymbol{V}_f$	Vertical Fluid Velocity Component
V_j	Volume Of Particle
W_{ij}, ω_{ij}	Kernel Function
X_0	Excitation Amplitude
x_s	Structural Displacement
$\dot{x}_s$	Structural Velocity
$\ddot{x}_s$	Structural Acceleration
x_{tank}	Probe Coordinate
x_{screen}	Screen x-Coordinate
α	PPE blending factor
α_x	External acceleration force vector
β	excitation frequency ratio
Γ	Modal Participation factor
δ_{ij}	Kronecker delta function
δ_R	Relative error
γ^*	TLD excitation factor
ε	convergence deviation
μ	Fluid dynamic viscosity
ν	Fluid kinematic viscosity

ν_t	Smagorinsky turbulent viscosity
ρ_0	Fluid density
ρ_n	Free surface false density
$\rho*$	intermediate particle density
σ	Root Mean Square
ζ_0	damping ratio constant
τ	SPS Turbulence stress term
φ	arbitrary field variable
ϕ_s	Particle sphericity
χ	Peak value
Ψ_{sc}	Screen drag force acceleration vector
ω	Angular frequency
ω_e	excitation angular frequency
Ω	Kernel Domain
ϵ	Normalized error

List of Abbreviations

CFD	Computational Fluid Dynamics
CFL	Courant–Friedrichs–Lewy Condition
DVA	Dynamic Vibration Absorber
ER	Ergun Resistance
FDM	Finite Difference Method
FEM	Finite Element Method

FR	Fire Reserve Tank
ISPH	Incompressible Smoothed Particle hydrodynamics
K-C	Karman-Cozeny model
ME	Morison's Equation
MM	Microscopic Implicit Model
MAF	Mecahnical Admittance Factor
NS	Navier-Stokes Equations
PPE	Pressure Poisson Equation
PF	Perforated Floor Tank
SDOF	Single Degree of Freedom
SPS	Sub-Particle Scale
SF	Intermediate Solid Floor Tank
TLD	Tuned Liquid damper
TMD	Tuned Mass Damper
VOF	Volume of Fluid
WCSPH	Weakly Compressible Smoothed Particle hydrodynamics

List of Subscript

f	Fluid particle
i	Particle of interest
j	Neighbour particles
n	Number of dimensions
s	Structure
sc	Screen particle
w	Wall (boundary) particle

CO-AUTHORSHIP

This thesis has been prepared according to the "sandwich" thesis format set out by the Faculty of Graduate Studies at McMaster University. The thesis has been co-authored as follows:

Chapter 2: Macroscopic modelling for screens inside a tuned liquid damper using incompressible smoothed particle hydrodynamics.

Authors: B.N. Awad and M.J. Tait

The SPH model code was developed by B.N. Awad under the supervision of Dr. M.J. Tait. Experimental data was provided by Dr. M.J. Tait. All the numerical simulations and analyses were conducted by B.N. Awad. The manuscript was written by B.N. Awad, and modifications were completed under the close supervision of Dr. M.J. Tait. Chapter 2 has been published in the Ocean Engineering Journal.

Chapter 3: Modelling of sloped and curved bottom sloshing tanks with screens using smoothed particle hydrodynamics.

Authors: B.N. Awad and M.J. Tait

The SPH model code was upgraded and modified by B.N. Awad under the supervision of Dr. M.J. Tait. All the numerical simulations and analyses were conducted by B.N. Awad. The manuscript was written by B.N. Awad, and modifications were completed under the close supervision of Dr. M.J. Tait. Chapter 3 has been submitted for possible publication in the International Journal of Dynamics and Control.

Chapter 4: Numerical modelling of Dual-Function Tanks for Fire Suppression and Tuned Liquid Damper Applications.

Authors: B.N. Awad, M.J. Tait and J.S. Love

The SPH model code, numerical simulations and analysis were completed by B.N. Awad under the supervision of Dr. M.J. Tait and Dr. J.S. Love. The manuscript was written by B.N. Awad, and modifications were completed under the close supervision of Dr. M.J. Tait and Dr. J.S. Love. Chapter 4 has been submitted for possible publication in Engineering Structures.

Chapter 1: Introduction and Study Overview

1.1 Background

Modern architecture and structural design advances have influenced building trends to extend their vertical profile. Recent construction innovations include new light materials to build tall structures, achieving unprecedented building heights with significant materials savings and reduced environmental impact. However, these new lightweight structures are more flexible and prone to dynamic responses caused by wind (i.e., small amplitude excitation) or earthquake (i.e., high amplitude excitation) events. Due to their low inherent damping and flexibility, modern tall buildings experience significant wind-induced sway motions, which introduce discomfort for building occupants and may impact the integrity of nonstructural elements and elevator operations (Lawrence G. Griffis, 1993). Although tall buildings have sufficient strength to resist dynamic loading, their habitability is a concern, which has led to building code modifications to address serviceability limit concerns - including building acceleration levels.

To comply with building code acceleration limits, various strategies have been proposed to control the sway of the structures. For instance, they introduced aerodynamic features such as corner softening (e.g., Petronas Towers, Malaysia) and tapering the structure as it rises (e.g., Burj Khalifa, UAE). Moreover, openings have been introduced into buildings to allow wind to pass through to reduce wind impacts (e.g., World Finance Center, China). However, in some cases, these solutions may be impractical due to aesthetics or architectural design criteria. Therefore, adding auxiliary structural vibration

control devices near the top of the structures can be an affordable alternative to reduce building motions (Vickery et al., 1983).

1.2 Overview of Dynamic Vibration Absorbers

Auxiliary vibration dampers have been a focus of researchers for several decades due to their effectiveness in controlling the resonant response of structures (Housner et al., 1997). Auxiliary vibration dampers are often categorized into passive and active systems (Koutsoloukas et al., 2022). Active vibrational systems use sensors for real-time vibration measurements, typically requiring an external power source, increasing installation, operation, and maintenance costs. Passive systems are the most common structural vibration control devices due to their simplicity and reliability. One type of passive system is the dynamic vibration absorber (DVA), which Frahm initially introduced in 1909 and is illustrated as a spring-mass-dashpot system coupled to a single degree of freedom (SDOF) system as shown in Figure 1.1(a) (Rana, 1996). A passive DVA is tuned to resonate at a frequency near the natural frequency of the structure, which reduces its response motion. The Tuned Mass Damper (TMD) (Figure 1.2(a)) and Tuned Liquid Damper (TLD) (Figure 1.2(b)) are the most common DVA implemented on structures to reduce wind-induced structural motion.

1.2.1 Tuned Liquid Damper

A Tuned Liquid Damper (TLD) comprises a rigid tank partially filled with water and attached near the top of a structure (as shown in Figure 1.1(b)). A TLD utilizes the sloshing liquid inside the tank to counteract the motion of the structure. This technique has been developed and used in different applications, including anti-rolling tanks, to stabilize sea

vessels and suppress satellite oscillations (Bhuta and Koval, 1966). In the mid-1980s, Bauer (1984) introduced this concept to civil engineering by utilizing a rectangular tank filled with immiscible liquids to reduce the wind-induced response of a structure. A cost/benefit analysis performed by Irwin et al. (2008) on a 75-story building showed a reduction in structural costs by approximately $400,000 to $500,000 and a significant reduction in carbon dioxide emissions by approximately 670 tons with the addition of a TLD.

It has been proposed that TLD tanks could be used to store water required for fire suppression, making it a dual-function system if adequately designed and maintained (i.e., prevent microbial growth and water freezing) (Chen et al., 1995; Kareem et al., 1999; Love et al., 2021).

TLDs are categorized into two groups based on their fluid depth to tank length ratios (Sun et al., 1992). TLDs with a high fluid depth ratio that depends solely on the fluid viscosity do not achieve sufficient inherent TLD damping (Fujino et al., 1992). Conversely, shallow water TLDs (i.e., TLDs with low fluid depth ratio) can achieve higher inherent damping levels due to high nonlinear response and wave breaking. Nevertheless, implementing shallow water TLDs is often impractical as several tanks are typically needed to achieve the required water mass ratio, which can be unfeasible due to limited floor space. As a remedy, alternative approaches have been proposed to enhance TLD damping levels. For instance, the addition of damping devices, such as baffles (Kim, 2001), screens (Tait et al., 2005; Warnitchai and Pinkaew, 1998), and floating roofs (Konar and Ghosh, 2021; Ruiz, Taflanidis, et al., 2016). Furthermore, the percentage of effective liquid mass that

participates in the sloshing motion can be enhanced by modifying the tank bottom geometry (Gardarsson et al., 2001; Modi and Seto, 1998; Tait and Deng, 2008).

1.3 TLD Modelling

The aforementioned TLD advantages constitute a significant motivation for their use. Tamura et al. (1995) found that TLDs can decrease the acceleration response of a building by up to half compared to that of a building without a TLD. Despite their simplicity, the complex free surface and wave-breaking response are typically associated with the sloshing motion inside the TLD, which introduces simulation challenges. However, modelling the sloshing motion is a key facet to understanding and predicting their response and the impact on the building to which they are attached.

Initial research on TLDs used shaking tables to experimentally investigate the sloshing response of TLDs (Akyildiz and Ünal, 2005; Fediw et al., 1995; Tait et al., 2005). However, due to the nonlinear nature of the free surface flow inside the tank, comprehensive experimental setups can be both expensive and time-consuming. Therefore, numerical models have been proposed as an affordable alternative to simulate the response of TLDs and to investigate the flow inside.

1.3.1 Linear Models

Initial numerical studies of TLDs employed linear models, assuming irrotational and inviscid flow. For example, potential flow theory has been utilized in several numerical studies due to its simplicity and computational efficiency at low excitation amplitudes (Fediw et al., 1995). Warnitchai and Pinkaew (1998) simulated sloshing motion inside a flat bottom (i.e., rectangular) tank under sinusoidal excitation, equipped with a wire-mesh

screen, using a linear model based on potential flow theory. Results showed the effectiveness of the additional damping devices; however, the model was limited to the first sloshing mode. Faltinsen et al. (2011) used a linear model based on potential flow theory to simulate screens inside tanks, but the model was limited to wind events with low amplitude excitations. Based on the same theory, Deng and Tait (2008) have captured the wave height response for different tank geometries. Results indicated that the validity of the model is limited to small free surface response amplitudes.

Other researchers have used shallow water wave theory to model TLDs (Shimizu and Hayama, 1987; Sun et al., 1992; Yalla and Kareem, 2001). Although this theory solves the nonlinear Navier Stokes (NS) equations, the wave height amplitude is assumed to be small relative to the initial fluid depth, and the horizontal velocity is uniform through the fluid depth (Reed et al., 1998). These assumptions limit the application of this model to shallow water depths (e.g., $0.15< h_{fluid}/L_{tank} <0.05$) (Tait, 2004). Under 2D excitation, the shallow wave theory has been used to model a TLD numerically, and the model results showed acceptable results versus experimental data at low excitation amplitudes (Tait et al., 2005).

1.3.1 Equivalent Mechanical Models

Several researchers have focused on developing equivalent mechanical models of TLDs based on linear TMD analogy (Sun et al., 1995; Yu et al., 1999). Tait et al. (2004) developed an equivalent nonlinear TMD mechanical model and validated it against experimental results. However, these models have similar limitations on excitation amplitudes as the potential flow theory models as they failed to capture the non-linear free surface response of the TLD (M. J. Tait, 2008).

1.3.2 Nonlinear Models

As previously discussed, insufficient inherent damping of TLDs has led to different techniques to enhance their performance (Kaneko and Yoshida, 1999). Despite the proven effectiveness of these techniques, they introduce obstructions into the flow that are challenging to model. Tait et al. (2004) used an equivalent nonlinear equivalent mechanical model coupled with a linearized equivalent damping ratio to model the effect of submerged screens inside the TLD. Moreover, the model was coupled to a structure to study the effect of TLD with screens on a building under both sinusoidal and random excitation (Tait, 2008). Good agreement between the model and experimental results was found for the fundamental sloshing mode, while the model performance deteriorated significantly for higher modes.

Faltinsen et al. (2011) added a nonlinear ordinary differential equation to a linear potential flow theory model to model slat screens inside the TLD. However, the model showed satisfactory results only for the first natural frequency, and discrepancies were noticed for higher frequencies. Cassolato et al. (2011) used an equivalent mechanical model with an amplitude-dependent damping ratio and natural frequency to consider the nonlinearities associated with TLD equipped with inclined screens. Hamelin et al. (2013) proposed a nonlinear equivalent mechanical model based on the shallow water wave theory to model slat screens inside TLDs. The model depended on the Keulegan-Carpenter number (KC), proving the TLD performance sensitivity to the KC drag coefficient. However, their models were limited to low excitation amplitudes.

Deng (2007) studied the performance of TLD equipped with screens with different tank geometries, using an equivalent mechanical model based on the linear long wave theory (Deng and Tait, 2008). Tait and Deng (2008) theoretically modelled a structure-TLD system with different tank geometries and investigated their performance under random excitation. Deng and Tait (2009) developed equivalent mechanical properties (e.g., effective mass, natural frequency, and damping ratio) for triangular-bottom, sloped-bottom, parabolic-bottom, and flat-bottom tanks outfitted with screens. It was concluded that changing the tank bottom geometry influences the effective mass ratio of the TLD. Moreover, increasing the effective mass ratio (i.e., more water participates in the sloshing motion) increases the damping performance of the TLD. Also, these studies helped derive parameters for each tank that can aid the engineers in the preliminary stage of the design process. However, the assumptions of small fluid response, exclusion of nonlinear terms, and considering only the fundamental sloshing mode have limited their applications to low amplitudes and shallow water depths. Furthermore, screen locations and the number of screens were limited as the screen-damping equations are mathematically challenging to integrate.

Another study developed an equivalent linearized mechanical model coupled with the Finite Element Method (FEM) to model TLD with arbitrary tank geometry under small amplitude excitation (Love and Tait, 2011a). A nonlinear multimodal model, which employs the Runge-Kutta-Gill Method (Love and Tait, 2011b) to solve, was used to simulate a structure-TLD system under random excitation and compared to shaking table test results (Love and Tait, 2013a). The model showed good results compared to the

experimental results and facilitated the investigation of different tank geometries, which is essential for fitting the tanks in limited floor spaces. However, it was limited to fluid depth ratios below 0.15 (Love and Tait, 2013a).

1.3.3 Computational Fluid Dynamics (CFD) Models

As the above models have limitations with respect to different parameters (e.g., shallow water depth, low excitation/ response amplitudes, screen placement), computational fluid dynamics (CFD), a mesh-based method, has been employed to solve the full nonlinear NS equations, which is necessary for designing an efficient and effective TLD (G. X. Wu et al., 1998). Conventional CFD methods (e.g., Finite Element, Finite Difference, and Finite Volume) have simulation limitations in handling complex, and large deformations free surface flows due to their pre-defined mesh. Therefore, improvements, such as free surface capturing, mesh rezoning, and tracking algorithms, have been added to enhance their simulation performance. However, these improvements are often mathematically challenging and require high computational costs.

Ramaswamy et al. (1986) used the 2D Lagrangian Finite Element Method (FEM) with a velocity correction algorithm to simulate sloshing for small excitation amplitudes. Flow with large deformations was predicted inside a rectangular TLD using moving boundary algorithms; however, the studies did not include screens (Floryan and Rasmussen, 1989; Siddique et al., 2005).

Another study used the Finite Difference Method (FDM) with the Volume-Of-Fluid (VOF) algorithm and the Partial-Cell treatment to model TLD with screens under small and large amplitude excitations (Maravani and Hamed, 2011a). Simulations captured the fine

flow around the screens and demonstrated the effectiveness of the screens and their pattern on the frequency of the TLD (Maravani and Hamed, 2011a). Later, the same researchers developed a pressure drop model to model the effect of the screens as a hydraulic resistance and showed that decreasing the slat height of the screens is inversely proportional to the inherent damping of the TLD (Marivani and Hamed, 2017). However, these studies used free surface capturing and tracking techniques, which are computationally expensive and mathematically complex (Gao, 2011). Additionally, the study was limited to a fluid depth ratio <0.13 and specific screen solidity ratios (Marivani and Hamed, 2017).

1.3.4 Smoothed Particle Hydrodynamics (SPH) Models

Alternatively, numerical investigations on the sloshing motion inside TLDs have been increasingly adopting the Lagrangian mesh-free methods where grids are not required as needed by traditional CFD methods (Koshizuka et al., 1998). The Smoothed Particle Hydrodynamics (SPH) method is one of the standard mesh-free methods, where the computational domain is discretized into particles that carry the fluid properties. SPH was initially developed for astrophysical applications (Gingold and Monaghan, 1977). Since then, SPH has been widely used to solve different engineering problems, including Fluid-Structure interactions, damp breaking problems, seepage, and porous flow (Liu and Liu, 2010). The significant advantage of the SPH method is its formulation, as it inherently traces particles while conserving the particle energy, mass and momentum and does not need expensive tracking algorithms to capture large deformations flows (Monaghan, 1992). The SPH formulations approximate any field function using a kernel function (Figure 1.3). A kernel is a smoothing function that averages any field function or variable based on its

kernel radius (h_r) and domain (Ω). For each domain, any field variable for a particle of interest (i) is calculated by multiplying the field variable of the surrounding particles (j) by the kernel and integrating it over the domain. Subsequently, SPH formulations use particle approximation to convert the integration to summation over the domain, constituting the SPH technique's real essence (Monaghan, 1985).

Early SPH studies proposed an explicit scheme to solve the governing equations by relating the density and pressure using the equation of state (Monaghan, 1994). This approach is known as Weakly Compressible SPH (WCSPH) (Monaghan, 1994), where the equation of state results in unphysical pressure propagations and leads to numerical noises, as reported in the SPH literature (Lee et al., 2008). The Incompressible SPH (ISPH) approach, on the other hand, has shown enhanced computational accuracy over the WCSPH (Violeau and Rogers, 2016). The ISPH approach solves the NS equations using the Pressure Poisson Equation (PPE) to enforce incompressibility (Cummins and Rudman, 1999). ISPH can solve the PPE implicitly or explicitly in time, with either a divergence-free condition (Cummins and Rudman, 1999) or a density invariant condition (S. Shao and Lo, 2003).

Due to the numerical accuracy and meshless nature of the ISPH, various studies have used the SPH method in simulation fluid sloshing in TLD applications. Long-duration sloshing simulations are studied in a rectangular tank using a corrected δ-SPH scheme (Green and Peiró, 2018). The model employed the fixed ghost particle method adopted by Adami et al. (2012), which was found to be straight forward to implement. However, the model was computationally demanding and required an efficient parallelization scheme for practical applications. Moreover, the model was applied to low fill ratios, and screens were

not incorporated in this study (Green and Peiró, 2018). SPH has been used to model tanks without damping screens subjected to impulse-type loading with different tank shapes and has produced good results compared to experimental results (Marsh et al., 2011). Jiang et al. (2019) proposed a combined Pressure Poisson Equation (PPE) that includes divergence-free and density-invariant conditions to impose incompressibility to model violent sloshing resulting from water jet flow. The 2D SPH predicted impact pressures and free surface responses that agreed with the experimental data (Jiang et al., 2019). Although the reported SPH numerical modelling leaps in TLD problems, they need significant computational requirements, especially for TLD applications incorporating damping screens and perforated baffles.

1.3.5 Modelling of Damping Screens

A review of SPH-TLD literature reveals that researchers have modelled screens using microscopic and macroscopic models. The first approach models the screens on a microscopic level, where the screen geometry is modelled explicitly, and the detailed localized flow is replicated in the vicinity of the screens. However, this technique requires a small particle size, resulting in large particle numbers and high computational costs. The second approach implements the screens at the macroscopic level, where the overall effect of the screens is captured implicitly without simulating the localized flow around the screen particles. This technique allows for larger particle sizes, reduces computational costs, and can be implemented in applications when the general influence of the screens is of more significance than the characteristics of the local flow around the screens.

Fluid interactions with submerged slotted (i.e., perforated) walls have been studied on a microscopic level using SPH (Aristodemo et al., 2016; Meringolo et al., 2015). Kashani et al. (2018) developed an equivalent mechanical model using ISPH to model TLD outfitted with screens microscopically. The model results were in good agreement with experimental data and indicated that the location of the screens inside the TLD could achieve a more robust performance if placed where higher harmonics are prevalent (Kashani et al., 2018). SPH has been used to investigate a TLD-structure system, where a rectangular TLD performance is evaluated under seismic excitation (Halabian et al., 2019).

For TLD applications, where the influence of the screen drag on the wave heights and sloshing forces in the tank is the primary interest (Tait et al., 2005), macroscopic modelling is an effective alternative. Valizadeh and Rudman (2017) modelled the screens macroscopically based on a 1D pressure drop model and validated the results using experimental data. Although the model showed excellent computing efficiency in modelling screens and thin porous media implicitly with reduced computational time, it was only tested under steady-state flow.

An in-house SPH code capable of modelling TLDs with screens on a macroscopic scale has been developed recently by McNamara et al. (2021). This model is capable of solving the governing equations in an explicit incompressible scheme as per Yeylaghi et al. (2016) and employed the combined divergence-free and density-invariant version of the PPE for a stable pressure field as proposed by Jiang et al. (2019). The model used the boundary conditions presented by Adami et al. (2012) to calculate the pressure of the boundary particles. The complete code was written in Fortran, consisting of different subroutines that

compute serially. A neighbour search algorithm was implemented to determine the neighbouring particles once per time step, which reduces computational time. The code enables the user to setup the simulation time, time step, initial particle spacing, kernel function, kernel radius, free surface artificial density and free-slip or no-slip boundary conditions in a simple input file before commencing the simulation.

Moreover, the code uses a multiplier for the kernel radius and particle spacing, enabling more flexibility in determining the parameters used for the screens and boundary particles. The model records the position, velocity components, pressure, and forces for all particles at a pre-determined sampling rate. Several scenarios were modelled for a hydrostatic tank case to validate the code performance against theoretical static pressure values. Furthermore, the code was validated against multiple dam-break simulation scenarios and showed good agreement with the numerical results available in the literature (Nomeritae et al., 2016).

The code also implemented a novel macroscopic screen model based on Morison's equation (ME) to calculate the force on a submerged object. The SPH code with the ME model has been used to simulate the response of rectangular TLDs under sinusoidal excitation having different tank dimensions, screen geometries, water depths and excitation amplitudes (McNamara et al., 2021). A frequency response analysis was conducted for various excitation frequencies and validated using experimental shake table testing data (Love and Tait, 2010, 2013b; Tait et al., 2005). The model could accurately capture wave heights and sloshing forces under simulation conditions (Figure 1.4); however, some discrepancy was observed for shallow water depths and low amplitude excitations

(McNamara et al., 2021). Additionally, the ME method relies on the screen drag coefficient, which often must be determined experimentally for individual screen geometries prior to numerical modelling.

In another study, the SPH model was coupled to an SDOF structure to model the response of a structure-TLD system under various excitation amplitudes for long-duration simulations (McNamara and Tait, 2022). Although the model performance deteriorated near the end of the simulation due to particles escaping through the tank boundaries, the model results agreed with the experimental data. The model predicted structure-TLD response at levels far exceeding serviceability limits (McNamara and Tait, 2022). Additionally, the model was used to simulate the response of a TMD-TLD-structure system using a simplified pendulum equation to model the TMD. Successful implementation of the SPH code was reported; however, the results showed an underestimation of the system response (McNamara et al., 2022a). Finally, the SPH model was used to investigate a TLD where the tank had limited freeboard to evaluate its effectiveness. The model did not show any limitations in capturing the highly non-linear flow associated with ceiling impact (McNamara et al., 2022b)

The above studies show that ISPH, along with a macroscopic screen model, can serve as a robust tool to model TLD tanks efficiently outfitted with screens over a wide range of excitation amplitude, fluid depth and screen setup while using reduced computational intensity. It can also be coupled to a structure-TLD system to investigate the structure response for real-life scenarios.

1.4 Impetus of Study

TLDs exhibit highly nonlinear flow with large free surface deformations requiring an expensive physical setup to study experimentally. Numerical modelling has proved to be an efficient alternative to experimental testing; however, existing numerical models have various limitations, including excitation amplitude, fluid depth, screen locations, and high computational cost.

This thesis focuses on developing an SPH model capable of simulating the fluid sloshing response in tanks with different bottom geometries with screens or perforated floors in real-life scenarios, which has not been possible using existing numerical models. The SPH model uses an implicit algorithm to model screens at a macroscopic level, allowing significant reductions in computational cost and feasible simulations. The efficient SPH model can provide a comprehensive understanding of TLD behaviour over a wide range of fluid depths and under high excitation amplitudes exceeding serviceability limit levels.

A TLD can be designed with different tank geometries to accommodate available floor space. An SPH model can be adjusted to efficiently model irregular bottom tank geometries with sloped and curved tank walls. The flexibility of the model allows it to model tanks with perforated intermediate floors that could serve as both TLD and water reservoir tanks for fire suppression. The SPH model can be readily coupled to a structure to study structure-TLD system response under harmonic and random wind loading for different tank configurations. Understating the behaviour of various tank configurations, such as dual-

function tanks, is expected to expand TLD applications and make more efficient use of floor space.

1.5 Research Objectives

This study uses an in-house numerical code to model TLDs with screens and perforated floors. The scope of this thesis lies in presenting a practical, computationally efficient numerical method that can study different TLD configurations without the limitations reported in the previous numerical models found in the literature. The main objectives of this thesis are:

- Develop an in-house SPH code to investigate TLDs with screens under sinusoidal excitation.
- Present a macroscopic screen model, based on Ergun's Equation, to capture the effect of the screen implicitly, using reduced computational power relative to the available numerical models and without the need for experimental testing to determine screen parameters.
- Investigate the internal response characteristics of a TLD equipped with screens under a wide range of excitation amplitudes and frequencies and at different fluid depth-to-tank length ratios.
- Study the sloshing response of TLDs with different tank bottom geometries excited at large excitation amplitude greater than serviceability limit levels (e.g., 100-year return period event).

- Enhance the boundary conditions of existing SPH code to model sloped and curved bottom tanks with efficient computational power while maintaining fluid particles within the defined boundaries during the simulation period.
- Perform a parametric investigation of tanks with different tank bottom geometries to assess their response and internal pressure distribution at different fluid depths and with multiple screens.
- Utilize the SPH model to study the sloshing behaviour of a dual-function TLD with two compartments at and exceeding serviceability limit levels.
- Evaluate the performance of the macroscopic screen model in capturing the drag effect of the gaps and seepage associated with the perforated floor inside the dual-function tank.
- When coupled to TLD with a perforated floor, evaluate the structural response for an SDOF structure-TLD system under random excitation.

1.6 Thesis Organization

This thesis is prepared in accordance with the regulations for a Sandwich-Thesis format conforming with the requirements of the School of Graduate Studies. Each chapter consists of a manuscript either published or submitted to peer-reviewed journals, with a discrete bibliography at the end of each chapter. It should be noted that the Sandwich-Thesis format does result in some overlap between chapters.

Chapter 2 presents a 2D macroscopic model based on Ergun's equation, developed within an in-house SPH model, for modelling TLDs with screens under a wide range of harmonic excitation amplitudes and fluid depths. Using reduced relative computational

power, the numerical investigations showed good agreement with available experimental results. Moreover, the model could capture the effect of any screen geometry independently of the drag-loss coefficient and experimental data.

Chapter 3 describes modifications to the SPH model presented in Chapter 2 to accommodate different tank bottom geometries. The damping performance was studied for four tank bottom geometries with screens under large excitation amplitudes, exceeding serviceability limits, for a targeted frequency and constant free surface fluid length ratio cases. Additionally, the effect of multiple screens on damping performance was carried out using the macroscopic screen model developed in Chapter 2. Finally, a parametric depth study was conducted for each tank-bottom geometry covering a wide range of shallow and deep fluid depth ratios using a constant water mass for comparative purposes. Findings show that the SPH and macroscopic screen models can capture a wide range of sloped and curved tank bottom shapes with multiple screens over various fluid depth ratios and under small and large excitation amplitudes.

Chapter 4 examines a dual-function configuration TLD, which consists of a rectangular tank with an intermediate perforated floor to accommodate fire protection water requirements and damping characteristics in parallel. The SPH model developed in Chapter 2 is used to model the intermediate perforated floor on a macroscopic scale. The results revealed good agreement compared to microscopic modelling of the perforated floor, with a significant reduction in computational effort. The SPH model was coupled with an SDOF structure to investigate its response under random excitation. Results are used to assess the performance of the dual-function TLD.

Chapter 5 reviews the key findings from the research and summarizes the main contributions of this work. The chapter discusses the present work's limitations and recommendations for future research.

1.7 References

Adami, S., Hu, X. Y., & Adams, N. A. (2012). A generalized wall boundary condition for smoothed particle hydrodynamics. *Journal of Computational Physics*, *231*(21), 7057–7075. https://doi.org/10.1016/j.jcp.2012.05.005

Akyildiz, H., & Ünal, E. (2005). Experimental investigation of pressure distribution on a rectangular tank due to the liquid sloshing. *Ocean Engineering*, *32*(11–12), 1503–1516. https://doi.org/10.1016/j.oceaneng.2004.11.006

Aristodemo, F., Meringolo, D. D., & Veltri, P. (2016). A multi-node approach to simulate thin coastal structures in the SPH context. *Proceedings of the Coastal Engineering Conference*, *35*, 1–12.

Bauer, H. F. (1984). Oscillations of immiscible liquids in a rectangular container: A new damper for excited structures. *Journal of Sound and Vibration*, *93*(1), 117–133. https://doi.org/10.1016/0022-460X(84)90354-7

Bhuta, P. G., & Koval, L. R. (1966). A Viscous RIng Damper For a Freely Precessing Satellite. *International Journal of Mechanical Sciences*, *8*, 383–395.

Cassolato, M. R., Love, J. S., & Tait, M. J. (2011). Modelling of a tuned liquid damper with inclined damping screens. *Structural Control and Health Monitoring*, *18*(May 2011), 674–681. https://doi.org/10.1002/stc

Chen, Y. H., Hwang, W. S., Chiu, L. T., & Sheu, S. M. (1995). Flexibility of TLD to high-rise building by simple experiment and comparison. *Computers and Structures*, *57*(5), 855–861. https://doi.org/10.1016/0045-7949(95)00083-S

Cummins, S. J., & Rudman, M. (1999). An SPH Projection Method. *Journal of Computational Physics*, *607*(2), 584–607.

Deng, X. (2007). *The performance of tuned liquid dampers with different tank geometries*. McMaster University.

Deng, X., & Tait, M. J. (2008). Equivalent mechanical models of tuned liquid dampers with different tank geometries. *Canadian Journal of Civil Engineering*, *35*(10), 1088–1101. https://doi.org/10.1139/L08-044

Deng, X., & Tait, M. J. (2009). Theoretical modeling of TLD with different tank geometries

using linear long wave theory. *Journal of Vibration and Acoustics, Transactions of the ASME*, *131*(4), 0410141–04101410. https://doi.org/10.1115/1.3142873

Faltinsen, O. M., Firoozkoohi, R., & Timokha, A. N. (2011). Analytical modeling of liquid sloshing in a two-dimensional rectangular tank with a slat screen. *Journal of Engineering Mathematics*, *70*(1–3), 93–109. https://doi.org/10.1007/s10665-010-9397-5

Fediw, A. A., Isyumov, N., & Vickery, B. J. (1995). Performance of a tuned sloshing water damper. *Journal of Wind Engineering and Industrial Aerodynamics*, *57*(2–3), 237–247. https://doi.org/10.1016/0167-6105(94)00107-O

Floryan, J. M., & Rasmussen, H. (1989). Numerical methods for viscous flows with moving boundaries. *Applied Mechanics Reviews*, *42*(12), 323–341.https://doi.org/10.1115/1.3152416

Fujino, Y., Sun, L., Pacheco, B., & Chaiseri, P. (1992). Tuned liquid damper (TLD) for suppressing horizontal motion of structures. *ASCE Journal of Engineering Mechanics*, *118*(10), 2017–2030.

Gao, M. (2011). *Numerical simulation of liquid sloshing in rectangular tanks using consistent particle method and experimental verification*. 207.

Gardarsson, S., Yeh, H., & Reed, D. (2001). Behavior of Sloped-Bottom Tuned Liquid Dampers. *Journal of Engineering Mechanics*, *127*(3), 266–271. https://doi.org/10.1061/(asce)0733-9399(2001)127:3(266)

Gingold, R. A., & Monaghan, J. J. (1977). Smoothed particle hydrodynamics: theory and application to non-spherical stars. *Monthly Notices of the Royal Astronomical Society*, *181*(3), 375–389.

Green, M. D., & Peiró, J. (2018). Long duration SPH simulations of sloshing in tanks with a low fill ratio and high stretching. *Computers and Fluids*, *174*, 179–199. https://doi.org/10.1016/j.compfluid.2018.07.006

Halabian, A. M., Karamnasab, A., & Chamani, M. R. (2019). A New Hybrid SPH-FEM Model to Evaluate Seismic Response of TSD Equipped-Structures. *Journal of Earthquake and Tsunami*, *13*(2), 1–27. https://doi.org/10.1142/S1793431119500076

Hamelin, J. A., Love, J. S., Tait, M. J., & Wilson, J. C. (2013). Tuned liquid dampers with a Keulegan-Carpenter number-dependent screen drag coefficient. *Journal of Fluids and Structures*, *43*, 271–286. https://doi.org/10.1016/j.jfluidstructs.2013.09.006

Housner, G. W., Bergman, L. A., Caughey, T. K., Chassiakos, A. G., Claus, R. O., Masri, S. F., Skelton, R. E., Soong, T. T., Spencer, B. F., & Yao, J. T. P. (1997). Structural Control: Past, Present, and Future. *Journal of Engineering Mechanics*, *123*(9), 897–971. https://doi.org/10.1061/(asce)0733-9399(1997)123:9(897)

Irwin, P., Kilpatrick, J., Robinson, J., & Frisque, A. (2008). WIND AND TALL BUILDINGS : NEGATIVES AND POSITIVES. *The Structural Design of Tall and Special Buildings*, *928*(November), 915–928.

Jiang, H., You, Y., Hu, Z., Zheng, X., & Ma, Q. (2019). Comparative study on violent sloshing withwater jet flows by using the ISPH method. *Water (Switzerland)*, *11*(12). https://doi.org/10.3390/w11122590

Kaneko, S., & Yoshida, O. (1999). Modeling of deepwater-type rectangular tuned liquid damper with submerged nets. *Journal of Pressure Vessel Technology, Transactions of the ASME*, *121*(4), 413–422. https://doi.org/10.1115/1.2883724

Kareem, A., Kijewski, T., & Tamura, Y. (1999). Mitigation of motions of tall buildings with specific examples of recent applications. *Wind and Structures, An International Journal*, *2*(3), 201–251. https://doi.org/10.12989/was.1999.2.3.201

Kashani, A. H., Halabian, A. M., & Asghari, K. (2018). A numerical study of tuned liquid damper based on incompressible SPH method combined with TMD analogy. *Journal of Fluids and Structures*, *82*, 394–411. https://doi.org/10.1016/j.jfluidstructs.2018.07.013

Kim, Y. (2001). *Numerical simulation of sloshing flows with impact load*. *23*.

Konar, T., & Ghosh, A. (2021). Development of a novel tuned liquid damper with floating base for converting deep tanks into effective vibration control devices. *Advances in Structural Engineering*, *24*(2), 401–407. https://doi.org/10.1177/1369433220953539

Koshizuka, S., Nobe, A., & Oka, Y. (1998). Numerical analysis of breaking waves using the moving particle semi-implicit method. *International Journal for Numerical*

Methods in Fluids, *26*(7), 751–769. https://doi.org/10.1002/(sici)1097-0363(19980415)26:7<751::aid-fld671>3.0.co;2-c

Koutsoloukas, L., Nikitas, N., & Aristidou, P. (2022). Passive, semi-active, active and hybrid mass dampers: A literature review with associated applications on building-like structures. *Developments in the Built Environment*, *12* (October). https://doi.org/10.1016/j.dibe.2022.100094

Lawrence G. Griffis. (1993). Serviceability limit states under wind load. *Engineering Journal, American Institute of Steel Construction*, *30*(1), 1–16.

Lee, E. S., Moulinec, C., Xu, R., Violeau, D., Laurence, D., & Stansby, P. (2008). Comparisons of weakly compressible and truly incompressible algorithms for the SPH mesh free particle method. *Journal of Computational Physics*, *227*(18), 8417–8436. https://doi.org/10.1016/j.jcp.2008.06.005

Liu, M. B., & Liu, G. R. (2010). Smoothed particle hydrodynamics (SPH): An overview and recent developments. In *Archives of Computational Methods in Engineering* (Vol. 17, Issue 1). https://doi.org/10.1007/s11831-010-9040-7

Love, J. S., Morava, B., Robinson, J. K., & Haskett, T. C. (2021). Tuned Sloshing Dampers in Tall Buildings: A Practical Performance-Based Design Approach. *Practice Periodical on Structural Design and Construction*, *26*(3), 1–13. https://doi.org/10.1061/(asce)sc.1943-5576.0000582

Love, J. S., & Tait, M. J. (2010). Nonlinear simulation of a tuned liquid damper with damping screens using a modal expansion technique. *Journal of Fluids and Structures*, *26*(7–8), 1058–1077. https://doi.org/10.1016/j.jfluidstructs.2010.07.004

Love, J. S., & Tait, M. J. (2011a). Equivalent linearized mechanical model for tuned liquid dampers of arbitrary tank shape. *Journal of Fluids Engineering, Transactions of the ASME*, *133*(6), 61105-1-61105–61109. https://doi.org/10.1115/1.4004080

Love, J. S., & Tait, M. J. (2011b). Non-linear multimodal model for tuned liquid dampers of arbitrary tank geometry. *International Journal of Non-Linear Mechanics*, *46*(8), 1065–1075. https://doi.org/10.1016/j.ijnonlinmec.2011.04.028

Love, J. S., & Tait, M. J. (2013a). Nonlinear multimodal model for TLD of irregular tank

geometry and small fluid depth. *Journal of Fluids and Structures*, *43*, 83–99. https://doi.org/10.1016/j.jfluidstructs.2013.09.009

Love, J. S., & Tait, M. J. (2013b). Parametric depth ratio study on tuned liquid dampers: Fluid modelling and experimental work. *Computers and Fluids*, *79*, 13–26. https://doi.org/10.1016/j.compfluid.2013.03.004

Maravani, M., & Hamed, M. S. (2011). Numerical modeling of sloshing motion in a tuned liquid damper outfitted with a submerged slat screen. *International Journal for Numerical Methods in Fluids*, *65*(January 2010), 834–855. https://doi.org/10.1002/fld

Marivani, M., & Hamed, M. S. (2017). Evaluate pressure drop of slat screen in an oscillating fluid in a tuned liquid damper. *Computers and Fluids*, *156*, 384–401. https://doi.org/10.1016/j.compfluid.2017.08.008

Marsh, A., Prakash, M., Semercigil, E., & Turan, Ö. F. (2011). A study of sloshing absorber geometry for structural control with SPH. *Journal of Fluids and Structures*, *27*(8), 1165–1181. https://doi.org/10.1016/j.jfluidstructs.2011.02.010

McNamara, K. P., Awad, B. N., Tait, M. J., & Love, J. S. (2021). Incompressible smoothed particle hydrodynamics model of a rectangular tuned liquid damper containing screens. *Journal of Fluids and Structures*, *103*, 103295. https://doi.org/10.1016/j.jfluidstructs.2021.103295

McNamara, K. P., Love, J. S., & Tait, M. J. (2022a). Nonlinear modelling of series-type pendulum tuned mass damper-tuned liquid damper. *Journal of Vibration and Acoustics*, 1–26. https://doi.org/10.1115/1.4053636

McNamara, K. P., Love, J. S., & Tait, M. J. (2022b). Numerical investigation of the response of structures equipped with a limited freeboard tuned liquid damper. *Journal of Fluids and Structures*, *108*, 103426. https://doi.org/10.1016/j.jfluidstructs.2021.103426

McNamara, K. P., & Tait, M. J. (2022). Modeling the Response of Structure–Tuned Liquid Damper Systems Under Large Amplitude Excitation Using Smoothed Particle Hydrodynamics. *Journal of Vibration and Acoustics*, *144*(1), 1–13. https://doi.org/10.1115/1.4051266

Meringolo, D. D., Aristodemo, F., & Veltri, P. (2015). SPH numerical modeling of wave-perforated breakwater interaction. *Coastal Engineering*, *101*, 48–68. https://doi.org/10.1016/j.coastaleng.2015.04.004

Modi, V. J., & Seto, M. L. (1998). Passive control of flow-induced oscillations using rectangular nutation dampers. *JVC/Journal of Vibration and Control*, *4*(4), 381–404. https://doi.org/10.1177/107754639800400403

Monaghan, J. J. (1985). Particle Method for Hydrodynamics. *Computer Physics Reports*, *3*(2), 71–124.http://adsabs.harvard.edu/cgibin/nphdata_query?bibcode=1985CoPhR...3...71M&link_type=EJOURNAL%0Apapers3://publication/doi/10.1016/0167-7977(85)90010-3

Monaghan, J. J. (1992). Smoothed Particle Hydrodynamics. *Annual Review of Astronomy and Astrophysics*, *30*(1), 543–574. https://doi.org/10.1146/annurev.aa.30.090192.002551

Monaghan, J. J. (1994). Simulating free surface flows with SPH. In *Journal of Computational Physics* (Vol. 110, Issue 2, pp. 399–406). https://doi.org/10.1006/jcph.1994.1034

Nomeritae, Daly, E., Grimaldi, S., & Bui, H. H. (2016). Explicit incompressible SPH algorithm for free-surface flow modelling: A comparison with weakly compressible schemes. *Advances in Water Resources*, *97*, 156–167. https://doi.org/10.1016/j.advwatres.2016.09.008

Ramaswamy, B., Kawahara, M., & Nakayama, T. (1986). Lagrangian finite element method for the analysis of two-dimensional sloshing problems. *International Journal for Numerical Methods in Fluids*, *6*(9), 659–670. https://doi.org/10.1002/fld.1650060907

Rana, R. (1996). Response Control of Structures by Tuned Mass Dampers and Their Generalizations. *Eleventh World Conference on Earthquake Engineering*.

Reed, D., Yu, J., Yeh, H., & Gardarsson, S. (1998). Investigation of Tuned Liquid Dampers under Large Amplitude Excitation. *Journal of Engineering Mechanics*, *124*(4), 405–

413. https://doi.org/10.1061/(asce)0733-9399(1998)124:4(405)

Ruiz, R. O., Taflanidis, A. A., & Lopez-Garcia, D. (2016). Characterization and design of tuned liquid dampers with floating roof considering arbitrary tank cross-sections. *Journal of Sound and Vibration*, *368*, 36–54. https://doi.org/10.1016/j.jsv.2016.01.014

Shao, S., & Lo, E. Y. M. (2003). Incompressible SPH method for simulating Newtonian and non-Newtonian flows with a free surface. *Advances in Water Resources*, *26*(7), 787–800. https://doi.org/10.1016/S0309-1708(03)00030-7

Shimizu, T., & Hayama, S. (1987). Nonlinear Responsed of Sloshing Based on the Shallow Water Wave Theory. *JSME International Journal*, *30*(263), 806–813.

Siddique, M. R., Hamed, M. S., & El Damatty, A. A. (2005). A nonlinear numerical model for sloshing motion in tuned liquid dampers. *International Journal of Numerical Methods for Heat and Fluid Flow*, *15*(3), 306–324. https://doi.org/10.1108/09615530510583900

Sun, L. M., Fujino, Y., Chaiseri, P., & Pacheco, B. M. (1995). The properties of tuned liquid dampers using a TMD analogy. *Earthquake Engineering & Structural Dynamics*, *24*(7), 967–976. https://doi.org/10.1002/eqe.4290240704

Sun, L. M., Fujino, Y., Pacheco, B. M., & Chaiseri, P. (1992). Modelling of tuned liquid damper (TLD). *Journal of Wind Engineering and Industrial Aerodynamics*, *43*(1–3), 1883–1894. https://doi.org/10.1016/0167-6105(92)90609-E

Tait, M., El Damatty, A. A., & Isyumov, N. (2004). Testing of tuned liquid damper with screens and development of equivalent TMD model. *Wind and Structures, An International Journal*, *7*(4), 215--234.

Tait, M. J. (2004). *The Performance of 1-D and 2-D Tuned Liquid Dampers*.

Tait, M. J. (2008). Modelling and preliminary design of a structure-TLD system. *Engineering Structures*, *30*(10), 2644–2655. https://doi.org/10.1016/j.engstruct.2008.02.017

Tait, M. J., & Deng, X. (2008). The performance of structure-tuned liquid damper systems with different tank geometries M. *Structural Control and Health Monitoring*, *17*(3),

254–277. https://doi.org/10.1002/stc

Tait, M. J., El Damatty, A. A., & Isyumov, N. (2005). An investigation of tuned liquid dampers equipped with damping screens under 2D excitation. *Earthquake Engineering and Structural Dynamics*, *34*(7), 719–735. https://doi.org/10.1002/eqe.452

Tait, M. J., El Damatty, A. A., Isyumov, N., & Siddique, M. R. (2005). Numerical flow models to simulate tuned liquid dampers (TLD) with slat screens. *Journal of Fluids and Structures*, *20*(8), 1007–1023. https://doi.org/10.1016/j.jfluidstructs.2005.04.004

Valizadeh, A., & Rudman, M. (2017). A numerical approach for simulating flow through thin porous media. *European Journal of Mechanics, B/Fluids*, *65*, 31–44. https://doi.org/10.1016/j.euromechflu.2017.03.004

Vickery, B. J., Isyumov, N., & Davenport, A. G. (1983). The role of damping, mass and stiffness in the reduction of wind effects on structures. *Journal of Wind Engineering and Industrial Aerodynamics*, *11*, 285–294.

Violeau, D., & Rogers, B. D. (2016). Smoothed particle hydrodynamics (SPH) for free-surface flows: Past, present and future. *Journal of Hydraulic Research*, *54*(1), 1–26. https://doi.org/10.1080/00221686.2015.1119209

Warnitchai, P., & Pinkaew, T. (1998). Modelling of liquid sloshing in rectangular tanks with flow-dampening devices. *Engineering Structures*, *20*(7). https://doi.org/10.1016/S0141-0296(97)00068-0

Wu, G. X., Ma, Q. W., & Eatock Taylor, R. (1998). Numerical simulation of sloshing waves in a 3D tank based on a finite element method. *Applied Ocean Research*, *20*(6), 337–355. https://doi.org/10.1016/S0141-1187(98)00030-3

Yalla, S. K., & Kareem, A. (2001). Beat phenomenon in combined structure-liquid damper systems. *Engineering Structures*, *23*(6), 622–630. https://doi.org/10.1016/S0141-0296(00)00085-7

Yeylaghi, S., Moa, B., Oshkai, P., Buckham, B., & Crawford, C. (2016). ISPH modelling of an oscillating wave surge converter using an OpenMP-based parallel approach. *Journal of Ocean Engineering and Marine Energy*, *2*(3), 301–312.

https://doi.org/10.1007/s40722-016-0053-7

Yu, J. K., Wakahara, T., & Reed, D. A. (1999). A non-linear numerical model of the tuned liquid damper. *Earthquake Engineering and Structural Dynamics*, *28*(6), 671–686. https://doi.org/10.1002/(SICI)1096-9845(199906)28:6<671::AID-EQE835>3.0.CO;2-X

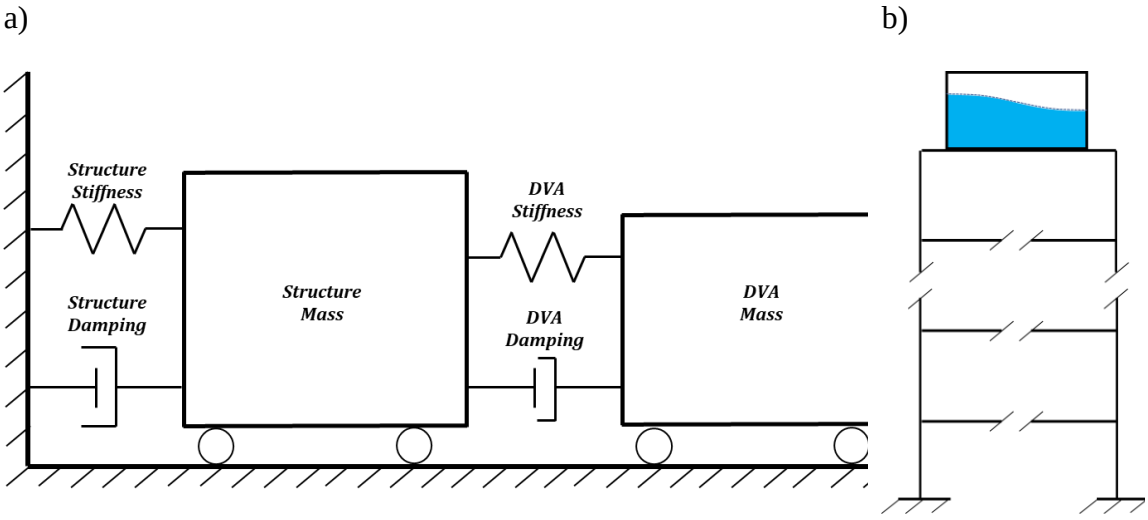

Figure 1.1 Schematic of a) Structure-DVA system b) Structure-TLD installation

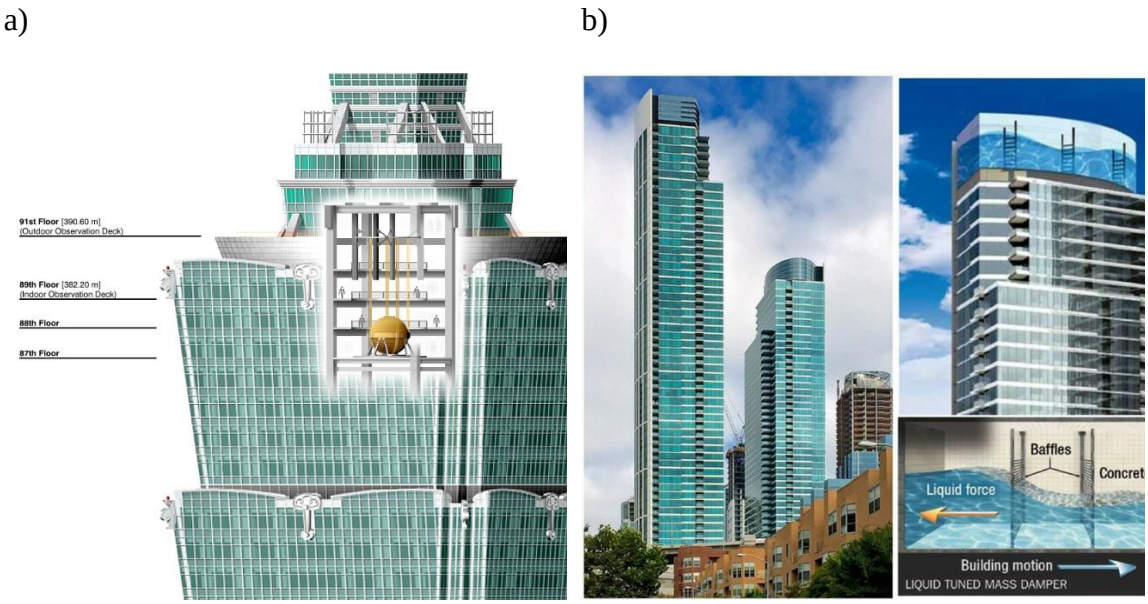

Figure 1.2 a) Taipei 101 TMD sketch [Courtesy Taipei 101 official website], b) One Rincon Hill TLD [Courtesy The Chronicle]

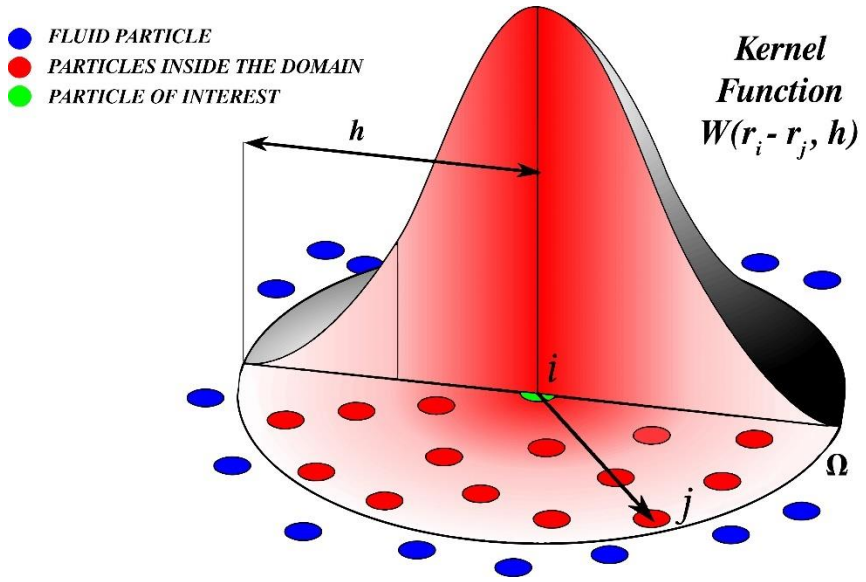

Figure 1.3 illustration of the SPH approximation

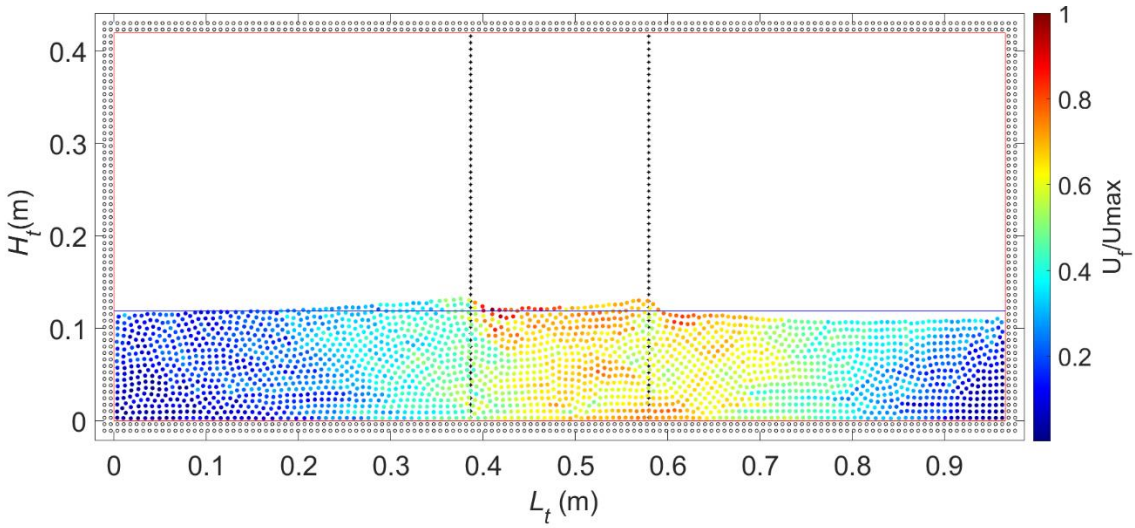

Figure 1.4 SPH particles snapshot coloured by velocity value.

Chapter 2: Macroscopic Modelling For Screens Inside A Tuned Liquid Damper Using Incompressible Smoothed Particle Hydrodynamics

Bishoy N. Awad[a*], Michael J. Tait[a],
[a] McMaster University, 1280 Main Street West, Hamilton, ON, Canada L8S 4L8
*Corresponding Author, e-mail: bawad@mcmaster.ca, +1(905)-962-5200

Abstract

Liquid sloshing inside a Tuned Liquid Damper (TLD) equipped with screens introduces significant numerical modelling challenges. A 2D incompressible Smoothed Particle Hydrodynamics (SPH) model employing a novel macroscopic screen model is presented to capture the complex flow associated with screens and significantly minimize the high computation cost of traditional microscopic screen models. The macroscopic screen model is based on Ergun's equation for pressure drop in porous media. The Sub-Particle Scale (SPS) turbulence model is added to the base code. The modified ISPH code is validated for a hydrostatic case and tank without screens scenario. The predicted sloshing forces and wave heights are validated against experimental data and are compared to numerical results of an existing macroscopic screen model. Findings indicate that the proposed model agrees with experimental results for different fluid depths and under a broad range of excitation amplitudes. The proposed macroscopic screen model and updated SPH code can more accurately capture the response at small excitation amplitudes and requires less computation time than an existing macroscopic model. The proposed model can be an efficient tool for studying internal tank responses over various excitation amplitudes and frequencies without the need for experimental data to determine the drag coefficient for different screen geometries.

Keywords: 2D Incompressible Smoothed particle Hydrodynamics (ISPH), Tuned liquid damper (TLD), Screens, Sloshing tanks, Macroscopic modelling, Ergun equation.

2.1 Introduction

Sloshing fluid within a rigid tank has been used as a Dynamic Vibration Absorber (DVA) on large ships, space satellites, offshore structures, and high-rise buildings to control resonant response (M. J. Tait, 2004). The Tuned Liquid Damper (TLD), a popular type of DVA for high-rise buildings, comprises a partially water-filled tank with a sloshing frequency tuned to a structure's natural frequency (Bauer, 1984). Typically, the inherent damping of a TLD is significantly lower than the optimal target level. As such, various devices have been investigated to increase the inherent damping of TLDs (Bouscasse et al., 2013). For example, researchers have used different tank geometries (Deng & Tait, 2008, 2009; Gardarsson et al., 2001; Olson & Reed, 2001; S. S. Hosseini et al., 2012), baffles (Akyildiz, 2012; Chu et al., 2018; D. Liu & Lin, 2009), and porous media (Tsao & Hwang, 2018).

The addition of screens has been found to be an effective way to increase the inherent damping characteristics of a TLD (Modi & Seto, 1998). However, the introduction of screens also adds modelling challenges (Faltinsen et al., 2011). Previous studies have employed linear models based on shallow water wave theory (M. J. Tait, El Damatty, Isyumov, et al., 2005), equivalent TMD mechanical models (M. J. Tait, 2008), and potential flow theory (J. Hamelin, 2007) to model a TLD equipped with screens. However, these models are typically limited to the first mode response and are restricted to small excitation amplitudes.

Nonlinear models have been developed to handle the complex flow around the screens. These include nonlinear models based on the finite-amplitude theory (Kaneko & Mizota,

2000; Kaneko & Yoshida, 1999), shallow water theory (M. J. Tait, El Damatty, & Isyumov, 2005), or multi-modal techniques (Faltinsen et al., 2000; Love & Tait, 2013b, 2015). However, these models can experience convergence issues and, as such, are often limited to shallow fluid depths and small amplitudes. Several studies have investigated the response of TLDs equipped with screens using computational fluid dynamics (CFD), which captures the full flow by resolving the Navier-Stokes equation through the entire computational domain. Numerical models based on the Volume-Of-Fluid (VOF) (Maravani & Hamed, 2011b), using the Partial-Cell treatment method and a pressure drop model, have been used to model a TLD with screens (Marivani & Hamed, 2017). However, these studies were validated over a limited range of fluid sloshing responses corresponding to small excitation amplitudes.

Complex free-surface flow, including wave breaking associated with large excitation amplitudes, introduces challenges to mesh-based numerical models (M. B. Liu & Liu, 2010). Although many advancements have been made in Eulerian mesh-based methods, these improvements are complex and require substantial computational time and effort (Gao, 2011). As a remedy, the Lagrangian mesh-free Smoothed Particle Hydrodynamics (SPH) method possesses advantages over traditional mesh-based methods for accurately simulating the wave-breaking phenomena, as it does not require computationally expensive tracking algorithms (Monaghan, 1994). The Weakly Compressible Smoothed Particle Hydrodynamics (WCSPH) method has been found to exhibit oscillations in pressure values due to fluctuations in density (Monaghan, 1992). An alternative method to WCSPH is the fully Incompressible Smoothed Particle Hydrodynamics (ISPH) method. Cummins and

Rudman (1999) proposed a projection method, also known as the divergence-free method, which eliminated the use of the equation of state. Their formulation uses the discrete Pressure Poisson Equation (PPE) to calculate the fluid pressure and enforce incompressibility while eliminating spurious pressure fluctuations and the sound speed variable associated with WCSPH (Rouzbahani & Hejranfar, 2017). A density-invariance ISPH formulation was introduced to solve free-surface flows based on a prediction-correction scheme (S. Shao & Lo, 2003). A combination of the two ISPH formulations has been used to enhance the accuracy and stability of the simulations (Hu & Adams, 2007; Jiang et al., 2019). ISPH is often selected over WCSPH as it has been found to provide more accurate results and numerically robust behaviour when studying the sloshing response of a TLD (Halabian et al., 2019; Kashani et al., 2018)

Researchers have explicitly modelled the interaction between screen particles and the flow using rigid boundary particles at the microscopic scale in the SPH literature. This technique explicitly models the fluid-solid interactions and solves all flow quantities (i.e., pressure and velocity) in the vicinity of the screens that influence the fluid motion. Several studies have used this technique to model damping screens inside a TLD and reported good agreement between simulated values and experimental results (Aristodemo et al., 2016; Halabian et al., 2019; Kashani et al., 2018; Meringolo et al., 2015). However, modelling at the microscopic scale requires suitable spacing between particles to adequately capture screen details, which can be impractical due to the high computational effort needed.

As a remedy, a macroscopic SPH model based on Morison's equation (ME) has recently been introduced to model screens for TLD applications (McNamara et al., 2021).

The macroscopic model (i.e., implicit screen model) represents the screens as dummy particles and captures the screen's overall influence without explicitly modelling the screens. This technique is advantageous as the larger particle spacing permitted by this method can significantly reduce computational time. For example, in simulations completed by McNamara et al. (2021), they noted a reduction in computational time by approximately a factor of 700 when using a macroscopic model compared to a microscopic model. For TLD applications, where detailed flow response in the vicinity of the screens is not the main interest, this method was found to be an efficient choice over the traditional microscopic method. However, model accuracy deterioration was observed at small excitation amplitudes. Moreover, the ME model requires knowledge of the screen loss coefficient value specific for each screen geometry, which must often be determined experimentally (McNamara et al., 2021). Furthermore, to the best of the authors' knowledge, the internal response characteristics (i.e., pressure field) within a TLD have not been investigated with SPH using a macroscopic screen model.

Motivated by these limitations, this study presents a novel application for Ergun's porous flow model as an alternative solution to model screens inside a TLD in an SPH environment. Several researchers have coupled numerical porous flow models with SPH. Shao (2010) simulated the wave interactions with a submerged porous media in an ISPH environment, where good agreement was observed between the experimental and ISPH results. Other studies investigated wave interaction with porous structures using SPH simulations (Ren et al., 2014, 2016). Based on Ergun's model, Peng et al. (2015) studied a multi-phase free surface flow in porous media using SPH and found excellent convergence

rates and satisfactory agreement between experimental and numerical data. Recently, Ergun's equation has been used to model the interfacial interaction of flow with porous media on a macroscopic level using an additional stress term in the Navier-Stokes momentum equation without solving the localized flow inside the porous (Kazemi et al., 2020a, 2020b). It was shown that Ergun's equation model effectively simulates different porosities and captures the flow's turbulences through porous media across different engineering applications (Kazemi et al., 2020a). Furthermore, the model combines the laminar and turbulent flow components in porous media (J. Wu et al., 2008). Therefore, Ergun's equation model and its coefficient are adopted to study the response of TLDs equipped with screens.

This chapter develops a novel integration between Ergun's resistance (ER) equation and an ISPH model based on the screen and porous media analogy (i.e., characteristics, porosity, permeability, and solidity ratio). The ER model discretizes the screens into a series of dummy particles of identical shapes and sizes, having a specific porosity and solidity ratio. The porous media parameters are determined based solely on the screen characteristics to accommodate the screen geometry. An extra acceleration term is added to the Navier-Stokes (NS) momentum equation as a closure model to capture the influence of the screen's drag forces on a macroscopic scale. The proposed model presented in this chapter has been customized for SPH application. The ISPH base code introduced in a previous study by McNamara et al. (2021) is modified to incorporate a turbulence model based on the Sub-Particle Scale (SPS) turbulence model. The ISPH code is validated against a hydrostatic case and an excited tank without screens. Convergence is evaluated

for a sloshing tank with screens. The ER model results are subsequently validated against experimental data reported by Tait et al. (2005b) for various excitation amplitudes. The proposed ER and existing ME macroscopic models are compared to experimental results for three different fluid fill ratios studied by Love and Tait (2013). The internal pressure field distribution is also investigated, and the overall performance of the proposed model is assessed.

2.2 SPH Fundamentals

SPH uses a set of discrete particles with initial particle spacing (*dp*) that have representative fluid characteristics to approximate the fluid domain. In SPH nature, the properties of a particle of interest, particle *i*, are interpolated using the values of the surrounding particles, particles *j*, in the neighborhood of particle *i*. This domain is calculated using a weighting function called the kernel function for each particle. The number of particles interacting with particle *i* is determined based on the kernel radius.

2.2.1 SPH Interpolation

Any field variable φ at any position $\boldsymbol{r}$, like velocity, position, or pressure, is transformed into a particle through the kernel approximation defined as

$$\varphi(\boldsymbol{r_i}) \approx \int_{\Omega} \varphi(\boldsymbol{r_j})\ \omega(\boldsymbol{r_{ij}}, h_r)\, \boldsymbol{dr} \tag{2.1}$$

where Ω is the solution domain, ω is the kernel function, and h_r is the kernel radius (i.e., smoothing length), with vector quantities denoted by bold letters. The approximation of the above integral is calculated by the summation of particles inside the domain

$$\varphi(\boldsymbol{r_i}) \approx \sum_{j=1}^{N} \varphi_j V_j \omega\left(|\boldsymbol{r_i} - \boldsymbol{r_j}|, h_r\right) \tag{2.2}$$

where *j* indicates all particles within the neighborhood of particle *i* (*j=1,2, 3,…, N*) and V_j is the volume of particle *j* equal to $(dp)^n$; *n*=2 for two-dimensional simulations. The mass of each particle remains constant throughout the entire simulation and is initially set at the first-time step to be $m_j = \rho_0 V_j$.

2.2.2 Kernel Function

The kernel function influences the stability of the SPH algorithm as it minimizes the error caused by the SPH interpolation (Monaghan, 1992). Several kernels exist in the SPH literature, such as the Gaussian, Spline, Polynomial and others (Hosseini et al., 2007). The fifth-order Wendland kernel function is used in this study for all cases to approximate the delta function (Wendland, 1995)

$$\omega(q) = \omega_c \begin{cases} (1+2q)\left(1-\frac{q}{2}\right)^4 & 0 \le q \le 2 \\ 0 & q \ge 2 \end{cases} \tag{2.3}$$

where, $\omega_c = \frac{7}{4\pi {h_r}^2}$ and $q = \frac{|r_i - r_j|}{h_r}$ (for 2D simulation).

2.2.3 Gradient and Laplacian operators

The SPH literature has several different approaches for these operators. In this study, the symmetrized form of the first-order kernel derivative is used

$$\frac{1}{\rho_i}\nabla\varphi_i = \sum_j m_j \left(\frac{\varphi_j}{\rho_j^2} + \frac{\varphi_i}{\rho_i^2}\right)\nabla_i \omega_{ij} \tag{2.4}$$

where both the linear and angular momentum are conserved (Monaghan, 1992). Following Cummins and Rudman (1999), the Laplacian operator is presented as follows

$$\nabla\left(\frac{1}{\rho_i}\nabla\varphi_i\right) = \sum_j m_j \frac{8}{\left(\rho_i^2+\rho_j^2\right)} \frac{\varphi_{ij}\boldsymbol{r}_{ij}.\nabla_i\omega_{ij}}{\left|\boldsymbol{r}_{ij}^2\right|+\eta^2} \quad \textbf{(2.5)}$$

where, $\varphi_{ij} = \varphi_i - \varphi_j$, $\boldsymbol{r}_{ij} = \boldsymbol{r}_i - \boldsymbol{r}_j$, $\eta=0.01h_r$,m_j and ρ_j are the mass and density of particle j, respectively. For both operators, the $\nabla_i\omega_{ij}$ represents the gradient of the kernel function and is equal to $\frac{\omega_c}{h_r}\left(-5q\left(1-\frac{q}{3}\right)^3\right)\frac{\boldsymbol{r_{ij}}}{||\boldsymbol{r_{ij}}||}$.

2.3 Governing Equations

The Lagrangian form of Navier-Stokes equations for a two-dimensional Newtonian incompressible flow is represented as follows

$$\frac{d\rho}{dt} + \rho_0\nabla\mathbf{u} = 0, \quad \textbf{(2.6)}$$

$$\frac{d\boldsymbol{u}}{dt} = -\frac{1}{\rho_0}\nabla P + v_0\nabla^2\mathbf{u} + \mathbf{g} + \frac{1}{\rho_0}\nabla.\boldsymbol{\tau}\,, \quad \textbf{(2.7)}$$

where $\boldsymbol{u}$, v_0, t, P, $\boldsymbol{g}$ are the fluid velocity, kinematic viscosity, time, pressure, and gravitational acceleration. This study uses water in all simulations with v_0 =1.005X10^{-6} m^2/s, and ρ_0 is 1000 kg/m^3. Here $\boldsymbol{\tau}$ is the Sub-Particle Scale (SPS) turbulence stress term represented as

$$\frac{\tau_{ij}}{\rho_0} = 2\nu_t D_{ij} - \frac{2}{3}k_t\delta_{ij} \quad \textbf{(2.8)}$$

where D_{ij} is the shear strain rate tensor of mean flow and is equal to $\left(\frac{\partial u_i}{\partial x_j}+\frac{\partial u_j}{dx_i}\right)/2$; k_t is the turbulence kinetic energy, and δ_{ij} is the Kronecker delta function (Gotoh et al., 2001). In this study, the Smagorinsky turbulent viscosity (ν_t) is used following Shao (S. Shao & Ji, 2006) as

$$\nu_t = (C_S.\, d_E)^2.\,|\mathrm{D}| \tag{2.9}$$

where C_s is the Smagorinsky constant, d_E is the characteristic length and $|\mathrm{D}| = \sqrt{|2D_{ij}D_{ij}|}$ (Vola et al., 2004). In this model, C_s =0.1, d_E is assumed to be equal to the initial particle spacing dp, and $k_t = \left(\frac{\nu_t}{C_t.dp}\right)^2$; C_t = 0.08 (Gotoh et al., 2001).

2.4 ISPH Formulation

2.4.1 Solution Algorithm

The ISPH algorithm follows the two-step projection method to solve the 2D governing equations, as summarized in the flow chart shown in Figure 2.1 (Cummins & Rudman, 1999). Following the density-invariant ISPH method, also known as the predictor-corrector scheme, the predictive step calculates an intermediate velocity $\boldsymbol{u^*}$ explicitly in time, considering only viscous and gravitational forces (S. Shao & Lo, 2003)

$$\boldsymbol{u}^* = \mathbf{u}(t) + \left(v_0\nabla^2\mathbf{u} + \frac{1}{\rho_0}\nabla.\boldsymbol{\tau} + \mathbf{g} + \boldsymbol{\alpha}_x + \boldsymbol{\psi_{sc}}\right)\Delta t \tag{2.10}$$

where $v_0\nabla^2\mathbf{u}$ is the viscous force, $\boldsymbol{\alpha}_x$ is an external acceleration from excitation force, Δt is the time step, and $\boldsymbol{\psi_{sc}}$ is the extra acceleration term added to represent the drag force of the screens on the macroscopic flow field, introduced in Section 2.5. The value of the

intermediate velocity $\boldsymbol{u}^*$ is used to calculate the intermediate position $\boldsymbol{r}^*$ at each time step without imposing incompressibility, which is expressed as

$$\boldsymbol{r}^* = \mathbf{r}(t) + \boldsymbol{u}^* \Delta t \tag{2.11}$$

Subsequently, an intermediate density ρ^* is calculated from mass conservation

$$\frac{\rho^* - \rho_0}{\Delta t} = -\rho_0 \nabla . \boldsymbol{u}^* \tag{2.12}$$

using the intermediate velocity values (Nomeritae et al., 2016).

The fluid pressure is calculated at each time step using the pressure Poisson's equation (PPE) equation. The PPE equation adopted in this chapter used an extra stabilizing force term following Jiang et al. (2019)

$$\nabla^2 P_i = \alpha \frac{\rho_0 - \rho^*}{\Delta t^2} + (1 - \alpha) \frac{\rho_0 \nabla . \boldsymbol{u}^*}{\Delta t} \tag{2.13}$$

The first term on the RHS represents the density variant effect, the second term represents the velocity-divergence effect, P_i is the pressure at particle i, and the α is the blending factor that controls each term's contribution. In this study, α is equal to 0.01 based on multiple simulation trials presented in section 2.6.1.

This is followed by the correction step, which comprises velocity, position, and density correction to impose incompressibility. The velocity is corrected using the fluid pressure and reference fluid density expressed as

$$\mathbf{u}(\mathrm{t} + \Delta t) = \mathbf{u}^* + \left(-\frac{1}{\rho} \nabla \mathrm{P}\right) \Delta t \tag{2.14}$$

At the end of each time step, the positions are updated based on the corrected velocity

$$\mathbf{r}(\mathrm{t}+\Delta t)=\mathbf{r}(t)+\left(\frac{\mathbf{u}(\mathrm{t}+\Delta t)+\mathbf{u}(\mathrm{t})}{2}\right)\Delta t \tag{2.15}$$

2.4.2 SPH Discretization

Just as in Lo and Shao (2002), the Laplacian of the viscous stress term is discretized as

$$v_0\nabla^2\mathbf{u}=\sum_j \lambda\,\mu_j\boldsymbol{u}_{ij} \tag{2.16}$$

where $\lambda=\left(\frac{8m_j}{(\rho_i+\rho_j)^2}\frac{\boldsymbol{r_{ij}}.\nabla_i\omega_{ij}}{\boldsymbol{r_{ij}^2}+\eta^2}\right)$, and μ= ρv, which is the dynamic viscosity. The turbulent stress term is expressed as

$$\frac{1}{\rho}\nabla.\boldsymbol{\tau}=\sum_j m_j\left(\frac{\tau_{\boldsymbol{j}}}{\rho_j^2}+\frac{\tau_i}{\rho_i^2}\right).\nabla_i\omega_{ij} \tag{2.17}$$

The discretization of the PPE equation used in Yeylaghi et al. (2016) is employed. With a relatively small

timestep than the particle spacing ($\Delta t \ll dp$), the pressure of any particle at the next time step is calculated from the pressure value of all the neighbour fluid particles at the current time step by solving the rearranged PPE equation as follows

$$P_i(t+\Delta t) = \frac{\sum_{j=1}^{N}\lambda P_j(t)+(1-\alpha)\left(\frac{-1}{\Delta t}\right)\sum_{j=1}^{N}\frac{m_j}{\rho_j}\left(\boldsymbol{u}_j^*-\boldsymbol{u}_i^*\right)\nabla_j\omega_{ij}+\alpha\frac{\rho_0-\rho^*}{\Delta \mathrm{t}^2}}{\sum_{j=1}^{N}\lambda} \tag{2.18}$$

where a constant time step (Δt) is used based on a convergence study discussed in section 6.3.2. Additional details on PPE discretization can be found in Yeylaghi et al. (2016).

2.4.3 Boundary Conditions

2.4.3.1. Solid Boundary Treatment

The fixed dummy particles method has been employed for its simplicity, geometry-independency and coding effort requirements (Yeylaghi et al., 2016). Two layers of dummy particles are used with constant density and mass. The pressure of the boundary particles p_w is extrapolated from the pressure of the surrounding fluid particles p_i, as proposed by Adami et al. (2012)

$$P_w = \frac{\sum_{i=1}^{N} P_i \omega_{wi} + \mathrm{g} \left(\sum_{i=1}^{N} \rho_i \boldsymbol{r}_{wi} \omega_{wi}\right)}{\sum_{i=1}^{N} \omega_{wi}} \tag{2.19}$$

where, $\boldsymbol{r}_{wi}$ is the distance between the wall and the fluid particle. The free-slip condition is implemented by mirroring the vertical $\boldsymbol{V}_f$ fluid velocity to the wall and imposing the exact value of the parallel fluid velocity $\boldsymbol{u}_f$ to the wall (i.e., $\boldsymbol{u}_f = \boldsymbol{u}_w$ and $\boldsymbol{v}_f = -\boldsymbol{v}_w$).

2.4.3.2. Free Surface Treatment

The method used in this study is a hybrid method presented in Liu et al. (2013). This method calculates a false density ρ_n

$$\rho_n = \sum_{j=1}^{N} m_j W_{ij} \tag{2.20}$$

Near the free surface region, the number of particles is smaller than the area fully occupied within the fluid (i.e., no fluid particles exist on the outer region of the free surface). Thus, the kernel will be truncated, and the false density ρ_n falls below $\alpha_0 \rho_0$. In this study, α_0 is equal to 0.90 and $\rho_0$is the initial fluid density. The Dirichlet boundary

condition is imposed by enforcing zero pressure for the identified free surface particles (S. Shao & Lo, 2003).

2.5 Fluid-Screen Interface Model

Macroscopic modelling of screens using the ME model has been shown to result in a significant reduction in computational cost for TLD applications compared to capturing the screen geometry explicitly as rigid boundaries (McNamara et al., 2021). However, the ME model showed reduced accuracy at small excitation amplitudes and required knowledge of the screen drag coefficient. As such, Ergun's Resistance (ER) model is proposed in this study as an alternative to the ME model. Several researchers have used the widely applied Ergun Resistance model to simulate flow through porous media (Huang et al., 2003; Nield & Bejan, 2013; Pan et al., 2001). The quadratic formulation of the Ergun equation, which includes the turbulence and laminar flow components, has been found to be an efficient resistance model through a wide range of porosity and permeability values (J. Wu et al., 2008). Moreover, the ER model is compatible with the SPH approximation technique, as shown by previous studies (Kazemi et al., 2020a, 2020b; Peng et al., 2017). Finally, its computational affordability and the analogy between the screens and the porous media parameters were the primary motivation for using the ER model in this study.

Macroscopic models do not capture the detailed geometry of the screen but rather represent the influence of the screen using a medium of dummy particles (shown in Figure 2.2). The screen dummy particles are employed only during the intermediate step, and a closure model is used to calculate the drag force from the surrounding fluid particles in its neighborhood. In the first step, the drag force is computed for each dummy screen particle

from the properties of the surrounding fluid particles (i.e., velocity) in its domain (i.e., based on the screen kernel radius). The fluid particles are not physically obstructed at the location of the dummy screen particles. Thus, fluid particles can travel through the location of the dummy screen particles, as shown in Figure 2.19. As such, the screen particles interact with the fluid particles from every direction (i.e., not only from one side) and use the fluid properties from the previous time step to compute the drag force. If a fluid particle of interest is in the domain of the dummy screen particle, an acceleration term is calculated based on a fraction of the screen drag forces. This fraction is proposed to be proportional to the screen kernel function and opposite to the direction of the flow. Finally, the calculated drag force is converted to an acceleration term and is added to the fluid particle intermediate velocity equation (2.10) to capture the effect of the screen on the flow, which is discussed in detail below.

2.5.1 Ergun's Equation

The Ergun equation is a superposition of laminar and turbulent flow, where the first term is the linear Darcy's law term representing the laminar flow, and the second term represents the nonlinear inertial force term (Ergun & Orning, 1949). SPH has been reported to efficiently handle the coupling between Navier-Stokes and Ergun's equations to model the flow through a porous medium (Kazemi et al., 2020a, 2020b). Similarly, this study uses the Ergun quadratic law (Ergun & Orning, 1949) as a closure model to predict $\boldsymbol{\psi_{sc}}$ in the momentum equation as follows

$$\frac{\Delta P}{L} = \frac{\mu}{K_P}\boldsymbol{u}_s + \frac{1.75}{\sqrt{150}} \cdot \frac{\rho}{\sqrt{K_P} \cdot n_w^{1.5}} \|\boldsymbol{u}_s\| \boldsymbol{u}_s \quad \textbf{(2.21)}$$

where L is the length of the macroscopic pressure gradient in the flow direction, K_P is the permeability, and $\boldsymbol{u}_S$ is the average superficial velocity. The Karman-Cozeny (K-C) model is used to calculate the absolute permeability (Carman, 1937)

$$K_P = \emptyset_s^2 \frac{n_w^3 D_c^2}{150(1-n_w)^2} \quad \textbf{(2.22)}$$

ϕ_s is the sphericity of the particles (=1.0), n_w is the porosity, and D_c is the average particle diameter. Equations (2.21) and (2.22) combine the prediction of flow through porous media at laminar (i.e., Reynold number of packed beds R_{eb}<10) and high turbulent flows (i.e., R_{eb}>1000) and between the two limits (Pal, 2019). However, Ergun's equation is applicable for beds with nearly uniform particle sizes and tends to predict the pressure drop better across sphere particles (Allen et al., 2013) and appreciable rough surfaces (Mayerhofer et al., 2011).

2.5.2 Screen Parameter Values

The screens used in this study are implemented perpendicular to the flow direction and consisted of solid slats with gaps between them having heights h_{slat} and h_{gap}, respectively. The screens are characterized by a loss coefficient (C_l) and solidity ratio (M. J. Tait, El Damatty, Isyumov, et al., 2005). For a two-dimensional simulation, the screen length (t_{sc}) in the flow direction (i.e., excitation direction) will be relatively very thin compared to the length of the tank in the same direction ($t_{sc} \ll L_{tank}$).

To implement the screen macroscopically, the screen domain is presented as a single-phase continuum and discretized by a set of dummy particles spaced evenly at a distance (dp_{sc}). The screen porosity is expressed as follows

$$n_w = 1.0 - S \tag{2.23}$$

where S is the screen's solidity ratio, the average particle diameter D_c of the screen particles is taken as the distance between the screen particles (dp_{sc}). As such, the permeability of the screen can be calculated using (Eqn. 22).

2.5.3 Drag Force Computation

In a 2D simulation, the drag forces of the screens can be calculated from Ergun's equation (2.21) by considering the pressure lost through the screen thickness. First, the difference in pressure before and after the screen can be calculated as

$$\Delta P = \left(\frac{\mu}{K_P} \boldsymbol{u}_s + \frac{1.75}{\sqrt{150}} \cdot \frac{\rho}{\sqrt{K_P} \cdot n_w^{1.5}} \|\boldsymbol{u}_s\| \boldsymbol{u}_s \right) L \tag{2.24}$$

where L can be approximated as the screen thickness $t_{sc,}$ and $\boldsymbol{u}_s$ is taken as the average fluid velocity in the neighbourhood of the screen particle considered. Equation (2.24) is then multiplied by the particle surface area A_p (equivalent to $1.dp_{sc}$ in 2D) to predict the drag force from each screen particle

$$\boldsymbol{F_d} = \left(\frac{\mu}{K_P} \sum_{\boldsymbol{f}} \overline{\boldsymbol{U}}_{s,j} + \frac{1.75}{\sqrt{150}} \cdot \frac{\rho}{\sqrt{K_P} \cdot n_w^{1.5}} \sum_{\boldsymbol{f}} \overline{\boldsymbol{U}}_{s,j} \left\| \overline{\boldsymbol{U}}_{s,j} \right\| \right) t_{sc} . dp_{sc} \tag{2.25}$$

Equation (2.25) is considered only for screen particles in contact with the fluid (i.e., within the fluid height) with the help of kernel truncation. Using the SPH approximation

technique, $\bar{\boldsymbol{U}}_S$ can be calculated as the summation of neighbouring fluid velocities around the screen particle as follows

$$\bar{\boldsymbol{U}}_{s,j} = \sum_f \frac{m_f}{\rho_f} \boldsymbol{u}_f \omega_{jf} \tag{2.26}$$

where $\boldsymbol{u}_f$ is the fluid velocity, ω_{jf} is the kernel function with a kernel radius h_{sc}. This study adopts the Wendland kernel for the screens, and the h_{sc} used equals $2.5h_r$.

A similar treatment of the screen forces, as proposed by McNamara et al. (2021), is implemented in this study, where the influence of the screen on the fluid particle is calculated by adding all the drag forces from the neighbour screen particles proportional to the kernel function weight. Each fluid particle near the screen domain will be influenced by a portion of the screen forces depending on their location, as shown in Figure 2.2. Thus, the force applied to each fluid particle from neighbouring screen particles can be calculated as:

$$\boldsymbol{F}_{\boldsymbol{sc,i}} = -\sum_j \boldsymbol{F}_{\boldsymbol{d}} \frac{\omega_{jf}}{\sum_f \omega_{jf}} \tag{2.27}$$

where j is summed over the neighbouring screen particles, and the negative value reflects the opposite direction of the drag force.

2.5.4 Integration with SPH Model and Interface Zone

During the prediction step, the drag forces are calculated as described in the previous section and are substituted in the intermediate velocity calculation as

$$\boldsymbol{\psi_{sc,i}} = \boldsymbol{F_{sc,i}}/m \tag{2.28}$$

where the screen forces are divided by mass to convert it to acceleration. All calculations associated with the $\boldsymbol{\psi_{sc,i}}$ term are only carried out for fluid particles within the interfacial zone distance, where the fluid interacts with the screen particles (show in Figure 2.2) and is taken to be equal to h_{sc}. $\boldsymbol{\psi_{sc,i}}$ is enforced to have a zero value elsewhere (i.e., in the pure-fluid region) for stable numerical simulation. For this study, a convergence study (discussed in section 2.6.3) determined that the proposed ER model requires an interface radius to be between the limits of ($3dp \leq h_{sc} \leq 4dp$) to capture the effect of the screens and allow for a smooth transition of field variables between the two sub-zones (i.e., free-fluid region and fluid-screen).

2.6 Model Validation

In addition to developing and implementing a novel macroscopic screen model based on the Ergun resistance (ER) model, the existing ISPH code (McNamara et al., 2021) is modified to include a new turbulence model and the integration of the additional acceleration term in the momentum equation. This updated ISPH model was first validated against a hydrostatic case and a sloshing tank with no screens to ensure model stability. Numerical convergence is evaluated on a sloshing case and compared to experimental data. The performance of the ER model was then assessed against experimental results of a TLD with screens at different excitation amplitudes. All simulations considered in this study were for rectangular tanks having dimensions as stated in each section and summarized in Table 2.1.

2.6.1 At Rest Simulation

A hydrostatic case is conducted to validate the base SPH code. For this case, a tank filled with water is tested for 15 seconds with no external acceleration, and as such, the pressure should be equal to $\rho g h_{fluid}$. The pressure profile is captured from the ISPH model after 15 seconds to ensure the model is stable. A rectangular tank with 500 mm length, 400 mm height, and 250 mm initial fluid height is selected for all hydrostatic cases. Five cases were conducted to compare the performance of different simulation parameters such as dp, α, dt, h_r and their influence on the simulation stability. The simulation performance is evaluated by comparing the computed pressure against theoretical values, and the stability is investigated by measuring the percentage of fluid particles exiting through the tank boundaries.

The first case employed the following parameter values, dp=5mm, α=0.01, dt=5X10^{-4}sec, and h_r=1.4. These parameters are subsequently modified to investigate their influence. The pressure gradient for the five cases is represented in Figure 2.3, where the pressure values were normalized by the maximum theoretical pressure, the heights were normalized by the undisturbed fluid height h_{fluid}, and the blue markers presented the free surface particles (i.e., p=0).

Under a static condition, the pressure values should remain constant throughout the simulation period. For nearly all cases (Figure 2.3), the results at the end of the simulations are in agreement with theoretical values, and particles remain inside the tank for the entire simulation period. Slight variations are observed in the pressure and position values, which

may be attributed to where the kernel derivative function approaches zero (i.e., SPH approximation errors). Similar results were reported by Green and Peiró (2018).

However, for the α=0.1 case (bottom right-corner plot in Figure 2.3), approximately 56% of the fluid particles exited the tank, and the simulation failed. It was found that $\alpha <$ 0.05 results in a stable simulation, similar to the value suggested by Jiang et al. (2019). As such, the updated ISPH base model is found to be in good agreement with theoretical hydrostatic results.

2.6.2 Sloshing Motion in TLD Without Screens

The sloshing motion within a TLD with no screen is investigated under horizontal sinusoidal excitation given as $\ddot{X}(t)=-X_0\,\omega_e^2\,sin(\omega_e t)$, where ω_e is the excitation frequency in radians/second, X_0 is the amplitude, and the excitation frequency ratio β is equal to $\frac{f_e}{f_w} = \frac{\omega_e}{\omega_w}$; $f_w = \frac{1}{2\pi}\sqrt{\frac{\pi g}{L}\tanh\left(\frac{\pi h}{L}\right)}$ for a rectangular tank (M. J. Tait, El Damatty, Isyumov, et al., 2005).

This case modelled the same non-linear sloshing motion adopted by Liu and Lin (2008) for a rectangular tank having length = 570 mm, water depth = 150 mm, and excited at X_0/L_{tank} = 0.0088 and β =1. The simulation was run for 7 seconds, dp = 5 mm, α = 0.01, dt = 5X10^{-4} sec, h_r = 1.4, C_s = 0.1, and wave heights were recorded at 20 mm from the left wall of the tank to match the location of the experimental probe. Figure 2.4 shows the wave height (η) response history comparing the results with and without the turbulence model. It is shown that the turbulence model has little influence on the overall results, which indicates that the turbulence effects are negligible in the cases considered. However, the difference

in CPU time between both simulations (i.e., with and without turbulence model) was insignificant. As such, the implemented turbulence model was maintained within the model.

2.6.3 Sloshing Motion in TLD with Screens

2.6.3.1. Test Parameters and Data Analysis

In this section, results from the proposed ER model are compared with experimental data from Tait et al. (2005b) and Love and Tait (2013) and ME model results from McNamara et al. (2021). For all cases presented here, the TLD (shown in Figure 2.5) had a tank length (L_{tank}) of 966mm and was equipped with two screens placed at 40% and 60% of L_{tank}. The screens have a thickness (t_{sc}) of 1mm, a slat height (h_{slat}) of 5mm, and an opening height (h_{gap}) of 7mm. Each simulation time was set to 120 seconds (in order to reach a steady-state response) and the wave probe is positioned at x/L_{tank} =0.95 as shown in Figure 2.5. Pressure is recorded at five different points (arrangement is illustrated in Figure 2.5) near the tank boundaries. The first two points are facing the left tank wall, where P1 is located at the initial fluid height and P2 is at the bottom left corner. Near the tank floor, P3, P4 and P5 are located at x/L_{tank} =0.5, 0.595 & 0.605, respectively.

The experimental data have been low-pass filtered to eliminate noise, and as such, the ISPH results are low-pass filtered using the same low-pass 5 Hz cut-off frequency. For comparison purposes, wave heights (η) are normalized over the initial fluid depth (h_{fluid}) and base shear force (F_w), and sloshing force (F_{sw}) are normalized over the highest value of the inertial water force $F_I = m_w X_0 \omega_e^2$, where m_w is the total water mass and $F_{sw} = F_w - m_w \ddot{X}$.

2.6.3.2. Convergence Study

The SPH particle size (*dp*) is independently evaluated for a sloshing tank under different horizontal excitation amplitudes (X_0/L_{tank} = 0.005 and 0.031) with a constant fluid depth (h_{fluid}/L_{tank} = 0.123) and for different fluid heights (h_{fluid}/L_{tank} = 0.05,0.15 and 0.25) at a constant excitation amplitude (X_0/L_{tank} = 0.0026). The normalized maximum and minimum average wave height response from each simulation are compared to Tait et al. (2005b) and Love and Tait (2013) experimental data. The particle resolution was tested independently using *dt* =5X10^{-4} sec and *dp* values ranging between 3 mm and 11 mm.

Figure 2.6 shows the relative error (δ_R) for the average maximum and minimum normalized wave heights and sloshing forces. Particle resolution independence is observed for *dp* ≤ 7mm at X_0/L_{tank} = 0.031, yielding acceptable results with $\delta_R \leq 10.0\%$ for wave heights and $\delta_R \leq 5.0\%$ for sloshing forces. For simulations with a low free surface response (e.g., $X_0/L_{tank} \leq 0.005$), these acceptable relative error percentages are observed for *dp* =5mm. Further reduction in particle size resulted in a slight improvement (<2%) at *dp* = 3mm and a significant increase in computational time (by approximately a factor of 4). For instance, the relative difference of the wave peaks between SPH results and experimental results at X_0/L_{tank} = 0.0026 and h_{fluid}/L_{tank} = 0.05 is 2.3% for *dp* =5mm and 1.0% for *dp* =3mm, while the computational time is 14.6 CPU hrs for *dp* =3mm and 3.5 CPU hrs for *dp* =5mm. As such, in this study, *dp* =7mm is employed for excitation amplitudes greater than 0.005, and *dp* = 5mm is used for excitation amplitudes $X_0/L_{tank} \leq 0.005$.

As shown in Figure 2.7, a constant time step is tested using values from 1X10^{-3} sec to 1X10^{-4} sec with *dp* =7 mm. The results show a time step independency below 5X10^{-4} sec,

which agrees with the CFL condition $\Delta t \leq min\left(0.1\left(\frac{dp}{U_{max}}\right), 0.1\left(\frac{dp^2}{v}\right)\right)$ (S. Shao & Lo, 2003). As such, this study employed a fixed time step for all simulations. Finally, the blending factor α and the screen kernel radius h_{sc} are independently investigated. Figure 2.8 shows that the best results are achieved for α= 0.01, while Figure 2.9 illustrates good agreement with experimental results for $3dp \leq h_{sc} \leq 4dp$.

2.6.3.3. High Excitation Amplitudes Simulations

The proposed ER model is compared to the experimental shake table testing from Tait et al. (2005b) for two excitation amplitudes (X_0/L_{tank} = 0.016 and 0.031) at a frequency ratio of β =1.01 and h_{fluid}/L_{tank} =0.123. Figure 2.10 and Figure 2.11 show the normalized wave heights and the normalized base shear force-time response curves for X_0/L_{tank} = 0.016 and 0.031, respectively. The model is able to accurately capture the wave height peaks and troughs for the high amplitude values considered and is observed to agree with the experimental results. Furthermore, the simulation took 126 minutes to complete using the ME model and 103 minutes using the ER model (approximately 20% less time).

2.6.3.4. Low Excitation Amplitude Simulations

The first case presented simulates the smallest excitation amplitude (X_0/L_{tank} = 0.005) tested by Tait et al. (2005b). Based on multiple simulations (Figure 2.6), a particle size of dp=5 mm was determined to enhance model predictions near troughs at low amplitudes compared to multiple simulations of finer and coarser particle sizes. This can be attributed to the nature of the free surface response formulation used in the base model, which requires the product of the kernel radius and the initial particle spacing to be sufficiently larger than

the wave height amplitude ($h_r\ dp < \eta$) to capture the sloshing response. A similar observation was noted by McNamara et al. (2021).

For β =1.01 and h_{fluid}/L_{tank} =0.123, the normalized wave height and base shear force response history curves are shown in Figure 2.12 and compared to the numerical results from the ME model. The ER model showed good agreement with the experimental results and slightly better estimated the peaks and troughs than the ME model.

Nevertheless, the previous cases only considered the response near resonance and did not count for different fluid depths. As such, five additional cases with different fluid fill ratios (h_{fluid}/L_{tank} = 0.05, 0.1, 0.15, 0.2 and 0.25) reported by Love and Tait (2013) were also investigated. For each fluid height, 60 sloshing frequencies, ranging from β =0.8 to 1.2, were investigated at X_0/L_{tank} = 0.0026.

For brevity, only the frequency response curves for three representable fill ratios are presented (h_{fluid}/L_{tank} =0.05, 0.15, and 0.2). Figure 2.13 to Figure 2.15 show the frequency response curves of the normalized wave heights and sloshing forces, comparing the ER model and ME model results to the experimental data from Love and Tait (2013). The ER model is observed to be in better agreement with the experimental data than the ME model for the lowest fill ratio. The ER model is also found to predict the minimum and maximum response quantities more accurately than the ME model.

To furtherly quantify the performance and applicability of the ER model, the normalized error (Love & Tait, 2013b) for the sloshing forces was calculated as follows

$$\epsilon_{F_{sw}} = \sqrt{\frac{\sum_i \left(F_i^{SPH} - F_i^{exp}\right)^2}{\sum_i \left(F_i^{exp}\right)^2}} \tag{2.29}$$

where F_i is the frequency response force value at frequency i. Figure 2.16 plots the error values computed from the ER versus the ME models' error values obtained from McNamara et al. (2021). The maximum error value is recorded for the shallowest fluid depth, and the error values tend to decrease for deeper h_{fluid}/L_{tank} values considered. However, an acceptable value of normalized error ($\epsilon \leq 0.1$), as suggested by Love and Tait (2013), is found for the sloshing forces predicted by the ER model and with better performance compared to the ME model.

2.7 Internal Response Characteristics

The current ISPH model facilitates the evaluation of different fields (e.g., velocities and pressures) at any location inside the tank throughout the simulation period, which can be helpful for designers (Nakashima, 2010). This section will present the results of the ER model for localized pressures and velocities that could aid in the advanced design of a TLD.

2.7.1 Pressure and Velocity Distribution

Figure 2.17 and Figure 2.18 present images taken at different successive time instants within one period showing the hydrodynamic pressure (P_H) and the fluid velocity distribution simulated by the ER model for X_0/L_{tank} = 0.031 at β =1.01, respectively. The sloshing motion is initiated at the tank wall, and the generated wave travels across the tank, hitting the adjacent tank wall. The particles accumulate, and pressure builds up gradually at the tank wall. Then the wave travels back to the other side and reciprocates the tank wall.

The model was cable of capturing this motion by emulating the two spikes in each period observed near tank walls in Figure 2.20.

Meanwhile, it can be observed that the fluid particles lose pressure after crossing the screen location, which reflects the influence of the screen drag forces and how the model captures the effect of the screens. The particle velocity illustrated in Figure 2.18 shows that the maximum vertical velocities occur near the tank walls, where fluid impacts the wall, and the fundamental frequency is dominant. While the maximum horizontal velocities are observed in the middle of the tank and near the free surface, where breaking waves occur, and the second harmonic frequency is dominant. Meanwhile, the fluid particles are not obstructed by the dummy screen particles, demonstrating the robustness of the model. Similar results were reported by Kashani et al. (2018) under similar conditions using a microscopic screen model with 1mm particle spacing. The ER model employed in this study used approximately 98% fewer particles to run the same simulation, highlighting its computational effectiveness.

To further visualize the effect of the screens on the fluid pressure, Figure 2.19 shows two images taken simultaneously for the same simulation parameters for comparing a TLD with and without the screens at $X_0/L_{tank} = 0.031$. For the tank with screens, the fluid particles exhibit a significant pressure drop in the interface region with the screens (the upper image in Figure 2.19), as demonstrated by the change in colour gradient, and the effect of the screen limits the sloshing amplitude. For the tank without screens shown in the lower image of Figure 2.19, the fluid wave propagates across the tank without pressure dissipation compared to the tank with screens.

2.7.2 Pressure Response History

Pressure evaluation data for TLD with screens are scarce in the literature. Therefore, three representative nodes are selected on the tank perimeter to observe fluid dynamic loading at different locations inside the TLD excited at $X_0/L_{tank} = 0.031$. Figure 2.20 shows the hydrodynamic pressure (P_H) response history normalized by the static pressure at nodes P1, P2 and P3, respectively. The maximum fluid pressure amplitudes are observed at point P1 (e.g., near the initial fluid depth), and the minimum amplitudes are observed at point P3 (e.g., at the bottom center). Higher pressure fluctuations are observed near the free surface, decreasing gradually from point P1 to P3. It can be observed that the dominant pressure period at the center of the tank is twice the value of the excitation frequency, as the dominant pressure at the center of the tank corresponds to the second harmonic, while the fundamental frequency is dominant at the tank walls. These observations agree with the conclusions made by Saghi (2016) for a partially-filled rectangular sloshing tank exposed to a horizontal periodic excitation using FEM. The above results show that the ISPH code with the ER model is capable of evaluating pressure values at any location inside the TLD with screens.

The pressure time series are recorded near the bottom of the tank at the center (P3) and before (P4) and after (P5) the second screen for a tank with and without screens to evaluate the effect of the screen. The upper graph in Figure 2.21 compares the pressure at P3 (i.e., the bottom center of the tank), showing a reduction in pressure due to the influence of the screens, which reduce the fluid response resulting in lower maximum pressure values. The lower graph in Figure 2.21 shows the pressure difference between P4 and P5

for both cases, where the difference is minor between the two points for the tank without screens. However, a noticeable pressure loss due to screens is visible for the tank with screens, which confirms the macroscopic ER resistance model's influence on the fluid at the screen locations.

2.8 Conclusions

Motivated by the analogy between the porous media particles and the screens, this study presents a novel application for the porous media flow model for implementing screens macroscopically inside the TLD based on Ergun's equation using SPH interpolation. Macroscopic modelling allows for a significant reduction in the number of particles needed to model the influence of the screens, which eliminates the impractical computational power and makes it more computationally affordable.

The macroscopic (i.e., ER) model utilized Ergun's equation to describe the pressure loss through porous media to predict the pressure loss through the screens. An existing 2D ISPH code is modified in order to include an extra acceleration term in the momentum equation to capture the drag forces of the screens. The model is also outfitted with the Sub-Particle Scale (SPS) model to artificially add extra viscosity to mimic the missing boundary layers and 3D effects; however, turbulence effects were negligible. The full SPH discretization and fluid-screen interface are described in detail. Subsequently, the ISPH model is validated against a hydrostatic tank case and experimental data for a rectangular tank with no screens under horizontal harmonic excitation to test the stability and performance of the model with and without the turbulence closure model. The model convergence is independently studied on a sloshing tank with screens for parameters. The

model is then validated using experimental results of a rectangular TLD tank with two screens for a wide range of shallow and deep fill ratios and under different sinusoidal amplitude excitations. Finally, the ability of the model to evaluate internal response characteristics (e.g., pressure) is investigated. The following conclusions are made:

- ER model showed excellent agreement against shake table test results for all excitation amplitudes and fluid fill ratios considered without explicitly modelling the detailed flow inside the screens, which significantly decreases computational time.
- The model is not dependent on the screen loss coefficient, which eliminates the need for experimental testing for different screen geometries.
- For small-amplitude excitations considered, the ER model showed better agreement with the experimental results than the ME model for the time domain and frequency responses considered.
- The ER model formulation resulted in faster simulation times, which may facilitate greater use of SPH for modelling purposes.
- The model can also investigate and visualize the pressure field inside the tank, which can aid in TLD design.

Based on these findings, the ER model can serve as a robust tool for the analysis and the design of the TLD equipped with screens for screen geometries over a wide range of excitation amplitudes and frequencies. The above computations indicate that the ER model can capture the influence of the screens more efficiently than other microscopic and

macroscopic methods currently available. No limitations in terms of fluid fill ratios or excitation amplitudes were observed for the range of values considered in this study.

2.9 Acknowledgement

Financial support has been provided by the Natural Sciences and Engineering Research Council of Canada (NSERC). This work was made possible by the Shared Hierarchical Academic Research Computing Network (SHARCNET: www.sharcnet.ca) and Compute/Calcul Canada (www.computecanada.ca). This study forms a part of an ongoing research program at McMaster University Centre for Effective Design of Structures (CEDS).

2.10 References

Adami, S., Hu, X. Y., & Adams, N. A. (2012). A generalized wall boundary condition for smoothed particle hydrodynamics. *Journal of Computational Physics*, *231*(21), 7057–7075. https://doi.org/10.1016/j.jcp.2012.05.005

Agresta, A., Cavalagli, N., Biscarini, C., & Ubertini, F. (2021). Effect of bottom geometry on the natural sloshing motion of water inside tanks: An experimental analysis. *Applied Sciences (Switzerland)*, *11*(2), 1–15. https://doi.org/10.3390/app11020605

Akyildiz, H. (2012). A numerical study of the effects of the vertical baffle on liquid sloshing in two-dimensional rectangular tank. *Journal of Sound and Vibration*, *331*(1), 41–52. https://doi.org/10.1016/j.jsv.2011.08.002

Akyildiz, H., & Ünal, E. (2005). Experimental investigation of pressure distribution on a rectangular tank due to the liquid sloshing. *Ocean Engineering*, *32*(11–12), 1503–1516. https://doi.org/10.1016/j.oceaneng.2004.11.006

Allen, K. G., von Backström, T. W., & Kröger, D. G. (2013). Packed bed pressure drop dependence on particle shape, size distribution, packing arrangement and roughness. *Powder Technology*, *246*, 590–600. https://doi.org/10.1016/j.powtec.2013.06.022

Aristodemo, F., Meringolo, D. D., & Veltri, P. (2016). A multi-node approach to simulate thin coastal structures in the SPH context. *Proceedings of the Coastal Engineering Conference*, *35*, 1–12.

Awad, B. N., & Tait, M. J. (n.d.). Modelling of Sloped and Curved Bottom Tuned Liquid Dampers with Screens using Smoothed Particle Hydrodynamics. *International Journal of Dynamics and Control*.

Awad, B. N., & Tait, M. J. (2022). Macroscopic modelling for screens inside a tuned liquid damper using incompressible smoothed particle hydrodynamics. *Ocean Engineering*.

Bauer, H. F. (1984). Oscillations of immiscible liquids in a rectangular container: A new damper for excited structures. *Journal of Sound and Vibration*, *93*(1), 117–133. https://doi.org/10.1016/0022-460X(84)90354-7

Bhuta, P. G., & Koval, L. R. (1966). A Viscous RIng Damper For a Freely Precessing Satellite. *International Journal of Mechanical Sciences*, *8*, 383–395.

Biswal, K. C., Bhattacharyya, S. K., & Sinha, P. K. (2006). Non-linear sloshing in partially liquid filled containers with baffles. *International Journal for Numerical Methods in Engineering*, *68*(3), 317–337. https://doi.org/10.1002/nme.1709

Bouscasse, B., Antuono, M., Colagrossi, A., & Lugni, C. (2013). Numerical and experimental investigation of nonlinear shallow water sloshing. *International Journal of Nonlinear Sciences and Numerical Simulation*, *14*(2), 123–138. https://doi.org/10.1515/ijnsns-2012-0100

Burton, M., Fluid, B. M. T., Abdelrazaq, A., Samsung, C., & Corporation, T. (2015). *Wind-Induced Motion of Tall Buildings : Designing for Occupant Comfort*.

Calderon-Sanchez, J., Martinez-Carrascal, J., Gonzalez-Gutierrez, L. M., & Colagrossi, A. (2021). A global analysis of a coupled violent vertical sloshing problem using an SPH methodology. *Engineering Applications of Computational Fluid Mechanics*, *15*(1), 865–888. https://doi.org/10.1080/19942060.2021.1921849

Carman, P. G. (1937). Fluid flow through granular beds. *Chemical Engineering Research and Design*, *75*(1 SUPPL.), S32–S48. https://doi.org/10.1016/s0263-8762(97)80003-2

Cassolato, M. R., Love, J. S., & Tait, M. J. (2011). Modelling of a tuned liquid damper with inclined damping screens. *Structural Control and Health Monitoring*, *18*(May 2011), 674–681. https://doi.org/10.1002/stc

Chen, Y. H., Hwang, W. S., Chiu, L. T., & Sheu, S. M. (1995). Flexibility of TLD to high-rise building by simple experiment and comparison. *Computers and Structures*, *57*(5), 855–861. https://doi.org/10.1016/0045-7949(95)00083-S

Cherfils, J. M., Pinon, G., & Rivoalen, E. (2012). JOSEPHINE: A parallel SPH code for free-surface flows. *Computer Physics Communications*, *183*(7), 1468–1480. https://doi.org/10.1016/j.cpc.2012.02.007

Chu, C. R., Wu, Y. R., Wu, T. R., & Wang, C. Y. (2018). Slosh-induced hydrodynamic force in a water tank with multiple baffles. *Ocean Engineering*, *167*(July 2017), 282–292. https://doi.org/10.1016/j.oceaneng.2018.08.049

Crespo, A. J. C., Domínguez, J. M., Rogers, B. D., Gómez-Gesteira, M., Longshaw, S.,

Canelas, R., Vacondio, R., Barreiro, A., & García-Feal, O. (2014). DualSPHysics: Open-source parallel CFD solver based on Smoothed Particle Hydrodynamics (SPH). *Computer Physics Communications*. https://doi.org/10.1016/j.cpc.2014.10.004

Cummins, S. J., & Rudman, M. (1999). An SPH Projection Method. *Journal of Computational Physics*, *607*(2), 584–607.

Deng, X. (2007). *The performance of tuned liquid dampers with different tank geometries*. McMaster University.

Deng, X., & Tait, M. J. (2008). Equivalent mechanical models of tuned liquid dampers with different tank geometries. *Canadian Journal of Civil Engineering*, *35*(10), 1088–1101. https://doi.org/10.1139/L08-044

Deng, X., & Tait, M. J. (2009). Theoretical modeling of TLD with different tank geometries using linear long wave theory. *Journal of Vibration and Acoustics, Transactions of the ASME*, *131*(4), 0410141–04101410. https://doi.org/10.1115/1.3142873

Ergun, S., & Orning, A. A. (1949). Fluid Flow through Randomly Packed Columns and Fluidized Beds. *Industrial & Engineering Chemistry*, *41*(6), 1179–1184. https://doi.org/10.1021/ie50474a011

Faltinsen, O. M., Firoozkoohi, R., & Timokha, A. N. (2011). Analytical modeling of liquid sloshing in a two-dimensional rectangular tank with a slat screen. *Journal of Engineering Mathematics*, *70*(1–3), 93–109. https://doi.org/10.1007/s10665-010-9397-5

Faltinsen, O. M., Rognebakke, O. F., Lukovsky, I. A., & Timokha, A. N. (2000). Multidimensional modal analysis of nonlinear sloshing in a rectangular tank with finite water depth. *Journal of Fluid Mechanics*, *407*(March), 201–234. https://doi.org/10.1017/S0022112099007569

Fediw, A. A., Isyumov, N., & Vickery, B. J. (1995). Performance of a tuned sloshing water damper. *Journal of Wind Engineering and Industrial Aerodynamics*, *57*(2–3), 237–247. https://doi.org/10.1016/0167-6105(94)00107-O

Floryan, J. M., & Rasmussen, H. (1989). Numerical methods for viscous flows with moving boundaries. *Applied Mechanics Reviews*, *42*(12), 323–341.

https://doi.org/10.1115/1.3152416

Fujino, Y., Sun, L., Pacheco, B., & Chaiseri, P. (1992). Tuned liquid damper (TLD) for suppressing horizontal motion of structures. *ASCE Journal of Engineering Mechanics*, *118*(10), 2017–2030.

Gao, M. (2011). *Numerical simulation of liquid sloshing in rectangular tanks using consistent particle method and experimental verification*. 207.

Gardarsson, S., Yeh, H., & Reed, D. (2001). Behavior of Sloped-Bottom Tuned Liquid Dampers. *Journal of Engineering Mechanics*, *127*(3), 266–271. https://doi.org/10.1061/(asce)0733-9399(2001)127:3(266)

Gingold, R. A., & Monaghan, J. J. (1977). Smoothed particle hydrodynamics: theory and application to non-spherical stars. *Monthly Notices of the Royal Astronomical Society*, *181*(3), 375–389.

Gotoh, T, S., & T., S. (2001). Sub-particle-scale turbulence model for the MPS method—Lagrangian ?ow model for hydraulic engineering Title. *Computational Fluid Dynamics Journal*, *9*(4), 339–347.

Green, M. D., & Peiró, J. (2018). Long duration SPH simulations of sloshing in tanks with a low fill ratio and high stretching. *Computers and Fluids*, *174*, 179–199. https://doi.org/10.1016/j.compfluid.2018.07.006

Guan, Y., Yang, C., Chen, P., & Zhou, L. (2020). Numerical investigation on the effect of baffles on liquid sloshing in 3D rectangular tanks based on nonlinear boundary element method. *International Journal of Naval Architecture and Ocean Engineering*, *12*, 399–413. https://doi.org/10.1016/j.ijnaoe.2020.04.002

Halabian, A. M., Karamnasab, A., & Chamani, M. R. (2019). A New Hybrid SPH-FEM Model to Evaluate Seismic Response of TSD Equipped-Structures. *Journal of Earthquake and Tsunami*, *13*(2), 1–27. https://doi.org/10.1142/S1793431119500076

Hamelin, J. (2007). *the Effect of Screen Geometry on the Performance of a Tuned Liquid Damper*. 185.

Hamelin, J. A., Love, J. S., Tait, M. J., & Wilson, J. C. (2013). Tuned liquid dampers with a Keulegan-Carpenter number-dependent screen drag coefficient. *Journal of Fluids*

and Structures, *43*, 271–286. https://doi.org/10.1016/j.jfluidstructs.2013.09.006

Hosseini, S. M., Manzari, M. T., & Hannani, S. K. (2007). A fully explicit three-step SPH algorithm for simulation of non-Newtonian fluid flow. *International Journal of Numerical Methods for Heat and Fluid Flow*, *17*(7), 715–735. https://doi.org/10.1108/09615530710777976

Housner, G. W., Bergman, L. A., Caughey, T. K., Chassiakos, A. G., Claus, R. O., Masri, S. F., Skelton, R. E., Soong, T. T., Spencer, B. F., & Yao, J. T. P. (1997). Structural Control: Past, Present, and Future. *Journal of Engineering Mechanics*, *123*(9), 897–971. https://doi.org/10.1061/(asce)0733-9399(1997)123:9(897)

Hu, X. Y., & Adams, N. A. (2007). An incompressible multi-phase SPH method. *Journal of Computational Physics*, *227*(1), 264–278. https://doi.org/10.1016/j.jcp.2007.07.013

Huang, C., Chang, H., & Hwung, H. (2003). *Structural permeability effects on the interaction of a solitary wave and a submerged breakwater*. *49*, 1–24. https://doi.org/10.1016/S0378-3839(03)00034-6

Idir, M., Ding, X., Lou, M., & Chen, G. (2009). Fundamental frequency of water sloshing waves in a sloped-bottom tank as tuned liquid damper. *Proceedings of the 2009 Structures Congress - Don't Mess with Structural Engineers: Expanding Our Role*, 831–840. https://doi.org/10.1061/41031(341)91

Irwin, P., Kilpatrick, J., Robinson, J., & Frisque, A. (2008). WIND AND TALL BUILDINGS : NEGATIVES AND POSITIVES. *The Structural Design of Tall and Special Buildings*, *928*(November), 915–928.

ITTC Resistance Committee. (2017). Uncertainty analysis in CFD Verification and validation methodology and procedures. *ITTC - Recommended Procedures and Guidelines*, 1–13.

Jiang, H., You, Y., Hu, Z., Zheng, X., & Ma, Q. (2019). Comparative study on violent sloshing withwater jet flows by using the ISPH method. *Water (Switzerland)*, *11*(12). https://doi.org/10.3390/w11122590

Kaneko, S., & Mizota, Y. (2000). Dynamical modeling of deepwater-type cylindrical tuned

liquid damper with a submerged net. *Journal of Pressure Vessel Technology, Transactions of the ASME*, *122*(1), 96–104. https://doi.org/10.1115/1.556156

Kaneko, S., & Yoshida, O. (1999). Modeling of deepwater-type rectangular tuned liquid damper with submerged nets. *Journal of Pressure Vessel Technology, Transactions of the ASME*, *121*(4), 413–422. https://doi.org/10.1115/1.2883724

Kareem, A., Kijewski, T., & Tamura, Y. (1999). Mitigation of motions of tall buildings with specific examples of recent applications. *Wind and Structures, An International Journal*, *2*(3), 201–251. https://doi.org/10.12989/was.1999.2.3.201

Kashani, A. H., Halabian, A. M., & Asghari, K. (2018). A numerical study of tuned liquid damper based on incompressible SPH method combined with TMD analogy. *Journal of Fluids and Structures*, *82*, 394–411. https://doi.org/10.1016/j.jfluidstructs.2018.07.013

Kazemi, E., Koll, K., Tait, S., & Shao, S. (2020)a. SPH modelling of turbulent open channel flow over and within natural gravel beds with rough interfacial boundaries. *Advances in Water Resources*, *140*(January). https://doi.org/10.1016/j.advwatres.2020.103557

Kazemi, E., Tait, S., & Shao, S. (2020)b. SPH-based numerical treatment of the interfacial interaction of flow with porous media. *International Journal for Numerical Methods in Fluids*, *92*(4), 219–245. https://doi.org/10.1002/fld.4781

Kim, Y. (2001). *Numerical simulation of sloshing ¯ows with impact load*. *23*.

Konar, T., & Ghosh, A. (2021). Development of a novel tuned liquid damper with floating base for converting deep tanks into effective vibration control devices. *Advances in Structural Engineering*, *24*(2), 401–407. https://doi.org/10.1177/1369433220953539

Koshizuka, S., Nobe, A., & Oka, Y. (1998). Numerical analysis of breaking waves using the moving particle semi-implicit method. *International Journal for Numerical Methods in Fluids*, *26*(7), 751–769. https://doi.org/10.1002/(sici)1097-0363(19980415)26:7<751::aid-fld671>3.0.co;2-c

Koutsoloukas, L., Nikitas, N., & Aristidou, P. (2022). Passive, semi-active, active and hybrid mass dampers: A literature review with associated applications on building-like structures. *Developments in the Built Environment*, *12*(October).

https://doi.org/10.1016/j.dibe.2022.100094

Lawrence G. Griffis. (1993). Serviceability limit states under wind load. *Engineering Journal, American Institute of Steel Construction*, *30*(1), 1–16.

Lee, E. S., Moulinec, C., Xu, R., Violeau, D., Laurence, D., & Stansby, P. (2008). Comparisons of weakly compressible and truly incompressible algorithms for the SPH mesh free particle method. *Journal of Computational Physics*, *227*(18), 8417–8436. https://doi.org/10.1016/j.jcp.2008.06.005

Lishi, W., Zhuang, W., & Yuchun, L. (2013). A SPH simulation on large-amplitude sloshing for fluids in a two-dimensional tank. *Journal of Earthquake Engineering and Engineering Vibration*, *12*(1), 135–142. https://doi.org/10.1007/s11803-013-0157-1

Liu, D., & Lin, P. (2008). A numerical study of three-dimensional liquid sloshing in tanks. *Journal of Computational Physics*, *227*(8), 3921–3939. https://doi.org/10.1016/j.jcp.2007.12.006

Liu, D., & Lin, P. (2009). Three-dimensional liquid sloshing in a tank with baffles. *Ocean Engineering*, *36*(2), 202–212. https://doi.org/10.1016/j.oceaneng.2008.10.004

Liu, M. B., & Liu, G. R. (2010). Smoothed particle hydrodynamics (SPH): An overview and recent developments. In *Archives of Computational Methods in Engineering* (Vol. 17, Issue 1). https://doi.org/10.1007/s11831-010-9040-7

Liu, X., Xu, H., Shao, S., & Lin, P. (2013). An improved incompressible SPH model for simulation of wave-structure interaction. *Computers and Fluids*, *71*, 113–123. https://doi.org/10.1016/j.compfluid.2012.09.024

Lo, E. Y. M., & Shao, S. (2002). Simulation of near-shore solitary wave mechanics by an incompressible SPH method. *Applied Ocean Research*, *24*(5), 275–286. https://doi.org/10.1016/S0141-1187(03)00002-6

Love, J. S., D., L., & X., D. (2018). Tuning fire suppression tanks for tuned sloshing damper applications. *7th World Conf. on Structural Control and Monitoring. Los Angeles: International Association for Structural Control and Monitoring*.

Love, J. S., Morava, B., Robinson, J. K., & Haskett, T. C. (2021). Tuned Sloshing Dampers in Tall Buildings: A Practical Performance-Based Design Approach. *Practice*

Periodical on Structural Design and Construction, *26*(3), 1–13. https://doi.org/10.1061/(asce)sc.1943-5576.0000582

Love, J. S., & Tait, M. J. (2010). Nonlinear simulation of a tuned liquid damper with damping screens using a modal expansion technique. *Journal of Fluids and Structures*, *26*(7–8), 1058–1077. https://doi.org/10.1016/j.jfluidstructs.2010.07.004

Love, J. S., & Tait, M. J. (2011a). Equivalent linearized mechanical model for tuned liquid dampers of arbitrary tank shape. *Journal of Fluids Engineering, Transactions of the ASME*, *133*(6), 61105-1-61105–61109. https://doi.org/10.1115/1.4004080

Love, J. S., & Tait, M. J. (2011b). Non-linear multimodal model for tuned liquid dampers of arbitrary tank geometry. *International Journal of Non-Linear Mechanics*, *46*(8), 1065–1075. https://doi.org/10.1016/j.ijnonlinmec.2011.04.028

Love, J. S., & Tait, M. J. (2013a). Nonlinear multimodal model for TLD of irregular tank geometry and small fluid depth. *Journal of Fluids and Structures*, *43*, 83–99. https://doi.org/10.1016/j.jfluidstructs.2013.09.009

Love, J. S., & Tait, M. J. (2013b). Parametric depth ratio study on tuned liquid dampers: Fluid modelling and experimental work. *Computers and Fluids*, *79*, 13–26. https://doi.org/10.1016/j.compfluid.2013.03.004

Love, J. S., & Tait, M. J. (2014). Linearized sloshing model for 2D tuned liquid dampers with modified bottom geometries. *Canadian Journal of Civil Engineering*, *41*(2), 106–117. https://doi.org/10.1139/cjce-2013-0106

Love, J. S., & Tait, M. J. (2015). The response of structures equipped with tuned liquid dampers of complex geometry. *JVC/Journal of Vibration and Control*, *21*(6), 1171–1187. https://doi.org/10.1177/1077546313495074

Luo, M., Koh, C. G., & Bai, W. (2016). A three-dimensional particle method for violent sloshing under regular and irregular excitations. *Ocean Engineering*, *120*, 52–63. https://doi.org/10.1016/j.oceaneng.2016.05.015

Maravani, M., & Hamed, M. S. (2011a). Numerical modeling of sloshing motion in a tuned liquid damper outfitted with a submerged slat screen. *International Journal for Numerical Methods in Fluids*, *65*(January 2010), 834–855. https://doi.org/10.1002/fld

Maravani, M., & Hamed, M. S. (2011b). Numerical modeling of sloshing motion in a tuned liquid damper outfitted with a submerged slat screen. *International Journal for Numerical Methods in Fluids*, *65*(January 2010), 834–855. https://doi.org/10.1002/fld

Marivani, M., & Hamed, M. S. (2017). Evaluate pressure drop of slat screen in an oscillating fluid in a tuned liquid damper. *Computers and Fluids*, *156*, 384–401. https://doi.org/10.1016/j.compfluid.2017.08.008

Marsh, A., Prakash, M., Semercigil, E., & Turan, Ö. F. (2011). A study of sloshing absorber geometry for structural control with SPH. *Journal of Fluids and Structures*, *27*(8), 1165–1181. https://doi.org/10.1016/j.jfluidstructs.2011.02.010

Mayerhofer, M., Govaerts, J., Parmentier, N., Jeanmart, H., & Helsen, L. (2011). Experimental investigation of pressure drop in packed beds of irregular shaped wood particles. *Powder Technology*, *205*(1–3), 30–35. https://doi.org/10.1016/j.powtec.2010.08.006

McNamara, K. P., Awad, B. N., Tait, M. J., & Love, J. S. (2021). Incompressible smoothed particle hydrodynamics model of a rectangular tuned liquid damper containing screens. *Journal of Fluids and Structures*, *103*, 103295. https://doi.org/10.1016/j.jfluidstructs.2021.103295

McNamara, K. P., Love, J. S., & Tait, M. J. (2022a). Nonlinear modelling of series-type pendulum tuned mass damper-tuned liquid damper. *Journal of Vibration and Acoustics*, 1–26. https://doi.org/10.1115/1.4053636

McNamara, K. P., Love, J. S., & Tait, M. J. (2022b). Numerical investigation of the response of structures equipped with a limited freeboard tuned liquid damper. *Journal of Fluids and Structures*, *108*, 103426. https://doi.org/10.1016/j.jfluidstructs.2021.103426

McNamara, K. P., & Tait, M. J. (2022). Modeling the Response of Structure–Tuned Liquid Damper Systems Under Large Amplitude Excitation Using Smoothed Particle Hydrodynamics. *Journal of Vibration and Acoustics*, *144*(1), 1–13. https://doi.org/10.1115/1.4051266

Meringolo, D. D., Aristodemo, F., & Veltri, P. (2015). SPH numerical modeling of wave-

perforated breakwater interaction. *Coastal Engineering*, *101*, 48–68. https://doi.org/10.1016/j.coastaleng.2015.04.004

Modi, V. J., & Seto, M. L. (1998). Passive control of flow-induced oscillations using rectangular nutation dampers. *JVC/Journal of Vibration and Control*, *4*(4), 381–404. https://doi.org/10.1177/107754639800400403

Monaghan, J. J. (1985). Partcle Method for Hydrodynamics. *Computer Physics Reports*, *3*(2), 71–124. http://adsabs.harvard.edu/cgi-bin/nph-data_query?bibcode=1985CoPhR...3...71M&link_type=EJOURNAL%0Apapers3://publication/doi/10.1016/0167-7977(85)90010-3

Monaghan, J. J. (1992). Smoothed Particle Hydrodynamics. *Annual Review of Astronomy and Astrophysics*, *30*(1), 543–574. https://doi.org/10.1146/annurev.aa.30.090192.002551

Monaghan, J. J. (1994). Simulating free surface flows with SPH. In *Journal of Computational Physics* (Vol. 110, Issue 2, pp. 399–406). https://doi.org/10.1006/jcph.1994.1034

Monaghan, J. J. (2012). Smoothed Particle Hydrodynamics and Its Diverse Applications. *Annual Review of Fluid Mechanics*, *44*(1), 323–346. https://doi.org/10.1146/annurev-fluid-120710-101220

Nakashima, M. (2010). *Design Recommendation for Storage Tanks and Their Supports*. 179.

Nanda, B. (2014). A Review on Applications of Tuned Liquid Dampers in Vibration Control. *Advances in Civil Engineering*, *July*, 183–200.

Nield, D. A., & Bejan, A. (2013). Convection in porous media. *Convection in Porous Media*, 1–778. https://doi.org/10.1007/978-1-4614-5541-7

Nomeritae, Daly, E., Grimaldi, S., & Bui, H. H. (2016). Explicit incompressible SPH algorithm for free-surface flow modelling: A comparison with weakly compressible schemes. *Advances in Water Resources*, *97*, 156–167. https://doi.org/10.1016/j.advwatres.2016.09.008

Olson, D. E., & Reed, D. A. (2001). A nonlinear numerical model for sloped-bottom tuned

liquid dampers. *Earthquake Engineering and Structural Dynamics*, *30*(5), 731–743. https://doi.org/10.1002/eqe.34

Pan, W., Tartakovsky, A. M., Monaghan, J. J., Trimulyono, A., Hashimoto, H., Ma, H., Ruth, D. W., De Schampheleire, S., De Kerpel, K., Ameel, B., De Jaeger, P., Bagci, O., De Paepe, M., He, J., & Fu, Z.-F. (2001). A numerical analysis of the interfacial drag force for fluid flow in porous media. *Transport in Porous Media*, *17*(1), 49–78. https://doi.org/10.3390/jmse7010017

Patil, G. R., & Singh, K. D. (2016). Evaluation of Sloped Bottom Tuned Liquid Damper for Reduction of Seismic Response of Tall Buildings. *Journal of The Institution of Engineers (India): Series A*, *97*(4), 385–394. https://doi.org/10.1007/s40030-016-0185-8

Peng, C., Vienna, L. S., Xu, G., Wu, W., Vienna, L. S., & Wang, C. (2017). *Multiphase SPH modeling of free surface flow in porous media with variable porosity Multiphase SPH modeling of free surface flow in porous media with variable porosity*. *October*. https://doi.org/10.1016/j.compgeo.2016.08.022

Peng, C., Wu, W., Yu, H. sui, & Wang, C. (2015). A SPH approach for large deformation analysis with hypoplastic constitutive model. *Acta Geotechnica*, *10*(6), 703–717. https://doi.org/10.1007/s11440-015-0399-3

Ramaswamy, B., Kawahara, M., & Nakayama, T. (1986). Lagrangian finite element method for the analysis of two-dimensional sloshing problems. *International Journal for Numerical Methods in Fluids*, *6*(9), 659–670. https://doi.org/10.1002/fld.1650060907

Rana, R. (1996). Response Control of Structures by Tuned Mass Dampers and Their Generalizations. *Eleventh World Conference on Earthquake Engineering*.

Reed, D., Yu, J., Yeh, H., & Gardarsson, S. (1998). Investigation of Tuned Liquid Dampers under Large Amplitude Excitation. *Journal of Engineering Mechanics*, *124*(4), 405–413. https://doi.org/10.1061/(asce)0733-9399(1998)124:4(405)

Ren, B., Wen, H., Dong, P., & Wang, Y. (2014). Numerical simulation of wave interaction with porous structures using an improved smoothed particle hydrodynamic method.

Coastal Engineering, *88*, 88–100. https://doi.org/10.1016/j.coastaleng.2014.02.006

Ren, B., Wen, H., Dong, P., & Wang, Y. (2016). Improved SPH simulation of wave motions and turbulent fl ows through porous media. *Coastal Engineering*, *107*, 14–27. https://doi.org/10.1016/j.coastaleng.2015.10.004

Rouzbahani, F., & Hejranfar, K. (2017). A truly incompressible smoothed particle hydrodynamics based on artificial compressibility method. *Computer Physics Communications*, *210*, 10–28. https://doi.org/10.1016/j.cpc.2016.09.008

Ruiz, R. O., Taflanidis, A. A., & Lopez-Garcia, D. (2016). Characterization and design of tuned liquid dampers with floating roof considering arbitrary tank cross-sections. *Journal of Sound and Vibration*, *368*, 36–54. https://doi.org/10.1016/j.jsv.2016.01.014

S. S. Hosseini, A. K. Ghorbani-Tanha, & M. Rahimian. (2012). Performance of tuned liquid dampers with different tank geometries for vibration control of structures. *The 15th World Conference on Earthquake Engineering*, 1–9.

Saghi, H. (2016). The pressure distribution on the rectangular and trapezoidal storage tanks' perimeters due to liquid sloshing phenomenon. *International Journal of Naval Architecture and Ocean Engineering*, *8*(2), 153–168. https://doi.org/10.1016/j.ijnaoe.2015.12.001

Shao, J. R., Li, H. Q., Liu, G. R., & Liu, M. B. (2012). An improved SPH method for modeling liquid sloshing dynamics. *Computers and Structures*, *100–101*, 18–26. https://doi.org/10.1016/j.compstruc.2012.02.005

Shao, S. (2010). Incompressible SPH flow model for wave interactions with porous media. *Coastal Engineering*, *57*(3), 304–316. https://doi.org/10.1016/j.coastaleng.2009.10.012

Shao, S., & Ji, C. (2006). SPH computation of plunging waves using a 2-D sub-particle scale (SPS) turbulence model. *International Journal for Numerical Methods in Fluids*, *51*(8), 913–936. https://doi.org/10.1002/fld.1165

Shao, S., & Lo, E. Y. M. (2003). Incompressible SPH method for simulating Newtonian and non-Newtonian flows with a free surface. *Advances in Water Resources*, *26*(7),

787–800. https://doi.org/10.1016/S0309-1708(03)00030-7

Shimizu, T., & Hayama, S. (1987). Nonlinear Responsed of Sloshing Based on the Shallow Water Wave Theory. *JSME International Journal*, *30*(263), 806–813.

Siddique, M. R., Hamed, M. S., & El Damatty, A. A. (2005). A nonlinear numerical model for sloshing motion in tuned liquid dampers. *International Journal of Numerical Methods for Heat and Fluid Flow*, *15*(3), 306–324. https://doi.org/10.1108/09615530510583900

Smagorinsky, J. (1963). General Circulation Experiments With the Primitive Equations. *Monthly Weather Review*, *91*(3), 99–164. https://doi.org/10.1175/1520-0493(1963)091<0099:gcewtp>2.3.co;2

Sun, L. M., Fujino, Y., Chaiseri, P., & Pacheco, B. M. (1995). The properties of tuned liquid dampers using a TMD analogy. *Earthquake Engineering & Structural Dynamics*, *24*(7), 967–976. https://doi.org/10.1002/eqe.4290240704

Sun, L. M., Fujino, Y., Pacheco, B. M., & Chaiseri, P. (1992). Modelling of tuned liquid damper (TLD). *Journal of Wind Engineering and Industrial Aerodynamics*, *43*(1–3), 1883–1894. https://doi.org/10.1016/0167-6105(92)90609-E

Tait, M. (2018). *A Study on Unbonded Fiber - Reinforced Elastomeric Isolators for Improved Performance of Ontario Highway Bridges*.

Tait, M., El Damatty, A. A., & Isyumov, N. (2004). Testing of tuned liquid damper with screens and development of equivalent TMD model. *Wind and Structures, An International Journal*, *7*(4), 215--234.

Tait, M. J. (2004). *The Performance of 1-D and 2-D Tuned Liquid Dampers*.

Tait, M. J. (2008). Modelling and preliminary design of a structure-TLD system. *Engineering Structures*, *30*(10), 2644–2655. https://doi.org/10.1016/j.engstruct.2008.02.017

Tait, M. J., & Deng, X. (2008). The performance of structure-tuned liquid damper systems with different tank geometries M. *Structural Control and Health Monitoring*, *17*(3), 254–277. https://doi.org/10.1002/stc

Tait, M. J., El Damatty, A. A., & Isyumov, N. (2005). An investigation of tuned liquid

dampers equipped with damping screens under 2D excitation. *Earthquake Engineering and Structural Dynamics*, *34*(7), 719–735. https://doi.org/10.1002/eqe.452

Tait, M. J., El Damatty, A. A., Isyumov, N., & Siddique, M. R. (2005). Numerical flow models to simulate tuned liquid dampers (TLD) with slat screens. *Journal of Fluids and Structures*, *20*(8), 1007–1023. https://doi.org/10.1016/j.jfluidstructs.2005.04.004

Tait, M. J., Isyumov, N., & El Damatty, A. A. (2008). Performance of Tuned Liquid Dampers. *Journal of Engineering Mechanics*, *134*(5), 417–427. https://doi.org/10.1061/(asce)0733-9399(2008)134:5(417)

Tavakkol, S., Zarrati, A. R., & Khanpour, M. (2017). Curvilinear smoothed particle hydrodynamics. *International Journal for Numerical Methods in Fluids*, *83*(2), 115–131. https://doi.org/10.1002/fld.4261

Tsao, W. H., & Hwang, W. S. (2018). Tuned liquid dampers with porous media. *Ocean Engineering*, *167*(February), 55–64. https://doi.org/10.1016/j.oceaneng.2018.08.034

Valizadeh, A., & Rudman, M. (2017). A numerical approach for simulating flow through thin porous media. *European Journal of Mechanics, B/Fluids*, *65*, 31–44. https://doi.org/10.1016/j.euromechflu.2017.03.004

Vickery, B. J., Isyumov, N., & Davenport, A. G. (1983). The role of damping, mass and stiffness in the reduction of wind effects on structures. *Journal of Wind Engineering and Industrial Aerodynamics*, *11*, 285–294.

Violeau, D., & Rogers, B. D. (2016). Smoothed particle hydrodynamics (SPH) for free-surface flows: Past, present and future. *Journal of Hydraulic Research*, *54*(1), 1–26. https://doi.org/10.1080/00221686.2015.1119209

Vola, D., Babik, F., & Latché, J. C. (2004). On a numerical strategy to compute gravity currents of non-Newtonian fluids. *Journal of Computational Physics*, *201*(2), 397–420. https://doi.org/10.1016/j.jcp.2004.05.019

Wang, S., Gonzalez-cao, J., Islam, H., Gomez-Gesteira, M., & Guedes Soares, C. (2022). Uncertainty estimation of mesh-free and mesh-based simulations of the dynamics of floaters. *Ocean Engineering*, *256*(April).

https://doi.org/10.1016/j.oceaneng.2022.111386

Warnitchai, P., & Pinkaew, T. (1998). Modelling of liquid sloshing in rectangular tanks with flow-dampening devices. *Engineering Structures*, *20*(7). https://doi.org/10.1016/S0141-0296(97)00068-0

Wendland, H. (1995). Piecewise polynomial, positive definite and compactly supported radial functions of minimal degree. *Advances in Computational Mathematics*, *4*(1), 389–396. https://doi.org/10.1007/BF02123482

Wu, G. X., Ma, Q. W., & Eatock Taylor, R. (1998). Numerical simulation of sloshing waves in a 3D tank based on a finite element method. *Applied Ocean Research*, *20*(6), 337–355. https://doi.org/10.1016/S0141-1187(98)00030-3

Wu, J., Yu, B., & Yun, M. (2008). *A resistance model for flow through porous media*. *June 2007*, 331–343. https://doi.org/10.1007/s11242-007-9129-0

Xie, J. (2014). Aerodynamic optimization of super-tall buildings and its effectiveness assessment. *Journal of Wind Engineering and Industrial Aerodynamics*, *130*, 88–98. https://doi.org/10.1016/j.jweia.2014.04.004

Xue, M. A., Zheng, J., & Lin, P. (2012). Numerical simulation of sloshing phenomena in cubic tank with multiple baffles. *Journal of Applied Mathematics*, *2012*. https://doi.org/10.1155/2012/245702

Xue, M. A., Zheng, J., Lin, P., & Yuan, X. (2017). Experimental study on vertical baffles of different configurations in suppressing sloshing pressure. *Ocean Engineering*, *136*(December 2015), 178–189. https://doi.org/10.1016/j.oceaneng.2017.03.031

Yalla, S. K., & Kareem, A. (2001). Beat phenomenon in combined structure-liquid damper systems. *Engineering Structures*, *23*(6), 622–630. https://doi.org/10.1016/S0141-0296(00)00085-7

Yeylaghi, S., Moa, B., Oshkai, P., Buckham, B., & Crawford, C. (2016). ISPH modelling of an oscillating wave surge converter using an OpenMP-based parallel approach. *Journal of Ocean Engineering and Marine Energy*, *2*(3), 301–312. https://doi.org/10.1007/s40722-016-0053-7

Yu, J. K., Wakahara, T., & Reed, D. A. (1999). A non-linear numerical model of the tuned

liquid damper. *Earthquake Engineering and Structural Dynamics*, *28*(6), 671–686. https://doi.org/10.1002/(SICI)1096-9845(199906)28:6<671::AID-EQE835>3.0.CO;2-X

Table 2.1 Summary of simulation cases investigated.

Simulations		L_{tank} (mm)	h_{fluid} (mm)	Sim. Time (sec)	h_r	α	dp (mm)	dt (sec)	β	X_0/L_{tank}	h_{sc}	Notes
No motion	***Case 1***	500	250	15	1.4dp	0.01	5	$5X10^{-4}$	N/A	N/A	N/A	N/A
	Case 2				1.1dp	0.01	5	$5X10^{-4}$				
	Case 3					0.01	5	$1X10^{-4}$				
	Case 4				1.4dp	0.01	10	$5X10^{-4}$				
	Case 5					0.1	5	$5X10^{-4}$				
Sloshing motion in TLD without screens	***Case 1***	570	150	7	1.4dp	0.01	5	$5X10^{-4}$	1	0.009	N/A	Turbulence model on
	Case 2											Turbulence model off
Sloshing motion in TLD with screens (Convergence)	***Case 1***	966	119	120	1.4dp	0.01	3,5,7, 11	$5X10^{-4}$	1.01	0.005	$2.5h_r$	*dp* Conv. Test
	Case 2									0.031		
	Case 3		48.3						0.8 to 1.2	0.0026		
	Case 4		144.9									
	Case 5		241.5									
	Case 6							$1X10^{-3}$, $7X10^{-4}$, $5X10^{-4}$, $1X10^{-4}$				*dt* Conv. Test
	Case 7		119			0.005,0.01, 0.05,0.1	7	$5X10^{-4}$	1.01	0.031	2dp,3dp, 3.5dp, 4dp,5dp	α Conv. Test
	Case 8					0.01						h_{sc} Conv. Test
Sloshing motion in TLD with screens	***Case 1***	966	119	120	1.4dp	0.01	7	$5X10^{-4}$	1.01	0.016	$2.5h_r$	N/A
	Case 2									0.031		
	Case 3									0.005		
	Case 4		48.3				5		0.8 to 1.2	0.0026		
	Case 5		96.6									
	Case 6		144.9									
	Case 7		193.2									
	Case 8		241.5									

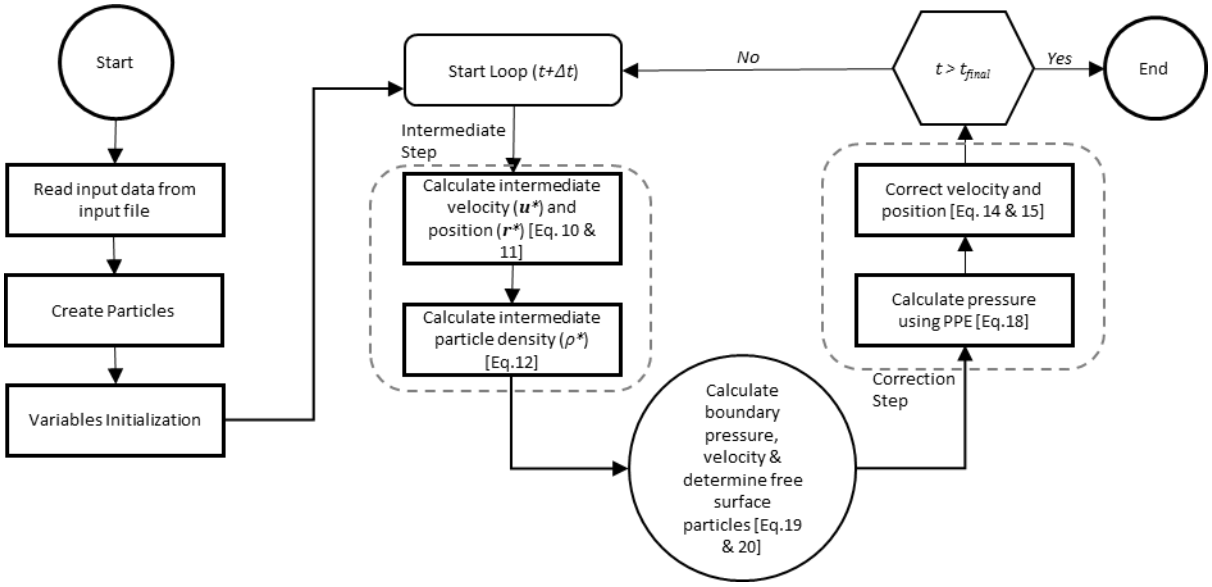

Figure 2.1 Flow chart of the ER model.

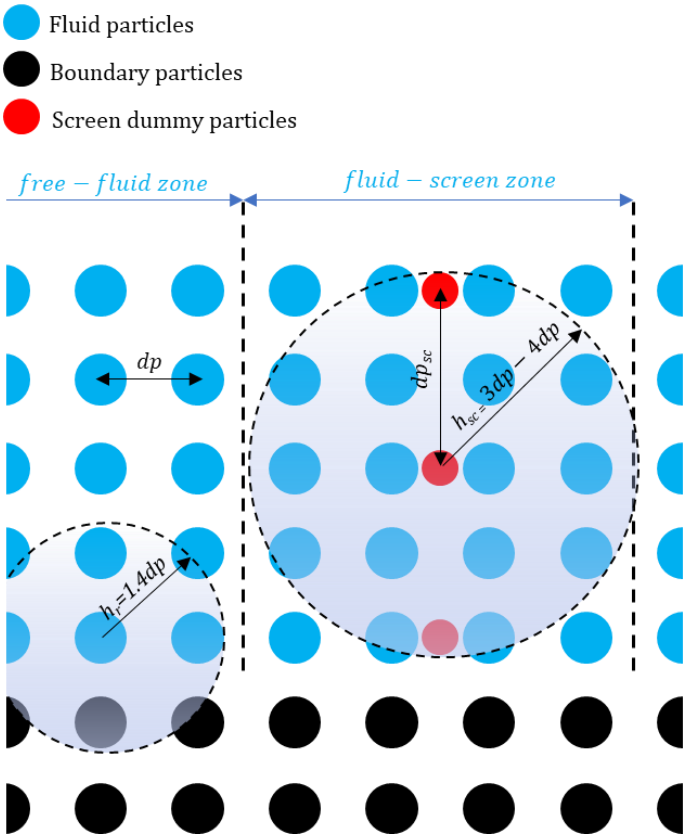

Figure 2.2 A schematic view of the ISPH domain discretization at the initial state showing the particle spacings, kernel radiuses, and simulation sub-zones.

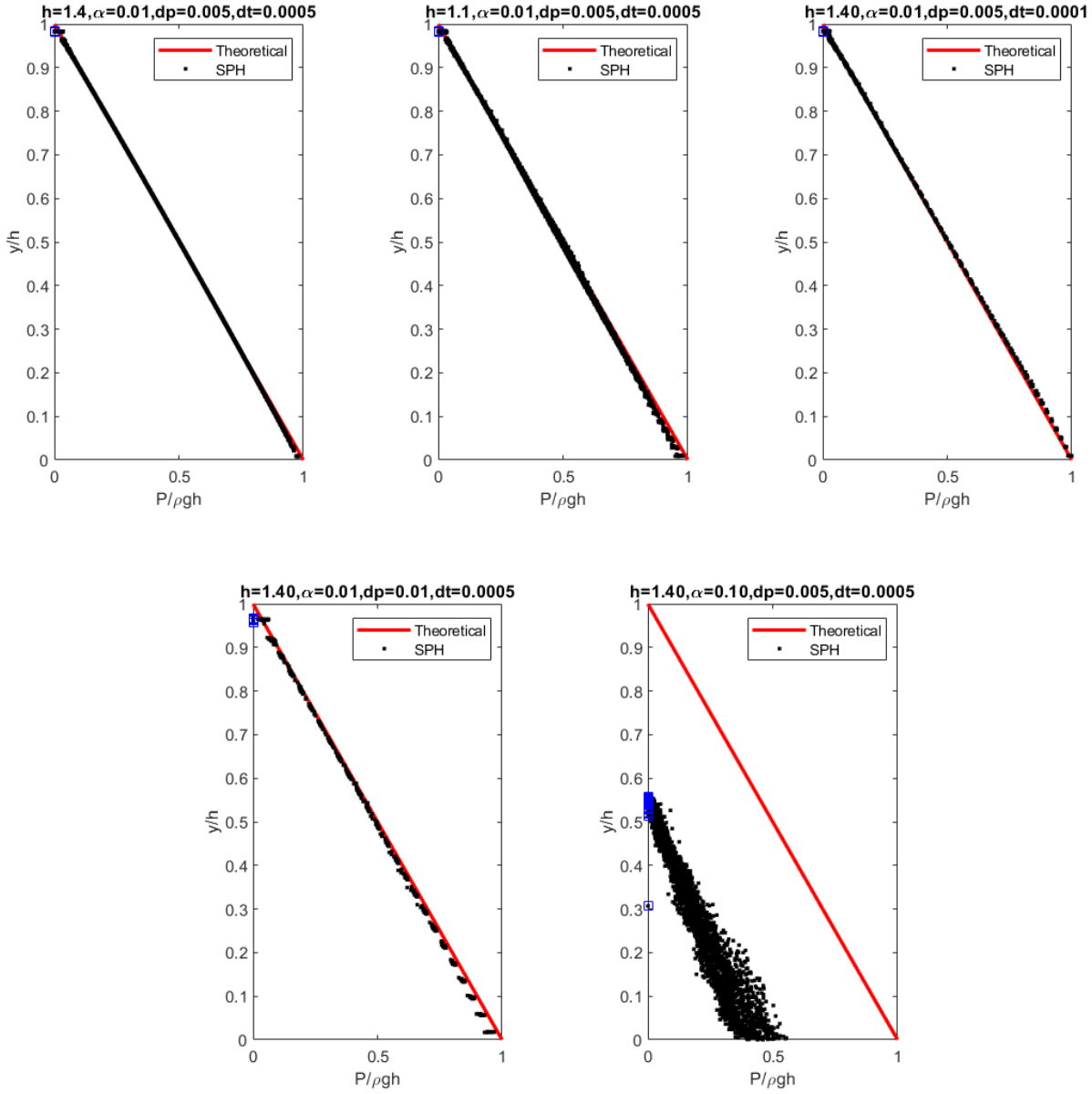

Figure 2.3 Computed pressure profiles for the no-motion simulations at (15 seconds) for different parameters are shown above each figure.

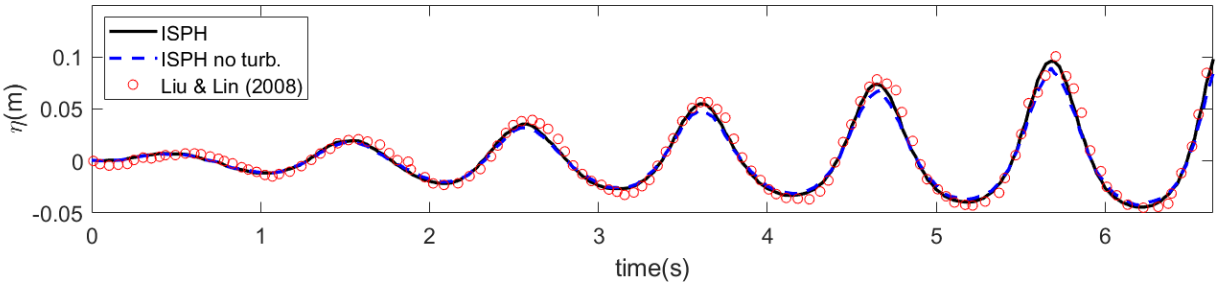

Figure 2.4 ER simulated wave height time response with and without turbulence model versus experimental results from Liu and Lin (2008). X_0/L_{tank} = 0.0088 and β =1

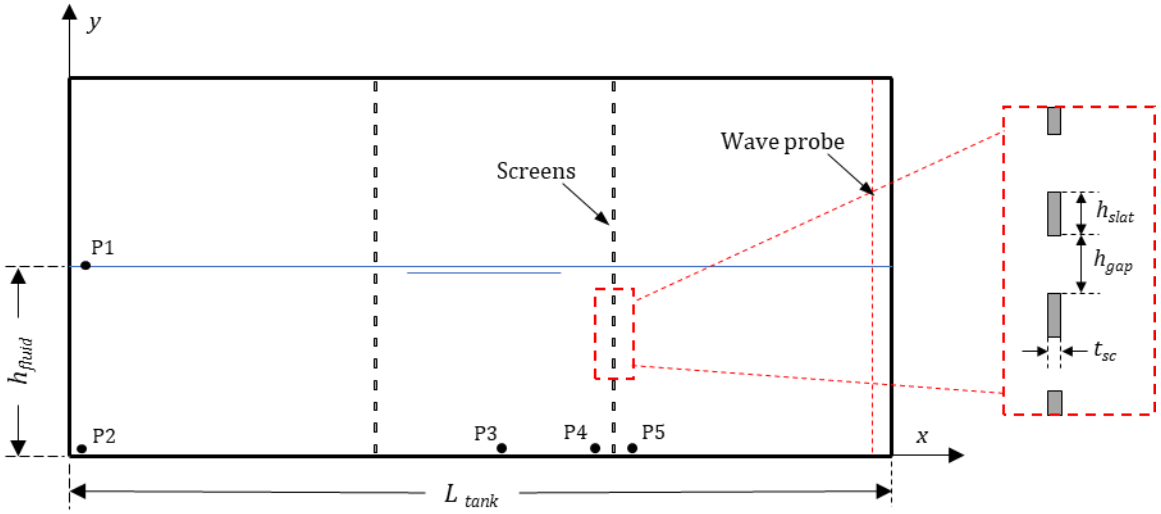

Figure 2.5 Problem setup of sloshing motion with screens in tank corresponding to Tait et al. (2005b).

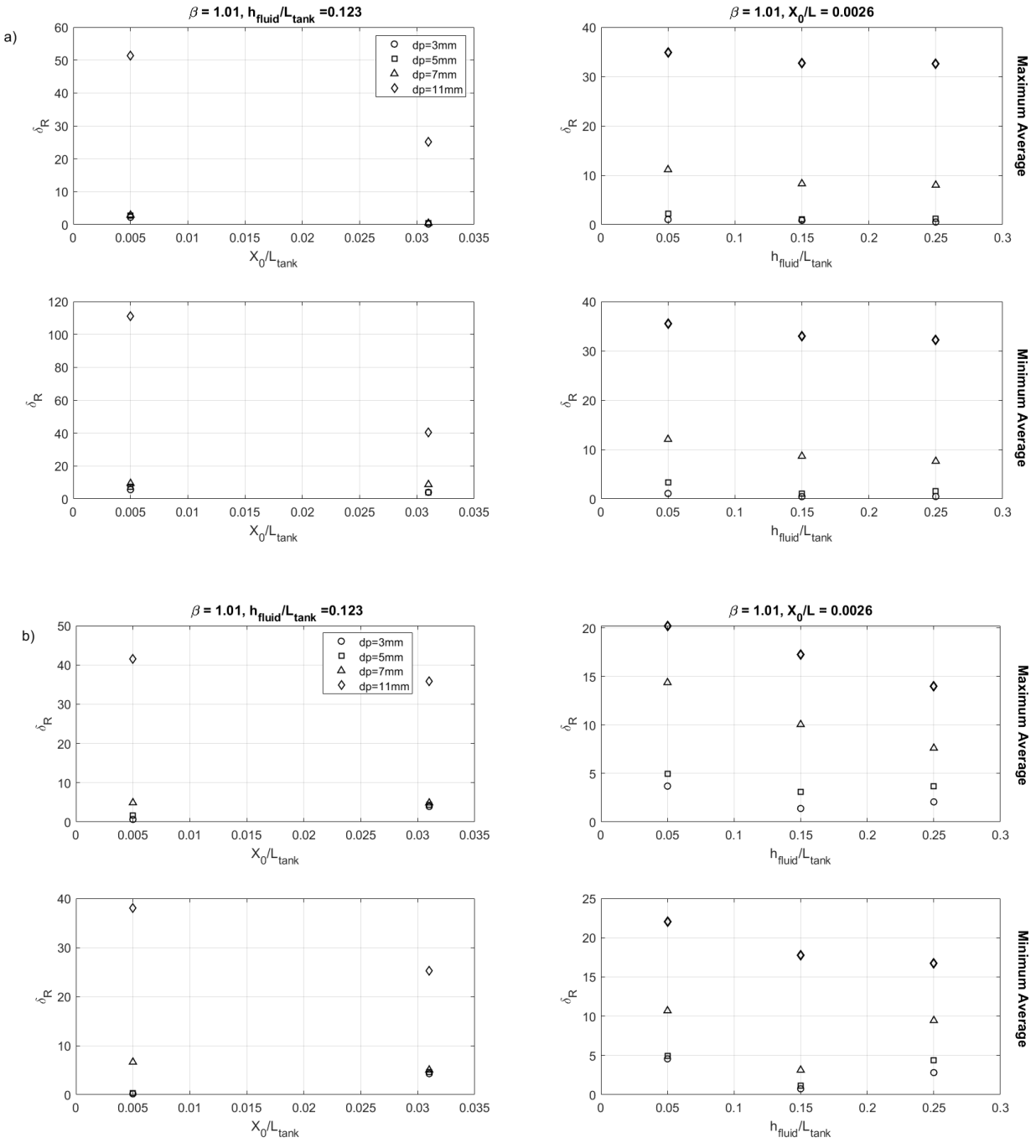

Figure 2.6 Relative error percentage for the normalized (a) wave heights and (b) sloshing forces using different particle sizes versus experimental (EXP) results from Tait et al. (2005b) and Love and Tait (2013).

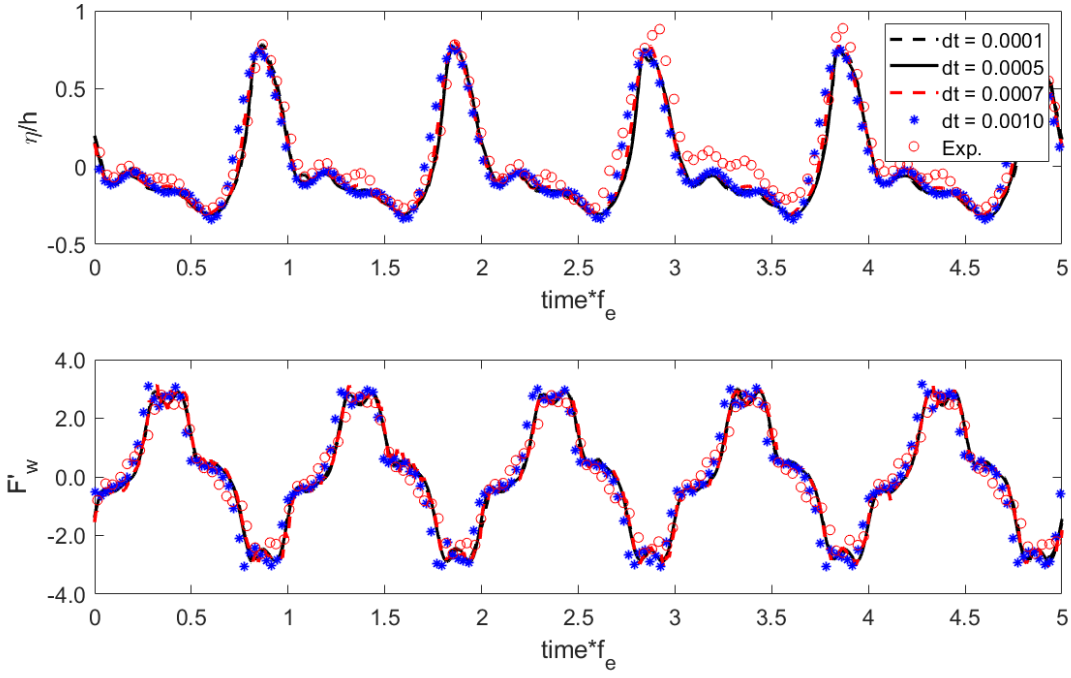

Figure 2.7 ER model simulated response history for the normalized wave heights and base shear forces for different time steps versus experimental (EXP) results from Tait et al. (2005b). X_0/L_{tank} = 0.031, β =1.01

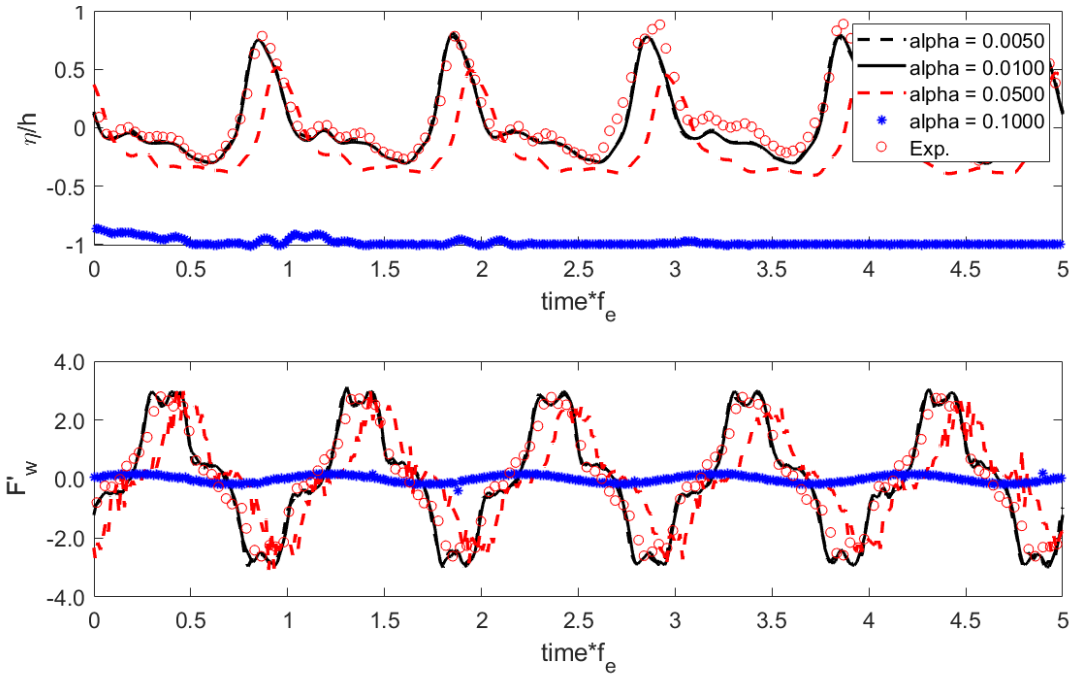

Figure 2.8 ER model simulated response history for the normalized wave heights and base shear forces for different blending factors versus experimental (EXP) results from Tait et al. (2005b). X_0/L_{tank} = 0.016, β =1.01

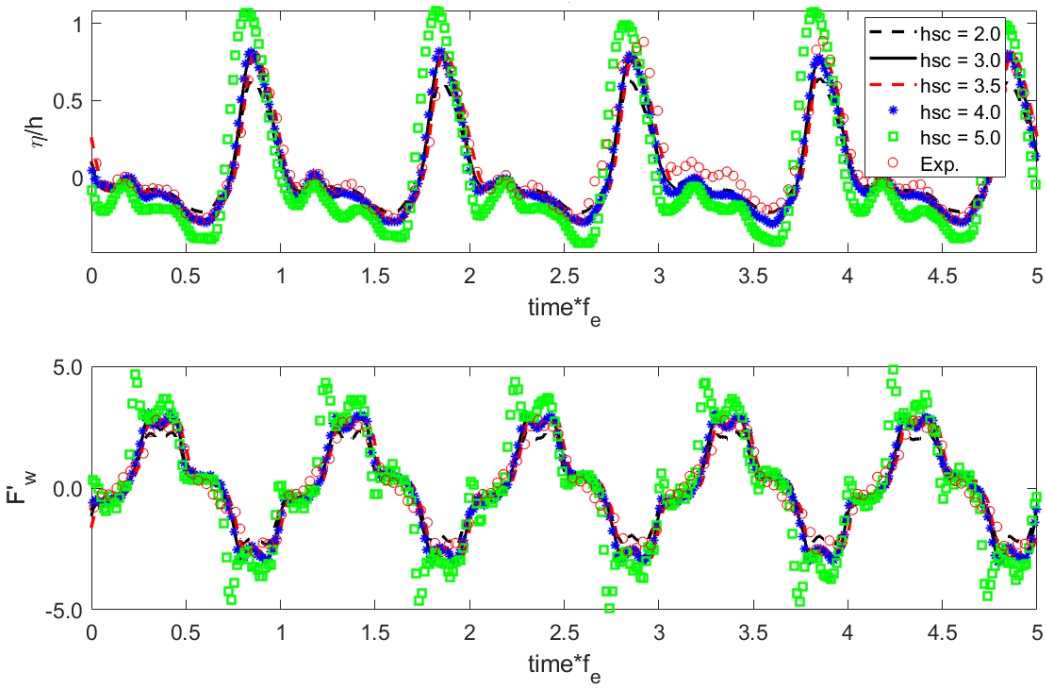

Figure 2.9 ER model simulated response history for the normalized wave heights and base shear forces for different screen kernel radii versus experimental (EXP) results from Tait et al. (2005b). X_0/L_{tank} = 0.016, β =1.01

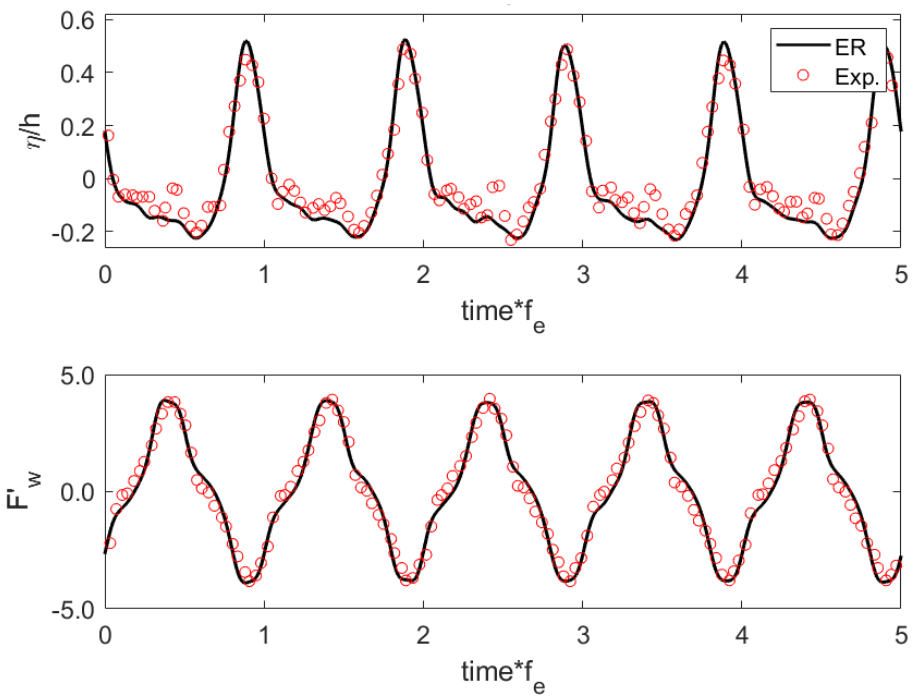

Figure 2.10 ER model simulated response history for the normalized wave heights and base shear forces versus experimental (EXP) results from Tait et al. (2005b). X_0/L_{tank} = 0.016, β =1.01

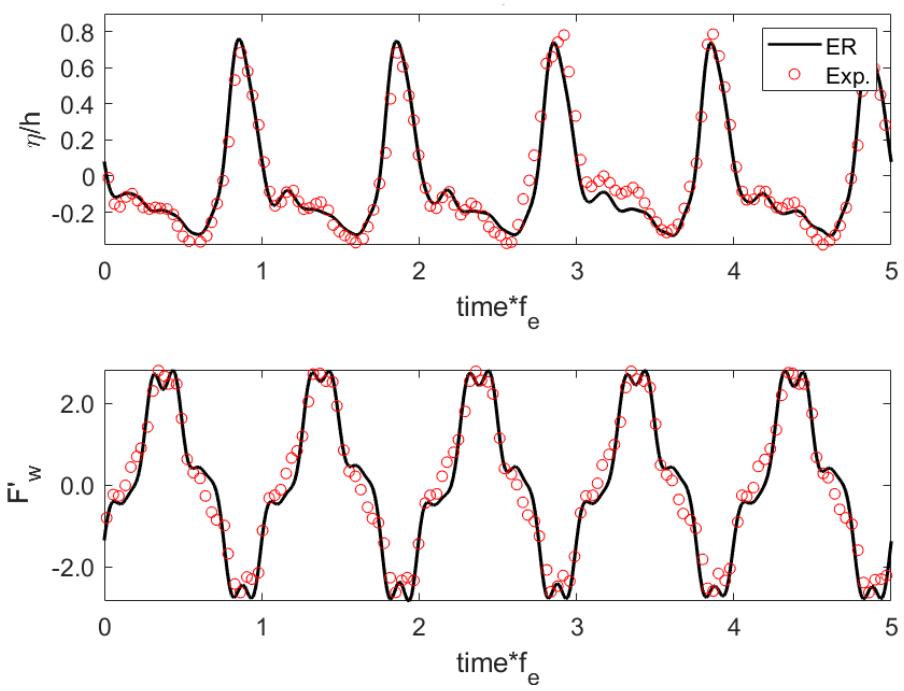

Figure 2.11 ER model simulated response history for the normalized wave heights and base shear forces versus experimental (EXP) results from Tait et al. (2005b). X_0/L_{tank} = 0.031, β =1.01

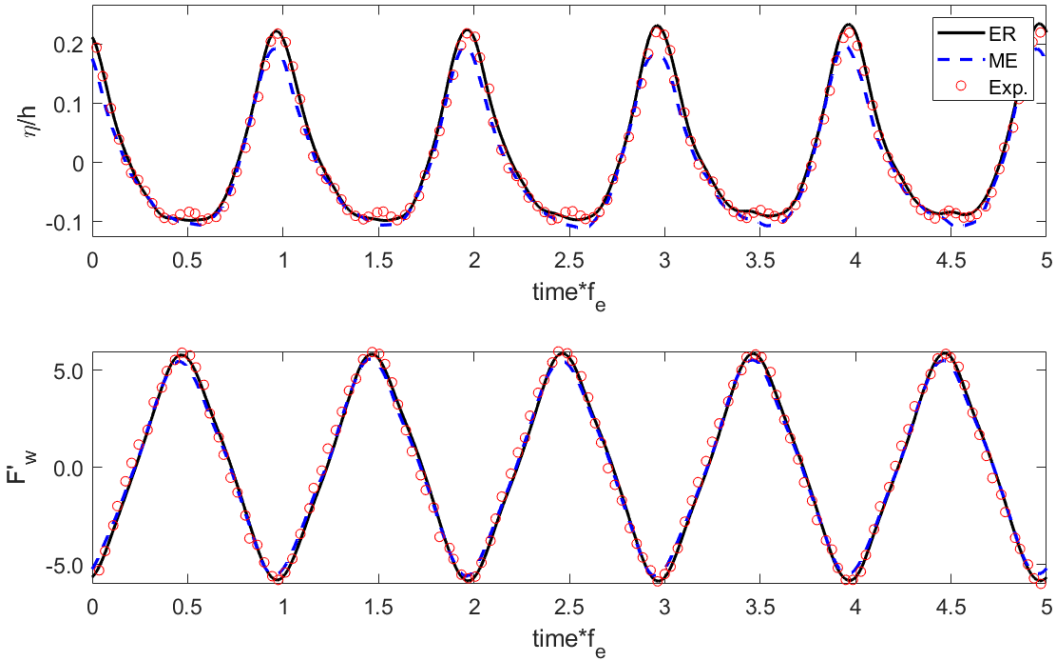

Figure 2.12 ER model and ME model simulated response history for the normalized wave heights and base shear forces experimental (EXP) results from Tait et al. (2005b). X_0/L_{tank} = 0.005, β =1.01

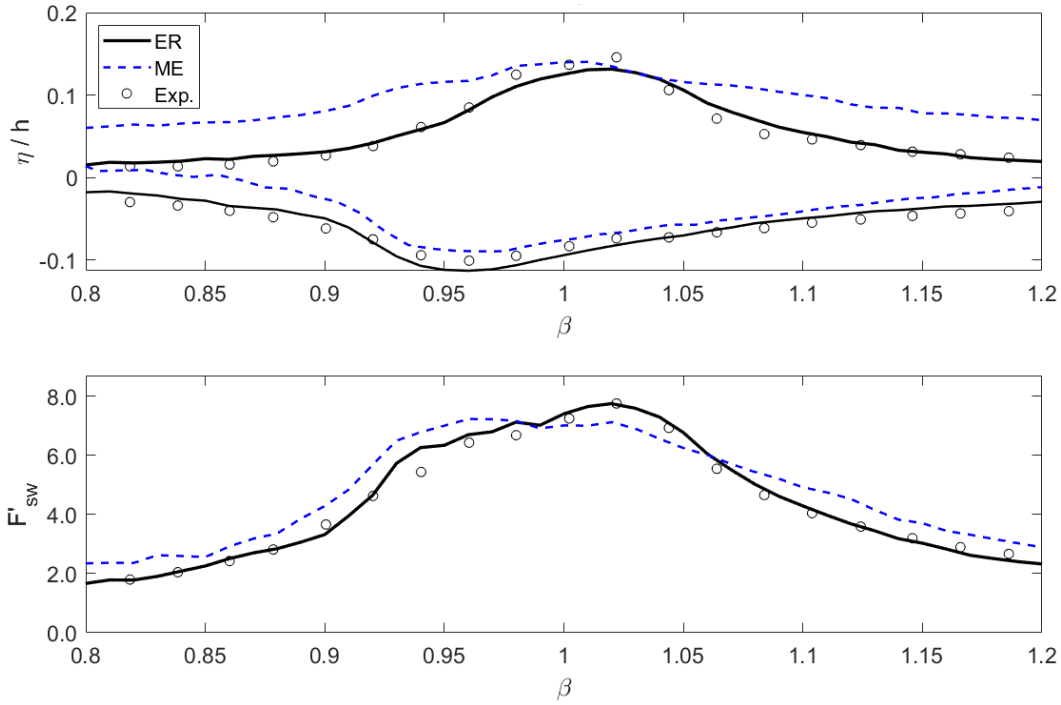

Figure 2.13 Wave heights and sloshing force frequency response curves computed by ER model and ME model versus experimental (EXP) results from Love and Tait (2013). h_{fluid}/L_{tank} = 0.05, X_0/L_{tank} = 0.0026

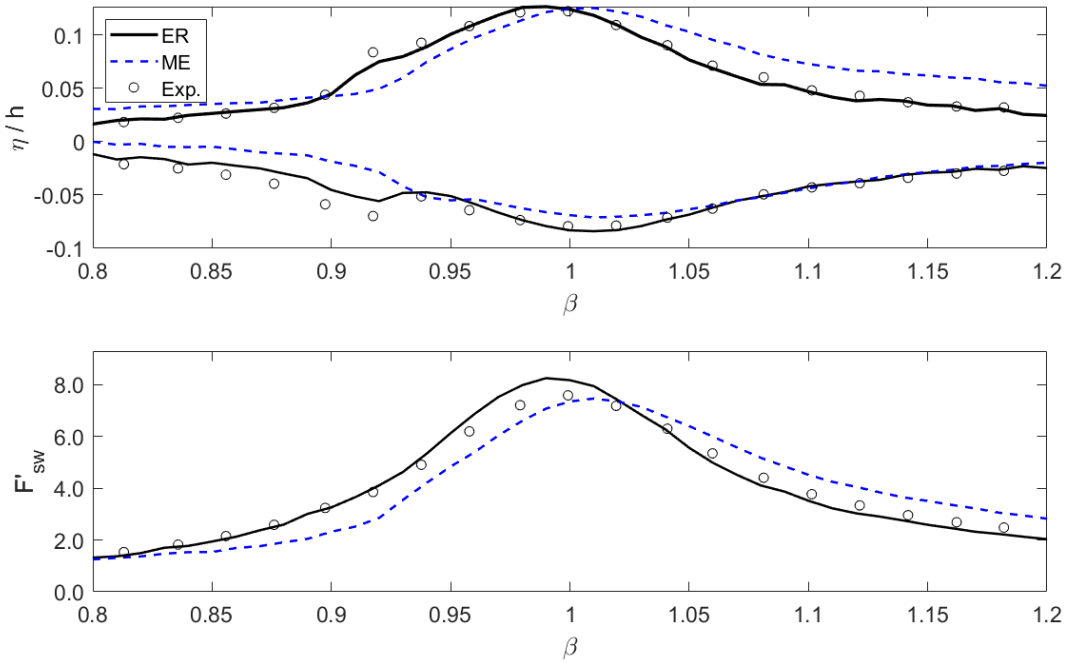

Figure 2.14 Wave heights and sloshing force frequency response curves computed by ER model and ME model versus experimental (EXP) results from Love and Tait (2013). h_{fluid}/L_{tank} = 0.15, X_0/L_{tank} = 0.0026

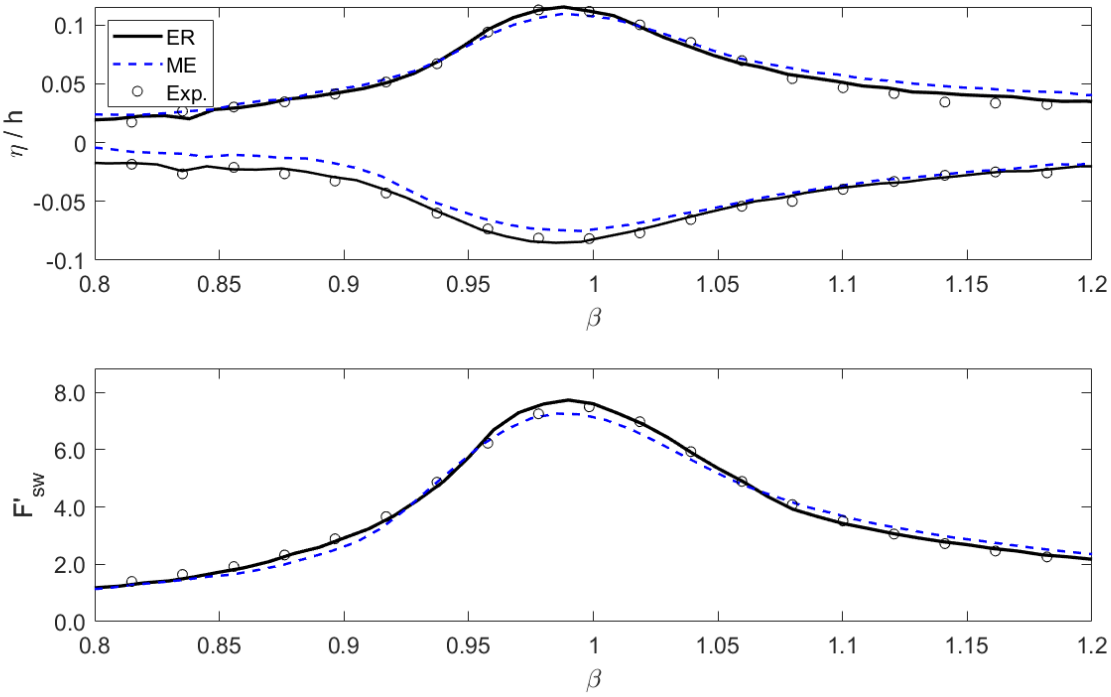

Figure 2.15 Wave heights and sloshing force frequency response curves computed by ER model and ME model versus experimental (EXP) results from Love and Tait (2013). h_{fluid}/L_{tank} = 0.25, X_0/L_{tank} = 0.0026

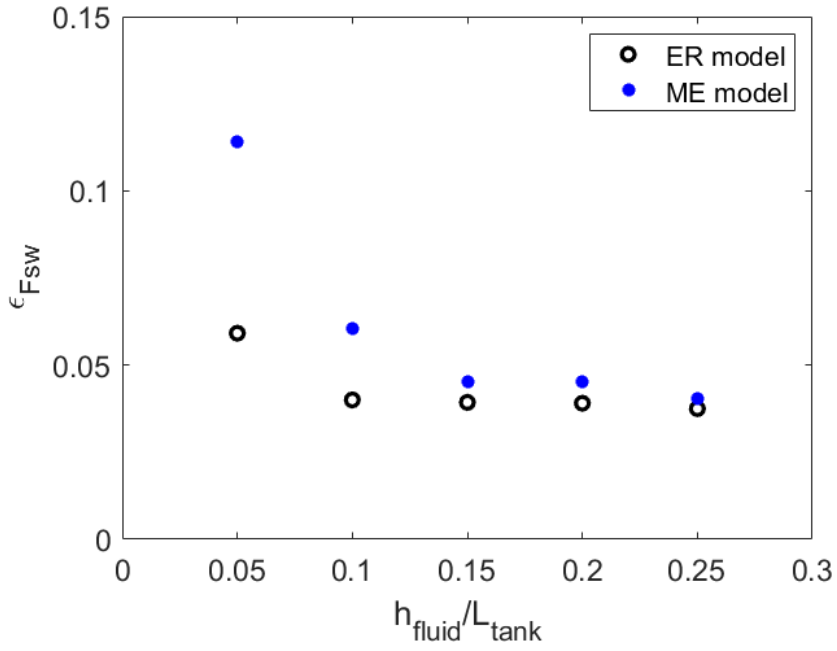

Figure 2.16 Normalized error for sloshing forces for ER model and ME model (McNamara et al., 2021).

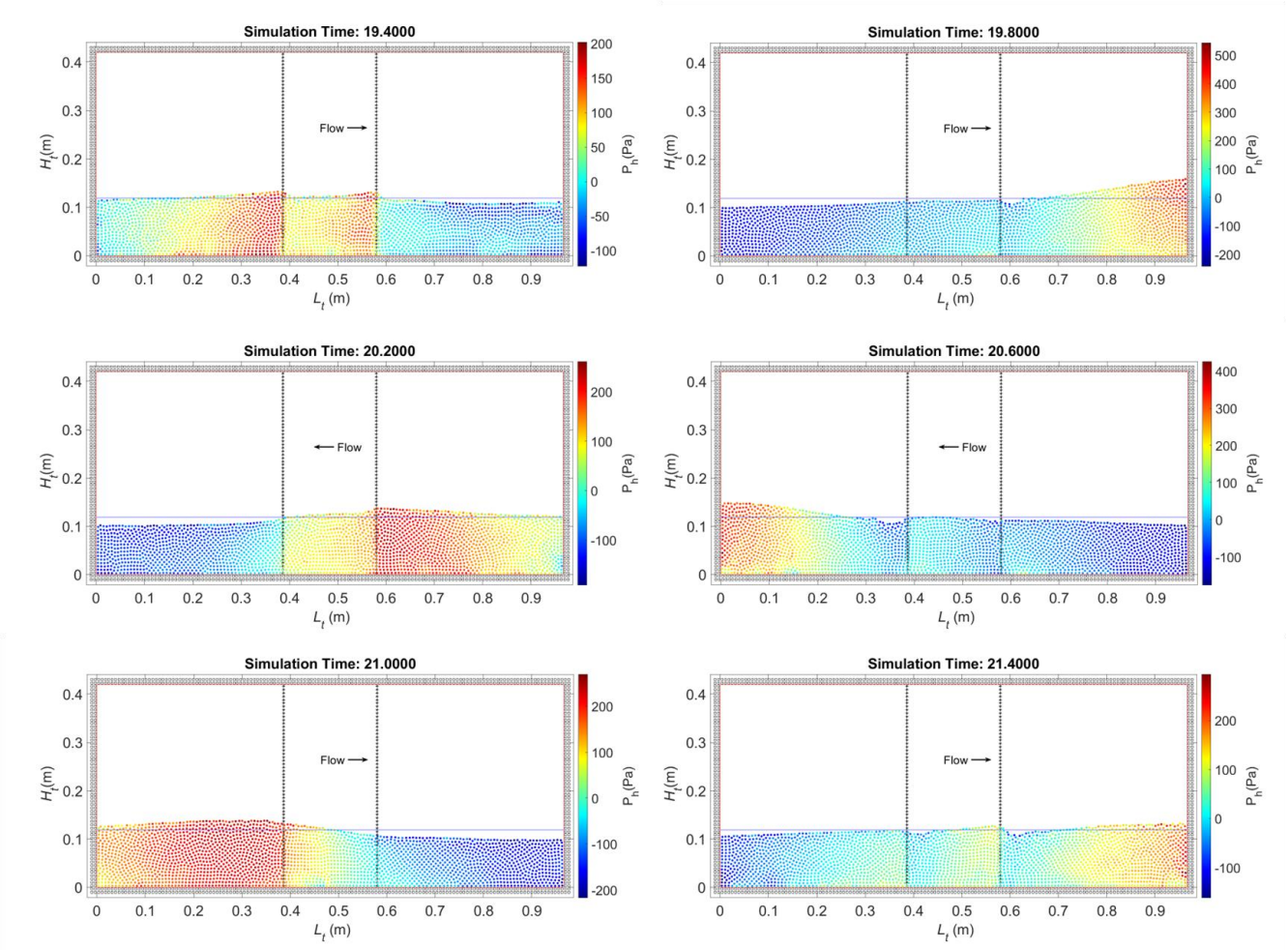

Figure 2.17 Snapshots of the ER model computed pressure fields and particle positions taken at different time instants within one period (The arrow denotes the direction of the flow at each snapshot). X_0/L_{tank} = 0.031, β =1.01

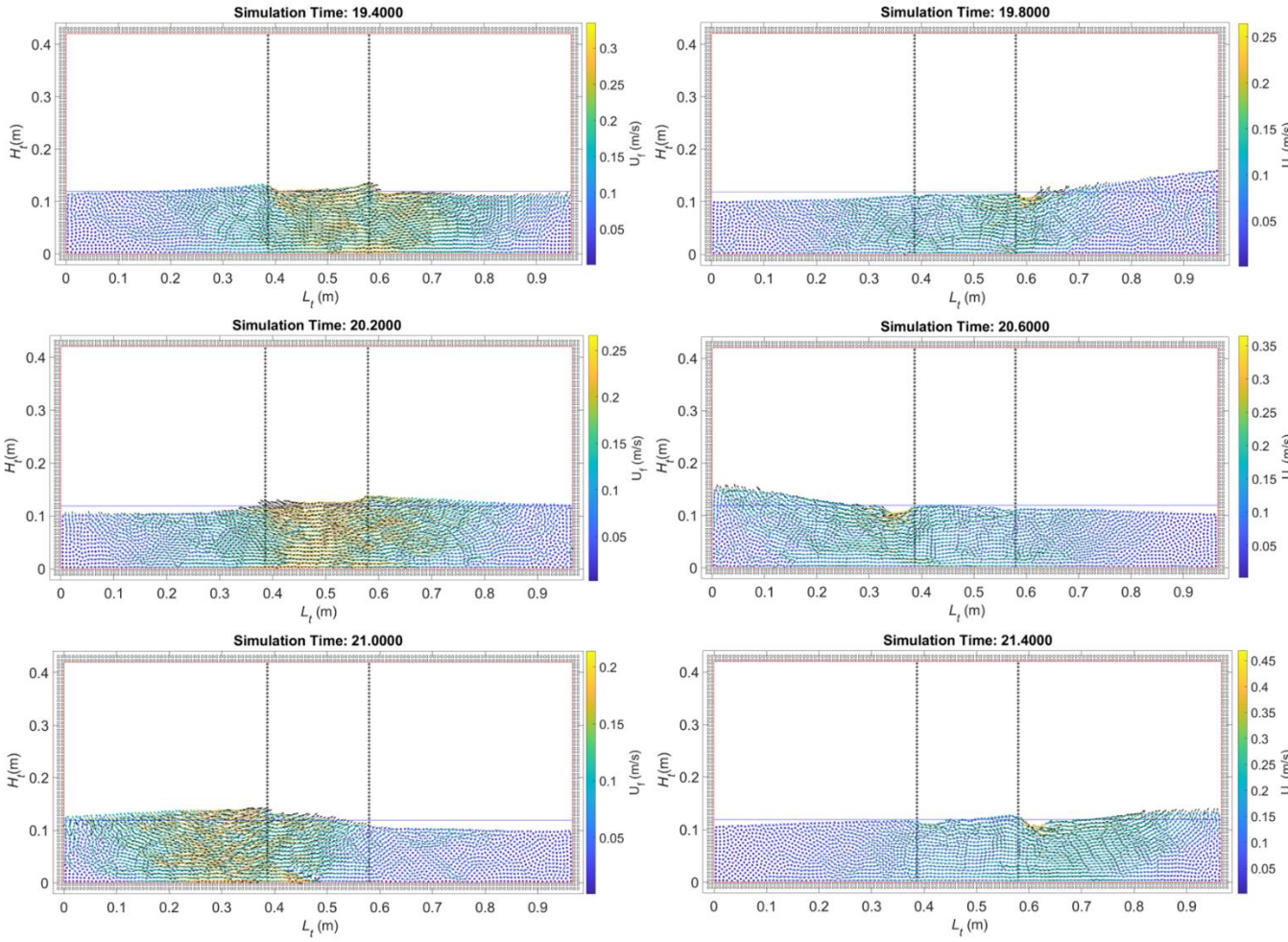

Figure 2.18 Snapshots of the ER model computed velocity vectors and magnitudes taken at different time instants within one period. X_0/L_{tank} = 0.031, β =1.01

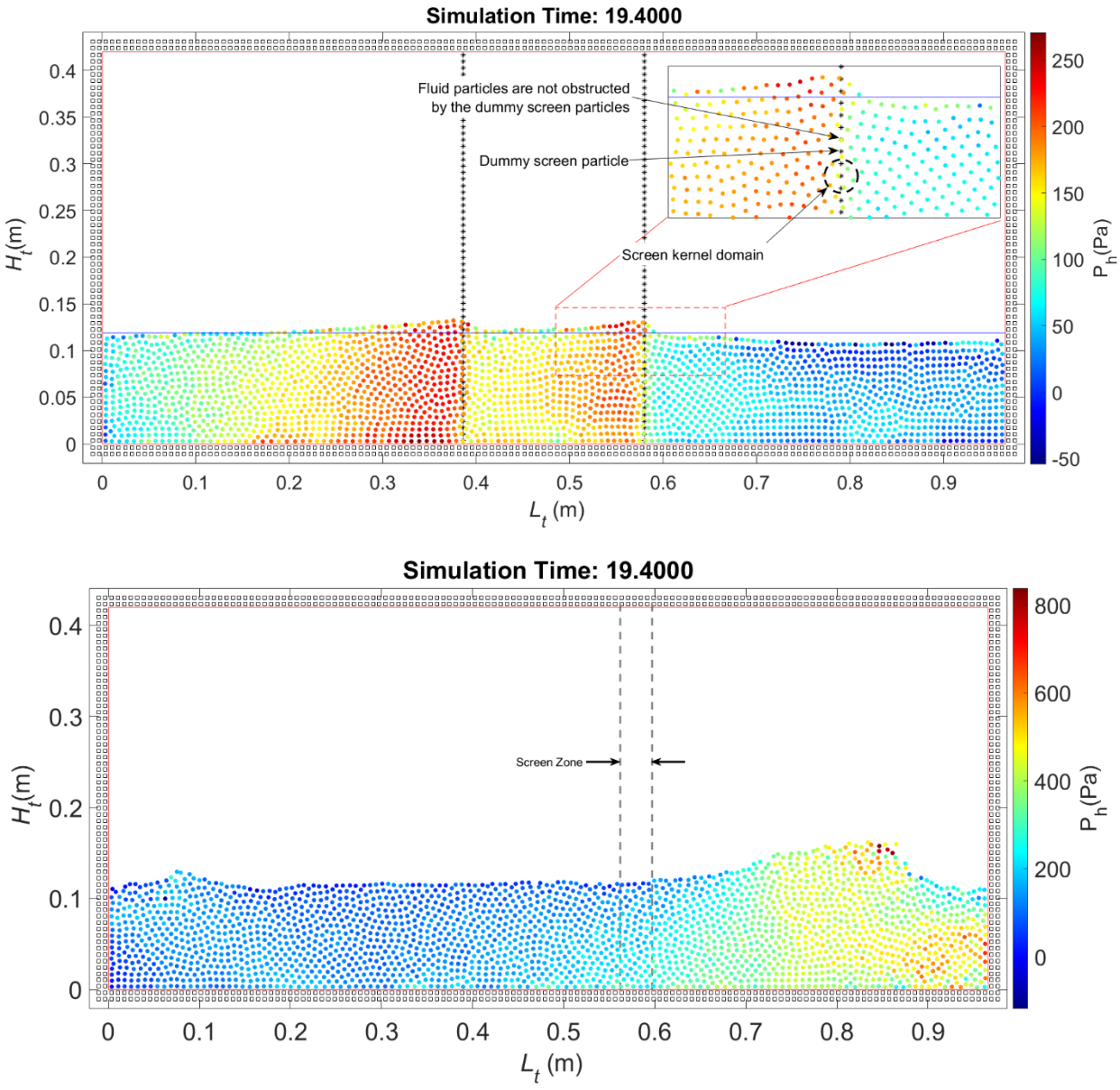

Figure 2.19 Snapshots at same time instant (t=19.4sec) showing the ER pressure and particle positions for a tank with screens (top figure) and without screens (bottom figure). X_0/L_{tank} = 0.031, β =1.01

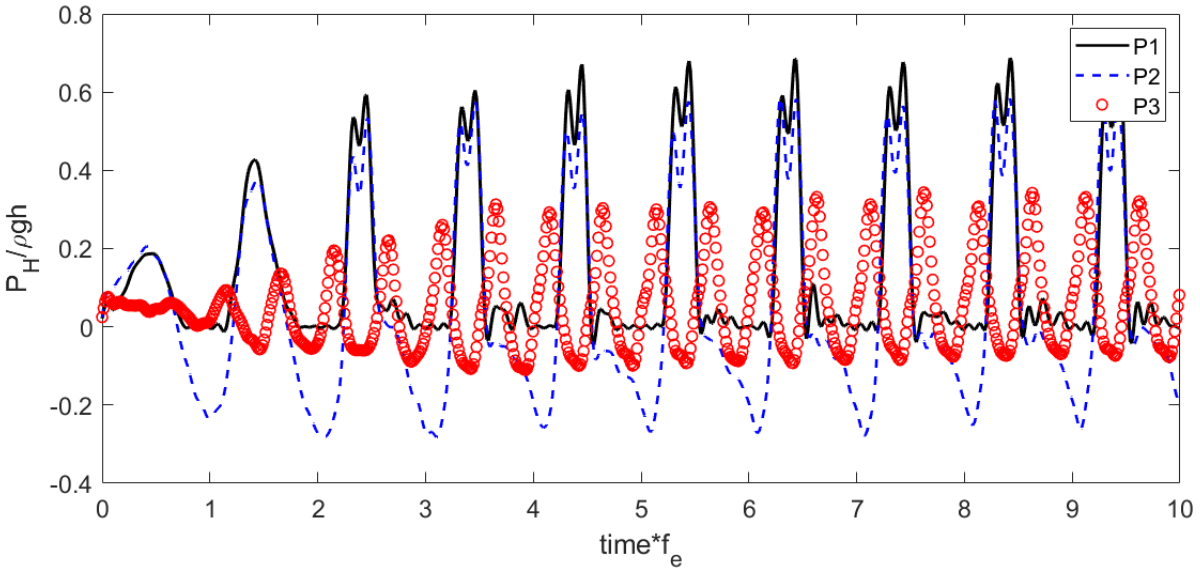

Figure 2.20 Normalized hydrodynamic pressure simulated by ER at three locations inside the TLD with screens. X_0/L_{tank} = 0.031, β =1.01.

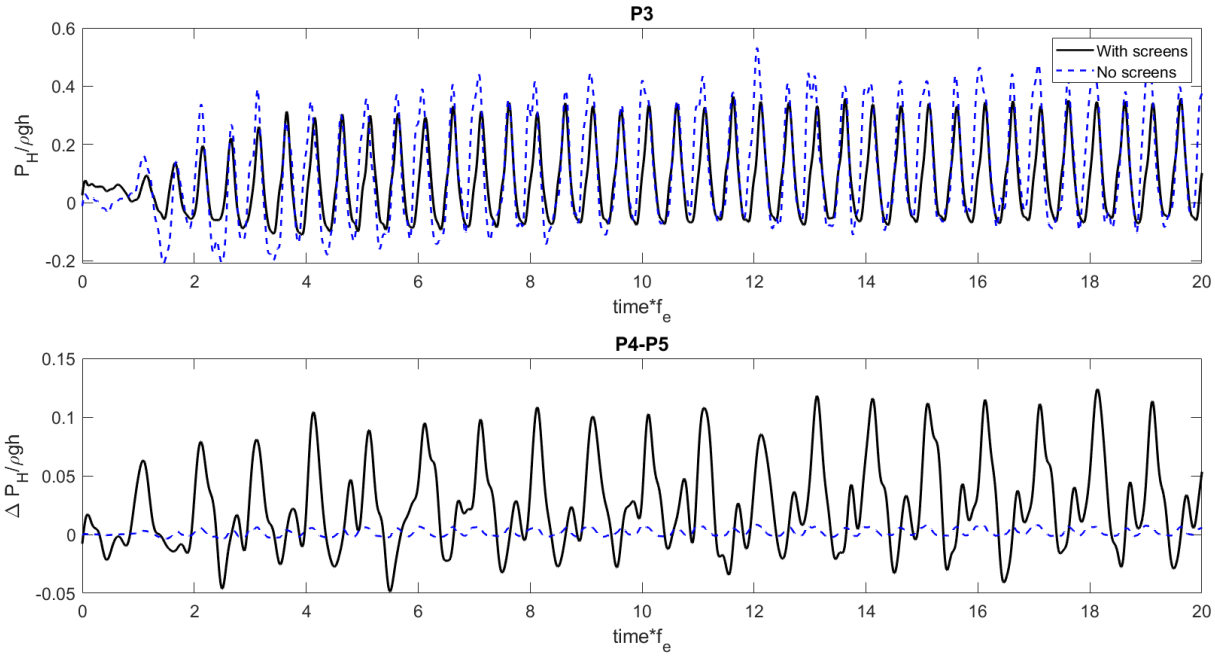

Figure 2.21 Normalized hydrodynamic pressure simulated by ER near the bottom of the tank at P3, P4 & P5. X_0/L_{tank} = 0.031, β =1.01.

Chapter 3: Modelling of Sloped and Curved Bottom Sloshing Tanks with Screens using Smoothed Particle Hydrodynamics

Bishoy N. Awad[a*], Michael J. Tait[a],
[a] McMaster University, 1280 Main Street West, Hamilton, ON, Canada L8S 4L8
*Corresponding Author, e-mail: awadb1@mcmaster.ca, +1(905)-962-5200

Abstract

A flat bottom tank geometry has traditionally been used for tuned liquid dampers (TLDs) to control the resonant response of tall buildings. However, the bottom geometry may be dictated by building space availability. Different bottom geometries have been proposed to conform to strict floor plans. Previous studies focused on modelling TLDs with irregular bottom geometries have limitations on excitation amplitudes or are computationally expensive. As structures may encounter extreme loading events, understanding the response of TLDs under large excitation amplitudes is imperative. A numerical model capable of accurately capturing the complex response of TLDs with irregular bottom geometries equipped with screens at high amplitude excitations with practical computational power requirements is currently unavailable. This study develops an incompressible smoothed particle hydrodynamics (ISPH) model to simulate any tank bottom geometry with screens macroscopically without the numerical limitations of existing models. The base model is modified to simulate any tank bottom geometry SPH results are found to be in good agreement with existing numerical models at shallow fluid depths and low excitation amplitudes. The response of different tank bottom geometries is investigated under large amplitude harmonic excitation, revealing that curved bottom tanks have higher sloshing response amplitude than sloped and flat bottom tanks. Overall, it was

found that the model did not encounter any limitations over the range of parameters considered and, as such, can efficiently (computationally) model TLDs with different tank bottom geometries over a wide range of excitation amplitudes.

Keywords: 2D incompressible smoothed particle hydrodynamics (ISPH), tuned liquid damper (TLD), liquid sloshing, macroscopic modelling, Ergun equation, tank bottom geometries, curved boundary conditions.

3.1 Introduction

Tuned liquid dampers (TLDs) are often installed near or at the top of tall structures to reduce resonant motions due to dynamic loading, such as wind or seismic events [1]. A flat bottom (rectangular) tank is the most common tank geometry employed because of currently available design and simulation tools, low installation and maintenance costs, and ease of tuning [2–6]. However, flat bottom tanks can require large footprints and may not conform to the building's floor plans. Additionally, the inherent damping of a typical TLD is not sufficient to reach the optimal damping level required to effectively control the structure. Thus, attempts have been made to improve the inherent damping of flat bottom tanks by introducing screens [7], nets [8], baffles [9–11], floating roofs [12, 13], and porous media [14, 15]. Other studies have proposed using a non-horizontal tank base to increase the percentage of liquid participating in sloshing to maximize the efficiency and damping performance of the TLD [16, 17].

Gardarsson et al. [18] experimentally investigated a sloped bottom tank and compared its response to a flat bottom tank with the same water mass. The sloped bottom tank with 30° sloped sides at both ends showed higher sloshing base shear forces than the equivalent flat bottom tank due to the larger fluid mass participating in sloshing motion compared to the flat bottom tank. Agresta et al. [19] experimentally studied the effect of flat, sloped (triangular) and circular bottom tank shapes on the sloshing motion inside TLDs. The circular bottom tank demonstrated higher sensitivity to water mass variations than the flat bottom tank. Idir et al. [20] numerically modelled different bottom-shaped tanks using linear wave theory. However, the model was found to be accurate only at low excitations.

Deng and Tait [21] used linear wave theory to compare the effective mass ratios of sloped, parabolic, and flat bottom tanks equipped with damping screens. The results revealed that the effective mass ratio for non-flat bottom tanks is more significant than for the flat bottom tank. However, the model was limited to low excitation amplitude values and shallow water depths. Tait and Deng [23] employed an equivalent linear mechanical model to evaluate the performance of TLDs with different tank geometries at small response amplitudes. It was found that the effective mass for the cylindrical tank was approximately 15% higher compared to a conventional flat bottom tank. Love and Tait [24] studied irregular tank geometries using a nonlinear multimodal model for small fluid depths. The response of chamfered bottom, boxed bottom and ramped bottom tanks was studied using a linearized Finite Element model [25]. Results indicate that the normalized equivalent mass of the TLD can be maximized by changing the shape of the tank bottom, which increases TLD performance and could also lead to reduced costs; however, the model was limited to low excitation amplitudes [25]. Pandit and Biswal [26] also studied the response of a partially filled sloped bottom tank without screens subjected to harmonic excitation at low excitation amplitudes. Recently, Amano et al. [27] used a nonlinear concentrated mass model to study the performance of a 1D triangular bottom tank at shallow fluid depths. The triangular bottom tank is found to be more effective than the flat bottom tank due to the difference in mode shapes, which confirms that the tank bottom geometry influences the effective mass of the TLD and can be appropriately altered to enhance TLD performance [28].

In addition to building geometry limitations, the above studies show that tanks with variable fluid depth have varying responses and sensitivities compared to the traditional

flat bottom tank, implying the importance of investigating the different tank bottom shapes. However, a thorough search of the relevant literature indicates that existing numerical models that can simulate different geometries have limitations regarding the water depth ratio, excitation amplitude, and the number of screens or require high computational effort.

Motivated by these limitations, the current study presents a 2D model based on incompressible smoothed particle hydrodynamics (ISPH), with a macroscopic screen modelling technique, to simulate the response of TLDs having different bottom geometries, with multiple screens, at high excitation amplitudes and different water depth to free surface fluid length ratio. With several advantages over conventional mesh-based methods, the meshless nature of SPH allows it to capture complex free-surface flows associated with TLDs [29–31]. SPH is a robust Lagrange method that discretizes the fluid into computational particles to solve the governing partial differential equations describing the fluid motion. Each computational particle carries the fluid properties and interacts with others in its neighbourhood to calculate the flow parameters at each time step [32, 33]. Two methods are commonly found in the SPH literature for solving the governing flow equations, namely the Weakly Compressible SPH (WCSPH) [34] and Incompressible SPH (ISPH) methods [35]. The first approach solves the Navier-Stokes (NS) equations using a stiff equation of state, leading to fluctuations in the pressure field [36]. To overcome this drawback, ISPH was introduced based on a two-step projection method [35].

For applications such as modelling a TLD with screens, ISPH has been reported to efficiently capture the flow associated with the addition of screens in the TLD by modelling the screens as rigid boundaries and solving the localized flow around screen particles [37–

39]. This approach is known as microscopic modelling but comes at a high computational cost as finer particle sizes are needed to capture the screen geometry. A more recent technique models the screens on a macroscopic level, where the overall effect of the screens is captured at a significantly lower computational cost as it does not necessitate the determination of the local flow around the screen particles. This method can be implemented for applications where the detailed localized flow around the screens is not the primary interest while capturing the overall influence of the screens on the flow is of greater importance. Since the free surface response and sloshing base shear forces are the primary interest in TLD design, macroscopic models can be a good fit for TLD applications. McNamara et al. [40] presented a macroscopic ISPH model that implements the slat screens based on Morison's equation (ME). Results were found to be in good agreement with experimental data from Tait et al. [41] over a range of excitation amplitudes and different fluid depths. An important finding was that the model effectively captured the drag forces of the screens but at a significantly reduced CPU time (by a factor of approximately 700) [40]. However, the model requires the screen drag coefficient, which can necessitate experimental testing prior to numerical modelling [40].

Extensive research was performed by Tsao et al. [42–44] in capturing the nonlinear damping force of porous media in flat bottom TLDs using Darcy's resistance law. Awad and Tait [45] recently proposed a novel ISPH macroscopic model based on the analogy between porous media particles and screens using Ergun's resistance (ER) model. The ER model was found to be an effective technique for modelling screens, eliminating the need for screen drag coefficient determination without limitations on fluid depths or excitation

amplitude. The model also showed faster performance and higher accuracy than the ME method.

TLDs are usually designed and tuned to work under serviceability conditions for loading conditions corresponding to 1 or 10-year return period events. However, TLDs may be exposed to extreme events (e.g., hurricanes, earthquakes, etc.) that generate highly nonlinear flow that is challenging to model [45].

To the best of the authors' knowledge, the literature has not reported modelling a full range of TLD bottom geometries with screens under large excitation amplitudes using a computationally efficient model. This study investigates different TLD tank bottom geometries equipped with screens using as SPH model employing the ER technique. The 2D SPH code is modified, and the boundary conditions are updated to accommodate sloped and curved bottom tanks. The SPH model is validated for flat, sloped, parabolic, and circular bottom tanks with screens at a low excitation amplitude and shallow water depths using existing linearized models introduced in Deng and Tait [21, 23]. The SPH model is validated at large amplitudes against available experimental data from [18, 27, 46] for different bottom tank geometries. The model is then used to investigate different tank bottom geometries under harmonic excitation with an amplitude corresponding to an approximately equivalent 100-year return period extreme wind event for a targeted frequency and constant free surface fluid length ratio cases. Finally, the effect of varying fluid depths and implementing multiple screens is studied for the same tank length and height. All simulations used a constant water mass for comparison purposes. The model performance and capabilities are subsequently discussed.

3.2 Numerical Model

3.2.1 SPH Approximation

The basic principle of SPH is smoothing any arbitrary function over a domain of particles through the formulation

$$\mathrm{A}(\boldsymbol{r}_i) \approx \int_{\Omega} A(\boldsymbol{r}_j)\ W(\boldsymbol{r}_{ij}, h_k)\, dr = \sum_{j=1}^{N} A(\boldsymbol{r}_j) \frac{m_j}{\rho_j} W(|\boldsymbol{r_i} - \boldsymbol{r_j}|, h_k) \qquad \textbf{(3.1)}$$

which is known as the kernel approximation. Herein, $A(\boldsymbol{r_i})$ is an arbitrary function (e.g., any field property such as density, velocity, pressure, etc.), Ω is the domain, ρ_j is fluid density, m_j is the particle mass, W is the kernel function, h_k is the smoothing length, and $\boldsymbol{r}_{ij}$ is the magnitude of the distance between the particle of interest $\boldsymbol{i}$ and any neighboring particle $\boldsymbol{j}$ (bold symbols indicate vector quantities).

Different formulations of the kernel functions can be found in the SPH literature, such as Polynomial, Gaussian, Quintic, etc. This study uses the fifth-order Wendland kernel

$$W(q) = W_c \begin{cases} (1+2q)\left(1-\frac{q}{2}\right)^4 & 0 \le q \le 2 \\ 0 & q \ge 2 \end{cases} \qquad \textbf{(3.2)}$$

where $W_c = \frac{7}{4\pi {h_k}^2}$, $q = \frac{|r_i - r_j|}{h_k}$ for 2D simulations [47]. Herein, h_k is the kernel radius, and dp is the initial particle spacing.

The SPH approximation of the gradient and the Laplacian of any vector-valued function are given by equations (3) and (4), respectively:

$$(\nabla A)_i = \rho_i \sum_{j=1}^{N} m_j \left(\frac{A_j}{\rho_j} + \frac{A_i}{\rho_i}\right) \nabla_j W_{ij} \tag{3.3}$$

$$\nabla . \left(\frac{\nabla \mathrm{A}}{\rho}\right)_i = \sum_{j=1}^{N} \left(\frac{8 m_j}{\left(\rho_i + \rho_j\right)^2} \frac{A_{ij} \boldsymbol{r}_{ij} . \nabla_i W_{ij}}{\boldsymbol{r}_{ij}^2 + \eta^2}\right) \tag{3.4}$$

The above expressions are used for the gradient of the velocity vector and the Laplacian of pressure in the pressure Poisson's equation (PPE), respectively [34]. In this study, the parameter η is equal to $0.001 h_k$ to ensure the denominator value remains greater than zero.

3.2.2 ISPH Time Integration

The governing equations of 2D incompressible flow presented in the Lagrangian form are given by

$$\frac{D\rho}{Dt} + \rho \nabla \mathbf{u} = 0, \tag{3.5}$$

$$\frac{\mathrm{D}\mathbf{u}}{Dt} = -\frac{1}{\rho_0} \nabla P + v_0 \nabla^2 \mathbf{u} + \mathbf{g} + \frac{1}{\rho_0} \nabla . \boldsymbol{\tau}\,, \tag{3.6}$$

which are used in this study to express the conservation of mass and linear momentum, respectively. *D/Dt* represents a material time derivative, ρ_0 is the fluid density, v_0 is the kinematic viscosity, **u** is the fluid velocity vector, *P* is the fluid pressure, $\boldsymbol{\tau}$ is the stress tensor, and **g** is the body force term (i.e., gravitational acceleration). A closure turbulence closure model was used based on the Sub-Particle Scale (SPS) turbulence stress term [48] as

$$\tau_{ij} = \rho_0 \left(2 \nu_t S_{ij} - \frac{2}{3} k_t \delta_{ij}\right) \tag{3.7}$$

$$\nu_t = (C_S.\, d_p)^2.\, |S| \tag{3.8}$$

$$S_{ij} = \left(\frac{\partial u_i}{\partial x_j} + \frac{\partial u_j}{dx_i}\right)/2 \tag{3.9}$$

where ν_t is the turbulent kinetic energy, k_t is the turbulence kinetic energy, δ_{ij} is the Kronecker delta function, D_{ij} is the shear strain rate tensor of the mean flow, and C_s is the Smagorinsky constant. In this study, $C_s = 0.1$.

The Incompressible solution of SPH considered in this work follows the two-step projection method proposed by Cummins and Rudman [35]. The first step predicts an intermediate velocity ($\boldsymbol{u}^*$) using the viscous and gravitational forces

$$\boldsymbol{u}^* = \mathbf{u}(t) + \left(v_0 \nabla^2 \mathbf{u} + \frac{1}{\rho_0} \nabla.\, \tau + \mathbf{g} + \boldsymbol{\alpha}_x + \boldsymbol{\psi}_{\boldsymbol{sc}} + f_{iw}\right) \Delta t \tag{3.10}$$

where $\boldsymbol{\alpha}_x$, $\boldsymbol{\psi}_{\boldsymbol{sc}}$, f_{iw} is the external excitation force, screen macroscopic forces term and repulsive force, respectively (discussed in Sections 3.2.4 and 3.3). Then the intermediate position ($\boldsymbol{r}^*$) is predicted using the intermediate velocity field at each time step (Δt), without imposing incompressibility [49], as

$$\boldsymbol{r}^* = \mathbf{r}(t) + \boldsymbol{u}^* \Delta t \tag{3.11}$$

Then the algorithm imposes incompressibility by explicitly calculating the pressure field ∇P using the updated pressure Poisson's equation (PPE) equation at each time step

$$\nabla.\left(\frac{\nabla P}{\rho_0}\right) = \alpha \frac{\rho_0 - \rho^*}{\rho_0 \Delta t^2} + (1 - \alpha) \frac{\nabla.\, \boldsymbol{u}^*}{\Delta t} \tag{3.12}$$

where an additional stabilizing term is added to the conventional PPE to add the effect of the divergence-free condition with the density invariant ISPH conditions and $\alpha = 0.01$ [50].

Finally, the computed pressure is used to calculate the corrected velocity field $\boldsymbol{u}(t + \Delta t)$ at the end of each time step

$$\boldsymbol{u}(t + \Delta t) = \boldsymbol{u}^* + \left(-\frac{1}{\rho}\nabla P\right)\Delta t \tag{3.13}$$

and the positions are updated based on the corrected velocity

$$\boldsymbol{r}(t + \Delta t) = \boldsymbol{r}(t) + \left(\frac{\boldsymbol{u}(t + \Delta t) + \boldsymbol{u}(t)}{2}\right)\Delta t \tag{3.14}$$

3.2.3 Free Surface and Solid Boundary

The Dirichlet boundary condition is imposed by enforcing zero pressure for the free surface particles [49]. A false density $\rho_n = \sum_{j=1}^{N} m_j W_{ij}$ is calculated for fluid particles, then the algorithm detects values of ρ_n that fall below 90% of the initial fluid density ρ_0 as a result of kernel truncation at the free surface.

For the tank walls, fixed dummy particles are used based on the method developed by Adami et al. [51]. Although the boundary particles are fixed in position, velocity and pressure values are calculated for these particles during the prediction step to prevent fluid particles from penetrating through the walls and to enforce the free-slip boundary condition, which showed better particle inclusion compared to the no-slip condition [40]. This is done by matching the parallel fluid velocity from the neighbour fluid particles to the parallel wall particle while reflecting the perpendicular fluid velocity equal and opposite to the wall particle. This method provides good results for horizontal and vertical walls; however, enhancements are made and discussed in Section 3.3.2 to accommodate sloped and curved boundaries.

3.2.4 Macroscopic Screen Technique Implementation

The macroscopic screen model represents the screens as a single-phase continuum discretized into a series of dummy particles, and a closure model approximates the pressure loss through this domain without solving flow quantities for these particles (i.e., fluid particles can move through screen particles). The Ergun resistance (ER) model proposed in previous work [46] is used as a closure model based on the Ergun quadratic law [52] for calculating pressure loss through porous media. The screen drag force for each screen particle can be approximated as

$$\boldsymbol{F_d} = \left(\frac{\mu}{K_P} \sum_{\boldsymbol{f}} \overline{\boldsymbol{U}}_{s,j} + \frac{1.75}{\sqrt{150}} \cdot \frac{\rho}{\sqrt{K_P} \cdot n_w^{1.5}} \sum_{\boldsymbol{f}} \overline{\boldsymbol{U}}_{s,j} \left\| \overline{\boldsymbol{U}}_{s,j} \right\| \right) t_{sc} . d_p \qquad \textbf{(3.15)}$$

where μ is the dynamic viscosity of water (taken as 1.0016 mPa.s), t_{sc} is the screen thickness, n_w the porosity of the screens (equal to one minus the screen solidity), $\overline{\boldsymbol{U}}_{s,j}$ is the mean interstitial velocity equal to $\overline{\boldsymbol{U}}_{s,j} = \sum_f \frac{m_f}{\rho_f} \boldsymbol{u_f} W_{jf}$, W_{jf} is the screens kernel function with a kernel radius h_{sc}, and K_P is the porous media permeability. Awad and Tait [46] validated and used the Karman-Cozeny (K-C) model to calculate the permeability coefficient for screens K_P, based on the analogy between screens and porous media [53]

$$K_P = \frac{n_w^3 D_c^2}{150(1 - n_w)^2} \qquad \textbf{(3.16)}$$

where D_c is characteristic diameter taken equal to *dp*. During the prediction step, the forces acting on the fluid particle from the surrounding screen particles are approximated as the

summation of the neighbour screen particles drag forces in the opposite direction of the flow and is proportional to the kernel function value

$$\boldsymbol{\psi_{sc}} = \frac{\left(-\sum_j \boldsymbol{F_d} \frac{W_{jf}}{\sum_f W_{jf}}\right)}{m_j} \tag{3.17}$$

where $\boldsymbol{\psi_{sc}}$ is calculated for the fluid-screen interaction zone taken equal to the screen's kernel radius h_{sc} =2.5h_k and enforcing zero value elsewhere (i.e., pure fluid region). The present study uses the Wendland kernel for the screens kernel function (W_{jf}).

The model imposes the effect of the screens on a macroscopic scale without calculating other field variables, such as velocity and pressure for the screen particles. Hence the fluid particles are not interfered with by the screen particles' position and are only influenced by their drag forces. More detail on the ISPH and the ER models can be found elsewhere [46].

3.3 SPH Model Modifications

3.3.1 Repulsive Force:

Sloped, curved and irregular boundaries may generate irregular particle spacings, resulting in particles escaping through boundary layers. Monaghan [54] suggested that an additional repulsive force term be added to the momentum equation to avoid unphysical fluid penetration of a boundary during the prediction step. Following Cherfils et al.[55], the added force is expressed as

$$f_{iw} = \begin{cases} \mathbf{g}\,\mathrm{H}\left[\left(\frac{h_k}{2\boldsymbol{r_{iw}}}\right)^4 - \left(\frac{h_k}{2\boldsymbol{r_{iw}}}\right)^2\right]\frac{\boldsymbol{x_{iw}}}{\boldsymbol{r_{iw}^2}} & \frac{h_k}{2\boldsymbol{r_{iw}}} \le 1 \\ 0 & Otherwise \end{cases} \tag{3.18}$$

where H, $\boldsymbol{r_{iw}}$ and $\boldsymbol{x_{iw}}$ are the fluid height above the corresponding boundary particle, the distance, and the vector between particle *i* and the corresponding boundary particle *w*, respectively. Equation (3.18) is valid for $\boldsymbol{r_{iw}} < \frac{h_k}{4}$ and the algorithm only applies in the fluid-boundary interaction zone.

3.3.2 Sloped and Curved Boundary Condition

3.3.2.1. Boundary Particles Generation Methods

An essential facet of SPH modelling is the flexibility associated with discretizing particles and the computational domain, thus enabling a wide range of tank bottom geometries to be investigated. However, in the current SPH TLD-related literature, fixed particle spacing (square grid) in the x- and y- directions have typically been employed. The model adopted by Adami et al. [51] has shown good performance and efficient simulations for flat bottom tank [40, 45]. However, this model is not practical for boundaries with different orders of magnitude in each direction (i.e., curved boundaries). Unlike horizontal and vertical boundaries, the gradient of the curved boundaries constantly changes along its perimeter, which creates sections with steeper or milder slopes. Thus, discretizing curved boundaries using fixed particle spacings (*dp*) in both directions may result in undesired fine particle spacing in the horizontal direction where milder slopes exist. Additionally, coarse spacing may be generated in the vertical direction for steeper slope zones, resulting in particles penetrating the boundaries. To avoid these drawbacks, this study investigates two formulations with an efficient particle-generating scheme to fit any parabolic function. Similar procedures were presented by Tavakkol et al. [56] with different and more complex

formulations; however, a comparison between these methods has not been studied for a TLD.

The square grid method was initially adapted using the original boundary particle generation proposed by Adami et al.[51] with a fixed distance between particles in both directions. However, this technique failed to capture the curvature of parabolic and circular tanks, as the boundary particles are generated in a staggered pattern and do not follow the curved line. Thus, a technique that uses the quadratic parabolic or circular equation for each tank to generate the tank walls along the curve path was investigated, which results in smoother curved walls, as shown in Figure 3.1.

Next, a linear-curved grid was employed to generate the particles of the first layer along the curve at a distance (dp) in the x-direction and the y-coordinate of the following boundary particle based on the parabolic equation $f(y)$ of the specific bottom geometry. The boundary layers are then copied parallel to the first layer at the same distance (dp) in the y-direction to form the subsequent boundary layer. This method enhanced the fitting of the boundary particles along the curve boundary. However, using fixed particle distance in both the x- and y- directions failed to contain all particles inside the tank boundaries, and a finer particle spacing was required to keep the particles inside the tank, leading to the increased computational effort.

Finally, a nonlinear curved grid has been used to generate particle distances in the x- and y- directions at a distance independent from each other for a balanced particle generation. To balance this, a hybrid algorithm was utilized to maintain a distance between the center of each particle (d_s) by adjusting the horizontal (dx) and vertical (dy) distances

between particles step-by-step. The first step utilizes the linear-curved grid method, where the first particle (p_i) is generated at the start of the curve, and the coordinate of the next point (p_{i+1}) is generated based on the initial particle spacing (dp) and curve function $f(y)$. The distance $d_{s_{(p_{i+1},p_i)}}$ between the two particles is computed as

$$d_{s_{(p_{i+1},p_i)}} = \sqrt{(y_{i+1} - y_i)^2 + (x_{i+1} - x_i)^2} \tag{3.19}$$

The algorithm then checks the distance as follows

$$d_{s_{(p_{i+1},p_i)}} : \begin{cases} d_s = \delta : & d_{s_{(p_{i+1},p_i)}} > \delta \\ d_s = d_s : & Otherwise \end{cases} \tag{3.20}$$

where δ is the maximum distance between particles, which depends on the curve function. For tanks investigated in this study, $\delta \leq dp$ has been found to be an appropriate space discretization in the horizontal and vertical directions. If d_s does not exceed δ, the algorithm exits the loop and creates the next particle. Otherwise, the x-coordinate of point (p_{i+1}) is recalculated by substituting $f(y)$ in equation (3.19) using $d_s = \delta$, and the y-coordinate can be obtained using $f(y)$. Subsequently, the rest of the first layer particles are created using the same process. Finally, the process is repeated by an offset of dp vertically to create the subsequent layer. This method maintains consistent spacing between particles along the curved boundary without sacrificing computation time or increased particle loss.

3.3.2.2. Velocity treatment

The velocity vector is analyzed in two components based on the position boundary particle to ensure the free-slip condition for curved and sloped boundaries. As illustrated in

Figure 3.2, the vertical and horizontal components of the velocity vector are solved for each particle using the angle $\theta_i = \tan^{-1}\left(\frac{dx_i}{dy_i}\right)$ calculated by the algorithm at each step.

3.4 Results and Discussion

3.4.1 Tank Bottom Setup

In this study, the sloped bottom tank, as shown in Figure 3.3(b), has a tank height (h_{tank}), tank length (L_{tank}) and exterior angle θ. The parabolic tanks follow a quadratic function

$$y = B + (x - C)^2 \tag{3.23}$$

where B and C are the y-intercept and x-intercept, respectively. In this study, the parabolic bottom tank has $B = 0$ and $C = L_{tank}/2$, with properties shown in Figure 3.3(c). Finally, as shown in Figure 3.3(d), the circular bottom tank is a semicircle with a radius equal to $L_{tank}/2$. The tank dimensions and properties used in the convergence, validation and analysis sections are summarized in Table 3.2, Table 3.4, to Table 3.10, respectively. Screens are adopted for all tank bottom geometries and have a slat height h_{slat} = 5mm, a distance between slats L_{slat} = 7 mm and a slat thickness t_{sc} = 1mm.

3.4.2 Normalization of Results

In this study, a sinusoidal base acceleration expressed as

$$\ddot{X}(t) = -X_0\, \omega_e^2 sin(\omega_e t) \tag{3.24}$$

is used for the simulations, where ω_e is the excitation frequency, and X_0 is the excitation amplitude. The fluid sloshing base shear force is calculated as

$$F_{sw} = F_w - \ddot{X} m_w \quad \textbf{(3.25)}$$

where m_w is the water mass, and F_w is the base shear force. The wave height η is normalized by the excitation amplitude (X_0), and the forces are normalized by ($m_w \eta_{avg} \omega_e^2$); where η_{avg} is the average wave height response, and time is normalized by the inverse of the excitation frequency f_e. The hydrodynamic pressure P_H is normalized by the hydrostatic pressure.

3.4.3 Numerical Setup and Convergence

Simulations adopted in this study used a water density $\rho = 1000\ kg/m^3$, kinematic viscosity $v = 1\text{x}10^{-6}\ m^2/s$, and kernel radius h_k set to $1.4dp$. Two layers of boundary particles were adopted for all cases based on the simulations conducted in Section 3.4. Wave heights were recorded at $X_{tank}/L_{tank} = 0.1$, and a constant time step $\Delta t = 5\text{x}10^{-4}$sec was used, which was determined based on multiple simulations and following the CFL conditions [49].

$$\Delta t \leq min\left(0.1\left(\frac{dp}{U_{max}}\right), 0.1\left(\frac{dp^2}{v}\right)\right) \quad \textbf{(3.26)}$$

All tanks were equipped with two screens, located at $0.1L_{tank}$ from the tank center, except for the circular bottom tank with only one screen in the center to match Ref. [25].

To evaluate mesh convergence, the ITTC guidelines [57] recommend three simulations for three particle resolutions (i.e., fine (dp_1), medium (dp_2), and coarse (dp_3)) using a refinement factor of $\sqrt{2}$, as summarized in Table 3.1, for the three bottom geometries. Tanks were excited for 10 seconds and subjected to a low-amplitude harmonic excitation at the natural frequency of each tank. Table 3.2 contains tank properties used in this section.

The average maxima and minima of the wave heights were calculated for each mesh size, and the convergence ratio was calculated for each case using the ITTC recommendations [57] and presented in Table 3.3. The deviation between medium-fine (i.e., $\varepsilon_{21} = \eta_2 - \eta_1$) and between coarse-medium (i.e., $\varepsilon_{32} = \eta_3 - \eta_2$) was used to calculate the convergence ratio ($R = \varepsilon_{21}/\varepsilon_{32}$). For R>1, the simulation diverges, while for R<0 or 0<R<1, the simulation exhibits oscillatory or monotonic convergence, respectively. Wang et al. [58] have recently used this method to evaluate mesh convergence in SPH simulations. Across the three tank bottom geometries, the resulting convergence ratio showed that the particle resolution converged monotonically (i.e., 0<R<1), as demonstrated in Table 3.3.

Figure 3.4 plots the free surface response history at different particle resolutions for all tank bottom geometries considered. It is observed that the results are nearly identical, and the relative error between the coarse and fine mesh does not exceed 5% for all cases. Therefore, for all the cases considered in this study, the medium mesh dp_2 = 5 mm is used to ensure stable and efficient simulations.

3.4.4 Model Validation

3.4.4.1. Hydrostatic Case

To study the performance of the three boundary generation algorithms introduced in Section 3.3.2 test the repulsive force term added to the base SPH model, a circular tank with a radius R = 0.5 m and a fluid height h_{fluid} = 0.241 m for 200 seconds was investigated. Figure 3.5 compares the simulation time versus the number of particles needed for each method to contain the particles inside the tank. For example, the square grid method required three levels of boundary layers at a particle spacing of dp = 1 mm to converge and

contain the particles inside the tank for the simulation period. The linear-curved grid showed higher efficiency than the fixed grid, with only two boundary layers and a 5 mm particle spacing needed to contain the fluid. The nonlinear curved grid method required two boundary layers and dp = 5mm, resulting in a reduced computational time of approximately 55% compared to the linear-curved grid.

Based on these results, the nonlinear curved grid method results are validated against the analytical results for the circular tank at rest. A simulation was run for 20 seconds, with dp = 5mm, Δt = 5x10^{-4}sec, and $h_k = 1.4dp$. The SPH results were compared to the analytical hydrostatic pressure profile, as shown in Figure 3.6, where y is the vertical particle position and h is the initial fluid depth. A good agreement was found between the results.

3.4.4.2. Sloshing Response Case

Simulation results from the SPH model for sloped, parabolic, and curved bottom tanks with similar screen properties are compared with results from linear models found in the literature [21, 23, 25] and discussed below. Using linear long wave theory, Deng and Tait [21] proposed linear models for the flat, sloped, and parabolic bottom tanks. The wave heights for the flat bottom tank (shown in Figure 3.3(a)) can be calculated by the following equation

$$\eta(x,t) = q(t)\cos\left(\frac{\omega}{\sqrt{gh}}x\right) \quad \textbf{(3.27)}$$

where

$$q(t) = q_0 \cos(\omega t) \tag{3.28}$$

$$\omega_1 = \sqrt{gh\left(\frac{\pi}{L}\right)^2} \tag{3.29}$$

For the sloped bottom tank shown in Figure 3.3(b), the wave height at any location along the tank length is given by

$$\eta(x,t) = J_0\left(2\sqrt{\kappa x}\right) q(t) \tag{3.30}$$

where

$$\kappa = \frac{\omega^2 s}{gh} \tag{3.31}$$

$$\omega_1 = \sqrt{5.783 \frac{gh}{L^2}} \tag{3.32}$$

and J_0 is the first kind of Bessel function of order 0. While the wave height for the parabolic bottom tank, shown in Figure 3.3(c), is calculated as

$$\eta(x,t) = \frac{q_0 x}{L_0} \tag{3.33}$$

and the frequency is given by

$$\omega_1 = \sqrt{2 \frac{gh}{L_0^2}} \tag{3.34}$$

Following the potential flow theory based model proposed by Deng and Tait [23] for the circular bottom tank, the wave height is expressed as

$$\eta(x,t) = \frac{2R(R-H)}{\sqrt{R^2 - H^2}} \cdot \frac{x}{x^2 + (H-R)^2} \cdot q(t) \tag{3.35}$$

and the frequency is given by

$$\omega_1 = \sqrt{\left[\left(\frac{h}{2R}\right)^{3.129} + 1.542^{\left(\frac{h}{2R}\right)}\right]\frac{g}{R}} \quad \textbf{(3.36)}$$

where R and H are the tank parameters described in Figure 3.3(d). Since a general closed-form of the screen model integration was not achieved in [23], a simple case for one screen at the center of the tank was used for validation following the formulation found in [25].

For all bottom geometries, the fluid sloshing base shear force is calculated as

$$F_{sw} = m_{eq}\omega^2 \frac{q_0}{\Gamma} \quad \textbf{(3.37)}$$

where the m_{eq} is the equivalent mass, q_0 is the amplitude of the fluid response, and Γ is the modal participation factor and is equal to the ratio of the excitation factor γ^* and the generalized mass m^*. The exact formulas and the other screen-damping formulations are presented elsewhere [21, 23]. The free surface time history at any instant in time for the first mode is given by

$$q(t) = q_0 \cos(\omega t) \quad \textbf{(3.38)}$$

where q_0 is expressed as

$$q_0 = \sqrt{\frac{2\Gamma^2 X_0^2 \beta^4}{(1-\beta^2)^2 + (2\zeta_0 \beta^3 \Gamma X_0)^2}} \quad \textbf{(3.39)}$$

where β is the excitation frequency ratio $\frac{\omega_e}{\omega_1}$ and ζ_0 is the damping ratio [59].

For validation purposes, a low-amplitude sinusoidal excitation with frequency β = 1.0 (i.e., fundamental frequency) is applied with h_{fluid}/L_{tank} = 0.1 (i.e., shallow water depth) for all bottom-geometries as summarized in Table 3.4, and the results are normalized as

described in Section 3.4.2. The normalized response history of the SPH results versus the linear model results is presented for each tank bottom geometry in Figure 3.7 for the free surface and Figure 3.8 for the sloshing base shear forces. The SPH data was low pass filtered with a cutoff frequency above the fundamental frequency of each tank to eliminate higher modes from the signal, as the linear model is limited to one or few sloshing modes [60]. The filtered SPH results showed good agreement with the linear models for all tank bottom geometries investigated. Although slight variations are observed between results, overall, good agreement is found between the filtered SPH results and the linear model results.

To further validate the SPH model, numerical results from SPH are compared with experimental data reported by Amano et al. [27] for a triangular bottom tank with vertical walls, as shown in Figure 3.9. Tests were carried out at an excitation amplitude of 2.25 mm over excitation frequencies ranging from 0.9 to 1.1 of the natural frequency of the tank (0.374 Hz). Figure 3.10 compares the wave height response history at an excitation frequency of 0.383 Hz, and Figure 3.11 compares wave height frequency response curves, respectively. It can be observed that there is excellent agreement between the SPH model results and the experimental data.

For further SPH model validation in the nonlinear response range, numerical results were compared to experimental data for a trapezoidal tank bottom geometry (Figure 3.12) at an excitation amplitude of 5mm, with additional experimental test details available in [18]. The wave height response history at $\beta = 1.03$ is presented in Figure 3.13, and the base shear force frequency response curve is presented in Figure 3.14. It can be observed that

results from the SPH model are in good agreement with experimental test results over a wide range of excitation frequencies.

The inherent Lagrangian characteristics of the SPH and solving the fully NS equations at a sufficiently small timestep make it a robust tool for capturing the nonlinear wave heights response [34]. Consequently, the SPH model is used to investigate the sloshing response at a high excitation amplitude and considers different fluid depths in the following section.

3.4.5 Extreme Loading Analysis for Different Bottom Geometries

TLDs are typically designed to work under serviceability accelerations, often associated with 10-year return period (or less) wind events. However, if located in seismic regions or areas that experience high wind-speed events (e.g., hurricanes), accurately predicting the nonlinear fluid response amplitude is essential as it dictates tank height requirements. This section investigates TLD tanks with different bottom geometries, outfitted with screens, at an acceleration value corresponding to a response level beyond serviceability limit levels. Direct comparison between the different bottom geometries is difficult as the fluid mass, natural frequency and nonlinearity are all impacted by the fluid depth and tank geometry. Thus, the water mass has been held constant for all tank bottom geometries for one case where all TLDs have been tuned to match a target frequency (i.e., the natural frequency of the building it is attached to). For a second case, the fluid depth to free surface length ratio is maintained. The effect of changing fluid heights on the natural frequency and sloshing response is investigated using the same water mass and tank height.

Finally, the effect of implementing multiple screens and fluid heights is investigated for each tank geometry.

3.4.5.1. Simulations Setup

For modelling purposes, the acceleration applied to the tank is the expected acceleration at the top of the structure where the TLD is attached. To estimate an hourly acceleration with an associated return period, Tait et al. [61] presented a relation between return periods and average hourly peak accelerations by assuming that the average hourly peak acceleration is proportional to the wind speed cubed [61]. In this study, an extreme wind event scenario is considered by assuming an hourly peak structural acceleration (a_c) equal to 44 milli-g (0.44 m^2/s), corresponding to an approximate 100-year return period, which exceeds serviceability limit levels. The wave heights are recorded at the left tank wall, and the sloshing base shear force is calculated using equation (25). The normalized wave heights and sloshing base shear forces (refer to section 3.4.2 for the normalization scheme) are calculated from the response histories, and average maximum and minimum responses are computed for each tank bottom geometry for comparison purposes.

3.4.5.2. Response at Constant Fluid Depth to Free Surface Fluid Length Ratio

A value of h_{fluid}/L_{fluid} = 0.25 is maintained for all the tank bottom geometries with simulation parameters summarized in Table 3.5, and the results are normalized as described in Section 3.4.2. Figure 3.15 illustrates the maximum and minimum average normalized wave height and sloshing base shear force. It can be observed that for the same water mass and fluid depth to free surface fluid length ratio, the parabolic tank showed the lowest normalized wave height response and largest normalized sloshing base shear force response

compared to other tank bottom geometries. Generally, the curved bottom (parabolic and circular) tanks exhibited higher normalized sloshing base shear force response and lower wave height response relative to the flat and sloped bottom tank geometries investigated. The reduction in wave heights for the curved bottom tanks can be attributed to the increased space available for wave runup due to the slope of the tank walls.Figure 3.16 shows higher pressure amplitudes were recorded for the curved bottom tanks compared to the other geometries. The higher dynamic pressure values contribute to the higher sloshing forces for curved bottom tanks than other geometries.

3.4.5.3. Response at a Target Frequency

A target frequency of ω_t = 4.43 rad/s was selected for all four tank bottom geometries investigated with the simulation parameters summarized in Table 3.6. Figure 3.17 shows the averaged maximum and minimum normalized wave height and sloshing base shear force values. With all the tank bottom configurations tuned to the same frequency, the parabolic bottom tank has been found to generate the lowest normalized wave heights and highest sloshing base shear force compared to other tank bottom geometries considered in this study. On the other hand, the flat bottom tank resulted in the highest wave height response and lowest sloshing base shear force values compared to the curved and sloped bottom tanks.

3.4.5.4. Response with Multiple Screens

To evaluate the influence of the number of screens on the flow, three cases were tested for each bottom geometry with a different number of screens while keeping the screen properties, the water mass (100 kg), excitation amplitude $X_0 = 0.44/(\omega_1)^2$, and the

frequency (β = 1.0) are equal for all four tank bottom geometries. The fluid depths and tank widths used for each tank are given in Table 3.6. The first case employed one screen at the center of each tank (e.g., X_{tank}/L_{tank} = 0), the second used two screens at X_{tank}/L_{tank} = -0.1 and 0.1, and the third case had three screens at X_{tank}/L_{tank} = -0.1, 0 and 0.1. The normalized average maximum and minimum responses have been recorded for each tank bottom geometry.

Figure 3.18 shows that increasing the number of screens reduces the normalized average maximum and minimum wave height and sloshing base shear force amplitude for all tank bottom geometries considered, which is an expected result due to the increased energy dissipated by the screens. However, the amount of reduction in wave height and sloshing base shear force was different for each tank bottom geometry considered. For instance, using two screens in the sloped bottom tank instead of one at the center reduced the wave heights by only 8%. However, using three screens further reduced the maximum normalized wave heights by approximately 30%. On the other hand, the effect of using three screens in a flat bottom tank showed only a 6% reduction in the maximum normalized wave heights. It can be observed that the effect of the screens is highly dependent on the tank bottom geometry, the number of screens, and the location of the screens.

3.4.5.5. Response at Varying Fluid Depth

This section investigates four fluid depth ratios, h_{fluid}/L_{tank} = 0.1, 0.15, 0.2 and 0.25, for a consistent tank length and height. Table 3.7, Table 3.8, Table 3.9, and Table 3.10 show the tank parameters used in this section for the flat, sloped, parabolic, and circular bottom tanks, respectively. The maximum and minimum averaged values for the normalized wave

heights and sloshing base shear forces are recorded for each fluid depth. Figure 3.19 shows the normalized response values for the different tank bottom geometries with respect to the variation of the fluid depth ratio for a constant tank footprint.

For this case, the flat bottom tank had the lowest sloshing frequency across the other tank bottom geometries, resulting in a relatively higher excitation amplitude (to maintain a consistent acceleration) at each fluid depth. For instance, at h_{fluid}/L_{tank} =0.1, the sloshing frequency for the flat bottom tank was 3.06 rad/s, while for the same water mass and tank footprint, the frequency was 11.91 rad/s for the sloped bottom tank. The findings indicate that increasing the fluid depth ratio (i.e., h_{fluid}/L_{tank} from 0.1 to 0.25) has an inverse effect on the wave height and sloshing base shear force response for all the tank bottom geometries investigated; however, the effect changes from one geometry to another. For example, it is shown in Figure 3.20 that the fluid height in the sloped tank bottom impacted the average normalized wave heights and sloshing base shear forces significantly as it increased from 0.1 to 0.25. In contrast, the circular tank showed only a slight difference in response for $h_{fluid}/L_{tank} > 0.1$.

Changing fluid depth in the flat and sloped bottom tanks results in significant changes in the natural sloshing frequency, as shown in Table 3.7 and Table 3.8. However, the sloshing frequency of the curved bottom tanks does not vary significantly when the fluid height is varied, as shown in Table 3.9 and Table 3.10.

Finally, the fluid velocity distribution shown in Figure 3.20 displays snapshots at t = 100 seconds for each tank bottom geometry. The left side of Figure 3.20 shows the velocity profile for a depth ratio h_{fluid}/L_{tank} = 0.1, while the right-side show the velocity profile for a

depth ratio h_{fluid}/L_{tank} = 0.25. It can be observed that a more significant variation between the maximum and minimum fluid velocity occurs with greater fluid depth for all the tank bottom geometries investigated.

3.4.5.6. Model Performance and Discussion

The presented model has shown excellent capabilities in the simulation of the fluid response in tanks with different tank bottom geometries having multiple screens and under high amplitude excitation with feasible computational requirements. No particle loss through the boundaries was observed in any of the tank bottom geometries investigated at any different fluid depth ratios considered, which confirms that the modified SPH model can simulate a wide range of scenarios without fluid particle loss through the boundaries, as reported in previous SPH models [45]. Overall, the macroscopic SPH model has effectively captured the fluid response for all cases investigated while containing all particles inside the tank boundaries.

The response of different tank bottom geometries reveals that the circular and parabolic tanks have higher sloshing base shear force amplitudes than the other bottom geometries for the same water mass and frequency. However, the sloshing frequency of the curved bottom tanks is less sensitive to changes in fluid depth for a given tank size relative to the flat and sloped tank bottom geometries. In addition, the sloped bottom tank showed a much lower normalized wave height response than the other tank bottom geometries, which could be beneficial in reducing tank height (freeboard) requirements.

3.5 Conclusion

This paper describes modifications to an existing macroscopic 2D SPH model to simulate the response of different TLD tank bottom geometries under a range of excitation amplitudes, fluid depth ratios and screen properties (i.e., geometry, locations, and number). The SPH model is modified to efficiently discretize any tank bottom shape, including sloped and curved bottom tanks, using a simple formulation presented in this study. A repulsive force is added to the algorithm to prevent particles from incorrectly crossing boundaries. The macroscopic SPH model was validated against theoretical hydrostatic pressure for a circular bottom tank at rest with the added boundary particle generation formula and repulsive force algorithm. The SPH model results for a sloped, a parabolic and a circular bottom tank with screens at low excitation amplitude and shallow fluid depth were validated against results from available linear models [21, 23, 25].

Subsequently, the response of the four different tank bottom geometries was studied under a large excitation amplitude while maintaining a constant water mass for different tank bottom geometries. The averaged maximum and minimum of the normalized wave heights and sloshing base shear forces were evaluated for a targeted frequency and the same fluid depth-to-length ratio. The effect of adding multiple screens and varying the fluid depth for each tank geometry was also investigated under large excitation amplitude. No particles were found to cross the tank wall boundaries for any of the simulations conducted, which is a direct result of the enhanced grid generation method and boundary condition technique implemented.

The following conclusions can be drawn from this study:

1. The nonlinear curved grid method can model any sloped or curved bottom tank geometry with a significant reduction in computational time while providing simulation stability by maintaining all fluid particles inside the tank boundaries for the simulation period.
2. The SPH model showed no limitations over the range of fluid depth ratios considered for the different tank bottom geometries investigated.
3. The SPH macroscopic model is a robust tool to model screens in different tank bottom geometries for any number of screens at any location inside the tank.
4. The curved bottom tanks showed the highest normalized sloshing and lowest normalized wave height responses.
5. Additional screens reduce the normalized sloshing base shear force and wave height amplitudes for all tank bottom geometries investigated, with varying percentages of reduction depending on the tank bottom geometry, number of screens, and location of screens.
6. Increasing the fluid depth ratio decreases the normalized wave height and sloshing base shear force amplitudes for the four tank bottom geometries considered in this study.
7. The SPH model can capture different internal response quantities for all tank bottom geometries investigated.

The presented boundary conditions show that the macroscopic SPH model can be used to investigate a wide range of TLD tank bottom geometries equipped with screens. The model can assist in efficiently determining and assessing the number and location of screens

required to achieve the desired level of energy dissipation. By employing the current model, TLD designers can investigate the behaviour of different tank bottom geometries outfitted with screens above the serviceability limits with practical computational power requirements.

3.6 Acknowledgement

Financial support has been provided by the Natural Sciences and Engineering Research Council of Canada (NSERC). This work was made possible by the facilities of the Shared Hierarchical Academic Research Computing Network (SHARCNET: www.sharcnet.ca) and Compute/Calcul Canada (www.computecanada.ca). This study forms a part of an ongoing research program at McMaster University Centre for Effective Design of Structures (CEDS).

3.7 References

1. Ueda T, Nakagaki R, Koshida K (1992) Suppression of wind-induced vibration by dynamic dampers in tower-like structures. J Wind Eng Ind Aerodyn 43:1907–1918. https://doi.org/10.1016/0167-6105(92)90611-D
2. Fujino Y, Sun L, Pacheco B, Chaiseri P (1992) Tuned Liquid Damper (TLD) for suppressing horizontal motion of structures. ASCE J Eng Mech 118:2017–2030
3. Koh CG, Mahatma S, Wang CM (1995) Reduction of structural vibrations by multiple-mode liquid dampers. Eng Struct 17:122–128. https://doi.org/10.1016/0141-0296(95)92643-M
4. Warnitchai P, Pinkaew T (1998) Modelling of liquid sloshing in rectangular tanks with flow-dampening devices. Eng Struct 20:
5. Modi VJ, Seto ML (1998) Passive control of flow-induced oscillations using rectangular nutation dampers. JVC/Journal Vib Control 4:381–404. https://doi.org/10.1177/107754639800400403
6. Lishi W, Zhuang W, Yuchun L (2013) A SPH simulation on large-amplitude sloshing for fluids in a two-dimensional tank. J Earthq Eng Eng Vib 12:135–142. https://doi.org/10.1007/s11803-013-0157-1
7. Fediw AA, Isyumov N, Vickery BJ (1995) Performance of a tuned sloshing water damper. J Wind Eng Ind Aerodyn 57:237–247. https://doi.org/10.1016/0167-6105(94)00107-O
8. Kaneko S, Yoshida O (1999) Modeling of deepwater-type rectangular tuned liquid damper with submerged nets. J Press Vessel Technol Trans ASME 121:413–422. https://doi.org/10.1115/1.2883724
9. Biswal KC, Bhattacharyya SK, Sinha PK (2006) Non-linear sloshing in partially liquid filled containers with baffles. Int J Numer Methods Eng 68:317–337. https://doi.org/10.1002/nme.1709
10. Yu L, Xue MA, Zhu A (2020) Numerical investigation of sloshing in rectangular tank with permeable baffle. J Mar Sci Eng 8:1–18. https://doi.org/10.3390/jmse8090671

11. Shamsoddini R, Abolpur B (2019) Investigation of the Effects of Baffles on the Shallow Water Sloshing in A Rectangular Tank Using A 2D Turbulent ISPH Method. China Ocean Eng 33:94–102. https://doi.org/10.1007/s13344-019-0010-z
12. Ruiz RO, Lopez-Garcia D, Taflanidis AA (2016) Modeling and experimental validation of a new type of tuned liquid damper. Acta Mech 227:3275–3294. https://doi.org/10.1007/s00707-015-1536-7
13. Ruiz RO, Taflanidis AA, Lopez-Garcia D (2016) Characterization and design of tuned liquid dampers with floating roof considering arbitrary tank cross-sections. J Sound Vib 368:36–54. https://doi.org/10.1016/j.jsv.2016.01.014
14. Tsao W, Huang Y (2021) Results in Engineering Sloshing force in a rectangular tank with porous media. Results Eng 11:100250. https://doi.org/10.1016/j.rineng.2021.100250
15. Huang C, Chang H, Hwung H (2003) Structural permeability effects on the interaction of a solitary wave and a submerged breakwater. 49:1–24. https://doi.org/10.1016/S0378-3839(03)00034-6
16. Soong TT, Dargush GF (1997) Passive energy dissipation systems in structural engineering. John Wiley Sons, Toronto 20:197–198. https://doi.org/10.1016/s0167-4730(97)00034-9
17. Patil GR, Singh KD (2016) Evaluation of Sloped Bottom Tuned Liquid Damper for Reduction of Seismic Response of Tall Buildings. J Inst Eng Ser A 97:385–394. https://doi.org/10.1007/s40030-016-0185-8
18. Gardarsson S, Yeh H, Reed D (2001) Behavior of Sloped-Bottom Tuned Liquid Dampers. J Eng Mech 127:266–271. https://doi.org/10.1061/(asce)0733-9399(2001)127:3(266)
19. Agresta A, Cavalagli N, Biscarini C, Ubertini F (2021) Effect of bottom geometry on the natural sloshing motion of water inside tanks: An experimental analysis. Appl Sci 11:1–15. https://doi.org/10.3390/app11020605
20. Idir M, Ding X, Lou M, Chen G (2009) Fundamental frequency of water sloshing waves in a sloped-bottom tank as tuned liquid damper. Proc 2009 Struct Congr -

Don’t Mess with Struct Eng 831–840. https://doi.org/10.1061/41031(341)91

21. Deng X, Tait MJ (2009) Theoretical modeling of TLD with different tank geometries using linear long wave theory. J Vib Acoust Trans ASME 131:0410141–04101410. https://doi.org/10.1115/1.3142873
22. Tait MJ, Deng X (2008) The performance of structure-tuned liquid damper systems with different tank geometries M. Struct Control Heal Monit 17:254–277. https://doi.org/10.1002/stc
23. Deng X, Tait MJ (2008) Equivalent mechanical models of tuned liquid dampers with different tank geometries. Can J Civ Eng 35:1088–1101. https://doi.org/10.1139/L08-044
24. Love JS, Tait MJ (2013) Nonlinear multimodal model for TLD of irregular tank geometry and small fluid depth. J Fluids Struct 43:83–99. https://doi.org/10.1016/j.jfluidstructs.2013.09.009
25. Love JS, Tait MJ (2014) Linearized sloshing model for 2D tuned liquid dampers with modified bottom geometries. Can J Civ Eng 41:106–117. https://doi.org/10.1139/cjce-2013-0106
26. Pandit AR, Biswal KC (2020) Evaluation of dynamic characteristics of liquid sloshing in sloped bottom tanks. Int J Dyn Control 8:162–177. https://doi.org/10.1007/s40435-019-00527-8
27. Amano Y, Ishikawa S, Yoshitake T, Kondou T (2021) Modeling and design of a tuned liquid damper using triangular-bottom tank by a concentrated mass model. Nonlinear Dyn 104:1917–1935. https://doi.org/10.1007/s11071-021-06433-z
28. Warburton GB, Ayorinde EO (1980) Optimum absorber parameters for simple systems. Earthq Eng Struct Dyn 8:197–217. https://doi.org/10.1002/eqe.4290080302
29. Bulian G, Architecture N, Dinma EE (2010) Smoothed particle hydrodynamics (SPH) simulation of a tuned liquid damper (TLD) with angular motion Simulation d ’ un amortisseur liquide (TLD) en rotation à l ’ aide de la méthode SPH. Engineering 48:28–39. https://doi.org/10.3826/jhr.2010.0001

30. Cao XY, Ming FR, Zhang AM (2014) Sloshing in a rectangular tank based on SPH simulation. Appl Ocean Res 47:241–254. https://doi.org/10.1016/j.apor.2014.06.006
31. Green MD, Peiró J (2018) Long duration SPH simulations of sloshing in tanks with a low fill ratio and high stretching. Comput Fluids 174:179–199. https://doi.org/10.1016/j.compfluid.2018.07.006
32. Monaghan JJ (1985) Partcle Method for Hydrodynamics. Comput Phys Reports 3:71–124
33. Monaghan JJ (2005) Smoothed particle hydrodynamics. Reports Prog Phys 68:1703–1759. https://doi.org/10.1088/0034-4885/68/8/R01
34. Monaghan JJ (1992) Smoothed Particle Hydrodynamics. Annu Rev Astron Astrophys 30:543–574. https://doi.org/10.1146/annurev.aa.30.090192.002551
35. Cummins SJ, Rudman M (1999) An SPH Projection Method. J Comput Phys 607:584–607
36. Akbari H (2018) Evaluatoin of Incompressible and Compressible SPH Methods in Modeling Dam Break Flows. Int J Coast offshore Eng 2:45–57. https://doi.org/10.29252/ijcoe.2.1.45
37. Meringolo DD, Aristodemo F, Veltri P (2015) SPH numerical modeling of wave-perforated breakwater interaction. Coast Eng 101:48–68. https://doi.org/10.1016/j.coastaleng.2015.04.004
38. Aristodemo F, Meringolo DD, Veltri P (2016) A multi-node approach to simulate thin coastal structures in the SPH context. Proc Coast Eng Conf 35:. https://doi.org/10.9753/icce.v35.structures.1
39. Kashani AH, Halabian AM, Asghari K (2018) A numerical study of tuned liquid damper based on incompressible SPH method combined with TMD analogy. J Fluids Struct 82:394–411. https://doi.org/10.1016/j.jfluidstructs.2018.07.013
40. McNamara KP, Awad BN, Tait MJ, Love JS (2021) Incompressible smoothed particle hydrodynamics model of a rectangular tuned liquid damper containing screens. J Fluids Struct 103:103295.

https://doi.org/10.1016/j.jfluidstructs.2021.103295

41. Tait MJ, El Damatty AA, Isyumov N, Siddique MR (2005) Numerical flow models to simulate tuned liquid dampers (TLD) with slat screens. J Fluids Struct 20:1007–1023. https://doi.org/10.1016/j.jfluidstructs.2005.04.004
42. Tsao WH, Hwang WS (2018) Tuned liquid dampers with porous media. Ocean Eng 167:55–64. https://doi.org/10.1016/j.oceaneng.2018.08.034
43. Tsao WH, Huang LH, Hwang WS (2021) An equivalent mechanical model with nonlinear damping for sloshing rectangular tank with porous media. Ocean Eng 242:110145. https://doi.org/10.1016/j.oceaneng.2021.110145
44. Tsao WH, Chen YC, Kees CE, Manuel L (2022) The Effect of Porous Media on Wave-Induced Sloshing in a Floating Tank. Appl Sci 12:. https://doi.org/10.3390/app12115587
45. McNamara KP, Tait MJ (2022) Modeling the Response of Structure–Tuned Liquid Damper Systems Under Large Amplitude Excitation Using Smoothed Particle Hydrodynamics. J Vib Acoust 144:1–13. https://doi.org/10.1115/1.4051266
46. Awad BN, Tait MJ (2022) Macroscopic modelling for screens inside a tuned liquid damper using incompressible smoothed particle hydrodynamics. Ocean Eng 263:. https://doi.org/10.1016/j.oceaneng.2022.112320
47. Wendland H (1995) Piecewise polynomial, positive definite and compactly supported radial functions of minimal degree. Adv Comput Math 4:389–396. https://doi.org/10.1007/BF02123482
48. Gotoh, T S, T. S (2001) Sub-particle-scale turbulence model for the MPS method—Lagrangian ?ow model for hydraulic engineering Title. Comput Fluid Dyn J 9:339–347
49. Shao S, Lo EYM (2003) Incompressible SPH method for simulating Newtonian and non-Newtonian flows with a free surface. Adv Water Resour 26:787–800. https://doi.org/10.1016/S0309-1708(03)00030-7
50. Jiang H, You Y, Hu Z, et al (2019) Comparative study on violent sloshing withwater jet flows by using the ISPH method. Water (Switzerland) 11:.

https://doi.org/10.3390/w11122590

51. Adami S, Hu XY, Adams NA (2012) A generalized wall boundary condition for smoothed particle hydrodynamics. J Comput Phys 231:7057–7075. https://doi.org/10.1016/j.jcp.2012.05.005
52. Ergun S, Orning AA (1949) Fluid Flow through Randomly Packed Columns and Fluidized Beds. Ind Eng Chem 41:1179–1184. https://doi.org/10.1021/ie50474a011
53. Carman PG (1937) Fluid flow through granular beds. Chem Eng Res Des 75:S32–S48. https://doi.org/10.1016/s0263-8762(97)80003-2
54. Monaghan JJ (1994) Simulating free surface flows with SPH. J. Comput. Phys. 110:399–406
55. Cherfils JM, Pinon G, Rivoalen E (2012) JOSEPHINE: A parallel SPH code for free-surface flows. Comput Phys Commun 183:1468–1480. https://doi.org/10.1016/j.cpc.2012.02.007
56. Tavakkol S, Zarrati AR, Khanpour M (2017) Curvilinear smoothed particle hydrodynamics. Int J Numer Methods Fluids 83:115–131. https://doi.org/10.1002/fld.4261
57. ITTC Resistance Committee (2017) Uncertainty analysis in CFD Verification and validation methodology and procedures. ITTC - Recomm Proced Guidel 1–13
58. Wang S, Gonzalez-cao J, Islam H, et al (2022) Uncertainty estimation of mesh-free and mesh-based simulations of the dynamics of floaters. Ocean Eng 256:. https://doi.org/10.1016/j.oceaneng.2022.111386
59. Cassolato MR, Love JS, Tait MJ (2011) Modelling of a tuned liquid damper with inclined damping screens. Struct Control Heal Monit 18:674–681. https://doi.org/10.1002/stc
60. Tait MJ (2008) Modelling and preliminary design of a structure-TLD system. Eng Struct 30:2644–2655. https://doi.org/10.1016/j.engstruct.2008.02.017
61. Tait MJ, Isyumov N, El Damatty AA (2008) Performance of Tuned Liquid Dampers. J Eng Mech 134:417–427. https://doi.org/10.1061/(asce)0733-9399(2008)134:5(417)

Table 3.1 Particle size convergence summary

Simulation	*dp* (mm)	Refinement Ratio	Total Particles number		
			Sloped	Parabolic	Circular
Case 1	3.5	-	2582	7464	4828
Case 2	5	$\sqrt{2}$	1540	4021	2804
Case 3	7	$\sqrt{2}$	976	2297	1708

Table 3.2 Tanks properties for convergence

	$L_{tank}(m)$	$h_{tank}(m)$	$L_{fluid}(m)$	$h_{fluid}(m)$	$B_{tank}(m)$	$\omega_1(rad/s)$	X_0	$m_w(kg)$
Sloped	1	0.5	0.2	0.1	1	11.909	0.002	10
Parabolic	1.4		0.748	0.14		4.431		
Circular	1		0.6	0.1		4.526		

Table 3.3 Convergence results (Section 3.4.3)

Simulated Results		Sloped		Parabolic		Circular	
		Avg. Max.	Avg. Min.	Avg. Max.	Avg. Min.	Avg. Max.	Avg. Min.
Wave heights (m)	η_1	0.0182	-0.0396	0.0396	-0.0396	0.0213	-0.033
	η_2	0.0186	-0.0399	0.0398	-0.0399	0.0222	-0.035
	η_3	0.0191	-0.0405	0.04	-0.0405	0.0235	-0.0368
Errors	ε_{21}	3.0×10^{-4}	-3.29×10^{-4}	1.21×10^{-4}	-3.29×10^{-4}	9.0×10^{-4}	-2.0×10^{-3}
	ε_{32}	6.0×10^{-4}	-6.0×10^{-4}	2.95×10^{-4}	-6.0×10^{-4}	1.3×10^{-3}	-1.8×10^{-3}
Convergence Ratio	R	0.542	0.565	0.41	0.565	0.692	1.111

Table 3.4 Test setup for sloshing validation cases. (Section 3.4.4.2)

Bottom Geometries	L_{tank} *(m)*	h_{tank} *(m)*	L_{fluid} *(m)*	h_{fluid} *(m)*	B_{tank} *(m)*	ω_1 *(rad/s)*	X_0 *(m)*	m_w *(kg)*
Flat	1	0.5	1	0.1	0.41	3.06	0.002	41
Sloped	1		0.2	0.1	4.1	11.909		
Parabolic	1.4		0.748	0.14	0.59	4.431		
Circular	1		0.6	0.1	1.03	4.526		

Table 3.5 Test setup for constant fluid depth ratio (Section 3.4.5.2)

Bottom Geometries	h_{fluid}/L_{fluid}	L_{fluid} *(m)*	h_{fluid} *(m)*	L_{tank} *(m)*	h_{tank} *(m)*	B_{tank} *(m)*	ω_1 *(rad/s)*	$X_0 = 0.44/\omega_1^2$	m_w *(kg)*
Flat	0.25	1	0.25	1	0.5	0.40	4.49	0.022	100
Sloped		0.5	0.125	1	0.25	3.20	5.33	0.016	
Parabolic		1	0.250	1.41	0.5	0.60	4.43	0.022	
Circular		0.8	0.2	1	0.5	0.89	4.63	0.021	

Table 3.6 Test setup for targeted frequency (Section 3.4.5.3)

Bottom Geometries	h_{fluid}/L_{fluid}	L_{fluid} *(m)*	h_{fluid} *(m)*	L_{tank} *(m)*	h_{tank} *(m)*	B_{tank} *(m)*	ω_1 *(rad/s)*	$X_0 = 0.44/\omega_1^2$	m_w *(kg)*
Flat	0.24	1	0.24	1	0.5	0.42	4.43	0.022	100
Sloped	0.25	0.72	0.18	1	0.27	1.54		0.022	
Parabolic	0.25	1	0.250	1.41	0.5	0.60		0.022	
Circular	0.271	0.921	0.25	1.1	0.55	0.65		0.022	

Table 3.7 Test setup for flat bottom tank. (Section 3.4.5.4)

h_{fluid}/L_{tank}	L_{tank} (m)	h_{tank} (m)	h_{fluid}/L_{fluid}	L_{fluid} (m)	h_{fluid} (m)	B_{tank} (m)	ω_1 (rad/s)	$X_0 = 0.44/\omega_1^2$	m_w (kg)
0.1			0.1		0.1	1	3.06	0.047	
0.15			0.15		0.15	0.67	3.68	0.033	
	1	0.5		1					100
0.2			0.2		0.2	0.5	4.14	0.026	
0.25			0.25		0.25	0.4	4.49	0.022	

Table 3.8 Test setup for sloped bottom tank. (Section 3.4.5.4)

h_{fluid}/L_{tank}	L_{tank} (m)	h_{tank} (m)	h_{fluid}/L_{fluid}	L_{fluid} (m)	h_{fluid} (m)	B_{tank} (m)	ω_1 (rad/s)	$X_0 = 0.44/\omega_1^2$	m_w (kg)
0.1				0.2	0.1	10	11.909	0.009	
0.15				0.3	0.15	4.4	9.724	0.013	100
	1	0.5	0.5						
0.2				0.4	0.2	2.5	8.421	0.017	
0.25				0.5	0.25	1.6	7.532	0.02	

Table 3.9 Test setup for parabolic bottom tank. (Section 3.4.5.4)

h_{fluid}/L_{tank}	L_{tank} (m)	h_{tank} (m)	h_{fluid}/L_{fluid}	L_{fluid} (m)	h_{fluid} (m)	B_{tank} (m)	ω_1 (rad/s)	$X_0 = 0.44/\omega_1^2$	m_w (kg)
0.1			0.16	0.63	0.1	0.042	4.430	0.022	
0.15			0.19	0.77	0.15	0.077	4.429	0.022	
	1	0.5							100
0.2			0.22	0.89	0.2	0.12	4.430	0.022	
0.25			0.25	1	0.25	0.17	4.429	0.022	

Table 3.10 Test setup for circular bottom tank. (Section 3.4.5.4)

h_{fluid}/L_{tank}	L_{tank} (m)	h_{tank} (m)	h_{fluid}/L_{fluid}	L_{fluid} (m)	h_{fluid} (m)	B_{tank} (m)	ω_1 (rad/s)	$X_0 = 0.44/\omega_1^2$	m_w (kg)
0.1	1	0.5	0.17	0.6	0.1	0.041	4.526	0.021	100
0.15			0.21	0.714	0.15	0.074	4.576	0.021	
0.2			0.25	0.8	0.2	0.112	4.626	0.020	
0.25			0.29	0.866	0.25	0.153	4.677	0.020	

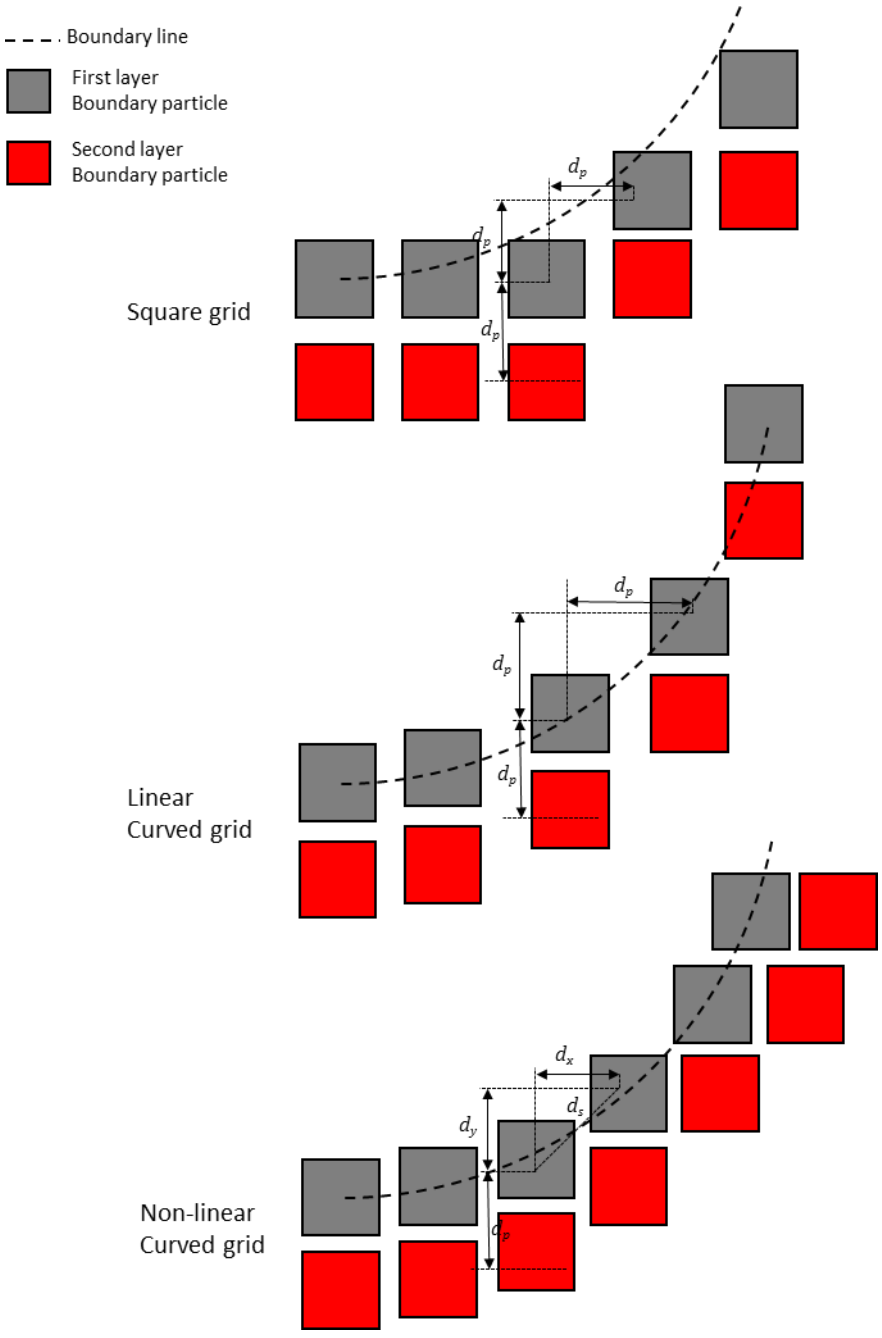

Figure 3.1 Boundary particles generation using different grid methods.

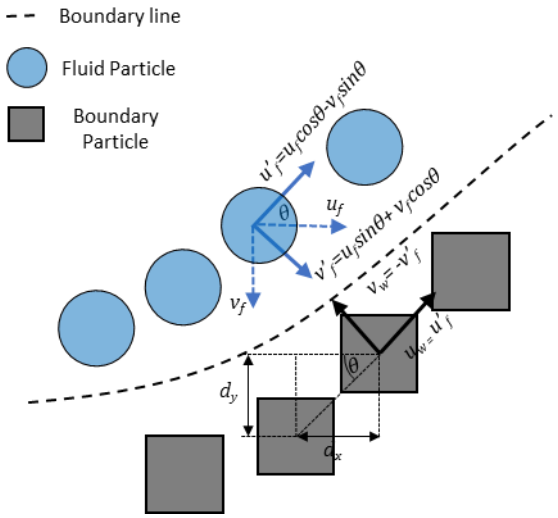

Figure 3.2 Illustration showing free-slip boundary conditions for sloped and curved walls

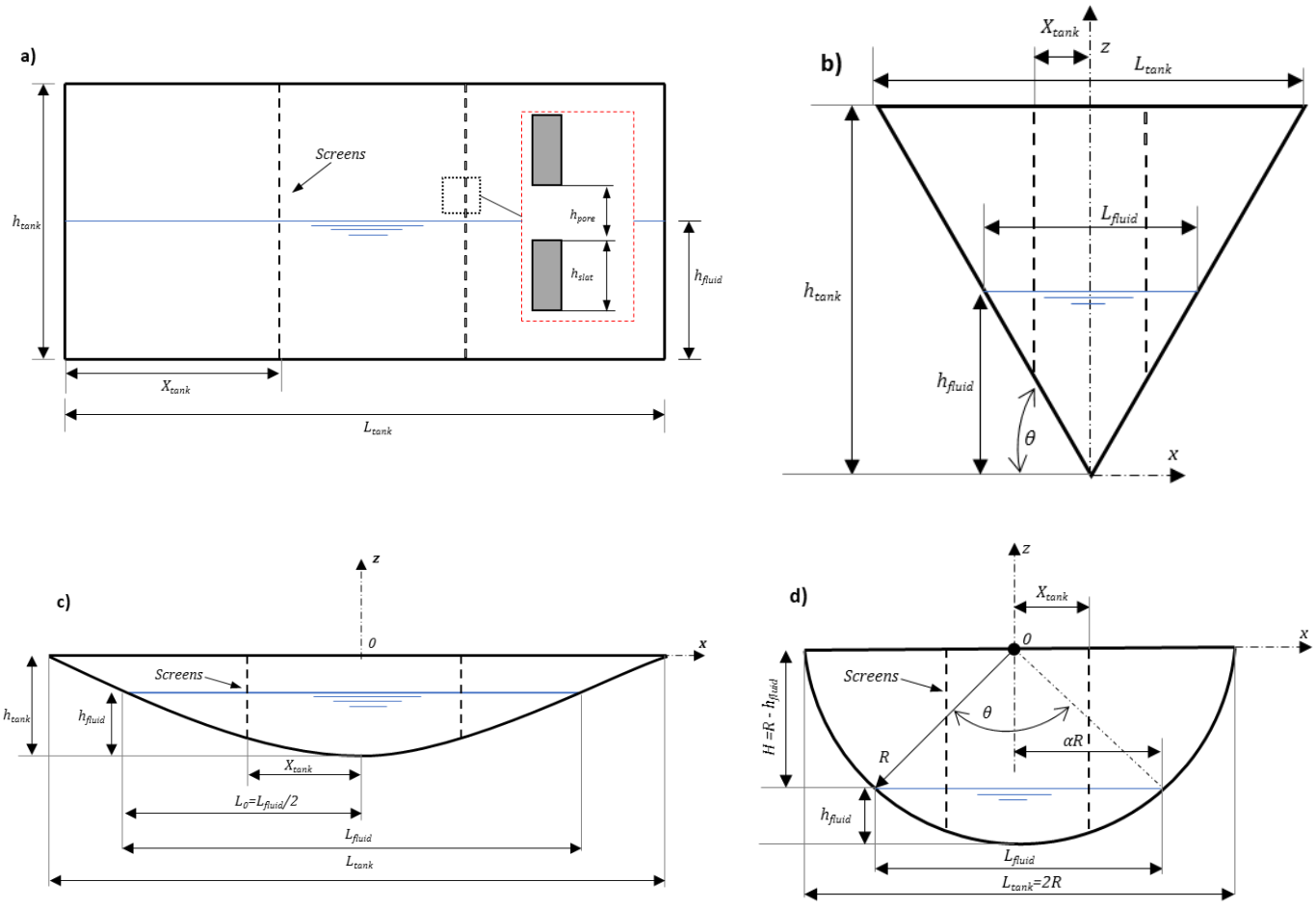

Figure 3.3 Sketch of a) Flat bottom, b) Sloped bottom, c) Parabolic bottom, and d) Circular bottom tanks

a)

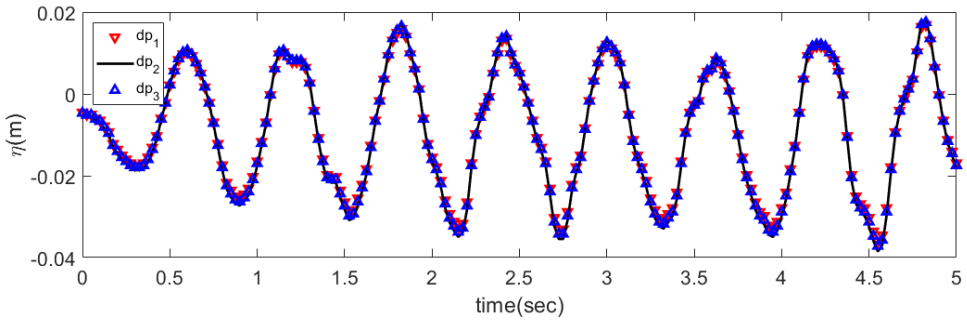

b)

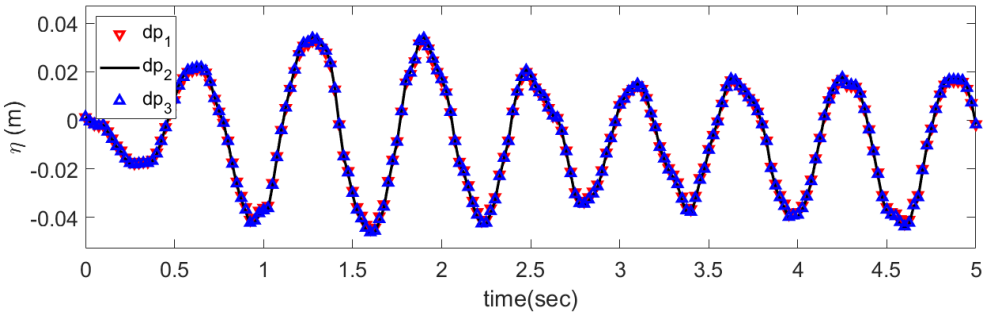

c)

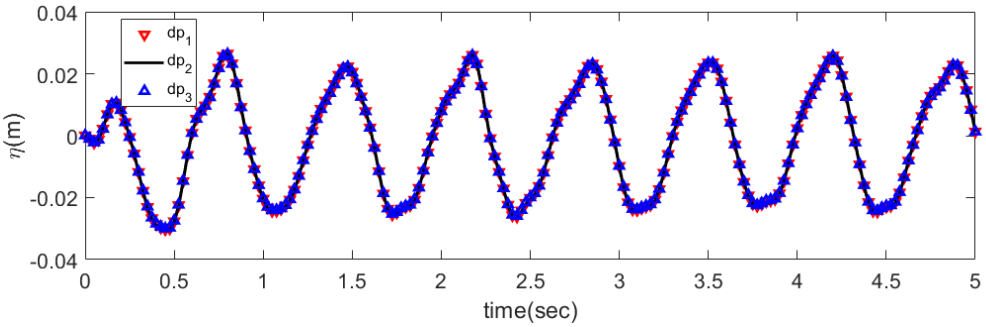

Figure 3.4 Wave heights obtained at coarse, medium, and fine particle resolution for a) Sloped, b) Parabolic, and d) Circular tank bottom geomtries. h_{fluid}/L_{tank} = 0.1, X_0 = 0.002m, β=1.0.

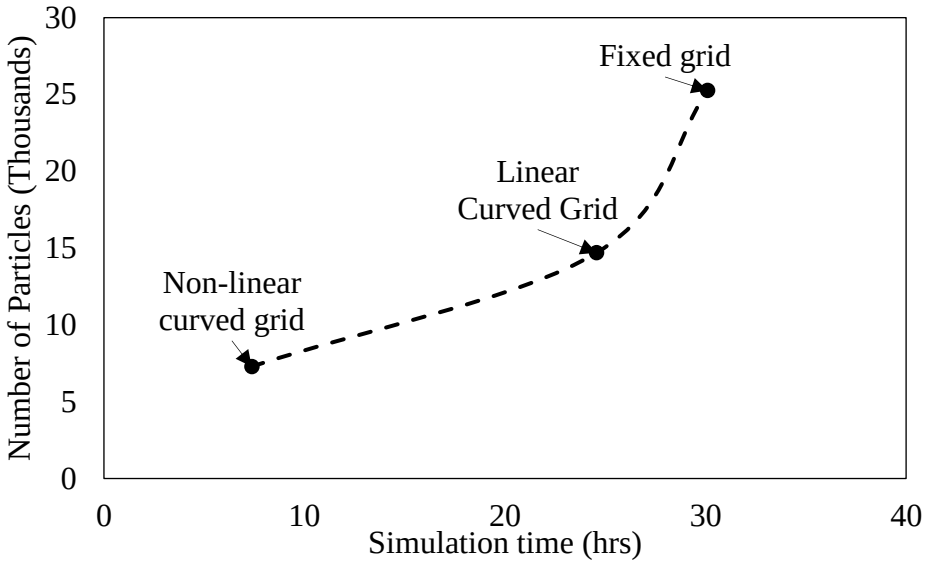

Figure 3.5 Number of particles versus the simulation time needed for each boundary particle generation method

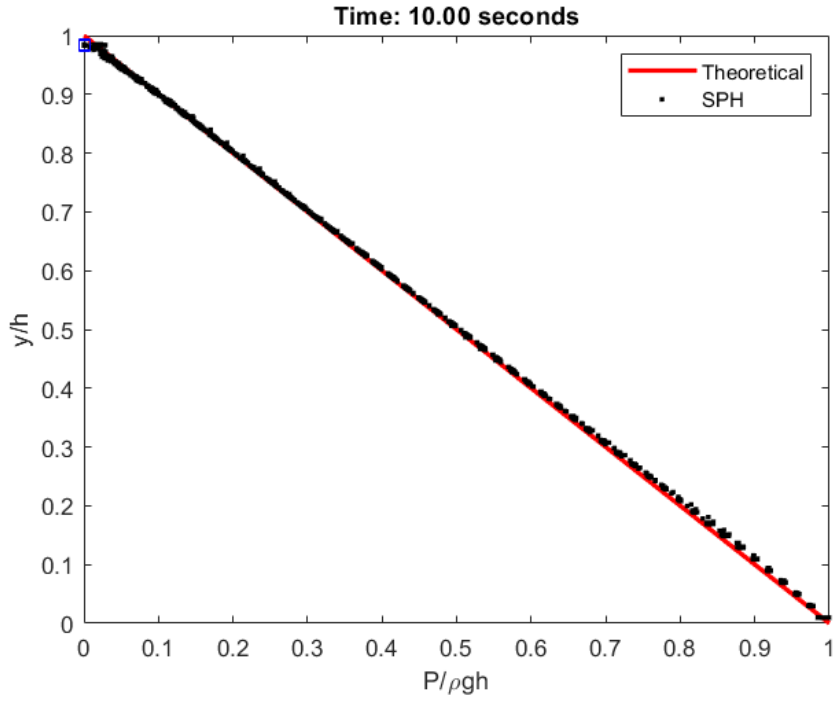

Figure 3.6 SPH hydrostatic pressure profile for a circular tank at rest against analytical results.

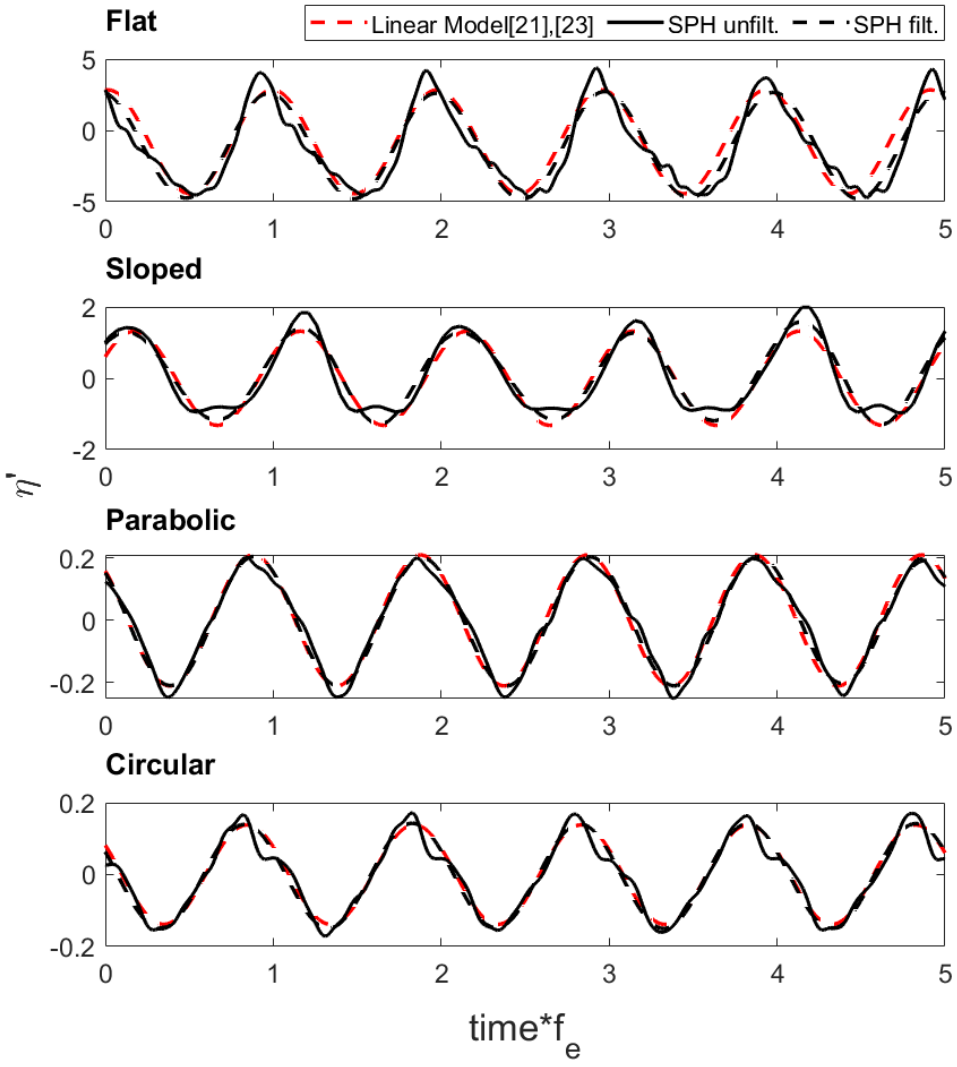

Figure 3.7 Normalized wave heights for different tank bottom geometries (h_{fluid}/ L_{tank} = 0.1, X_0 = 0.002m, β=1.0).

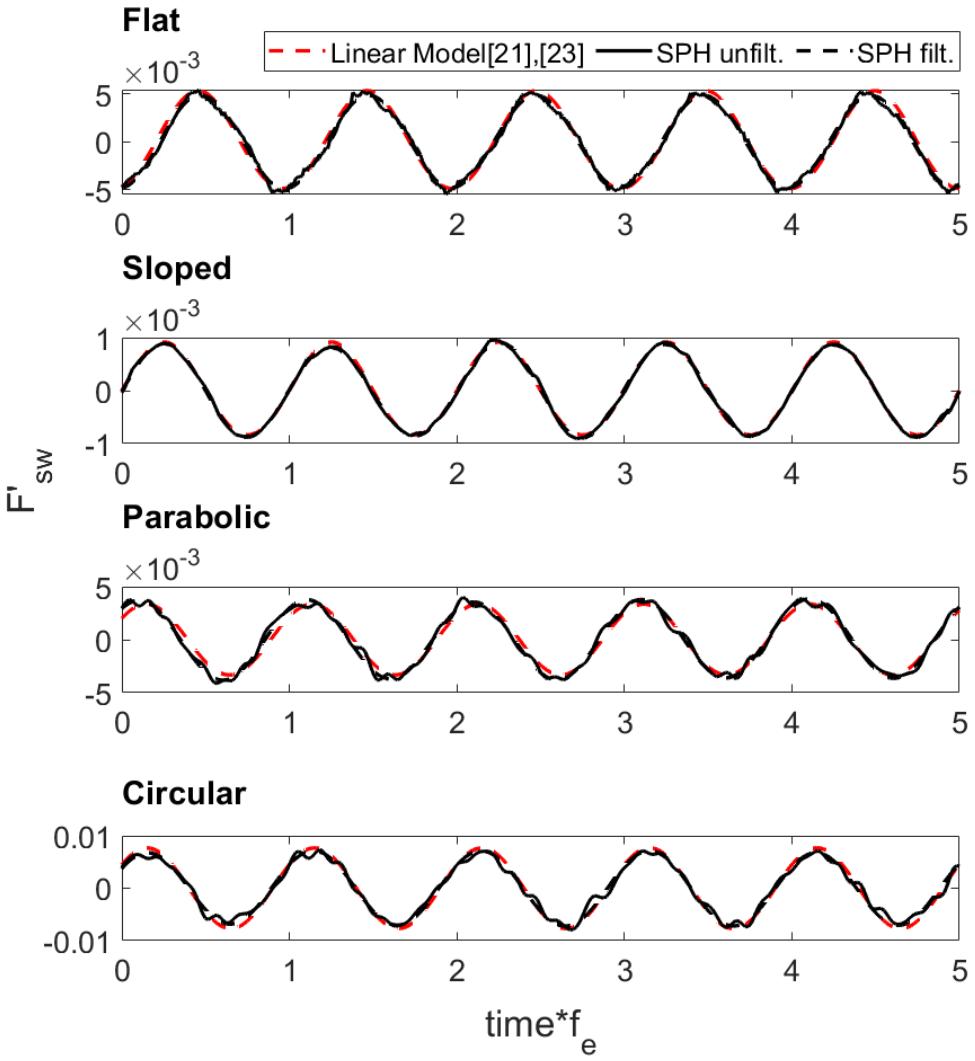

Figure 3.8 Normalized sloshing forces for different tank bottom geometries h_{fluid}/L_{tank} = 0.1, X_0 = 0.002m, β=1.0.

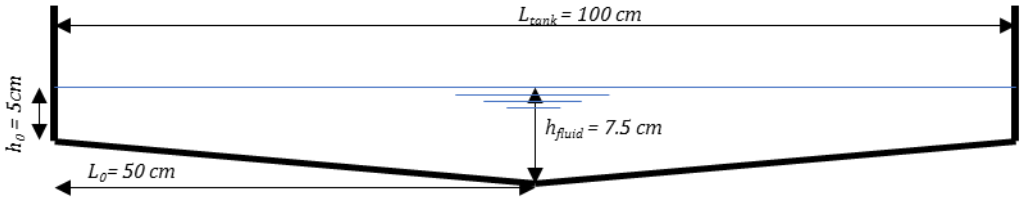

Figure 3.9 Triangular bottom tank sketch tested by Amano et al. [27]

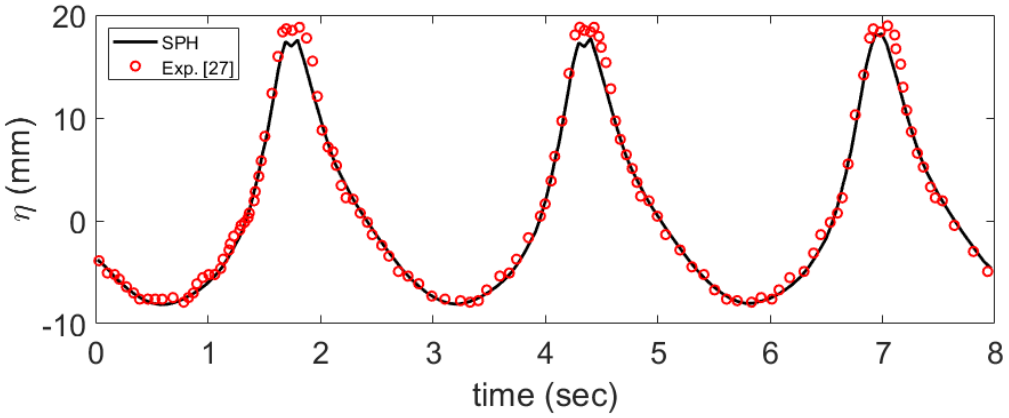

Figure 3.10 SPH wave heights response time history versus experimental data from Amano et al. [27] at β=1.2

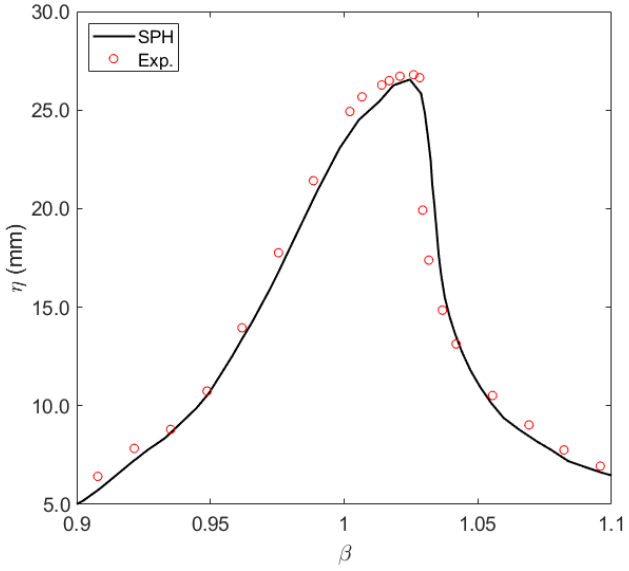

Figure 3.11 SPH wave height frequency response versus experimental data from Amano et al. [27]

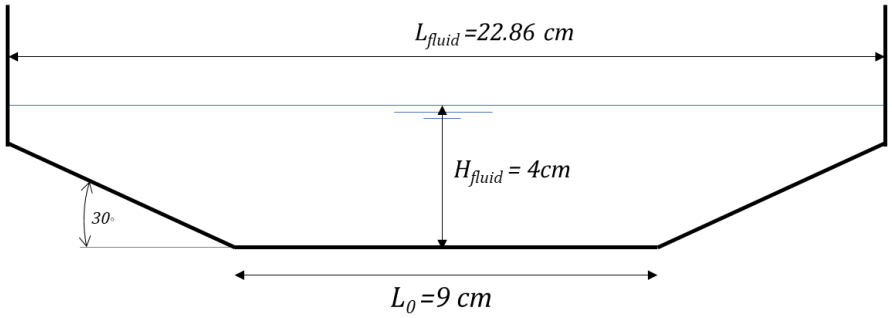

Figure 3.12 Trapezoidal bottom tank sketch tested by Gardarsson et al. [18]

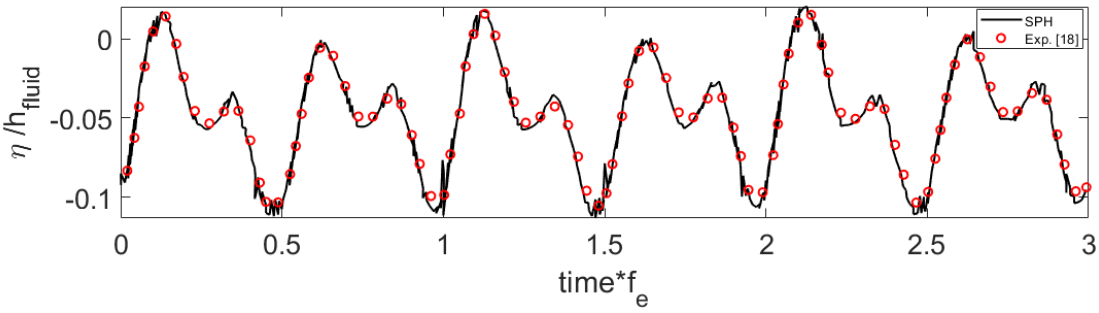

Figure 3.13 SPH wave heights response time history versus experimental data from Gardarsson et al. [18] at β=1.03

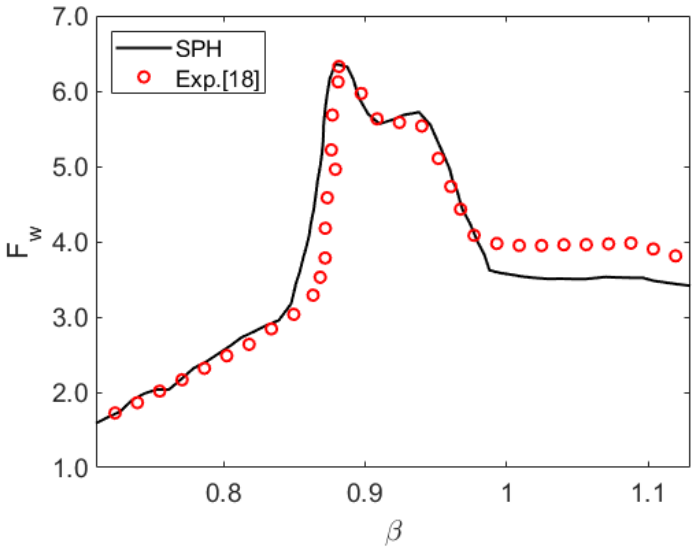

Figure 3.14 SPH base shear force frequency response versus experimental data from Gardarsson et al. [18]

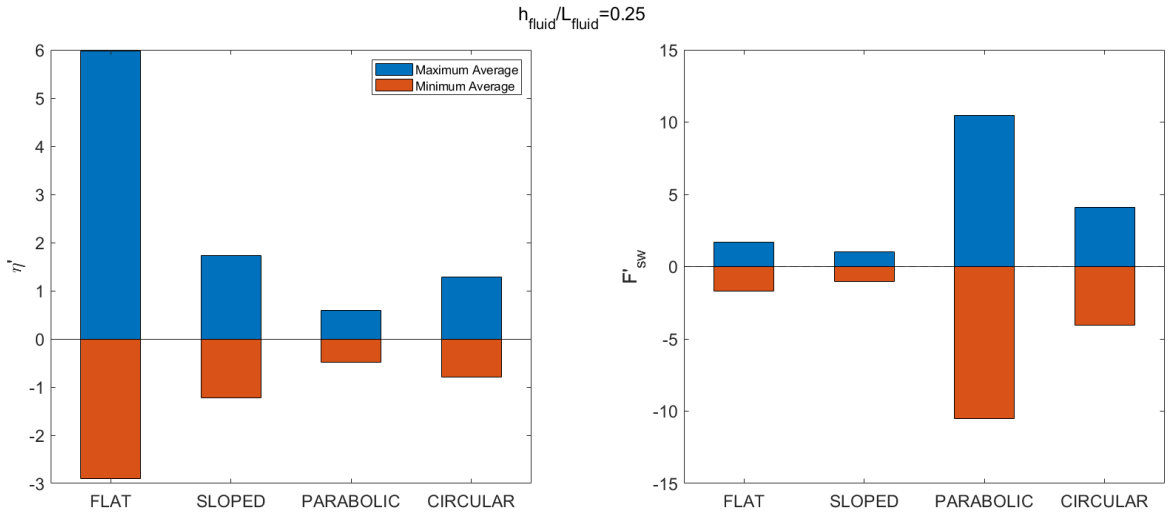

Figure 3.15 Maximum and Minimum normalized wave heights and sloshing forces for constant fluid height to free surface fluid length ratio m_w=100kg, $X_0 = 0.44/(\omega_1)^2$, β=1.0

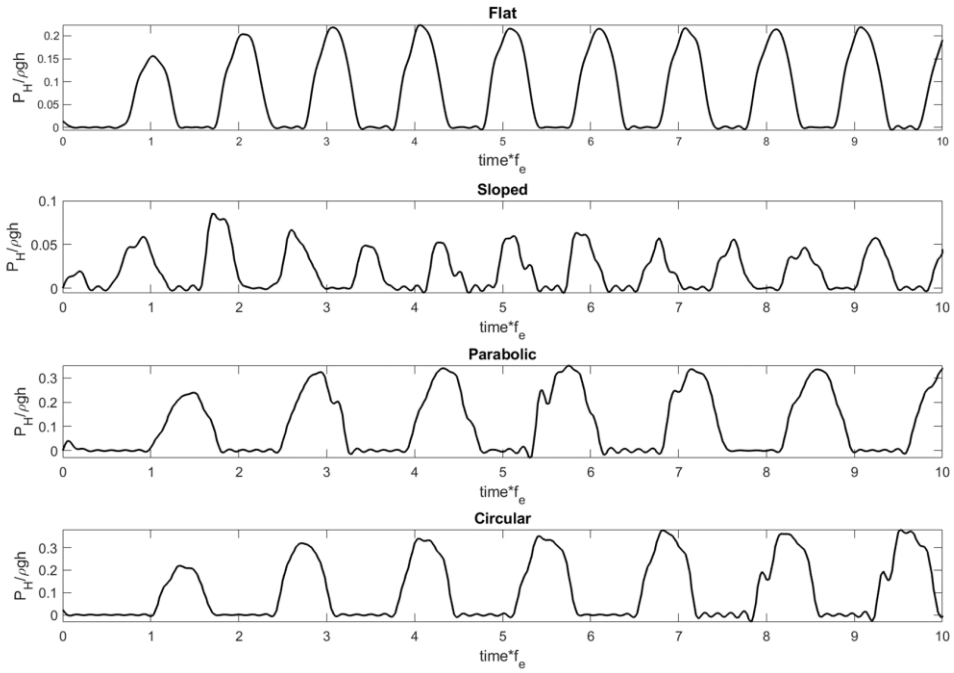

Figure 3.16 The hydrodynamic pressure time history for constant fluid height to free surface fluid length ratio m_w=100kg, $X_0 = 0.44/(\omega_1)^2$, β=1.0

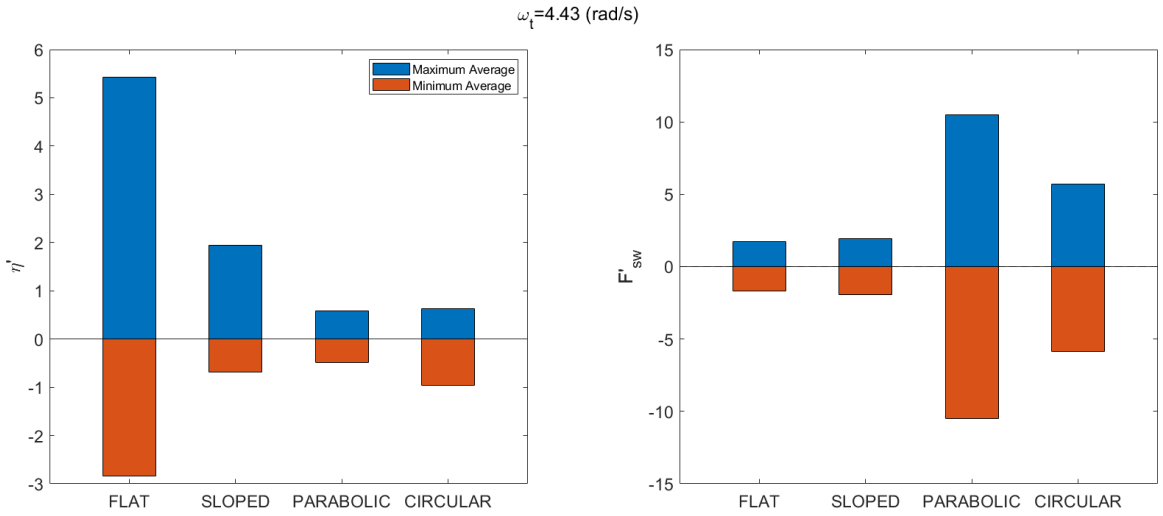

Figure 3.17 Maximum and Minimum response of the normalized wave heights and sloshing forces at a constant targeted frequency m_w=100kg, $X_0 = 0.44/(\omega_1)^2$, β=1.0.

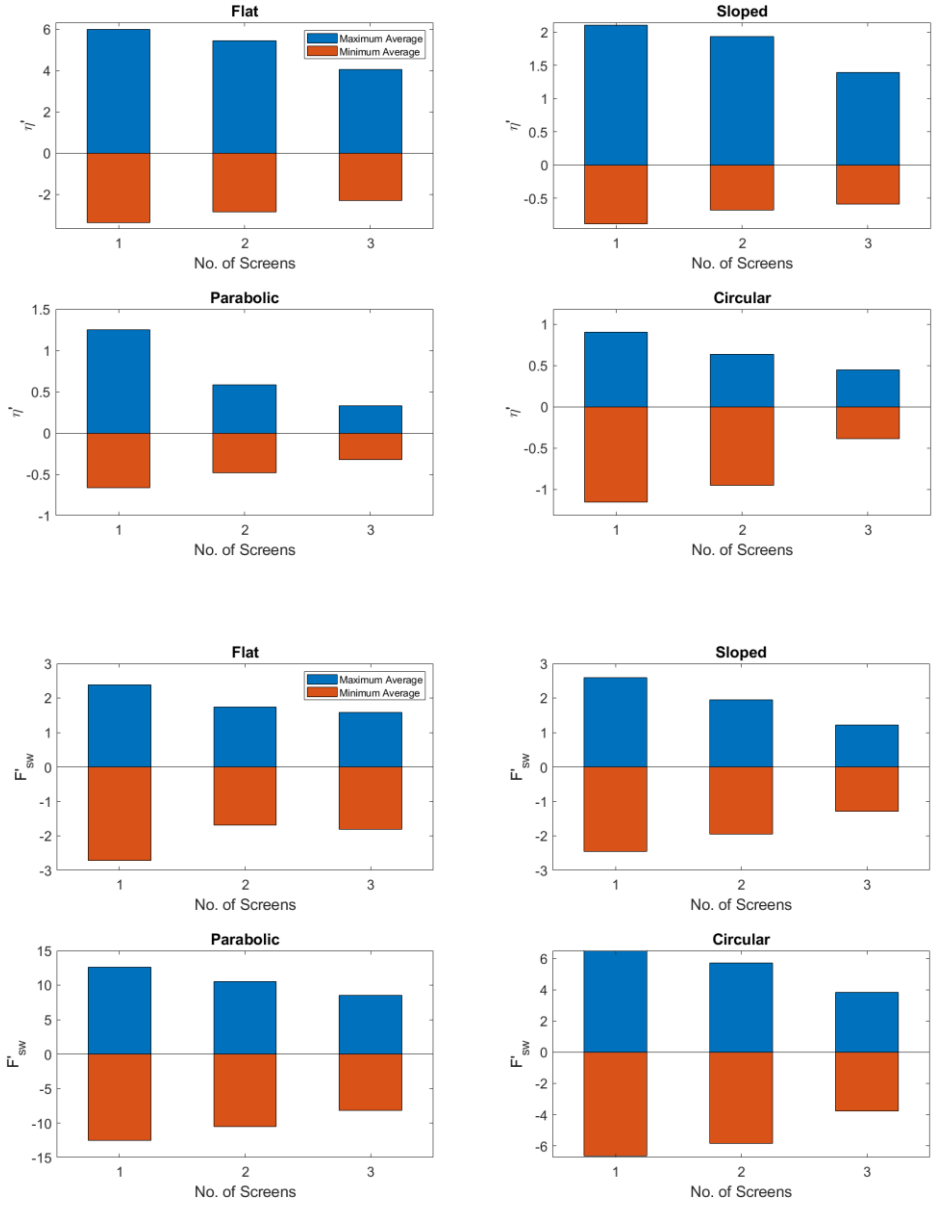

Figure 3.18 Maximum and Minimum response of the normalized wave heights and sloshing forces for different number of screens. m_w=100kg, $X_0 = 0.44/(\omega_1)^2$, β=1.0

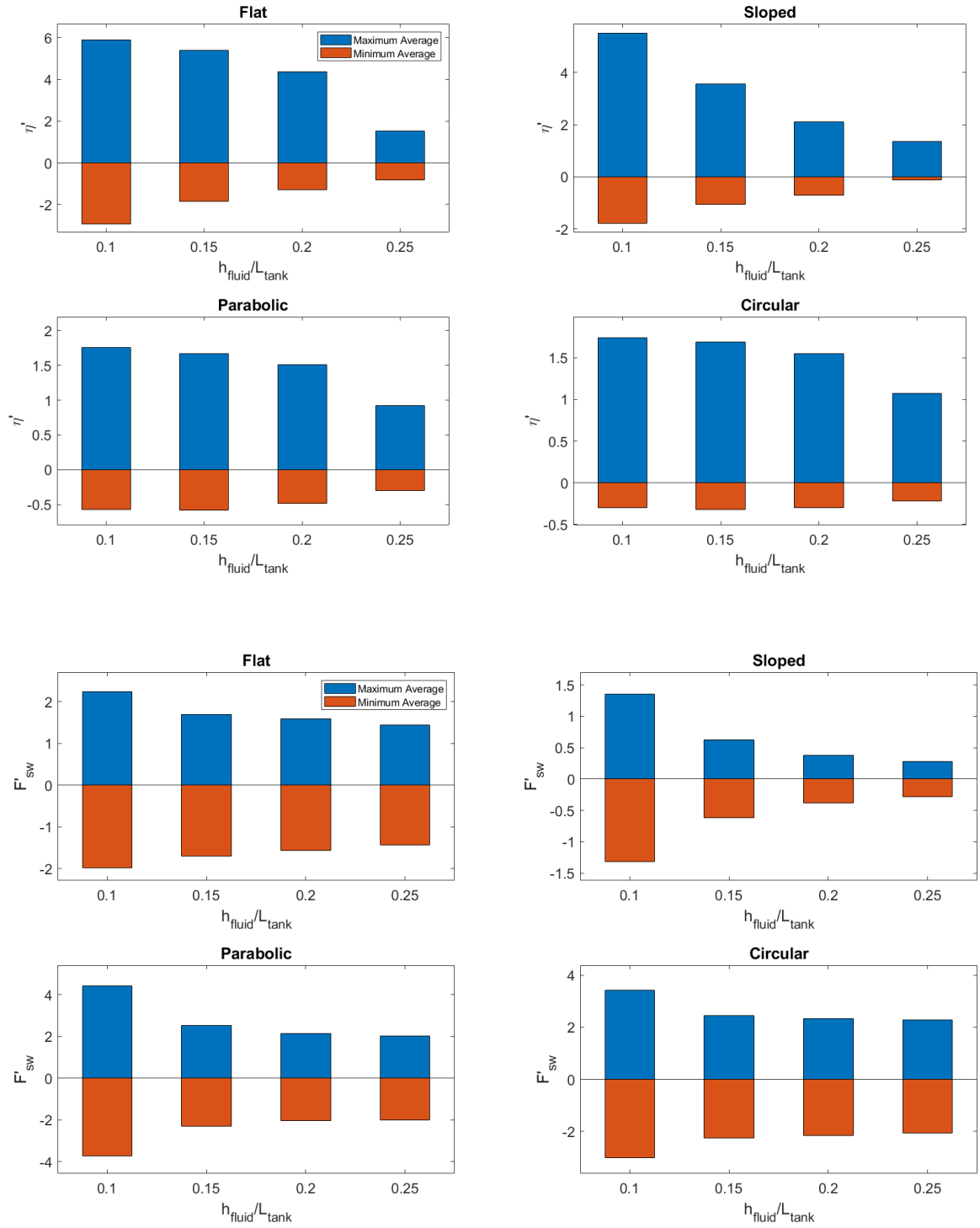

Figure 3.19 Maximum and Minimum response of the normalized wave heights and sloshing forces for different fluid depths. $X_0 = 0.44/(\omega_1)^2$, β=1.0

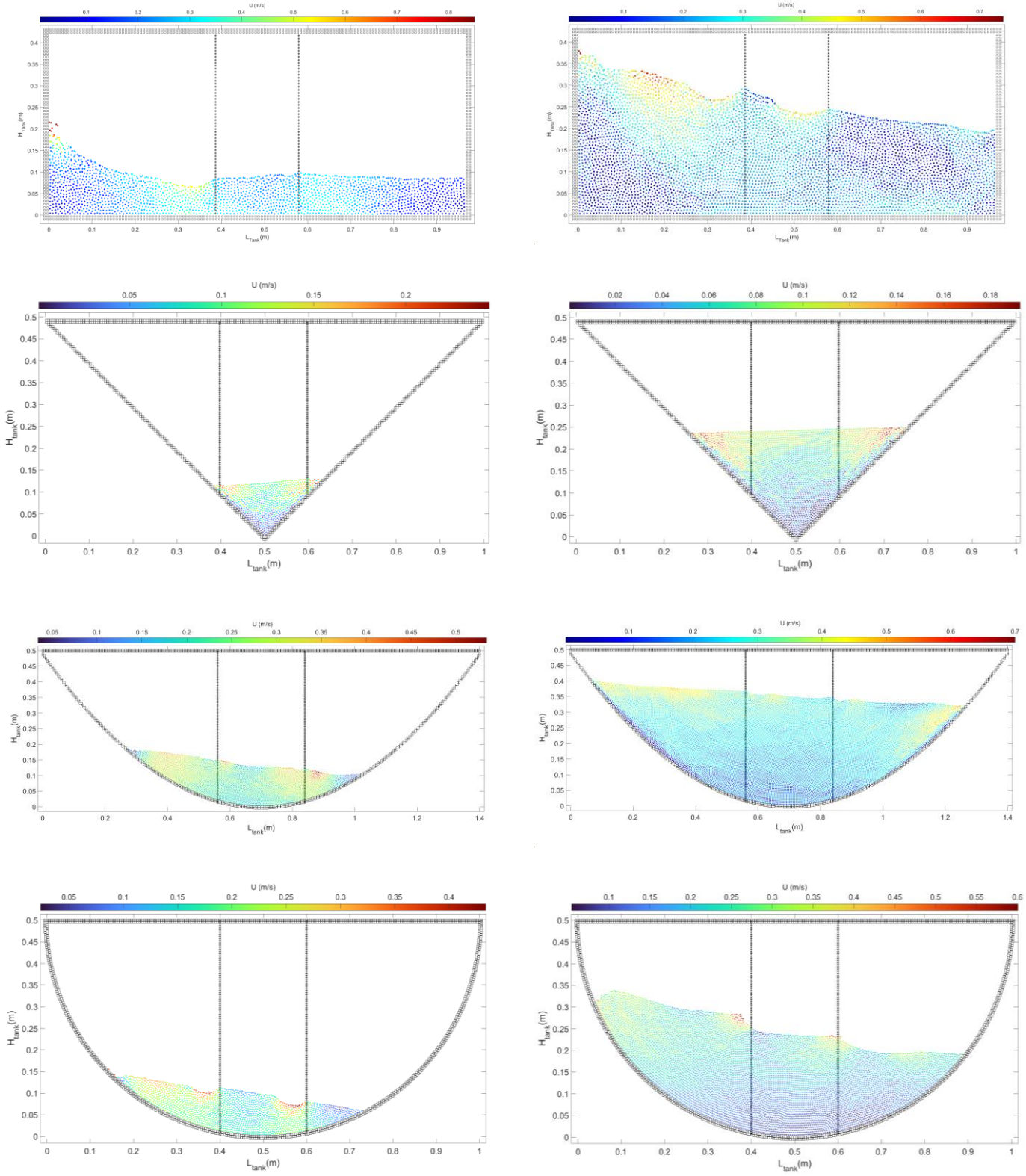

Figure 3.20 Snapshots of the SPH velocity magnitude distribution. $X_0 = 0.44/(\omega_1)^2$, β=1.0

Chapter 4: NUMERICAL MODELLING OF DUAL FUNCTION TANKS FOR FIRE SUPPRESSION AND TUNED LIQUID DAMPER APPLICATIONS

Bishoy N. Awad[a*], Michael J. Tait[a], J.S. Love[b,a]
[a] McMaster University, 1280 Main Street West, Hamilton, ON, Canada L8S 4L8
[b] Motioneering Inc. 600 Southgate Drive, Guelph, ON, Canada N1G 4P6
*Corresponding Author, e-mail: bawad@mcmaster.ca, +1(905)-962-5200

Abstract

Exceeding serviceability limits due to wind-induced motions in tall buildings can cause discomfort for residents and adversely affect auxiliary building services, such as elevator operations. A tuned liquid damper (TLD) is an attractive type of dynamic absorber because of its simplicity and affordability. However, its dimensions and geometry can be limited by available floor space. Utilizing dual-purpose water tanks for damping and fire suppression purposes can be a feasible resolution to fire code requirements and building motion control. Several design criteria need to be considered to accommodate the fire code requirements and the proper tuning of the TLD. Consequently, in this study, a TLD tank is fitted with a perforated floor to divide into two compartments that allow water transmission to meet fire code requirements. However, the sloshing motion within the tank is complex and computationally expensive to capture when using traditional simulation models. This chapter presents a 2D ISPH code equipped with a macro-level model to capture the effect of the perforated floor on the overall sloshing response of the tank. The model is first evaluated using existing results from previous studies on tanks with horizontal baffles. Next, the ISPH model is used to numerically model the perforated floor using the Ergun resistance (ER) macro-level model. In addition, the perforated floor is also explicitly micro-level modelled using rigid boundary particles to validate the proposed ER model. A

numerical analysis is then conducted under different excitation amplitudes and frequencies, presenting both time history and frequency response results. A structure-TLD model is subsequently used to capture the structure-TLD system response under random excitation. Results show that the ER model can efficiently model tanks with dual functions under harmonic and random excitation and across a wide range of amplitudes and frequencies, with appreciable computational time savings.

Keywords: 2D Incompressible Smoothed particle Hydrodynamics (ISPH), Tuned liquid damper (TLD), Screens, Macroscopic modelling, Ergun equation, tank geometries, curved boundary conditions.

4.1 Literature Review

Modernization of building technologies and the invention of lightweight materials have enabled the construction of increasingly tall buildings in metropolitan areas. Due to their low inherent damping and flexibility, modern tall buildings are susceptible to serviceability issues when subjected to wind loads [1]. Wind-induced building sway can impact occupant comfort, elevator operations, damage the façade, etc. [2]. Thus, various measures have been investigated to reduce wind-induced motion with the goal of obtaining economic buildings for property developers and comfort for occupants [3]. These measures have included aerodynamic improvements to the building to reduce wind-induced forces by using tapered geometry, softening the corners to reduce drag, and inclusion of openings or floor cut-outs to allow wind to pass through. However, these techniques may not always be applicable or aesthetically acceptable [4]. Other measures involve modifying the building design to change its mass or stiffness to shift the natural frequency; however, this can lead to increased material costs [5]. Alternatively, auxiliary damping devices have been successfully employed to effectively reduce the resonant response of tall buildings [3].

Implementation of tuned mass dampers (TMDs) and tuned liquid dampers (TLDs) has become increasingly common in tall buildings as they are simple, effective, have low maintenance and operation costs, and do not drastically modify the architectural design [1]. In addition to its simplicity, ease of tuning, and low maintenance costs [5], a TLD, also known as a tuned sloshing damper (TSD), can be implemented using the building water supply tank with minimal alterations. This can be achieved by dividing the tank into

connected compartments to simultaneously serve as a fire suppression water reserve tank(s) and an auxiliary damping system, which is an attractive option for building owners.

Nanda [6] has proposed utilizing the water inside the water storage tank to serve as an auxiliary damping system and water storage for fire suppression, given that both the TLD and fire suppression tanks are typically located near the top of the building. However, combining these two functionalities is often challenging due to conflicting dimensional requirements for TLD and fire suppression tanks [6].

Employing dual-function tanks can save a significant amount of floor space; however, strict fire codes set requirements that interfere with the design of a TLD [5]. A ubiquitous design challenge is satisfying the conflict between the desired water depth of the TLD, and the minimum water volume required for fire suppression within the available floor space. Since the final tuning of the TLD depends on the as-built frequencies measured after project completion, the water depth needed for optimal tuning of the TLD is not always accurately known at the early stages of the project. Conversely, fire requirements for the minimum volume of water needed are known and fixed, which presents a potential conflict and risk for the design of these dual-purpose tanks. To achieve this dual functionality, tank design requires considering the minimum water volume required for fire, conforming to space limitations, and adjusting the water depth to tune the TLD.

TLDs have been extensively studied both experimentally and numerically to better understand the response of their behavior under regular and irregular excitations [7–11]. Studies have investigated TLD performance and improvements that can be attained by adding baffles [12–15], using different tank geometries [16–19], adding damping devices

as screens [20–23] and introducing perforated floors to divide the tank into several compartments [24].

One potential solution is to employ a dual-function tank with a perforated floor [24]. The tank is designed to have the minimum water depth required by fire codes (shown in Figure 4.1), and the addition of a perforated floor (with some holes) enables the water above the perforated floor to be tuned to the natural frequency of the building. The perforated floor has sufficient openings (perforations) to maintain the minimum flow required and the total water volume needed for fire suppression. Modelling the proposed dual use TLD is challenging as it must capture the sloshing motion above the perforated floor and its interaction with the water below the perforated floor. Moreover, the model must accurately describe the fluid response during low excitation amplitudes associated with common wind events and high amplitude excitations to determine loads during design-level wind and seismic events [25].

It can be challenging to use traditional grid-based methods to simulate complex fluid motion that includes wave breaking and high turbulence [26], which often require complex and computationally expensive modelling techniques, such as re-meshing, to capture the free surface response [27,28]. Alternatively, the Lagrangian mesh-free Smoothed Particle Hydrodynamics (SPH) method has been used to model large-amplitude free-surface flows for various engineering applications [29]. Several researchers have used the incompressible SPH method to investigate TLD behaviour [30,31]. An ISPH model has been developed using a macro-level screen model utilizing the Ergun equation (ER) model, which captures the pressure loss in porous media. The ISPH, along with the ER model, is an effective

technique for modelling a TLD equipped with a screen and having any tank bottom geometry over a wide range of fluid depths and excitation amplitudes [32]. Macro-level models have been shown to effectively capture the overall effect of damping screens inside the TLD implicitly, without capturing the flow in the immediate vicinity of the screens. For TLD applications where wave heights and overall liquid sloshing forces are the main parameters of interest, using macro-level models can significantly reduce the computational memory and time (by approximately a factor of 700) needed to model the screens as they do not require fine particle spacing to capture the geometry of the screen [31]. Similarly, this technique can be adapted to model a perforated floor with holes inside the dual-function tank.

This study focuses on modelling a dual-function rectangular tank fitted with a perforated floor using the ISPH model. The perforated floor with holes and seepage through corners and connections is distributed over the entire length of the tank and modelled as a porous media using the ER model. An ISPH micro-level explicit (ME) model, which simulates the perforated floor as rigid boundary particles with gaps representing the holes, is also developed for comparison/ validation purposes. The ER and MM models are also validated using experimental results of a horizontal baffled tank with different baffle widths from Biswal et al. [13] under sinusoidal base excitation. The ER model is then used to investigate a practical case study of a dual-function tank under different excitation amplitudes and frequencies. The numerical simulations are conducted, and the time response of the wave heights and base force is presented along with frequency response plots of the free surface, sloshing forces and energy dissipation. Finally, the TLD model is

coupled to a single-degree-of-freedom (SDOF) structure to simulate the response of the structure-TLD system under random excitation for different tank configurations.

4.2 Numerical Modelling

4.2.1 SPH Model

The fluid response inside the TLD is modelled using a two-dimensional SPH model based on the incompressible scheme (Cummins & Rudman, 1999). An ISPH model developed in our previous work (Awad & Tait, 2022) uses the Lagrangian form of the Navier-Stokes (NS) continuity and momentum equations as follows:

$$\frac{D\rho}{Dt} + \rho\nabla\mathbf{u} = 0, \tag{4.1}$$

$$\frac{\mathrm{D}\mathbf{u}}{Dt} = -\frac{1}{\rho_0}\nabla P + v_0\nabla^2\mathbf{u} + \mathbf{g} + \frac{1}{\rho_0}\nabla.\boldsymbol{\tau} \tag{4.2}$$

where *D/Dt* is the material derivative, and ρ, v_0, p, $\boldsymbol{u}$, $\mathbf{g}$ are the fluid density, effective kinematic viscosity, pressure, flow velocity vector, and the external force vector (i.e., gravity), respectively (vector quantities are depicted in **bold**). The model uses a turbulence model based on the Smagorinsky eddy viscosity model (Smagorinsky, 1963) to model the sub-particle scale (SPS) stress tensor $\boldsymbol{\tau}$, where

$$\tau = \rho_0\left(2\nu_t S_{ij} - \frac{2}{3}k_t\delta_{ij}\right) \tag{4.3}$$

and the eddy viscosity is calculated as

$$\nu_t = (C_S.d_p)^2.|S| \tag{4.4}$$

where $C_s=0.1$ is the Smagorinsky constant (Gotoh et al., 2001).

The NS equations are discretized into tiny particles evenly spaced at an initial spacing *dp*. Both fluid and boundary particles interact together in a mesh-free domain, where the particle of interest (*i*) properties, such as velocity and pressure, are interpolated from the neighbouring particles (*j*) in the domain Ω using the SPH approximation formula:

$$\mathrm{A}(\boldsymbol{r}_i) = \sum_{j=1}^{N} A(\boldsymbol{r}_j)\frac{m_j}{\rho_j} W\left(|\boldsymbol{r}_i - \boldsymbol{r}_j|, h_k\right) \tag{4.5}$$

where *A* is any fluid property at position $\boldsymbol{r}$, m_j is the particle mass, *W* is the kernel function, and h_k is the smoothing length. Herein, the fifth-order Wendland kernel is used (Wendland, 1995)

$$W(q) = W_c \begin{cases} (1+2q)\left(1-\frac{q}{2}\right)^4 & 0 \le q \le 2 \\ 0 & q \ge 2 \end{cases} \tag{4.6}$$
$$; \; W_c = \frac{7}{4\pi {h_k}^2} \; ; \; q = \frac{|r_i - r_j|}{h_k}$$

where r_i and r_j are the position of the particle of interest and the neighbour particle, respectively. The kernel radius h_k used throughout this study is equal to *1.4dp*.

In the ISPH scheme, incompressibility is enforced through the two-step projection method proposed by Cummins and Rudman (Cummins & Rudman, 1999). In the intermediate step, known as the prediction step, an intermediate velocity ($\boldsymbol{u}^*$) is calculated based on the viscous and body forces only (S. Shao & Lo, 2003)

$$\boldsymbol{u}^* = \mathbf{u}(t) + \Delta \mathrm{t}\left(v\nabla^2\mathbf{u} + \mathbf{g} + \frac{1}{\rho_0}\nabla.\boldsymbol{\tau} + \ddot{\boldsymbol{x}}_s + \boldsymbol{F}_{floor}\right) \tag{4.7}$$

where $\ddot{\boldsymbol{x}}_s$ is the tank acceleration (structural acceleration vector at the location of the TLD), $\boldsymbol{F}_{floor}$ is the drag force from the perforated floor, which will be discussed in more detail in Section 4.2.2. This intermediate velocity is then used to calculate an intermediate value for the position ($\boldsymbol{r}$*)

$$\boldsymbol{r}^* = \boldsymbol{r}(t) + \boldsymbol{u}^* \Delta \mathrm{t} \tag{4.8}$$

The remaining part of the momentum equation, fluid pressure, is solved by an explicit time approach using the Pressure Poisson Equation (PPE) with an additional stabilizing term following Jiang et al. (Jiang et al., 2019) to combine both the divergence-free and density-invariant conditions

$$\nabla^2 p_i = \alpha \frac{\rho_0 - \rho^*}{\Delta \mathrm{t}^2} + (1-\alpha)\frac{\rho_0 \nabla . u^*}{\Delta t} \tag{4.9}$$

where the first and second terms represent the density-invariant effect and the velocity-divergence effect, respectively. Herein, the p_i is the particle pressure, ρ* is the intermediate density, and α is the blending factor taken as 0.01.

The gradient and the Laplacian operators of the NS and PPE equations are solved by equations (4.10) and (4.11), respectively (Monaghan, 1992).

$$(\nabla A)_i = \rho_i \sum_{j=1}^{N} m_j \left(\frac{A_j}{\rho_j} + \frac{A_i}{\rho_i}\right) \nabla_j W_{ij} \tag{4.10}$$

$$\nabla . (\frac{\nabla \mathrm{A}}{\rho})_i = \sum_{j=1}^{N} \left(\frac{8 m_j}{\left(\rho_i + \rho_j\right)^2} \frac{A_{ij} \boldsymbol{r_{ij}} . \nabla_i W_{ij}}{\boldsymbol{r_{ij}^2} + \eta^2}\right) \tag{4.11}$$

Where η is equal to $0.001h_k$ to keep a nonzero value in the denominator. Using these equations, the fluid pressure is solved explicitly in time (Yeylaghi et al., 2016) as

$$p_i(t+\Delta t) = \frac{\sum_{j=1}^{N}\left(\frac{8m_j}{\left(\rho_i+\rho_j\right)^2}\frac{p_j(t)\boldsymbol{r_{ij}}.\nabla_i W_{ij}}{\boldsymbol{r_{ij}^2}+\eta^2}\right)+\left(\frac{-1}{\Delta t}\right)\sum_{j=1}^{N}\frac{m_j}{\rho_j}\left(\boldsymbol{u_j^*}-\boldsymbol{u_i^*}\right)\nabla_j W_{ij}}{\sum_{j=1}^{N}\left(\frac{8m_j}{\left(\rho_i+\rho_j\right)^2}\frac{\boldsymbol{r_{ij}}.\nabla_i W_{ij}}{\boldsymbol{r_{ij}^2}+\eta^2}\right)} \quad \textbf{(4.12)}$$

Finally, the last step of the projection scheme involves using the calculated pressure values to correct the velocity and position values of the particles at the end of each time step as follows (Yeylaghi et al., 2016)

$$\boldsymbol{u}(t+\Delta t) = \boldsymbol{u}^* + \left(-\frac{1}{\rho}\nabla p\right)\Delta t \quad \textbf{(4.13)}$$

$$\boldsymbol{r}(t+\Delta t) = \boldsymbol{r}(t) + \left(\frac{\boldsymbol{u}(t+\Delta t)+\boldsymbol{u}(t)}{2}\right)\Delta t \quad \textbf{(4.14)}$$

The dummy particles method represents boundaries by two layers of boundary particles following Adami et al. (Adami et al., 2012), where their position is fixed in time, and the pressure is solved for each particle at each time step to prevent particles from penetrating through the walls. The boundary velocity is calculated based on a free-slip boundary condition at the interaction between fluid and boundary (i.e., tank walls, rigid intermediate floor) particles throughout the simulation, where the velocity is calculated from the surrounding fluid particles using equation (4.3). The perpendicular and parallel velocities at the boundary interface are reflected and enforced to equal the fluid velocity, respectively. For the free-surface particles, the ISPH scheme enforces the Dirichlet boundary. By

calculating a false density $\rho_n = \sum_{j=1}^{N} m_j W_{ij}$ for all fluid particles, the algorithm detects free surface particles based on kernel truncation if their density falls beyond 90% of the initial particle density and their pressure values are set to atmospheric pressure (Yeylaghi et al., 2016).

4.2.2 Perforated Floor Implementation

The perforated floor has been implemented to divide the tank into two compartments to achieve the minimum water required for fire protection (static zone under the perforated floor) and damping and tuning (active zone above the perforated floor) for the TLD. SPH macro-level models have been used to study submerged objects in TLD applications (McNamara et al., 2021). Previously, the Ergun resistance (ER) model was proposed to model screens inside a TLD and results were found to be in good agreement with experimental results for different fluid depths and excitation frequencies (Awad & Tait, 2022). It has also been shown to be capable of modelling TLDs with different tank bottom geometries under extreme loading events beyond serviceability levels (Awad & Tait, n.d.).

The perforated floor is modelled as a continuous porous media with porosity characteristics corresponding to the areas of holes throughout the floor, between connections, and around corners. The ER model defines the perforated floor particles as dummy particles, allowing the effect of the drag through them to be imposed on the surrounding fluid particles without influencing their velocity or position. Intrinsically, the localized perforated floor details are not captured; however, its influence on the flow is distributed over the entire length of the perforated floor, and the overall floor impact is captured.

To facilitate the permeability model's calculation, the perforated floor's porosity can be approximated as the fraction of the volume of all holes and gaps (V_v) over the total volume (V_t). Assuming a tank width of unity for 2D simulations, the porosity n_w can be calculated as

$$n_w = 1 - Solidity = \frac{A_V}{A_T} \tag{4.15}$$

where A_V and A_T are the total void and floor areas, respectively. Consequently, the permeability of the perforated floor can be calculated using the Karman-Cozeny model as follows (Carman, 1937)

$$K_P = \frac{n_w^3 D_c^2}{150(1 - n_w)^2} \tag{4.16}$$

where K_P is the porous media permeability, and D_c is the characteristic diameter. Herein, D_c is equal to the initial particle spacing *dp*. The formula of the Ergun quadratic law for calculating pressure loss through porous media is adopted (Ergun & Orning, 1949)

$$\boldsymbol{F}_d = \left(\frac{\mu}{K_P} \sum_{\boldsymbol{f}} \overline{\boldsymbol{U}}_{s,j} + \frac{1.75}{\sqrt{150}} \cdot \frac{\rho}{\sqrt{K_P} \cdot n_w^{1.5}} \sum_{\boldsymbol{f}} \overline{\boldsymbol{U}}_{s,j} \left\| \overline{\boldsymbol{U}}_{s,j} \right\| \right) t_{sc} . d_p \tag{4.17}$$

where F_d represents the drag force exerted by each perforated floor particle, μ is the dynamic viscosity of water equals 1.0016 mPa.s, and t_{sc} is the screen thickness. The mean interstitial velocity is calculated as

$$\overline{\boldsymbol{U}}_{s,j} = \sum_{f} \frac{m_f}{\rho_f} \boldsymbol{u_f} W_{jf} \tag{4.18}$$

The Wendland fifth-order kernel function is adopted herein for the perforated floor particle with a kernel radius of hsc equal to 2.5h_k. Finally, the effect of the perforated floor on fluid particles is assumed to be relative to the kernel function and opposite to the summation of the perforated floor drag forces particles in the neighborhood of each fluid particle as follows:

$$\boldsymbol{F}_{floor} = \frac{\left(-\sum_j \boldsymbol{F_d} \frac{W_{jf}}{\sum_f W_{jf}}\right)}{m_j} \tag{4.19}$$

where $\boldsymbol{F}_{floor}$ value is added to the intermediate velocity calculation (equation 4.7) at each time step. Since only the forces are solved for perforated-floor particles and other flow quantities are not solved (i.e., velocity and position), the fluid particles are impacted by the perforated-floor forces only while their positions remain uninterrupted by the perforated-floor particles.

4.2.3 Structure-TLD Interaction Model

The TLD model is coupled to an equivalent SDOF structure (illustrated in Figure 4.2) to represent the structure-TLD interaction model, where the structural acceleration and the base shear force for the TLD are interchanged between the two models at each time step to capture the interaction between the two systems. The SDOF model simulates the response of the building's fundamental sway mode (Sun et al., 1992). The equation of motion of this system is expressed as

$$M_s\ddot{x}_s + C_s\dot{x}_s + K_s x_s = F_e + F_{TLD} \tag{4.20}$$

where M_s, C_s, and K_s are the generalized structure mass, damping and stiffness, respectively. The structure acceleration, velocity and displacement are denoted by $\ddot{x}_s$, $\dot{x}_s$, x_s, correspondingly. The two forces on the right-hand side of equation (4.20) represent the external force applied on the structure F_e and the TLD base shear force, F_{TLD} calculated by the SPH model (Sun et al., 1992).

Since the TLD walls are modelled as fixed boundary particles, the motion of the structure is transferred to the fluid by applying the structural acceleration $\ddot{x}_s$ to the intermediate velocity equation (4.7). The influence of the TLD on the structure is applied through the force F_{TLD}. The force is calculated as follows (McNamara & Tait, 2022)

$$\frac{F_{TLD}}{b} = \sum_j m_j a_{xj} \tag{4.21}$$

where b is the tank width, and a_{xj} is an artificial acceleration for wall particles calculated as (Crespo et al., 2014)

$$a_{xj} = -\sum_f m_f \left(\frac{P_f}{\rho_f^2} + \frac{P_j}{\rho_j^2}\right)\nabla_f W_{jf} + \sum_f \rho_f \nu \left(\frac{8m_f}{\left(\rho_f + \rho_j\right)^2}\frac{(\boldsymbol{u_f} - \boldsymbol{u_j})\boldsymbol{r_{jf}}.\nabla_j W_{jf}}{\boldsymbol{r_{jf}^2} + \eta^2}\right) + \ddot{X} \tag{4.22}$$

The acceleration term is calculated based on the interaction between the boundary and fluid particles in their domain. Further TLD-structure model details have been discussed by McNamara & Tait (2022).

4.3 Model Validation

The existing ISPH and macro-level ER model are first validated, along with the micro-level explicit model (MM), using existing wave height data from Biswal et al. (Biswal et al., 2006) for a horizontal baffled tank (shown in Figure 4.3) with different baffle width ratios L_{baffle}/L_{tank}. The resulting sloshing forces from the ER model are subsequently compared to those from the MM model, having the same tank parameters and baffle width ratios.

4.3.1 Normalized Quantities

For comparison purposes, the results have been normalized. The undisturbed fluid depth is used to normalize wave heights, η

$$\eta' = \frac{\eta}{h_{fluid}} \tag{4.23}$$

The total base shear force (F_w) and sloshing force ($F_{sw} = F_w - \ddot{X}m_w$) are normalized by the maximum fluid inertial force

$$F_w{}' = \frac{F_w}{m_w X_0 \omega_e^2} \tag{4.24}$$

$$F_{sw}{}' = \frac{F_{sw}}{m_w X_0 \omega_e^2} \tag{4.25}$$

where m_w is the water mass, X_0 is the tank sinusoidal displacement amplitude, ω_e is the excitation frequency ($\omega_e = \beta\omega_1$), and $\ddot{X}$ is the sinusoidal base acceleration, which is calculated as

$$\ddot{X}(t) = -X_0 \omega_e^2 sin(\omega_e t) \quad \textbf{(4.26)}$$

for harmonic excitation. The energy dissipated per cycle is normalized by the maximum kinetic energy of the fluid and is defined as

$$E'_w = \frac{E_w}{\frac{1}{2} m_w (X_0 \omega_e)^2} \quad \textbf{(4.27)}$$

where E_w is calculated as

$$E_w = \int_t^{t+T} F_w dx(t) \quad \textbf{(4.28)}$$

(M. J. Tait, El Damatty, Isyumov, et al., 2005).

Finally, time, t, is normalized by the excitation period ($2\pi/\omega_1$), where fundamental sloshing frequency ω_1 for a rectangular tank is given by

$$\omega_1 = \sqrt{\frac{\pi g}{L_{tank}} \tanh\left(\frac{\pi h_{fluid}}{L_{tank}}\right)} \quad \textbf{(4.29)}$$

4.3.2 Horizontal Baffled Tank

A two-dimensional rectangular tank with rigid horizontal baffles is modelled following Biswal et al. (Biswal et al., 2006) to validate the results of the ER and MM models. The tank has a length of 1.0m and fluid depth of 0.5 m and is subjected to a sinusoidal base acceleration with X_0 = 0.002 m and β = 0.995. A horizontal baffle is attached at the tank's ends and placed at a distance of h_{baffle} = 0.1 m from the tank bottom. Figure 4.4 (a-c) shows the wave height time history recorded at the right tank wall for three baffle lengths

L_{baffle}/L_{tank} = 0.4, 0.6 and 0.8, respectively. The MM model had an initial particle spacing dp = 5 mm and approximately 21,000 computational particles. The ER model employed a particle spacing dp = 10 mm, resulting in approximately 5500 particles with n_w = 0.4, 0.6 and 0.8 for L_{baffle} / L_{tank} = 0.4, 0.6 and 0.8, respectively. Even with approximately one-quarter of the particles used and 28% less CPU time, it can be observed from Figure 4.4Figure 4.4 that the ER model results are in agreement with the microscopic model. Moreover, a good agreement can be observed between the ER and MM free surface response results and the non-linear model results from Biswal et al. (Biswal et al., 2006) at different baffle lengths and porosity ratios.

Since the effect of varying baffle width on the sloshing force response was not reported in the literature, the time history of the base shear forces from the ER model is validated against the results from the MM model. The normalized sloshing forces for L_{baffle}/L_{tank} = 0.4, 0.6, and 0.8 are plotted in Figure 4.5 (a-c), respectively. It is observed that the results from the ER model are in agreement with the MM model for the porosity ratios considered. The overall agreement between the model results shows that the ER model can model the baffles with openings as a continuous porous media and capture its effect on the flow at different porosity ratios corresponding to different opening lengths.

4.4 Dual-purpose Tank Analysis and Discussion

A 2D dual-purpose rectangular tank is investigated with a perforated floor that partially divides the tank into two compartments, as illustrated in Figure 4.1, where the upper section is partially filled with water and can slosh freely under external excitation. The water in the lower section is confined by the perforated floor, limiting its motion; however, it allows

water to flow from one section to another, ensuring that the volume needed for fire protection is maintained. This design allows the TLD to be tuned by adjusting the perforated floor height while preserving the minimum water required for fire suppression.

The following section investigates a rectangular tank with the dimensions summarized in Table 4.1. The tank is fitted with a perforated floor placed at h_{floor} = 0.8 m from the tank bottom and is equipped with three holes. The ER method is used to macro-level model the perforated floor as continuous porous media, with a pore ratio equal to the area of the total holes distributed over the entire perforated floor. Gaps at corners and between connections are assumed to be 5 mm wide. Assuming a tank width of unity in 2D, the porosity for the ER simulations is calculated as n_w = 0.87 in this study.

4.4.1 Perforated-floor Tank Analysis

4.4.1.1. Convergence Study

A convergence study was conducted to evaluate the particle resolution necessary to satisfy boundary condition requirements and study the effect on simulation convergence and time. Four ER simulations were run for 120 seconds under an amplitude excitation X_0/L_{tank} = 0.005 at β = 1.0. The simulations considered four particle spacings (dp = 15 mm, 10 mm, 7 mm, and 5 mm) for testing and comparing the performance with respect to particle spacing and simulation time needed to model the perforated floor tank. As shown in Figure 4.6, the number of particles migrating through the tank wall at the end of each simulation is indicated next to each simulation, showing that the simulations with 10 mm $\leq dp \leq$ 5 mm converged with all the particles intact. However, a significant difference in simulation time and particle numbers is observed between the resolutions. The ER

calculated wave heights and base forces time history are compared in Figure 4.7. For dp < 7 mm, similar wave heights and base forces are calculated with approximately double the CPU time required for dp = 5 mm compared to dp = 7 mm. Thus, dp = 7 mm is selected for all ER model simulations in this study.

4.4.1.2. Response History Results

For both the ER and MM models, two selected excitation amplitudes, X_0/L_{tank} = 0.005 and 0.031 are selected to investigate the fluid response at relatively low and high excitations. For comparative analysis, the perforated floor is modelled explicitly as rigid boundaries using the MM model, and a particle spacing dp = 7 mm has been used. Figure 4.8 shows the computed normalized wave height and sloshing force response for the ER and MM models at X_0/L_{tank} = 0.005 at resonance (β = 1.0). It can be observed that the ER model results are slightly less than the peak and trough wave height and sloshing fluid force values predicted by the MM model. Figure 4.9 shows that the ER model results were slightly greater than the peak and trough values of the wave heights and sloshing fluid forces predicted by the MM model at β = 1.2. Figure 4.10 and Figure 4.11 show the time history results of both models for X_0/L_{tank} = 0.031 at β = 1.0 and β = 1.2, respectively. The normalized wave height and sloshing shear force response simulated by the ER model agree with the MM model at both resonance and non-resonance frequency ratio values.

Overall, it can be observed that the wave forms generated by both models are in agreement for different excitation amplitudes and frequency ratio values. Furthermore, the ER model simulation time was completed in 9 hours and 15 minutes (8628 particles)

compared to 38 hours and 48 minutes (16244 particles) of simulation time needed for the MM model.

4.4.1.3. Frequency Response Results

This section presents frequency response results to assess the model performance at different excitation amplitudes and frequencies. The maximum and minimum wave height and sloshing force values and dissipated energy across 40 frequency values from $\beta = 0.8$ to $\beta = 1.2$ have been calculated for two excitation amplitudes.

Figure 4.12 shows the frequency response for an excitation amplitude of $X_0/L_{tank} = 0.005$, where the ER model is observed to predict lower peak wave heights, sloshing forces, and dissipated energy values near resonance relative to the MM model. Figure 4.13 shows the frequency response for the perforated floor tank corresponding to $X_0/L_{tank} = 0.031$. The ER models show closer agreement near resonance with the model at this amplitude. Overall, an agreement is observed between both models at both excitation amplitudes.

As shown in Figure 4.14, the sloshing wave generated at $X_0/L_{tank} = 0.031$ (bottom figure) is approximately double the height of the wave generated by $X_0/L_{tank} = 0.005$ (top figure), resulting in higher impact pressure of the tank wall and greater sloshing forces and energy dissipation compared to the lower excitation amplitude.

4.4.1.4. Effect of the Perforated Floor on Sloshing

A tank without a perforated floor (TLD) is simulated with SPH and compared to the tank with a perforated floor (PF) at different amplitudes (i.e., $X_0/L_{tank} = 0.005$ and 0.031), and frequencies (β) range from 0.75 to 1.25. A rectangular tank geometry was tested with length $L_{tank} = 19.5$ m and $h_{fluid} = 2.9$ m to simulate the free-sloshing part in the tank with a

perforated floor. A time history of the simulated wave heights and sloshing forces near resonance (β = 1.01), shown in Figure 4.15, presents significantly lower wave heights and sloshing forces amplitude at X_0/L_{tank} = 0.005 for the tank with the perforated floor than without the false floor. It can be observed from Figure 4.16 that similar amplitudes between the two tanks at high amplitudes (i.e., X_0/L_{tank} = 0.031). A reason for the greater discrepancy at the lower excitation amplitude is due to the significantly greater energy dissipation (damping) provided by the perforated floor. At the higher excitation amplitude, energy is dissipated as a result of wave breaking, leading to greater energy dissipation than that provided by the perforated floor.

The variation of the frequency response by both tanks is illustrated in Figure 4.17 and Figure 4.18. It can be observed that the maximum values of free surface elevation, sloshing forces and energy dissipation decreased significantly due to the perforated floor at X_0/L_{tank} = 0.005. Moreover, the peaks are shifted from β = 1.05 in the tank without the perforated floor to β = 0.95 for the tank with the perforated floor. By increasing the excitation amplitude, Figure 4.18 shows that the tank with the perforated floor exhibited a slightly higher sloshing response near resonance than the tank without a perforated floor. At both amplitudes, it can be observed that the peak locations for wave heights and sloshing forces are shifted due to the presence of the perforated floor, indicating the influence of both the perforated floor on the sloshing and the 0.8 m of water below the perforated floor having on the overall sloshing response.

4.4.2 Structure-TLD System Analysis

4.4.2.1. Structure Excitation Signal

A one-hour length signal of a random excitation force, F_e, is applied to the structure without the TLD (shown in Figure 4.2), resulting in a mean-peak hourly response acceleration $\hat{a}_{hourly}$ = 10 milli-g (where 1 mill-g is 0.001 of gravitational acceleration). The band-limited white noise signal has a frequency content ranging from 0.05-0.5Hz. Figure 4.19 shows a sample segment of the signal. The signal was subsequently scaled to $\hat{a}_{hourly}$ = 44 milli-g, corresponding to approximately a 100-year return period (M. J. Tait et al., 2008).

4.4.2.2. Test Setup and Results Normalization

The generalized properties of the structure considered in this study are $M_s = 70{,}000$ tons, damping C_s = 1,180,000 N. s/m, and stiffness K_s = 49,600,000 N/m, resulting in a natural frequency of ω_s = 0.134 Hz and the inherent structural damping ratio is set to ζ_s = 1%. Under random excitation, a benchmark case of a structure-TLD system with a TLD is first simulated. The TLD has screens with a solidity ratio of 33.3% and h_{fluid} = 2.9 m, which is optimized based on a linearized system (M. J. Tait, 2008). A second case is selected, considering a tank for fire purposes only where h_{fluid} = 3.7 m is required to accommodate the minimum water capacity needed for fire suppression. As such, this case is modelled as a Fire Reserve Tank (FR) in this study. Additionally, a tank with an intermediate solid floor (SF) is simulated to compare its performance to that of a perforated floor (i.e., containing holes). Table 4.1 summarizes the tank parameters for all four tank cases investigated. The perforated floor tank is also explicitly simulated using the MM to evaluate the ER model performance under random excitation.

The Root-Mean-Square (σ) and the peak (χ) values for the structural displacement and acceleration are calculated as indicators for system performance. A key parameter used to evaluate the performance of the structure is the Mechanical Admittance Function (MAF), which is defined as

$$|H(f)|^2 = \frac{S(f)K_S^2}{S_0(f)} \tag{4.30}$$

where $S(f)$ and $S_0(f)$ are the power spectra of the structural response being studied and the spectra of the applied force, respectively (M. J. Tait et al., 2008). The wave height $H_\eta(f)$ (to compare the fluid response in the tanks) and structural displacement $H_s(f)$ (to determine the effective damping) are both considered in this study. The effective damping parameter ζ_{eff} is used to compare the performance for each structure-tank case and is calculated from the area under the corresponding MAF curves (Vickery et al., 1983).

4.4.2.3. Model and System Response

The relative difference between the ER and MM model results of the RMS and peak values of the structural acceleration and displacement for the structure-dual purpose tank are presented in Table 4.2. The ER model showed excellent agreement with the MM model, with an absolute difference of under 3.5% for all values at two excitation levels. Meanwhile, the ER model reduced the simulation time to approximately 30% of that of the MM model.

Figure 4.20 shows the variation of the RMS of the structural acceleration (upper plots) and the RMS of the wave height response (lower plots) at both amplitudes. The RMS of the accelerations is normalized by the structure-only response accelerations for comparison

purposes. At the low excitation amplitude, it can be observed that the TLD has the best performance as the screen solidity was selected for this response amplitude. The behavior of the perforated floor tank possesses similar performance to the TLD. The fire reserve tank (FR) resulted in the highest structural response acceleration and wave height response at this amplitude.

At the higher excitation amplitude, the perforated floor tank was observed to have a higher performance level than the TLD tank, and the free surface fluid response was lower than that of fluid in the TLD tank. The solid floor tank also exhibited improved performance at the higher excitation amplitude; however, the free surface fluid response was significantly greater than that of the perforated floor and TLD tank cases. It can be observed that the perforated floor tank exhibited acceptable performance at both excitation amplitudes while limiting the wave height response (and required tank height) due to the added damping from the perforated floor.

The square modulus of the MAF for the structural displacement and the wave heights are presented in Figure 4.21 and Figure 4.22, respectively. The blue dashed line shows the structure's response without a tank, represented by a single sharp peak indicating its comparatively low damping level. However, the four cases involving the coupling of a partially filled tank connected to the structure result in lower peak values and, in some cases, multiple peak values. For the case of the TLD tank at the low excitation amplitude, double peaks can be observed in Figure 4.21(a), indicating a well-tuned and damped TLD. The behaviour of other tanks in Figure 4.21(a) shows that they are not as well-tuned or damped as the TLD. At the higher excitation amplitude (i.e., $\hat{a}_{hourly}$ = 44 milli-g), a single

peak is visible in Figure 4.21(b) for the FR, PF and TLD tanks, which indicates that the tanks are less effective and/ or have more than optimal damping. On the other hand, the SF tank showed improved performance over the other tanks at the high excitation amplitude, which comes at the cost of a large fluid response amplitude, as visible in Figure 4.21(b) and the inability to provide an adequate supply of water as required by the fire code.

The fluid response, recorded near the end tank wall, is significantly larger for the FR and SF tanks at both excitation amplitudes, as shown in Figure 4.22. The PF tank showed good damping performance at the high excitation amplitude and wave height response control relative to the TLD tank while ensuring adequate water supply through the perforated floor to satisfy fire suppression requirements.

The effective damping for each case is calculated and presented in Table 4.3. Typically, the effective damping of the TLD decreases as the excitation amplitudes increases due to the TLD being optimized for a specific response amplitude (M. J. Tait et al., 2008). A similar reduction of effective damping is observed for the FR tank case; however, the PF and SF tanks achieved higher effective damping values as the excitation amplitude increased. The peak structural accelerations are presented in Table 4.4. The TLD tank had the lowest peak acceleration at both excitation amplitudes.

4.4.3 Results Discussion

Overall, the ER model was found to be in good agreement compared to the MM model results for the PF tank under both harmonic and random excitation. For the amplitudes and frequencies considered, the ER model has shown excellent performance in capturing the sloshing characteristics of the perforated floor at lower computational costs than traditional

micro-level explicit methods. Moreover, the ER model did not show any limitations in capturing the complex flow associated with the free surface deformations for the depth of fluid considered.

The above findings show that the dual-function tanks (i.e., perforated floor tanks) provided similar damping performance compared to the optimized TLD tank. Although the SF tank without the perforated floor exhibited reasonable performance at the higher excitation amplitude, it also had a much higher free surface response amplitude, resulting in a significant amount of water hitting the roof, which could result in potential leakage and may require additional freeboard. Moreover, it does not provide the total water required to meet minimum fire suppression requirements.

4.5 Conclusion

This chapter employed a two-dimensional ISPH code to model a perforated floor dual-purpose tank. Operating as both a water storage tank for fire suppression and a TLD dual-purpose tank can significantly enhance the feasibility of a TLD and save considerable floor space. As such, a water storage tank is divided by a perforated floor into two compartments to accommodate the constraints of the fire code and simultaneously serve as a TLD. Also, the perforated floor is outfitted with holes to allow for sufficient water passage between compartments to meet the fire reserve requirements. Since the two compartments will have limited flow, the tank needs to be investigated extensively to determine its sloshing response.

Dual-function tank research is scarce in the literature, and modelling these tanks using mesh-based methods can be computationally expensive and requires simulation times that

are often impractical, especially to capture the geometry of the holes and seepage around connections and corners. Moreover, the response of a coupled structure-TLD system with a perforated floor has not been investigated. Motivated by these limitations and the potential of a dual-functionality tank, this chapter proposed to utilize ISPH and an ER model to discretize the perforated floor as porous media particles. The significance of this model is that it allows for larger particle spacings, resulting in more feasible simulations and practical computational requirements.

The ER model utilized in this study has shown excellent results in capturing the effect of screens inside the TLD (Awad & Tait, 2022); however, it was never tested on horizontal screens or baffles. As such, the ER model has been validated using the available data from Biswal et al. (Biswal et al., 2006) of a horizontal baffled rectangular tank with different horizontal baffle lengths and from the numerical results obtained from modelling the baffles explicitly (i.e., MM model) as rigid boundaries. Overall good agreement has been obtained using the ER model. Subsequently, a numerical analysis has been conducted on a practical case study of a rectangular tank with a perforated floor excited at different excitation amplitudes over a wide range of frequencies. The model achieved good overall performance when compared to the MM model results at different excitation amplitudes. Additionally, the ER and MM models were coupled to an SDOF structure to investigate the structural response under random excitation. Good agreement was found between the ER and MM models at both low and high excitation amplitudes. The ER model achieved these results and captured the effect of the perforated floor in approximately 30% of the simulation time needed to explicitly model the geometry of the perforated floor (MM

model). The results of the present study indicate that the tank with the perforated floor can act as an effect TLD while meeting fire code requirements over a range of excitation amplitudes. These findings confirm that it is possible to effectively use a dual purpose water tank to serve as both a TLD and fire suppression water storage tank in high-rise buildings.

In summary, the proposed macroscopic model can effectively simulate the liquid sloshing motion inside storage tanks divided by perforated floors. The model can also investigate the behavior of such tanks at serviceability limits and under extreme loading events. Future research should focus on studying different perforation scenarios (e.g., number, locations, dimensions) to optimize the damping performance of the perforated floor TLD.

4.6 Acknowledgement

Financial support has been provided by the Natural Sciences and Engineering Research Council of Canada (NSERC) Grant (RGPIN-2020-06864). This work was made possible by the facilities of the Shared Hierarchical Academic Research Computing Network (SHARCNET: www.sharcnet.ca) and Compute/Calcul Canada (www.computecanada.ca). This study forms a part of an ongoing research program at McMaster University Centre for Effective Design of Structures (CEDS).

4.7 References

[1] Patil GR, Singh KD. Evaluation of Sloped Bottom Tuned Liquid Damper for Reduction of Seismic Response of Tall Buildings. J Inst Eng Ser A 2016;97:385–94. https://doi.org/10.1007/s40030-016-0185-8.

[2] Lawrence G. Griffis. Serviceability limit states under wind load. Eng Journal, Am Inst Steel Constr 1993;30:1–16.

[3] Burton M, Fluid BMT, Abdelrazaq A, Samsung C, Corporation T. Wind-Induced Motion of Tall Buildings : Designing for Occupant Comfort 2015.

[4] Xie J. Aerodynamic optimization of super-tall buildings and its effectiveness assessment. J Wind Eng Ind Aerodyn 2014;130:88–98. https://doi.org/10.1016/j.jweia.2014.04.004.

[5] Kareem A, Kijewski T, Tamura Y. Mitigation of motions of tall buildings with specific examples of recent applications. Wind Struct An Int J 1999;2:201–51. https://doi.org/10.12989/was.1999.2.3.201.

[6] Nanda B. A Review on Applications of Tuned Liquid Dampers in Vibration Control. Adv Civ Eng 2014:183–200.

[7] Fediw AA, Isyumov N, Vickery BJ. Performance of a tuned sloshing water damper. J Wind Eng Ind Aerodyn 1995;57:237–47. https://doi.org/10.1016/0167-6105(94)00107-O.

[8] Xue MA, Zheng J, Lin P. Numerical simulation of sloshing phenomena in cubic tank with multiple baffles. J Appl Math 2012;2012. https://doi.org/10.1155/2012/245702.

[9] Lishi W, Zhuang W, Yuchun L. A SPH simulation on large-amplitude sloshing for fluids in a two-dimensional tank. J Earthq Eng Eng Vib 2013;12:135–42. https://doi.org/10.1007/s11803-013-0157-1.

[10] Green MD, Peiró J. Long duration SPH simulations of sloshing in tanks with a low fill ratio and high stretching. Comput Fluids 2018;174:179–99. https://doi.org/10.1016/j.compfluid.2018.07.006.

[11] Luo M, Koh CG, Bai W. A three-dimensional particle method for violent sloshing under regular and irregular excitations. Ocean Eng 2016;120:52–63.

https://doi.org/10.1016/j.oceaneng.2016.05.015.

[12] Xue MA, Zheng J, Lin P, Yuan X. Experimental study on vertical baffles of different configurations in suppressing sloshing pressure. Ocean Eng 2017;136:178–89. https://doi.org/10.1016/j.oceaneng.2017.03.031.

[13] Biswal KC, Bhattacharyya SK, Sinha PK. Non-linear sloshing in partially liquid filled containers with baffles. Int J Numer Methods Eng 2006;68:317–37. https://doi.org/10.1002/nme.1709.

[14] Akyildiz H, Ünal E. Experimental investigation of pressure distribution on a rectangular tank due to the liquid sloshing. Ocean Eng 2005;32:1503–16. https://doi.org/10.1016/j.oceaneng.2004.11.006.

[15] Guan Y, Yang C, Chen P, Zhou L. Numerical investigation on the effect of baffles on liquid sloshing in 3D rectangular tanks based on nonlinear boundary element method. Int J Nav Archit Ocean Eng 2020;12:399–413. https://doi.org/10.1016/j.ijnaoe.2020.04.002.

[16] Deng X, Tait MJ. Theoretical modeling of TLD with different tank geometries using linear long wave theory. J Vib Acoust Trans ASME 2009;131:0410141–04101410. https://doi.org/10.1115/1.3142873.

[17] Idir M, Ding X, Lou M, Chen G. Fundamental frequency of water sloshing waves in a sloped-bottom tank as tuned liquid damper. Proc 2009 Struct Congr - Don't Mess with Struct Eng Expand Our Role 2009:831–40. https://doi.org/10.1061/41031(341)91.

[18] Agresta A, Cavalagli N, Biscarini C, Ubertini F. Effect of bottom geometry on the natural sloshing motion of water inside tanks: An experimental analysis. Appl Sci 2021;11:1–15. https://doi.org/10.3390/app11020605.

[19] Love JS, Tait MJ. Nonlinear multimodal model for TLD of irregular tank geometry and small fluid depth. J Fluids Struct 2013;43:83–99. https://doi.org/10.1016/j.jfluidstructs.2013.09.009.

[20] Tait MJ, El Damatty AA, Isyumov N. An investigation of tuned liquid dampers equipped with damping screens under 2D excitation. Earthq Eng Struct Dyn

2005;34:719–35. https://doi.org/10.1002/eqe.452.

[21] Hamelin JA, Love JS, Tait MJ, Wilson JC. Tuned liquid dampers with a Keulegan-Carpenter number-dependent screen drag coefficient. J Fluids Struct 2013;43:271–86. https://doi.org/10.1016/j.jfluidstructs.2013.09.006.

[22] Maravani M, Hamed MS. Numerical modeling of sloshing motion in a tuned liquid damper outfitted with a submerged slat screen. Int J Numer Methods Fluids 2011;65:834–55. https://doi.org/10.1002/fld.

[23] Tait M. A Study on Unbonded Fiber - Reinforced Elastomeric Isolators for Improved Performance of Ontario Highway Bridges 2018.

[24] Love JS, D. L, X. D. Tuning fire suppression tanks for tuned sloshing damper applications. 7th World Conf. Struct. Control Monit. Los Angeles Int. Assoc. Struct. Control Monit., 2018.

[25] Love JS, Morava B, Robinson JK, Haskett TC. Tuned Sloshing Dampers in Tall Buildings: A Practical Performance-Based Design Approach. Pract Period Struct Des Constr 2021;26:1–13. https://doi.org/10.1061/(asce)sc.1943-5576.0000582.

[26] Shao JR, Li HQ, Liu GR, Liu MB. An improved SPH method for modeling liquid sloshing dynamics. Comput Struct 2012;100–101:18–26. https://doi.org/10.1016/j.compstruc.2012.02.005.

[27] Liu D, Lin P. A numerical study of three-dimensional liquid sloshing in tanks. J Comput Phys 2008;227:3921–39. https://doi.org/10.1016/j.jcp.2007.12.006.

[28] Liu D, Lin P. Three-dimensional liquid sloshing in a tank with baffles. Ocean Eng 2009;36:202–12. https://doi.org/10.1016/j.oceaneng.2008.10.004.

[29] Monaghan JJ. Smoothed Particle Hydrodynamics and Its Diverse Applications. Annu Rev Fluid Mech 2012;44:323–46. https://doi.org/10.1146/annurev-fluid-120710-101220.

[30] Kashani AH, Halabian AM, Asghari K. A numerical study of tuned liquid damper based on incompressible SPH method combined with TMD analogy. J Fluids Struct 2018;82:394–411. https://doi.org/10.1016/j.jfluidstructs.2018.07.013.

[31] McNamara KP, Awad BN, Tait MJ, Love JS. Incompressible smoothed particle

hydrodynamics model of a rectangular tuned liquid damper containing screens. J Fluids Struct 2021;103:103295. https://doi.org/10.1016/j.jfluidstructs.2021.103295.

[32] Awad BN, Tait MJ. Macroscopic modelling for screens inside a tuned liquid damper using incompressible smoothed particle hydrodynamics. Ocean Eng 2022.

[33] Cummins SJ, Rudman M. An SPH Projection Method. J Comput Phys 1999;607:584–607.

[34] SMAGORINSKY J. General Circulation Experiments With the Primitive Equations. Mon Weather Rev 1963;91:99–164. https://doi.org/10.1175/1520-0493(1963)091<0099:gcewtp>2.3.co;2.

[35] Gotoh, T S, T. S. Sub-particle-scale turbulence model for the MPS method—Lagrangian flow model for hydraulic engineering Title. Comput Fluid Dyn J 2001;9:339–47.

[36] Wendland H. Piecewise polynomial, positive definite and compactly supported radial functions of minimal degree. Adv Comput Math 1995;4:389–96. https://doi.org/10.1007/BF02123482.

[37] Shao S, Lo EYM. Incompressible SPH method for simulating Newtonian and non-Newtonian flows with a free surface. Adv Water Resour 2003;26:787–800. https://doi.org/10.1016/S0309-1708(03)00030-7.

[38] Jiang H, You Y, Hu Z, Zheng X, Ma Q. Comparative study on violent sloshing with water jet flows by using the ISPH method. Water (Switzerland) 2019;11. https://doi.org/10.3390/w11122590.

[39] Monaghan JJ. Smoothed Particle Hydrodynamics. Annu Rev Astron Astrophys 1992;30:543–74. https://doi.org/10.1146/annurev.aa.30.090192.002551.

[40] Yeylaghi S, Moa B, Oshkai P, Buckham B, Crawford C. ISPH modelling of an oscillating wave surge converter using an OpenMP-based parallel approach. J Ocean Eng Mar Energy 2016;2:301–12. https://doi.org/10.1007/s40722-016-0053-7.

[41] Adami S, Hu XY, Adams NA. A generalized wall boundary condition for smoothed particle hydrodynamics. J Comput Phys 2012;231:7057–75. https://doi.org/10.1016/j.jcp.2012.05.005.

[42] Awad BN, Tait MJ. Modelling of Sloped and Curved Bottom Tuned Liquid Dampers with Screens using Smoothed Particle Hydrodynamics. Int J Dyn Control n.d.

[43] Carman PG. Fluid flow through granular beds. Chem Eng Res Des 1937;75:S32–48. https://doi.org/10.1016/s0263-8762(97)80003-2.

[44] Ergun S, Orning AA. Fluid Flow through Randomly Packed Columns and Fluidized Beds. Ind Eng Chem 1949;41:1179–84. https://doi.org/10.1021/ie50474a011.

[45] Sun LM, Fujino Y, Pacheco BM, Chaiseri P. Modelling of tuned liquid damper (TLD). J Wind Eng Ind Aerodyn 1992;43:1883–94. https://doi.org/10.1016/0167-6105(92)90609-E.

[46] McNamara KP, Tait MJ. Modeling the Response of Structure–Tuned Liquid Damper Systems Under Large Amplitude Excitation Using Smoothed Particle Hydrodynamics. J Vib Acoust 2022;144:1–13. https://doi.org/10.1115/1.4051266.

[47] Crespo AJC, Domínguez JM, Rogers BD, Gómez-Gesteira M, Longshaw S, Canelas R, et al. DualSPHysics: Open-source parallel CFD solver based on Smoothed Particle Hydrodynamics (SPH). Comput Phys Commun 2014. https://doi.org/10.1016/j.cpc.2014.10.004.

[48] Tait MJ, El Damatty AA, Isyumov N, Siddique MR. Numerical flow models to simulate tuned liquid dampers (TLD) with slat screens. J Fluids Struct 2005;20:1007–23. https://doi.org/10.1016/j.jfluidstructs.2005.04.004.

[49] Tait MJ, Isyumov N, El Damatty AA. Performance of Tuned Liquid Dampers. J Eng Mech 2008;134:417–27. https://doi.org/10.1061/(asce)0733-9399(2008)134:5(417).

[50] Tait MJ. Modelling and preliminary design of a structure-TLD system. Eng Struct 2008;30:2644–55. https://doi.org/10.1016/j.engstruct.2008.02.017.

[51] Vickery BJ, Isyumov N, Davenport AG. The role of damping, mass and stiffness in the reduction of wind effects on structures. J Wind Eng Ind Aerodyn 1983;11:285–94.

Table 4.1 Tank dimensions

Cases	Symbol	Screens	L_{tank}(m)	h_{fire} (m)	h_{slosh} (m)	h_{fluid} (m)	L_{hole}(m)
Fire Reserve Tank	FR	-	19.6	-	-	3.7	0.8
Solid Floor Tank	SF	-	19.6	0.8	2.9	3.7	0
Perforated Floor Tank	PF	-	19.6	0.8	2.9	3.7	0.8
TLD with Screens	TLD	0.4L, 0.6L	19.6	-	-	2.9	-

Table 4.2 Relative difference between MM and ER simulations for perforated floor simulations

Simulation type	MM		ER		% Diff.	
$\hat{a}_{hourly}$ *(milli-g)*	*10*	*44*	*10*	*44*	*10*	*44*
Property						
$\sigma_{\ddot{X}}$ (m/s^2)	1.68	7.43	1.69	7.45	0.61	0.28
$\chi_{\ddot{X}}$ (m/s^2)	5.66	26.59	5.76	26.66	1.80	0.27
σ_X (m/s^2)	2.31	9.93	2.30	10.17	-0.44	2.46
χ_X (m/s^2)	8.69	37.56	8.38	38.36	-3.50	2.12
ζ_{eff} %	1.55	1.69	1.58	1.70	-1.94	-1.18
Simulation time (CPU hours)	4:56	5:14	3:24	3:38	-31.1	-30.6

Table 4.3 Effective damping of the Structure-TLD system

Cases	ζ_{eff} %	
	$\hat{a}_{hourly}$ =10 milli-g	$\hat{a}_{hourly}$ = 44 milli-g
FR	1.50	0.94
SF	1.53	2.28
PF	1.54	1.97
TLD	2.25	1.81

Table 4.4 The peak response of the structural acceleration

Cases	$\chi_{\ddot{x}}$ (m/s^2)	
	10 milli-g	44 milli-g
STR	10.16	44.75
FR	7.35	31.60
SF	5.26	24.87
PF	5.98	26.10
TLD	5.01	24.67

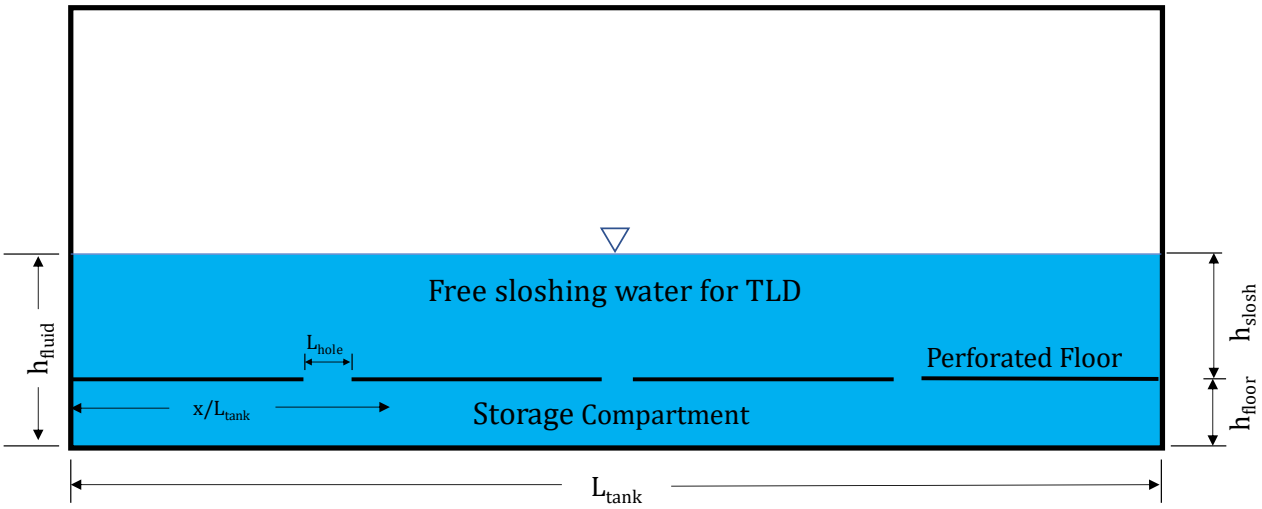

Figure 4.1 Schematic of the TLD with the perforated floor

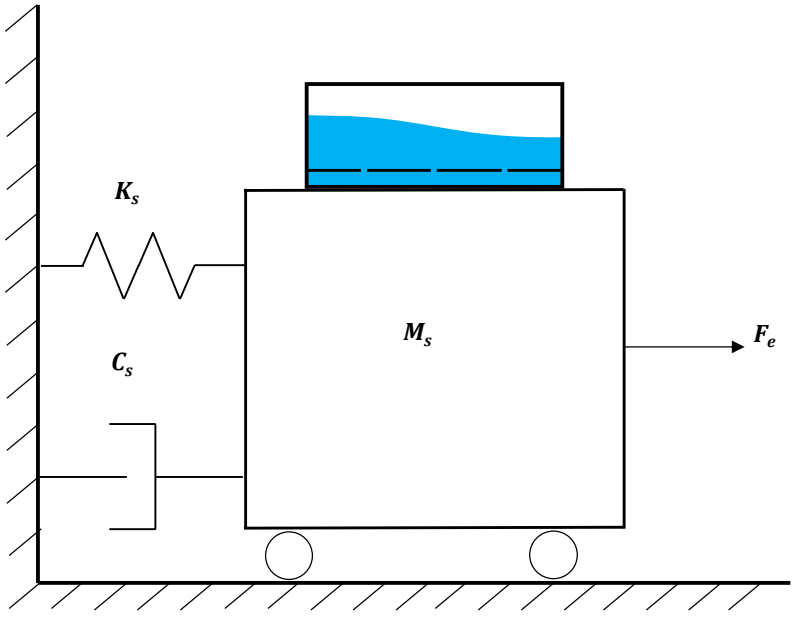

Figure 4.2 Structure-TLD system schematic

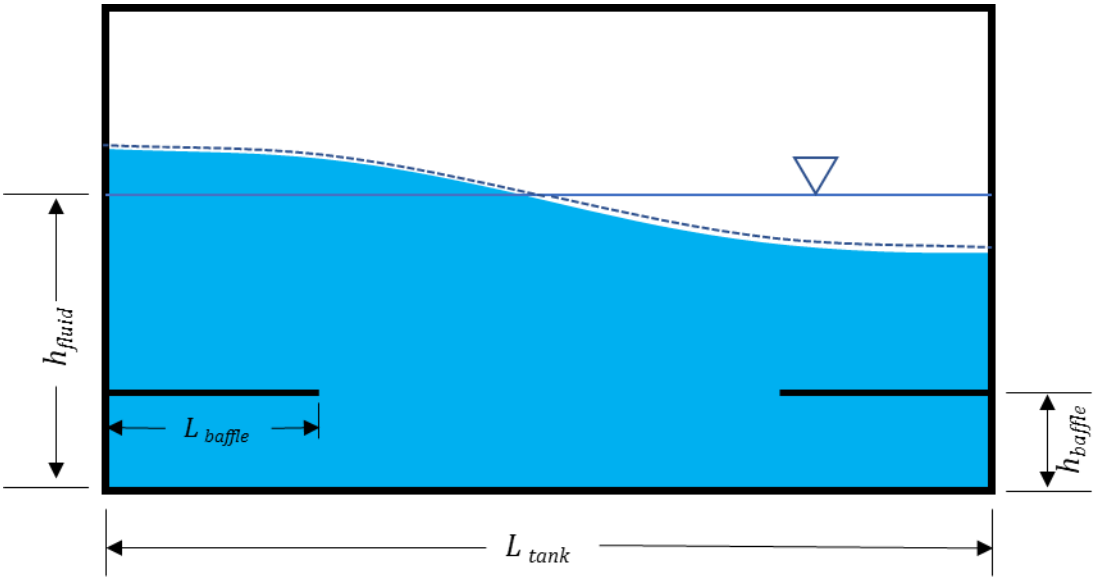

Figure 4.3 Tank with a horizontal baffle at h_{baffle}/h_{fluid} = 0.8. (Biswal et al., 2006)

(a)

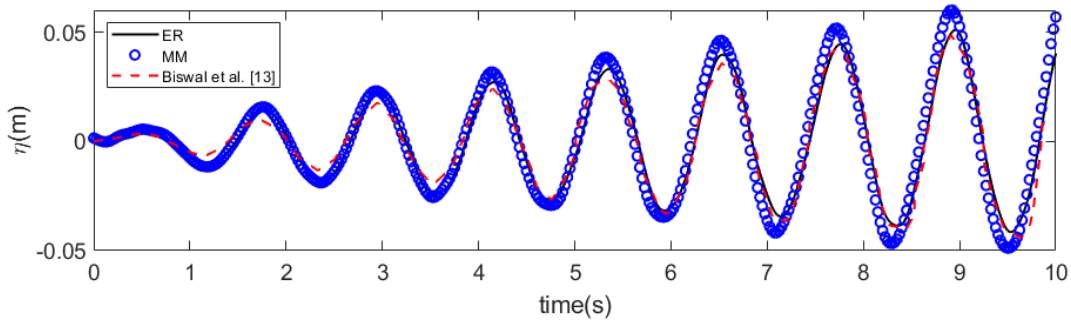

(b)

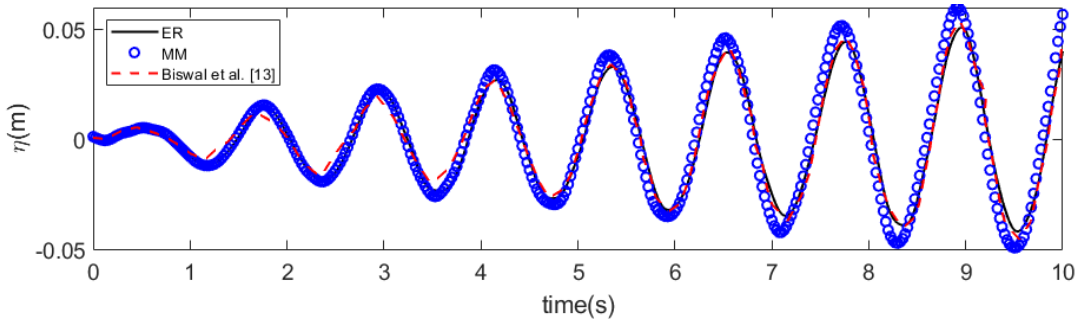

(c)

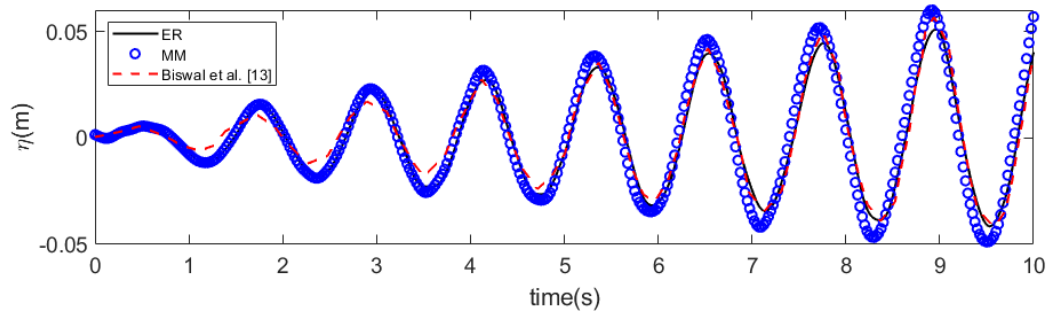

Figure 4.4 Wave heights time history comparison for the baffled tank at X_0=0.002m and β=0.995 for (a) L_{baffle}/L_{tank} = 0.4; (b) L_{baffle}/L_{tank} = 0.6; and (c) L_{baffle}/L_{tank} = 0.8.

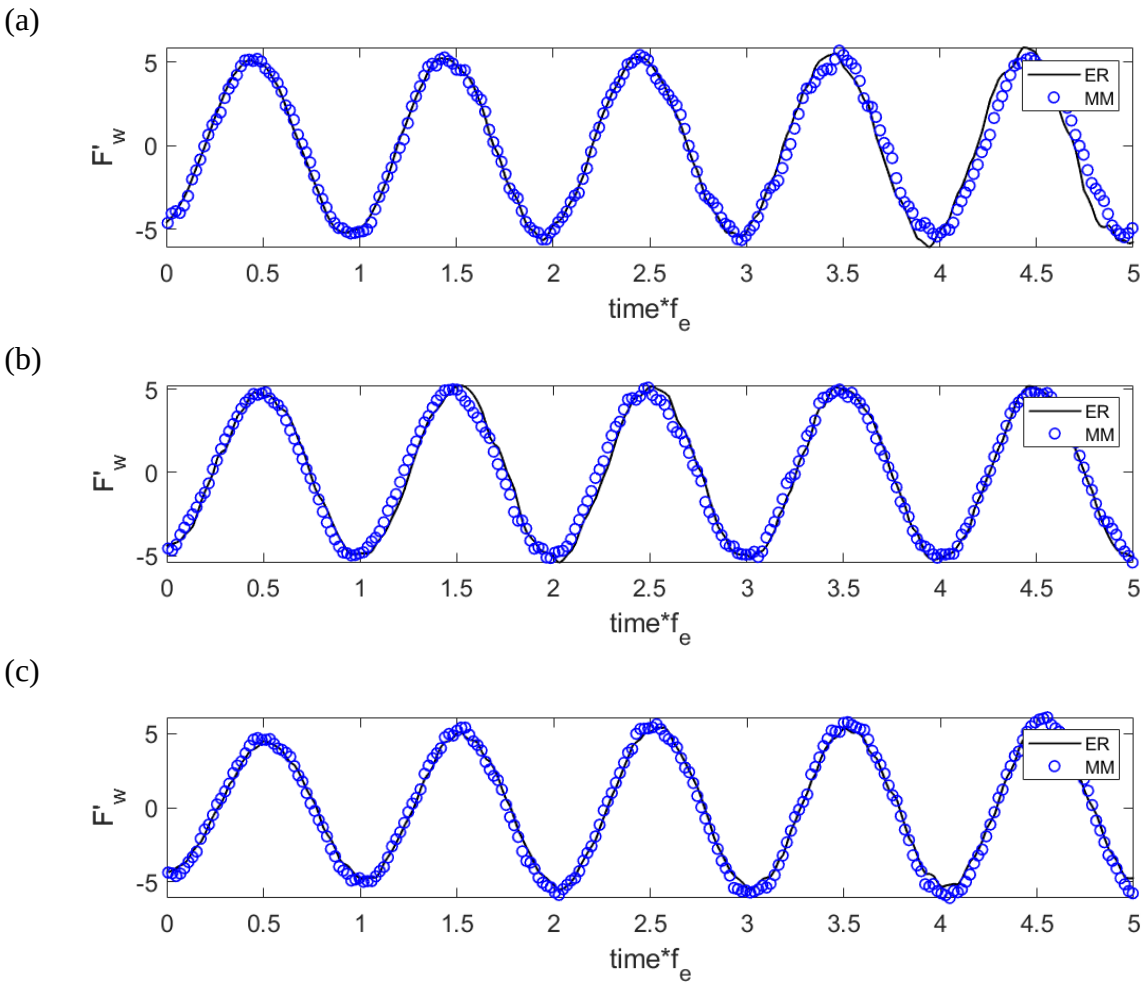

Figure 4.5 Base shear forces time history comparison for the baffled tank at X_0=0.002m and β=0.995 for (a) L_{baffle}/L_{tank} = 0.4; (b) L_{baffle}/L_{tank} = 0.6; and (c) L_{baffle}/L_{tank} = 0.8.

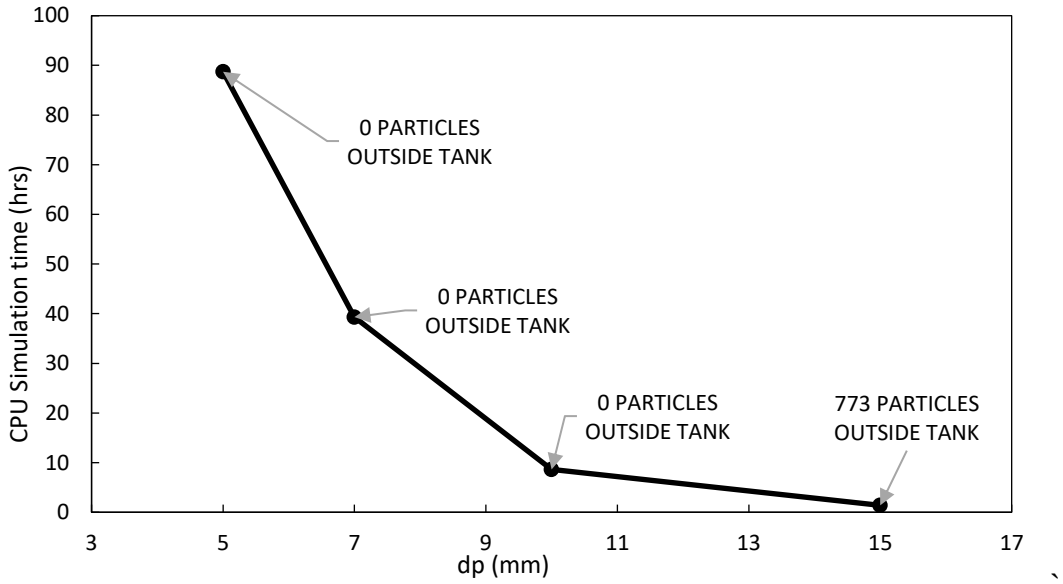

Figure 4.6 Particle resolution sensitivity analysis - 120 (sec), X_0/L_{tank}=0.005 and β=1.0.

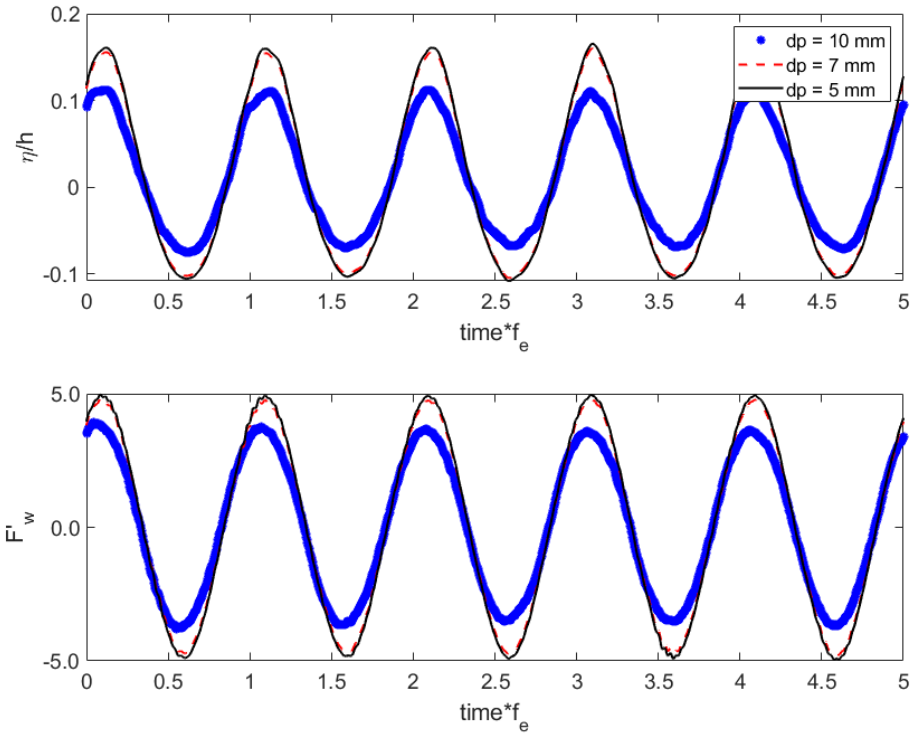

Figure 4.7 ER Simulated wave heights and forces time histories for different particle sizes at X_0/L_{tank}=0.005 and β=1.0.

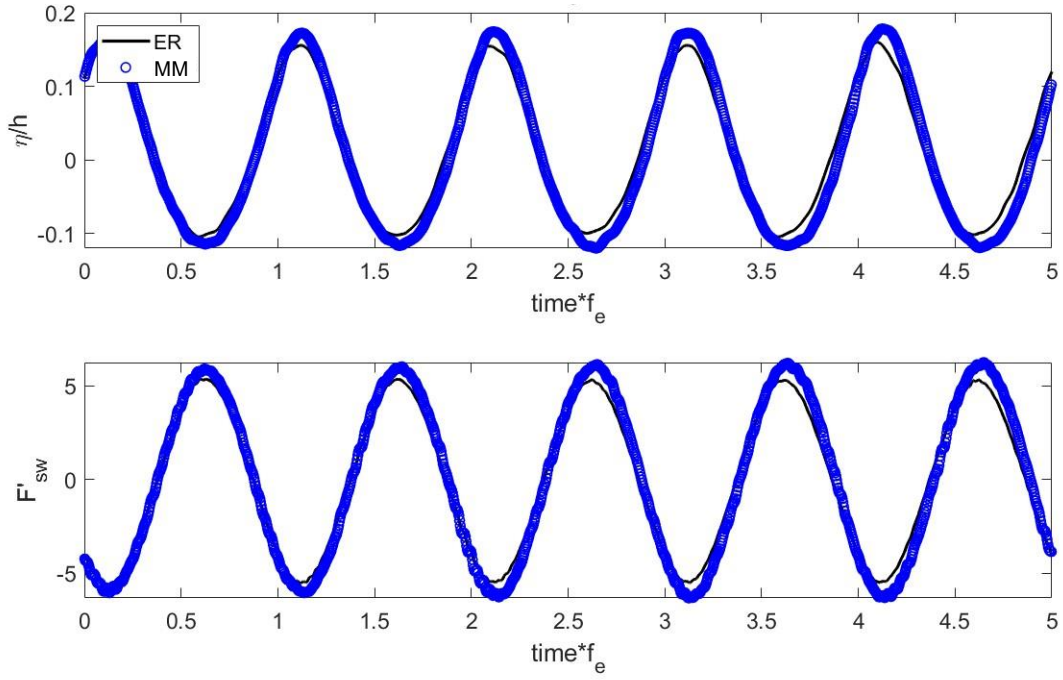

Figure 4.8 ER wave height and sloshing force time history compared to MM model at X_0/L=0.005 and β=1.0.

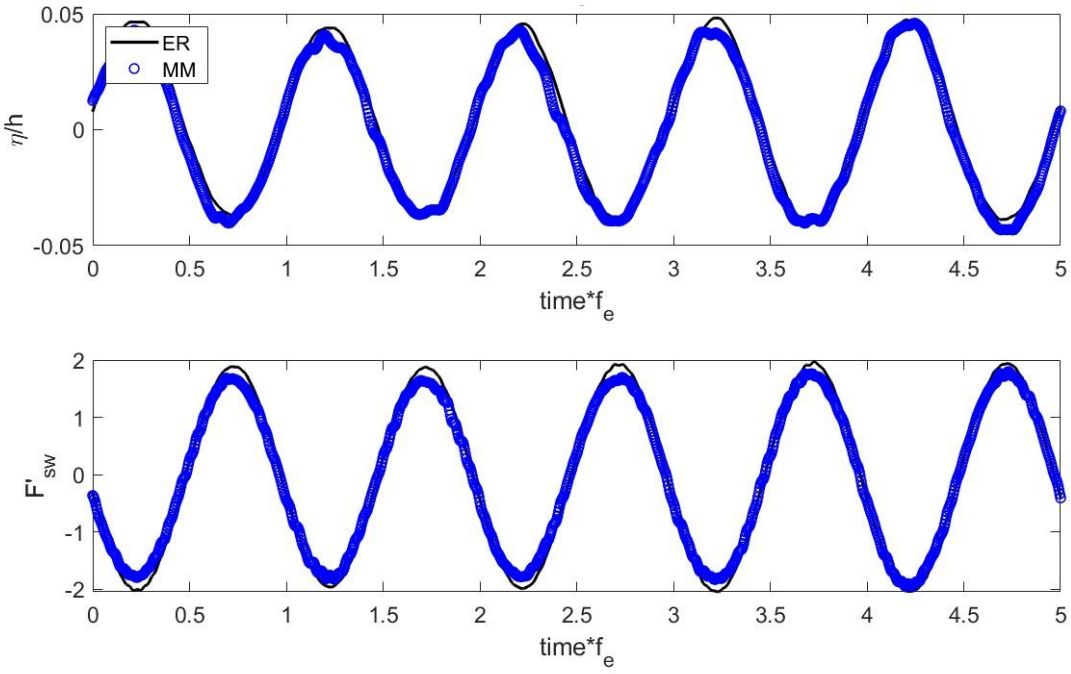

Figure 4.9 ER wave height and sloshing force time history compared to the MM model at X_0/L=0.005 and β=1.2.

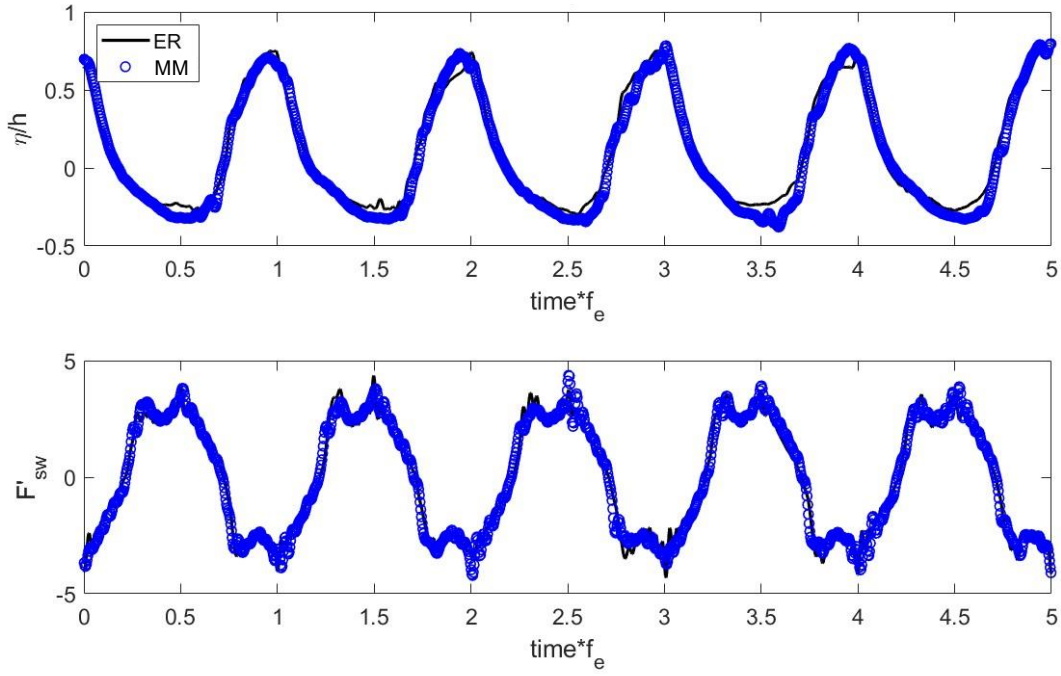

Figure 4.10 ER wave height and sloshing force time history compared to the MM model. X_0/L=0.031 and β=1.0.

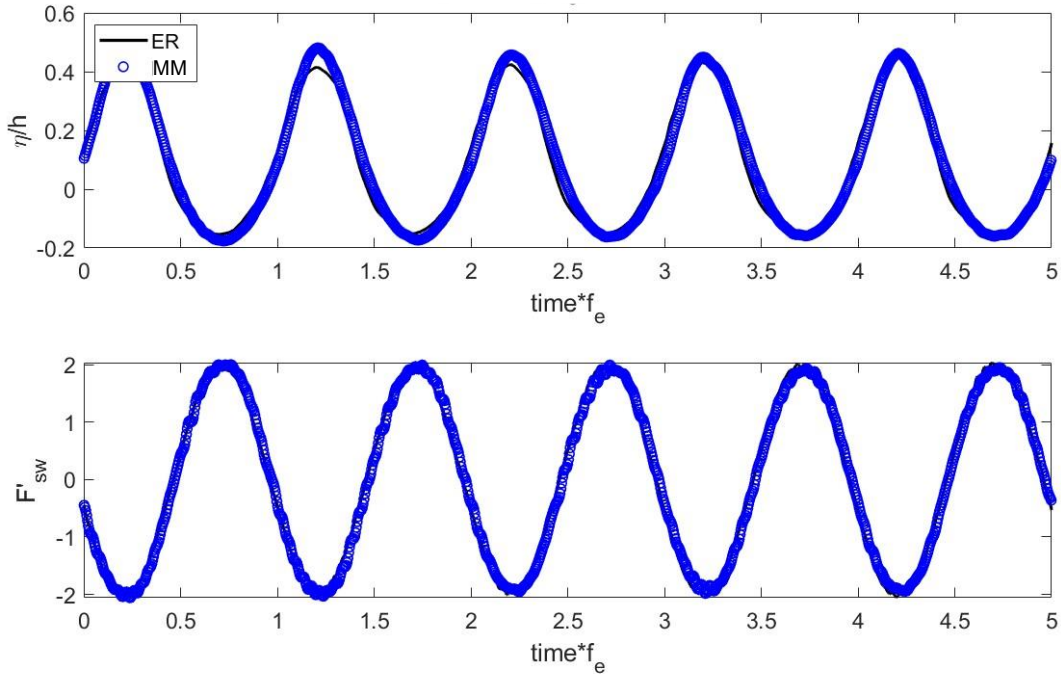

Figure 4.11 ER wave height and sloshing force time history compared to the MM model. X_0/L=0.031 and β=1.2.

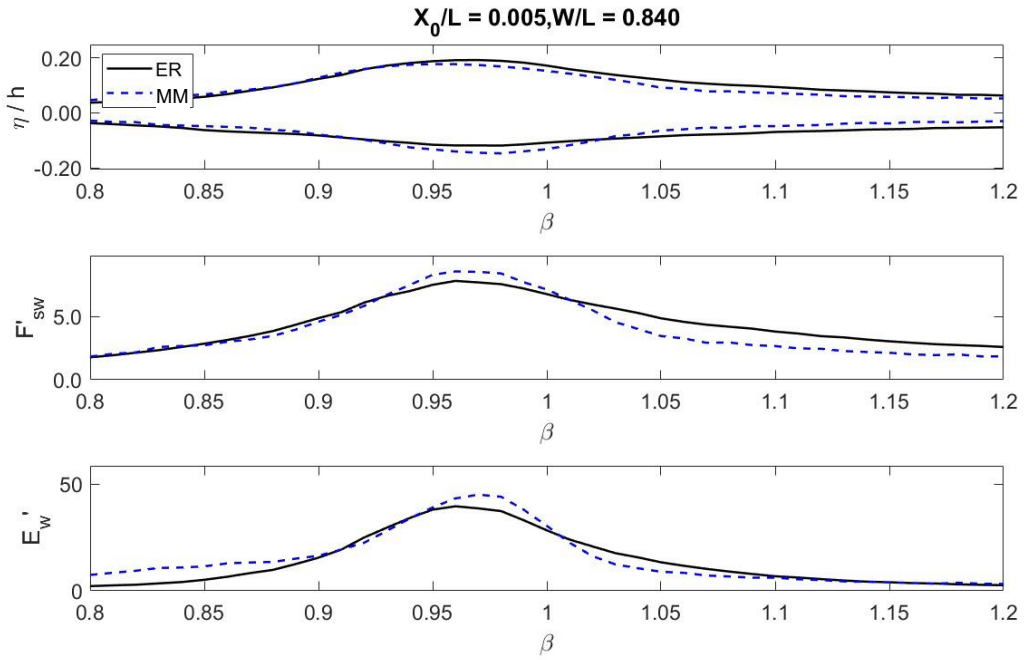

Figure 4.12 ER maximum wave heights, sloshing force, and dissipated energy response versus the MM model at X_0/L=0.005.

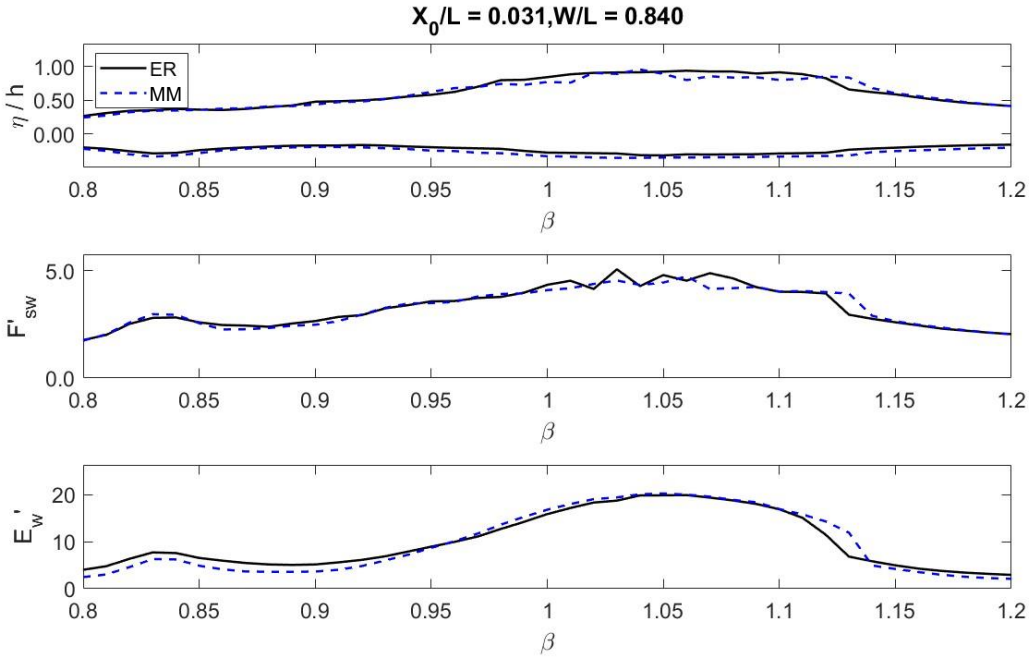

Figure 4.13 ER maximum wave heights, sloshing force, and dissipated energy response versus the MM model. X_0/L=0.031.

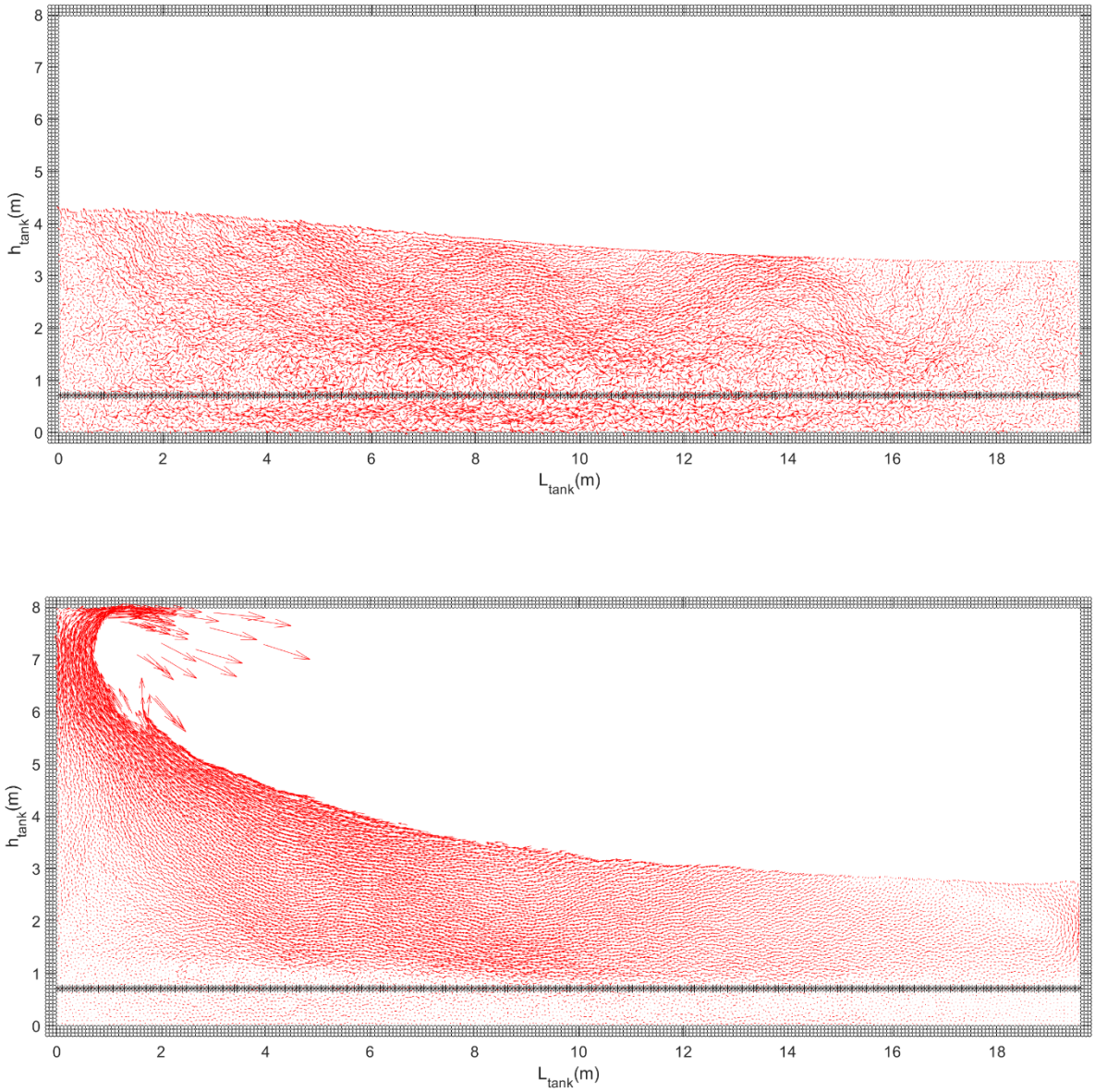

Figure 4.14 ER simulated fluid particles coloured according to their total pressure value at X_0/L=0.005, β=1.01(top figure) and X_0/L=0.031, β=1.01 (bottom figure).

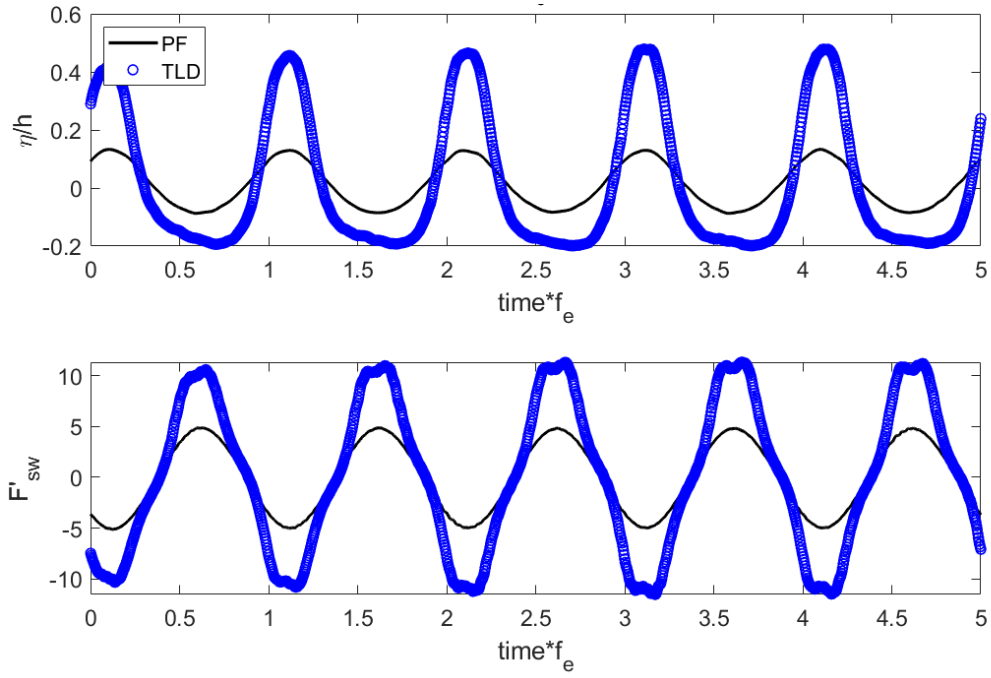

Figure 4.15 Perforated floor tank simulated wave height and sloshing force time history against tank without perforated floor case at X_0/L=0.005 and β=1.01

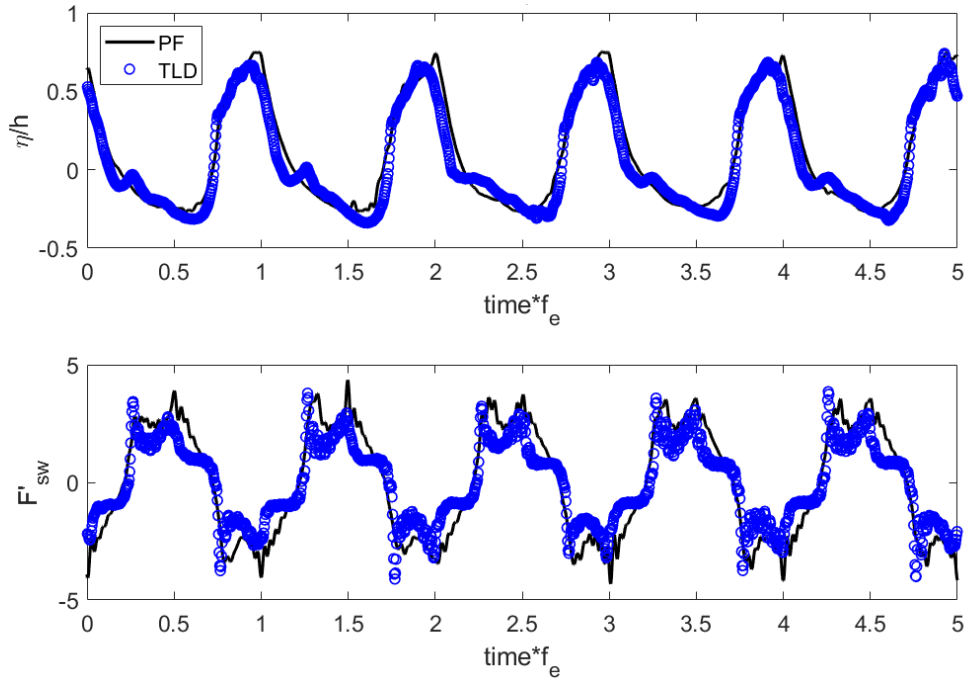

Figure 4.16 Perforated floor tank simulated wave height and sloshing force time history against tank without perforated floor case at X_0/L=0.031 and β=1.01

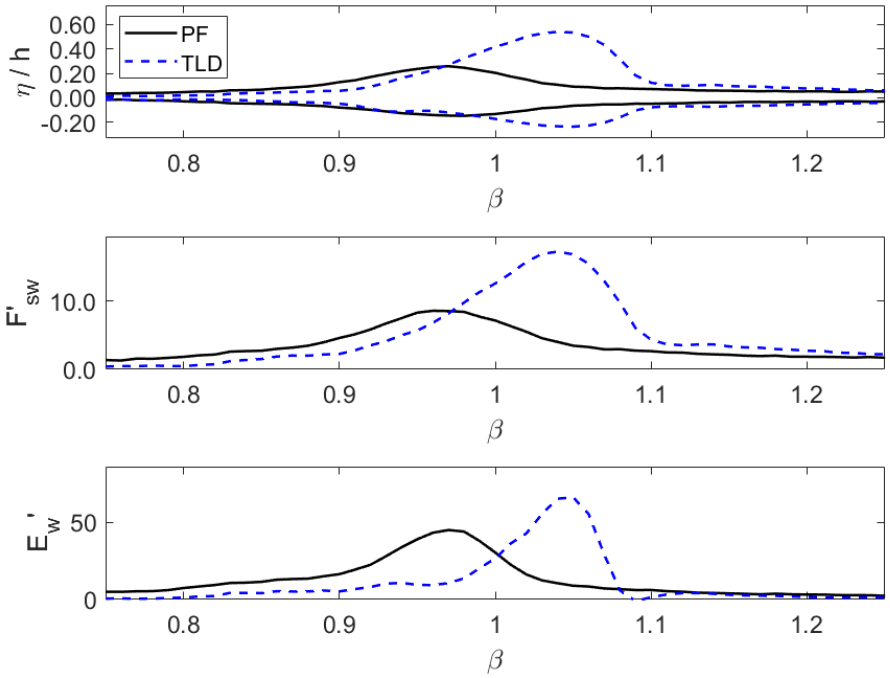

Figure 4.17 Perforated floor simulated maximum wave heights, sloshing force, and dissipated energy response versus tank without perforated floor case at X_0/L=0.005

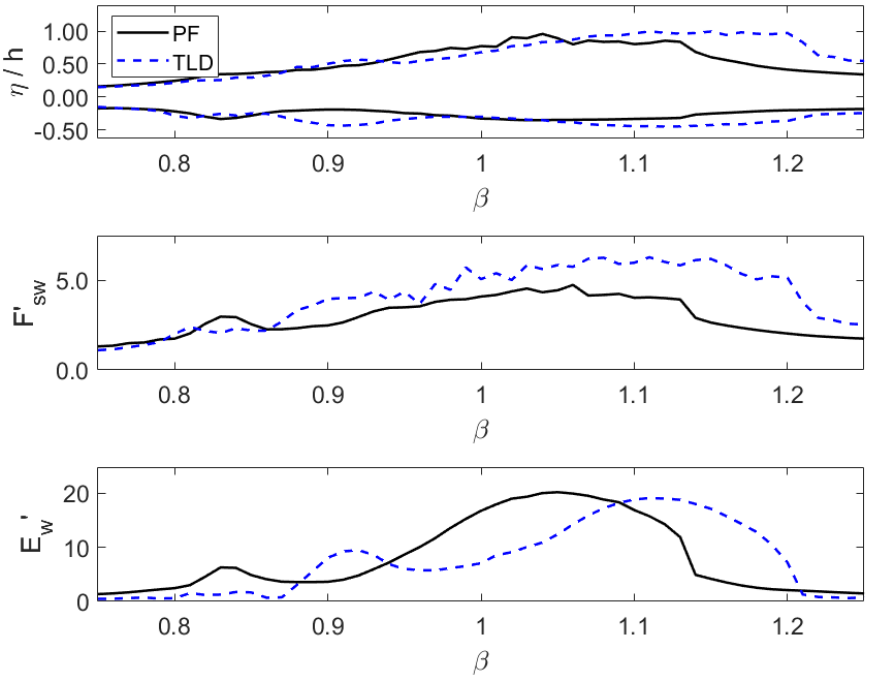

Figure 4.18 Perforated floor simulated maximum wave heights, sloshing force, and dissipated energy response versus tank without perforated floor case at X_0/L=0.031

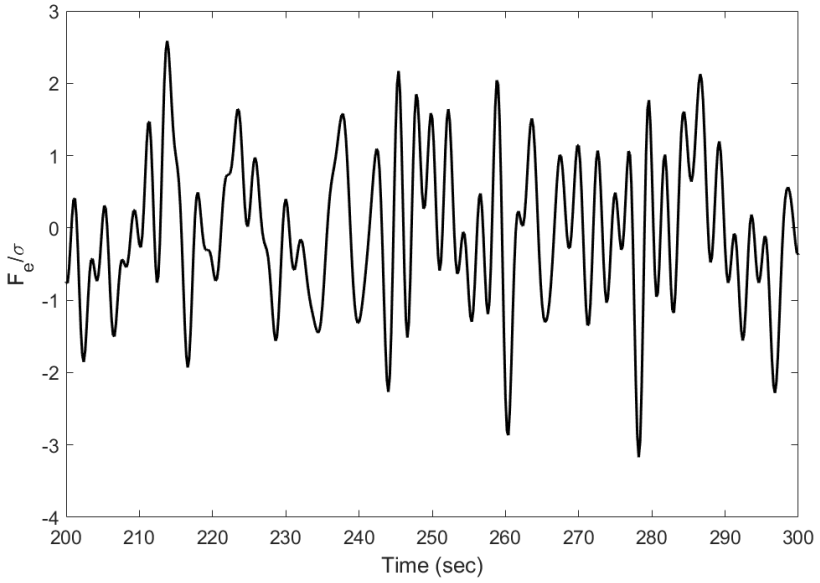

Figure 4.19 Sample segment for the random excitation used normalized by RMS of the signal.

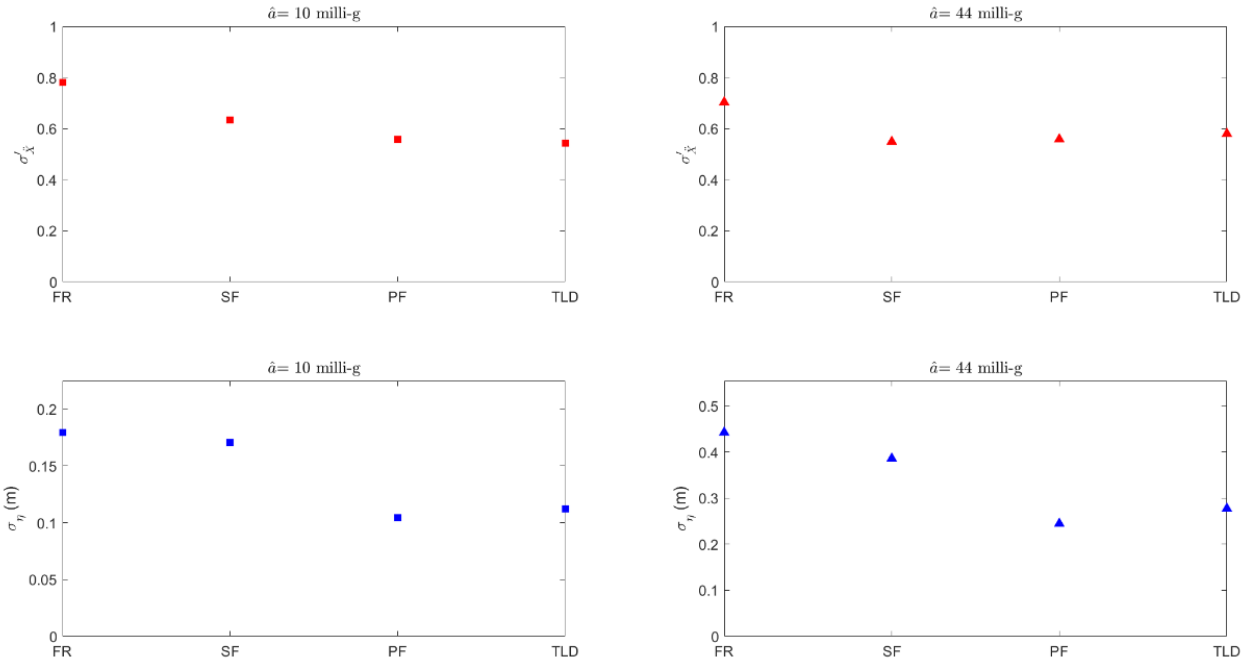

Figure 4.20 Normalized structural acceleration and wave height RMS for the structure only response values of $\hat{a}_{hourly}$= 10 milli-g and $\hat{a}_{hourly}$= 44 milli-g.

a) b)

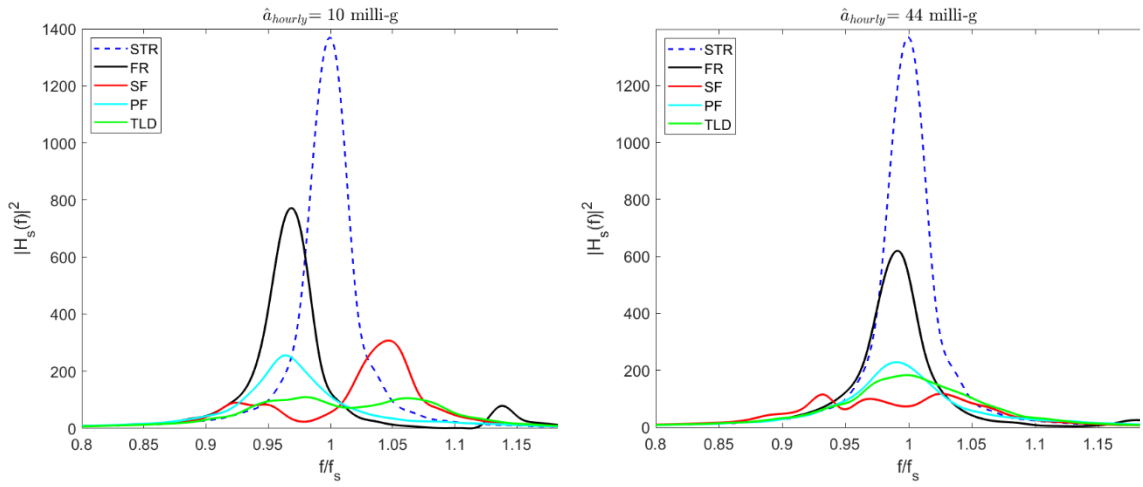

Figure 4.21 Comparison of the square modulus of the structure MAF: a) $\hat{a}_{hourly}$= 10 milli-g and b) $\hat{a}_{hourly}$= 44 milli-g.

a) b)

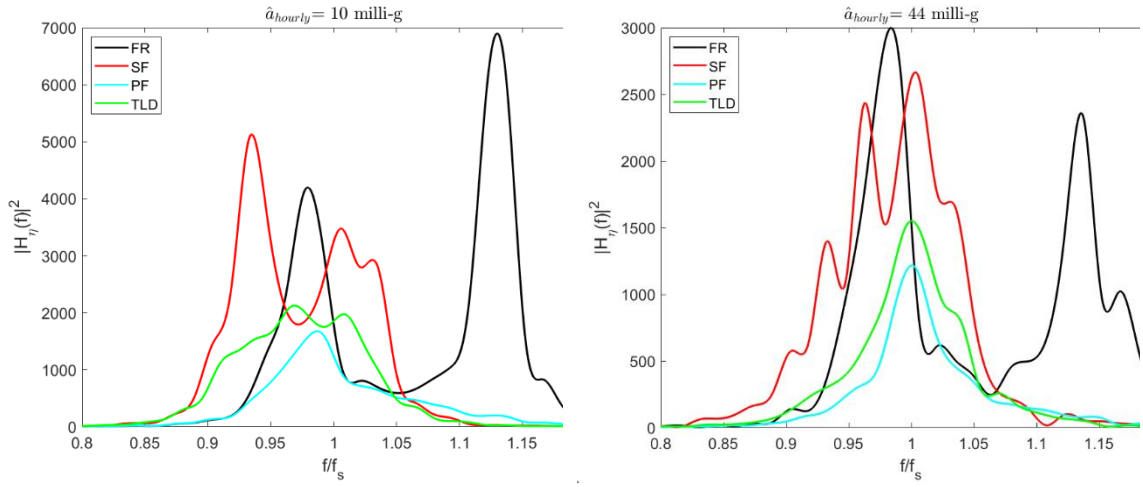

Figure 4.22 Comparison of the squared modulus of the frequency response function of wave heights of a) $\hat{a}_{hourly}$= 10 milli-g and b) $\hat{a}_{hourly}$= 44 milli-g.

Chapter 5: CONCLUSIONS AND RECOMMENDATIONS

5.1 Summary and Conclusions

Existing numerical models for tuned liquid dampers (TLDs) have limitations such as shallow fluid depths, low excitation amplitudes, specific tank bottom geometries and screen implementation and/or require substantial computer resources to execute. This study closes this research gap by developing a novel SPH model to efficiently numerically study tuned liquid dampers equipped with screens, using reduced computational requirements. The model provides an efficient tool for engineers to design and investigate a wide range of TLD applications and scenarios.

Chapter 2 presents and validates a novel macroscopic screen model using various existing experimental data. The model results are compared to a previously developed macroscopic model, and the model's ability to evaluate internal tank response fields, such as pressure and velocity fields, is tested.

Chapter 3 expands on the particle generation algorithm and boundary conditions to model tanks with sloped and curved bottom geometries with high flexibility to allow for any arbitrary tank bottom geometry. The performance of different tank bottom geometries is investigated ta large excitation amplitudes, which significantly exceed serviceability limit levels. A parametric study was conducted to assess the response of various tank bottom geometries and evaluate the model performance under different fluid depths and multiple screen configurations.

Chapter 4 investigates a realistic scenario of a dual-function tank with an intermediate perforated floor. Holes in the intermediate floor are simulated macroscopically using the

ER model and compared to microscopic results. The updated model was subsequently used to study the response of a structure-TLD system consisting of a dual-function tank coupled to an SDOF structure under random excitation.

The SPH model, along with the macroscopic screen model developed and tested in this study, has been found to provide efficient and robust results. In addition, is has flexible simulation capabilities allowing a wide range of tank bottom geometries, screens setup, fluid depths, and excitation amplitudes to be investigated.

Conclusions pertaining to each chapter are presented in the following sub-sections.

5.2 Macroscopic Screen Modelling in Rectangular TLDs

An existing in-house two-dimensional incompressible SPH model was modified by adding a Sub-Particle-Scale (SPS) turbulence model and energy calculation algorithm. The modified base code has been validated against the hydrostatic tank case and rectangular sloshing tank without screens. A novel macroscopic screen model has been proposed, based on the analogy between damping screen components and porous media, to capture the screens' drag effect on the flow implicitly. The model used Ergun’s equation to calculate the pressure drop in porous media to estimate the drag force of the screens due to their interaction with sloshing fluid. The main findings of this chapter are:

- The macroscopic SPH model efficiently modelled rectangular TLDs with screens across a wide range of excitation, frequencies and fluid depths using approximately 86% larger particle size than required by explicitly modelling the screen using a microscopic level model.

- The model eliminated the need for experimental screen data previously required by SPH macroscopic model to determine the loss coefficient, saving both time and experimental costs.
- Enhanced results were achieved using the new model ER model compared to the existing ME model for simulations at low excitation amplitudes and shallow water depths.

The ISPH model is able to capture the pressure and velocity fields inside the tank, which has not been reported previously with ISPH models. It can be observed that the model results were in good agreement with experimental data across a wide range of excitation amplitudes and frequencies while reducing the simulation time relative to both the ME (macroscopic) and microscopic screen models.

5.3 TLDs with Irregular Tank Bottom Geometries Equipped with Screens Under Large Amplitude Excitations

The SPH model with the ER screen model tested and validated in Chapter 2 was expanded to include an efficient boundary particle generation algorithm to model sloped and curved tank bottoms. An artificial repulsive force formulation was implemented to keep the fluid particles within the tank boundaries throughout the simulation. The modified model was first validated against a hydrostatic tank case. The model was then compared with results from available linear models under low harmonic excitation amplitudes for flat, sloped, parabolic, and circular bottom tank geometries. Subsequently, the response of the

four tanks was tested under large excitation amplitudes, and their performance was observed.

Significant conclusions from this study include the following:

- The implemented boundary-generating algorithm can model a variety of sloped or curved bottom geometries using an efficient number of boundary particles along the tank perimeter.
- The SPH model was found to be efficient and robust in modelling tanks equipped with multiple screens at different fluid depths under large excitation amplitudes.
- The curved bottom tanks exhibited the largest normalized sloshing force and lowest normalized wave height responses.
- Increasing the fluid depth ratio decreased the normalized wave height and sloshing force amplitudes for the different tank bottom geometries considered.

Internal pressure and velocities in different tanks can be captured efficiently, and the model allows the examination of various screen arrangements and locations. The flexibility and effectiveness of the model can aid in evaluating complex tank cases that previous models were unable to. It should be noted that careful tuning of simulation parameters (i.e., kernel radius, boundary particle spacings, etc.) is needed to ensure proper sizing and arrangement of fluid particles inside the tank borders, particularly at high excitation amplitudes.

5.4 Modelling Dual-function Tanks

Water storage tanks for fire suppression can theoretically function as TLDs. Typically, the fire water reserve is known at the early construction stages, while the TLD water depth is tuned near the completion of the structure. Also, fire codes require a constant continuous supply of water, which is challenging to accommodate in a TLD. A realistic situation of a dual-function tank is studied, having an adjustable intermediate perforated floor to tune the TLD without changing the overall capacity of the tank. Moreover, the perforated floor has holes sufficiently sized to allow water to move through the two compartments to provide a continuous water supply. The SPH model is employed to investigate the proposed dual-function tank by considering the holes and seepage around corners of the intermediate floor macroscopically using the ER model. The model was first validated using available horizontal baffled tank test results under low excitation. Subsequently, the macroscopic model of the dual-function tank was compared to other simulations where the intermediate perforated floor is modelled explicitly (MM). Frequency and time response studies were carried out at low and high excitation amplitudes. Finally, the TLD was coupled to an SDOF building to model the structure-TLD system response under band-limited white noise excitation. Some of the major conclusions from this study are summarized below.

- Water storage tanks for fire suppression can be utilized to fulfill the function of structure control as a Tuned Liquid Damper (TLD) if appropriately designed.
- To meet the fire code requirements, the perforated floor (e.g., with perforations) should be outfitted with holes that allow sufficient water passage between compartments to satisfy fire code requirements.

- The ER model was in good agreement with the explicit microscopic model (MM) for a tank with a perforated floor under harmonic excitation at different excitation amplitudes over a wide range of excitation frequencies, which eliminates the need for an expensive explicit model. This results in approximately a 30% reduction in computational time compared to the explicit simulation (MM model).
- When coupled to a structure, the perforated tank performance showed similar motion reduction performance compared to an optimized TL. It also had a lower free surface response amplitude than a tank with an intermediate solid floor and higher effective damping than a fire reserve tank (e.g. tank without an intermediate floor).

Accommodating fire codes and damping requirements using one tank can result in substantial floor savings and provides higher flexibility in utilizing existing water storage tanks as dampers. The simulations show that intermediate perforated floors can be adjusted to achieve efficient damping performance. SPH can be used to model a dual-function TLD coupled to a structure, demonstrating its ability to simulate a variety of TLD applications while maintaining feasible computational resources.

5.5 ISPH Model Setup

This section outlines the model setup and provides procedures to aid future researchers in implementing the SPH code in different applications. The code consists of subroutines written entirely in Fortran, and the code is structured in serial implementation that can be

executed on personal computers. Simulations of different frequencies or fluid depths were executed in parallel on individual CPU cores, using computing resources allocated by Compute Canada for efficient time management. Parallelization of the SPH code was not part of this study; however, it would be beneficial for 3D simulations.

The code uses a simple input file to select different simulation parameters based on the desired modelling case. The model can be adjusted to output time histories for wave heights, fluid pressure, fluid velocity, sloshing forces, base shear forces, and screen forces at each time step at defined locations inside or on the boundaries of the tank.

5.5.1 Tuning Simulation Parameters

Based on the tank characteristics and excitation amplitude, some parameters require adjustments to conduct a stable simulation and prevent fluid particles from escaping. As mentioned earlier, the base SPH code is equipped with a turbulence model, boundary generation algorithm, and repulsive force method to enhance simulation performance. The following steps are recommended for successful modelling.

- For low Reynolds number simulations, the effect of the turbulence model is negligible and can be turned off for faster simulations.
- The code can generate particles internally and read particles generated outside Fortran if MATLAB is used.
- The code follows the parabolic function $y = B + (x - C)^2$, where B is the y-intercept and C is the x-intercept. When entering input numbers, care should be taken to correctly simulate the desired parabolic function.

- Generating curved boundaries may require several iterations to ensure that the rule of $\delta \leq dp$ is satisfied for the appropriate discretization of boundaries.
- Wave and pressure probe locations on the tank boundaries must be placed on the first layer of boundary particles to eliminate spurious results.
- The simulation time step (dt) should be adjusted to conform to CFL conditions. However, throughout all the conducted simulations in this study, a time step of 10^{-4} was found to be adequate.
- Fluid and boundary particle spacing (dp) is critical for efficient and accurate simulation. Conducting a spatial convergence check, as mentioned in Chapter 4, is recommended to determine a suitable spacing value. Balancing this number is essential in reducing the number of boundary layers while keeping fluid particles intact and producing accurate results.
- Screen particle spacing (dp_{sc}) is advised to be $1dp$-$1.5dp$ for stable results.
- Fluid and boundary particle kernel radius (h_r) selection impact the simulation's performance and accuracy. Fine-tuning between $1.1dp$ to $1.5dp$ is suggested.
- The screen particle kernel radius (h_{sc}) is suggested to be between $3dp$ to $4dp$.
- A pressure blending factor (α) less than or equal to 0.01 provided similar results for the TLD applications investigated in this study.

5.6 Recommendations and Future Work

This section summarizes some recommendations for future research:

- **SPH Code Parallelization:** Several code upgrades could be implemented, including a parallel scheme instead of the current serial version. Code parallelization will improve code efficiency and reduce computational time.
- **3D Expansion:** The current code is restricted to two-dimensional simulations. However, expansion to 3D would allow the investigation of tanks with irregular geometries and shapes. The code grants the flexibility of expansion to 3D by providing corrections to the existing governing equations and boundary conditions. Boundary generation algorithms must be revisited to guarantee efficient particle spacing generation along tank walls.
- **SPH Code Applications:** The SPH code can be implemented to model any sloshing tank in different engineering fields, such as naval vessels, ocean engineering, satellites, LPG tanks, and offshore structures. Moreover, the macroscopic model can solve the flow in porous media or seepage in packed soil beds with minimal alterations.
- **Boundary Conditions:** Although the code provided suitable results using the current boundary conditions, several enhancements could be made to efficiently prevent particle escapement during long-duration simulations without using expensive numerical solutions (e.g., more boundary layers, small particle sizes, etc.).

- **Dual-function Tank Experiments**: Experimental data is scarce in the TLD literature for dual-function tanks with intermediate perforated floors. Conducting an experimental study on this type of tank would provide data for numerical validation.
- **Dual-function Tank Configurations**: This study only investigated a rectangular dual-function tank with an intermediate perforated floor. Future research could examine the response of different tank bottom geometries and different hole configurations in the intermediate perforated floor (e.g., number of holes, hole sizes, locations, etc.) to enhanced TLD performance.